

**Towards a Rational Design of  
Microcapsules  
-Mechanical Properties of the Shell-**

Dissertation

zur Erlangung des akademischen Grades eines

Doktors der Naturwissenschaften

-Dr. rer. nat.-

der Fakultät Biologie, Chemie und Geowissenschaften

der Universität Bayreuth

vorgelegt von

**Melanie Pöhlmann**

geboren in Burglengenfeld

Bayreuth, 2013







---

Die vorliegende Arbeit wurde in der Zeit von August 2007 bis Oktober 2013 in Bayreuth am Lehrstuhl Physikalische Chemie II unter der Betreuung von Herrn. Professor Dr. Andreas Fery angefertigt.

Vollständiger Abdruck der von der Fakultät für Biologie, Chemie und Geowissenschaften der Universität Bayreuth genehmigten Dissertation zur Erlangung des akademischen Grades eines Doktors der Naturwissenschaften (Dr. rer. nat.).

Dissertation eingereicht am:	11.12.2013
Zulassung durch die Promotionskommission:	18.12.2013
Wissenschaftliches Kolloquium:	20.05.2014

Amtierender Dekan:	Prof. Dr. Rhett Kempe
--------------------	-----------------------

Prüfungsausschuss:

Prof. Dr. Andreas Fery	(Erstgutachter)
Prof. Dr. Thomas Scheibel	(Zweitgutachter)
Prof. Dr. Georg Papastavrou	(Vorsitz)
Dr. habil. Seema Agarwal	

---

---

*„Der höchste Lohn für unsere Bemühungen ist nicht das,  
was wir dafür bekommen,  
sondern das, was wir dadurch werden.“*

John Ruskin

---

*Meiner Familie*

---

---

## Table of Contents

<b>Summary .....</b>	<b>1</b>
<b>Zusammenfassung .....</b>	<b>3</b>
<b>1. Introduction.....</b>	<b>5</b>
<b>2. Status of the Field .....</b>	<b>9</b>
2.1 Classification of Microcapsules .....	9
2.1.1 Mechanical Production Methods .....	10
2.1.2 Template-Assisted Production Methods .....	10
2.1.3 Self-Assembly Production Methods .....	12
2.1.4 Combination of Template-Assisted and Self-Assembly Methods.....	12
2.2 Mechanical Characterization of Microcapsules .....	13
2.2.1 Ensemble Methods.....	14
2.2.2 Single-Microcapsule Methods .....	15
2.3 Overview-Table - Mechanical Properties of Microcapsules.....	23
2.4 Atomic Force Microscopy - Working Principle.....	25
2.4.1 AFM Components .....	25
2.4.2 Cantilever Calibration.....	27
2.4.3 Colloidal Probe AFM .....	28
2.4.4 Force-Distance Curves.....	29
2.5 Capsule Mechanics – Models & Theory .....	30
2.5.1 Reissner -Thin Shells, Small Deformations.....	31
2.5.2 Pogorelov - Thin Shells, Large Deformations .....	33
2.5.3 Burst of Microcapsules .....	35
2.6 Objective of the thesis.....	35
2.7 References.....	36
<b>3. Overview of the thesis.....</b>	<b>43</b>
3.1 Mechanics of Microcapsules: From Stability to Function (Chapter 4).....	43
3.2 Polymeric Air-Filled Microbubbles for Theranostic Applications: Burst Release of Therapeutic Gases (Chapter 5).....	45

---

3.3 Hybrid Contrast Agents for Ultrasound and MRI Imaging: Impact of Nanoparticle Integration on Shell Properties in Low and High Frequency Mechanics (Chapter 6).....	49
3.4 Perfume-filled Aminoplast Microcapsules: Tuning Shell Properties for Controlled Release of Perfume in Fabric Softeners (Chapter 7) .....	52
3.5 Individual Contributions to Joint Publications .....	56
<b>4. Microcapsule Mechanics – A Review Article .....</b>	<b>61</b>
<b>5. Microbubbles for Theranostics .....</b>	<b>105</b>
<b>6. Magnetic Microbubbles -Hybrid Contrast Agents .....</b>	<b>129</b>
<b>7. Aminoplast Core/Shell Microcapsules .....</b>	<b>173</b>
<b>List of Abbreviations and Symbols .....</b>	<b>197</b>
<b>List of Publications .....</b>	<b>201</b>
<b>Danksagung .....</b>	<b>205</b>
<b>Erklärung.....</b>	<b>208</b>

## Summary

This thesis describes novel strategies for a rational design of microcapsules that are of fundamental interest for colloid and interface science as well as for industrial large-scale processes. In the focus of this work are artificial polymeric microcapsules, which find broad application in drug delivery, contrast imaging, flavor or fragrance encapsulation, phase change materials and functional textiles. A great demand for a rational microcapsule design is observed whenever new application fields are exploited, microcapsule production is up-scaled or the performance of microcapsules is optimized.

Mechanical properties of microcapsules are the central topic of this thesis because they play a key role in view of the mechanical stability, release behavior, shelf life, deformation behavior, and adhesion of microcapsules. Thus, mechanical properties are considered to have an essential impact on the macroscopic performance of microcapsules and thus on the application itself. Hence, the tailoring of microcapsule's shell mechanics has turned into one of today's challenges when microcapsule-based products are designed or optimized.

A basic requirement for tailoring microcapsule's mechanical properties is the knowledge of structure-property relations with regard to critical parameters such as the capsule's geometry, shell thickness, shell material properties, or core material properties. Within this thesis a concept was developed that allows for a straightforward analysis of structure-property relations in an efficient and reproducible way. One of the main questions answered by the developed approach is how synthesis process parameters affect shell properties, and thus the mechanical and macroscopical response of microcapsules. The approach is based on characterization techniques that allow experiments on the single-particle-level such as optical microscopy, transmission electron microscopy and atomic force microscopy. Even though the measurement of single particles does not represent a high throughput method, it provides the basis to link morphological with mechanical properties. Furthermore, single-particle-experiments are used for direct determination of critical parameters with sufficient high resolution in the nano- and micrometer regime and accurate information on their dispersity. Often there are knowledge gaps observed

between the synthesis of microcapsules and their performance measured via macroscopic tests (batch tests with a large number of microcapsules). The type of macroscopic test strongly depends on the intended application and can range from certified application tests to empirical panel tests. By analyzing and understanding, structure-property relations (synthesis –performance) gaps can be closed and macroscopic properties can be tailored.

Three types of polymeric microcapsules have been studied in this thesis:

- 1) Gas-filled microbubbles with a shell made of poly(vinyl alcohol) are used for theranostic applications (ultrasound imaging and drug delivery),
- 2) Magnetic microbubbles with a shell made of poly(vinyl alcohol) and super paramagnetic iron oxide nanoparticles are used as hybrid contrast agents for ultrasound and magnetic resonance imaging, and
- 3) Aminoresin (melamine formaldehyde) microcapsules are used for the industrial encapsulation of fragrances.

In summary, this thesis presents a reproducible and broad-applicable characterization concept for analyzing microcapsules' structure-property-relations. The developed concept proofed to be of value for the systematic design and sustainable optimization of microcapsules because it is closing existing knowledge gaps between synthesis and application. This was clearly illustrated by the successful clarification of structure-property relations in three different types of microcapsule systems. In conclusion, the presented concept shows great potential to tailor mechanical properties of microcapsules for a broad range of capsule systems.

## **Zusammenfassung**

Die vorliegende Arbeit stellt neue Strategien zum systematischen Design von Mikrokapseln vor, welche von fundamentalem Interesse für die Kolloid- und Grenzflächenforschung als auch für die industrielle Herstellung sind. Gegenstand der Arbeit sind künstliche polymere Mikrokapseln, die eine breite Anwendung in der gezielten Pharmakotherapie, der Kontrastmittel-unterstützten Bildgebung, der Verkapselung von Aroma- und Parfümstoffen, Latentwärmespeichern und Funktionsmaterialien finden. Die Frage nach einem rationalen Design von Mikrokapseln entsteht vor allem beim Erschließen neuer Anwendungsfelder, beim Anpassen von Aufskalierungsprozessen oder beim Optimieren makroskopischer Eigenschaften.

Die mechanischen Eigenschaften von Mikrokapseln sind zentrales Thema dieser Arbeit, weil sie eine Schlüsselrolle hinsichtlich der mechanischen Stabilität, der Freisetzung, der Haltbarkeit, und des Deformations- und Adhäsionsverhaltens einer Mikrokapsel einnehmen. Aus diesem Grund sind mechanische Eigenschaften extrem wichtig für das makroskopische Verhalten von Mikrokapseln während ihrer Anwendung. Die gezielte Anpassung der Schalenmechanik zählt deshalb auch zu den aktuellen Herausforderungen wenn mikrokapsel-basierter Produkte neu hergestellt oder optimiert werden.

Ein genaues Verständnis der Struktur-Eigenschafts-Beziehungen stellt eine grundlegende Anforderung dar, um mechanische Eigenschaften von Mikrokapseln systematisch anzupassen. Im Fokus stehen hier Parameter, wie zum Beispiel die Partikelgeometrie, die Wanddicke, das Schalenmaterial, und das verkapselten Materials. Diese Arbeit widmet sich der schrittweisen Aufklärung von Struktur-Eigenschafts-Beziehungen von Mikrokapseln auf einfache und reproduzierbare Art und Weise. Eine der Hauptfragen, die mit Hilfe dieser Charakterisierungs-Strategie beantwortet werden kann, ist wie der Herstellungsprozess die Eigenschaften der Kapselschale und somit das mechanische und makroskopische Verhalten beeinflusst. Realisiert wird dies durch Analyse-Techniken, die eine Charakterisierung auf der Einzelpartikel-Ebene zulassen wie zum Beispiel optische Mikroskopie, Transmissions-Elektronenmikroskopie und Rasterkraftmikroskopie. Obwohl

Einzelpartikel-Messungen keine hohen Durchsätze erlauben, so ermöglichen diese überhaupt erst eine Korrelation der morphologischen und mechanischen Eigenschaften. Außerdem ist eine direkte Bestimmung kritischer Parameter mit einer ausreichend hohen Auflösung im Nano- und Mikrometer-Bereich möglich, inklusive einer präzisen Angabe der Dispersität. Ein Brückenschlag zur Anwendung wird schließlich durch eine Korrelation der Ergebnisse mit den makroskopischen Eigenschaften erreicht. Die Art des makroskopischen Tests hängt von der Art der Anwendung ab und kann zertifizierte Qualitätstests als auch empirische Panel Tests umfassen. Durch das vorgestellte Charakterisierungskonzept können Struktur-Eigenschafts-Beziehungen aufgeklärt werden und eine Brücke zwischen der Herstellungsweise und der makroskopischen Funktion geschlagen werden.

In dieser Arbeit wurden drei verschiedene polymere Mikrokapselsysteme untersucht:

- 1) Gas-gefüllte Mikrobäschen mit einer Schale aus Polyvinylalkohol, die theragnostische Anwendungen im Bereich kontrastverstärkter Ultraschall und Pharmakotherapie ermöglichen sollen.
- 2) Magnetische Mikrobäschen mit einer Schale aus Polyvinylalkohol und superparamagnetischen Eisenoxid-Nanopartikeln, die als Hybrid Kontrast-Mittel für kombinierte Ultraschall- und Magnetresonanztomographie zum Einsatz kommen.
- 3) Aminoplast (Melamin Formaldehyd) Mikrokapseln, die industriell für die Verkapselung von Parfümstoffen eingesetzt werden.

Zusammenfassend stellt diese Arbeit ein reproduzierbares und breit-anwendbares Charakterisierungskonzept vor, mit dem Struktur-Eigenschafts-Beziehungen in Mikrokapseln analysiert werden können. Das vorgestellte Konzept ist wertvoll für ein rationales Design von Mikrokapseln sowie für deren nachhaltige Optimierung. Dies konnte anhand der erfolgreichen Aufklärung von Struktur-Eigenschafts-Beziehungen in drei Mikrokapselsystemen gezeigt werden. Die vorgestellte Methode besitzt großes Potential für die gezielte Anpassung mechanischer Eigenschaften für eine Vielzahl von Kapselsysteme.

## 1. Introduction

Encapsulation is a frequently used solution in research and industry and aims on the protection, transport and controlled release of substances. In nature plenty of biological capsule systems exist - ranging from plant seeds on the macroscopic level down to virus capsids on the microscopic level -, which served as paradigms for artificial intelligent packaging solutions.<sup>1</sup>

The first artificial man-made microcapsules were prepared by Bungenberg de Jong and his co-workers<sup>2</sup> in the 1930s when they introduced the concept of coacervation and produced droplets of colloidal size enveloped by macromolecules.<sup>3</sup> Two decades later, in the 1950s, the chemists Green and Schleicher<sup>4</sup> launched with the production of carbonless copy paper the first industrial large-scale production of microcapsules. Since then microcapsule research and production developed in a highly interdisciplinary research field, where experts from fundamental colloid- and interface science, physical chemistry, macromolecular chemistry, organic and inorganic chemistry, biophysics and experts from applied sciences such as medicine and engineering met. Thus it is not surprising that microcapsules find application in diverse fields such as pharmacy<sup>5-11</sup>, food industry<sup>12-20</sup>, agriculture<sup>21-24</sup>, cosmetics<sup>25,26</sup>, textile industry<sup>27-29</sup>, printing<sup>30</sup>, biosensor engineering<sup>31-33</sup>, active coatings<sup>34, 35</sup> and construction<sup>36-38</sup>.

The interdisciplinary user community and the resulting demand for custom-made microcapsules with distinct functionalities is constantly rising. Scientific interest in microcapsules was also further pushed in the last twenty years through the development of innovative bottom-up synthesis strategies for microcapsules such as the layer-by-layer assembly (late 1990s) and by novel characterization techniques on the single-capsule level (start 2000s). In the same time period, the industrial sector gained great expertise in continuous manufacturing processes for the production of microcapsules on a large-scale with manageable costs. Typically millimeter or micrometer-sized capsules are produced in these industrial processes by using physical-mechanical encapsulation techniques or up-scalable chemical processes such as coacervation or *in situ* polymerization.<sup>39</sup> However, structure-property

relations of microcapsules produced by these industrial manufacturing processes are not yet understood and controlled entirely.

Thus, a systematic design of microcapsules is of interest for both - industrial manufacturers and producers of novel custom-made microcapsules with multifunctional character.

## References

1. Sliwka, W., *Angew Chem Int Ed Engl* **1975**, 14, (8), 539-50.
2. Bungenberg de Jong, H. G., *Protoplasma* **1932**, 15, (1), 110-173.
3. Arshady, R., *Polym. Eng. Sci.* **1990**, 30, (15), 905-914.
4. Green, B. K.; Lowell, S. US 2730456 **1953**.
5. Youan, B. B. C.; Jackson, T. L.; Dickens, L.; Hernandez, C.; Owusu-Ababio, G., *J. Control. Release* **2001**, 76, (3), 313-326.
6. Kataoka, K.; Harada, A.; Nagasaki, Y., *Adv. Drug Deliv. Rev.* **2001**, 47, (1), 113-131.
7. Bae, Y.; Kataoka, K., *Adv. Drug Deliv. Rev.* **2009**, 61, (10), 768-784.
8. Discher, D. E.; Eisenberg, A., *Science* **2002**, 297, (5583), 967-973.
9. Langer, R., *Nature* **1998**, 392, (6679), 5-10.
10. De Geest, B. G.; De Koker, S.; Sukhorukov, G. B.; Kreft, O.; Parak, W. J.; Skirtach, A. G.; Demeester, J.; De Smedt, S. C.; Hennink, W. E., *Soft Matter* **2009**, 5, (2), 282-291.
11. Tong, W. J.; Gao, C. Y., *J. Mater. Chem.* **2008**, 18, (32), 3799-3812.
12. Madene, A.; Jacquot, M.; Scher, J.; Desobry, S., *International Journal of Food Science & Technology* **2006**, 41, (1), 1-21.
13. Rokka, S.; Rantamaki, P., *Eur. Food Res. Technol.* **2010**, 231, (1), 1-12.
14. Gharsallaoui, A.; Roudaut, G.; Chambin, O.; Voilley, A.; Saurel, R., *Food Res. Int.* **2007**, 40, (9), 1107-1121.
15. Onwulata, C. I., Encapsulation of New Active Ingredients. In *Annual Review of Food Science and Technology*, Annual Reviews: Palo Alto, **2012**; Vol. 3, 183-202.
16. Ezhilarasi, P. N.; Karthik, P.; Chhanwal, N.; Anandharamakrishnan, C., *Food Bioprocess Technol.* **2013**, 6, (3), 628-647.
17. Kandansamy, K.; Somasundaram, P. D., *Int. J. Food Eng.* **2012**, 8, (2), 1-15.
18. Shahidi, F.; Han, X. Q., *Crit. Rev. Food Sci. Nutr.* **1993**, 33, (6), 501-547.
19. Champagne, C. P.; Fustier, P., *Curr. Opin. Biotechnol.* **2007**, 18, (2), 184-190.
20. Desai, K. G. H.; Park, H. J., *Dry. Technol.* **2005**, 23, (7), 1361-1394.
21. Tsuji, K., *Journal of Microencapsulation* **2001**, 18, (2), 137-147.
22. Salem, M. A.; Al-Zayadneh, W.; Cheruth, A. J., *Water Resources Management* **2010**, 24, (10), 2237-2246.
23. Sopena, F.; Maqueda, C.; Morillo, E., *Cienc. Investig. Agrar.* **2009**, 36, (1), 27-42.

24. Hack, B.; Egger, H.; Uhlemann, J.; Henriët, M.; Wirth, W.; Vermeer, A. W. P.; Duff, D. G., *Chem. Ing. Tech.* **2012**, 84, (3), 223-234.
25. Sukhorukov, G. B.; Mohwald, H., *Trends Biotechnol.* **2007**, 25, (3), 93-98.
26. Ammala, A., *International Journal of Cosmetic Science* **2013**, 35, (2), 113-124.
27. Nelson, G., *Int. J. Pharm.* **2002**, 242, (1-2), 55-62.
28. Sanchez, L.; Lacasa, E.; Carmona, M.; Rodriguez, J. F.; Sanchez, P., *Ind. Eng. Chem. Res.* **2008**, 47, (23), 9783-9790.
29. Teixeira, C.; Martins, I. M. D.; Mata, V. L. G.; Barreiro, M. F. F.; Rodrigues, A. E., *J. Text. Inst.* **2011**, 103, (3), 269-282.
30. Akers Jr, C. E.; Sun X, J. US 7354962, **2008**.
31. Park, B. W.; Yoon, D. Y.; Kim, D. S., *Biosens. Bioelectron.* **2010**, 26, (1), 1-10.
32. Roitman, D. B. US 07312040, Dec 26 **2007**.
33. Chaudhary, A.; McShane, M. J.; Srivastava, R., *Analyst* **2010**, 135, (10), 2620-2628.
34. Shchukin, D. G.; Grigoriev, D. O.; Mohwald, H., *Soft Matter* **2010**, 6, (4), 720-725.
35. Shchukin, D. G.; Mohwald, H., *Chemical Communications* **2011**, 47, (31), 8730-8739.
36. Raj, V. A. A.; Velraj, R., *Renew. Sust. Energ. Rev.* **2010**, 14, (9), 2819-2829.
37. Waqas, A.; Din, Z. U., *Renew. Sust. Energ. Rev.* **2013**, 18, 607-625.
38. Boh, B. S., Bostjan, *RMZ - Materials and Geoenvironment* **2008**, 55, (3), 329-344.
39. Gouin, S., *Trends in Food Science & Technology* **2004**, 15, (7-8), 330-347.



## 2. Status of the field

### 2.1 Classification of Microcapsules

The term *microencapsulation* is used in a broad range of applications and by a large and very interdisciplinary community.<sup>1-5</sup> Thus, it is not surprising that diverging definitions are found in literature. The most general definition for *microencapsulation* is the process by which one material of microscopic dimension is entirely coated by another. The product of this process is called *microcapsule* and can be subdivided in an inner phase, also called core or interior, and an outer phase, the shell, wall or membrane.



Figure 2-1 Classification of microcapsules according to the core material (A), the encapsulation complexity, (B) and the shell design (C).

In 2006, Gosh et al.<sup>1</sup> classified capsules according to their encapsulation complexity: mono-nuclear, poly-nuclear and matrix-based. In Figure 2-1 an extended version of this classification is illustrated. Microcapsules can be classified according to the potential core materials that can take all aggregate states - solid, liquid or gaseous - (2-1 A), the encapsulation complexity of microcapsules that can increase from mono-shelled to poly-shelled to matrix-based structures (2-1 B) and possible shell materials, which can range from homogenous wall materials, colloidal particles to complex structured materials (e.g. multilayers or composite materials) (2-1 C). As Gosh et al.<sup>1</sup> points out in his review, the material - to be encapsulated - determines the synthesis method. Thus, the capsule design is predetermined and an optimization of microcapsules' properties is often limited to the adjustment of certain synthesis parameters. More options exist for the adjustment of physical-chemical properties -

solubility or colloidal stability - of produced microcapsules, by modifying the shell's surface properties in a post-synthesis step.

This thesis will concentrate on mono-shelled microcapsules, where the shell material dominates the mechanical properties. Thus, microcapsules with a fluid core and a solid shell are in the focus. Fery and co-workers<sup>6</sup> reviewed the mechanical properties of nano- and microcapsules, where they highlighted the dimensions of the shell - diameter and shell thickness - as critical parameters for the characterization and theoretical treatment of microcapsule mechanics. Hence, microcapsule-manufacturing processes are discussed with regard to the potential to adjust capsule radius and shell thickness. Even though a large variety of preparation techniques exists, the microcapsules' synthesis can be condensed into four types of manufacturing processes. The manufacturing techniques are ordered according to their increasing precision in adjusting shell thickness and capsule geometry:

- Physical-mechanical methods
- Template-assisted methods
- Self-assembly methods
- Combination of template-assisted and self-assembly methods.

### **2.1.1 Mechanical Production Methods**

*Physical-mechanical methods* are used in standard industrial large-scale processes. Examples are spray drying, co-extrusion, spinning disk, multiple-nozzle spraying, fluidized-bed coating or vacuum encapsulation.<sup>1, 5</sup> These are economic processes, which allow easy handling, upscaling and a multi-tonne production. However, these methods offer limited control over capsule radius and shell thickness. Diameter and shell thickness are only controlled in the range of millimeters, leading to rather high polydispersity in size and shell thickness. The majority of encapsulated particles used for this technique are solid and the shell is added for protective reasons (e.g. palm oil coating for e.g. sugar crystals). For this type of microcapsule the core material is dominating the microcapsule's mechanics.

### **2.1.2 Template-Assisted Production Methods**

Template-assisted methods allow for a precise adjustment of the capsule diameter. Different methods are available that can be classified according to their potential to

produce monodisperse microcapsules with defined diameter. The section starts with methods that offer control over the capsule diameter with certain polydispersity. Followed by techniques that offer the preparation of exact monodisperse microcapsules.

*Emulsion-based processes* belong to the soft template-assisted methods. They are intensively used in research and industry.<sup>5</sup> For soft-template-assisted methods the diameter of microcapsules is limited to the size distribution of the produced emulsion droplets.<sup>7</sup> Generally, emulsions are distinguished in microemulsions and macroemulsions. While microemulsions, stabilized by surfactants, are thermodynamically stable and offer a monodisperse droplet distribution, a broad range of droplet diameters characterizes the droplets of macroemulsions. Parameters that can be used to adjust the diameter of emulsion droplets are the interfacial tension (surfactants, dispersants), the used stirrer and the stirring speed. The majority of industrial processes is based on macroemulsions, because capsules with a maximum payload and minimum costs for encapsulation material can be produced. However, the droplets of macroemulsions are only kinetically stable and tend to coalesce, which is increasing the polydispersity in size. Examples for such processes are interfacial polymerizations<sup>8-11</sup>, interfacial assemblies<sup>12</sup>, and phase separation processes like coacervation<sup>13, 14, 15</sup>. The shell thickness is either weight- or time-controlled in such synthesis approaches. Moreover, also other parameters such as the interfacial area of the emulsion droplets need to be considered when the thickness of the shell needs to be adjusted.<sup>16</sup>

*Microfluidic processes*<sup>17-23</sup> take an exceptional position compared to industrial emulsion-based methods, because they allow producing microcapsules with ideal monodisperse diameter. Typically, microfluidic processes produce single microcapsules by dripping or jetting an inner fluid into a immiscible second fluid, which is then enveloped by a third fluid.<sup>17</sup> The volume of the inner phase determines the diameter of the core and is coarsely adjusted by the diameter of the used capillary and fine-tuned by the flow rate of the inner fluid.<sup>18</sup> Shells around the core phase are formed through consolidation of the middle phase (second fluid). The volume of the middle phase is controlled by the flow rate ratio of the inner and middle fluid. Thus, the flow can be used to adjust the shell thickness.<sup>18</sup> However, further fine-tuning of the microcapsule's diameter and shell thickness is limited, because they cannot be

adjusted independently from each other. In summary, this technique allows for a production of microcapsules with defined core volume and shell volume. However, inhomogen shells can occur by an off-centering of the core or changes of the cross-linking process.<sup>19</sup> The relation between flow rates and geometric parameters changes when the chemical composition of a fluid changes. Thus, new shell compositions still require a corresponding design map to control the capsule's geometry. Another method reported recently for the production of microcapsules is *inkjet printing*<sup>24, 25</sup>, using a piezoelectric inkjet head to adjust the capsule diameter.

Classic template-assisted<sup>26-32</sup> methods use hard colloidal particles as templates to produce microcapsules with defined shape and size.<sup>33</sup> A crucial point for the production of hollow fluid-filled microcapsules is the decomposition and dissolution of the core material.

### **2.1.3 Self-Assembly Production Methods**

Self-assembly methods are ideally suited to control the shell thickness. Examples for self-assembly processes controlling shell thicknesses are defined block copolymers for the production of polymerosomes<sup>6, 54-59</sup>, lipids used for shells made of bilayers, or colloidal particles for the production of colloidosomes<sup>34-36</sup>.

### **2.1.4 Combination of Template-Assisted and Self-Assembly Methods**

Layer-by-layer (LBL) deposition technique is a classic hard template-assisted method combined with a self-assembly of the shell. With the LbL-deposition techniques, the number of layers deposited on the template controls the shell thickness.<sup>6, 37-44</sup> First shells were made using classic polyelectrolyte multilayers. Afterwards researchers extended the shell material to proteins, peptides or polysaccharides layers for the production of biocompatible microcapsules. And then even more complex layer systems w by integrating e.g. nanoparticles or drug molecules into the shells to produce multifunctional microcapsules.<sup>45-48</sup> An outstanding advantage of the *LbL* method compared to other manufacturing processes is the adjustment of the shell thicknesses independently from the capsules diameter<sup>45, 49</sup>. This is one of the major reasons why LBL turned out as ideal systems to study relations between geometry and mechanics. This advantage and the option to use a broad range of materials for the built-up of shells were important factors for the success of polyelectrolyte multilayer capsules (PEMCs) in research.

## 2.2 Mechanical Characterization of Microcapsules

Mechanical properties of microcapsules are accessible through a variety of experimental techniques, which can be static, quasi-static or dynamic. Before discussing the different techniques in detail, a short introduction on the mechanical characterization of materials is given. Typically, mechanical properties of materials are tested with an apparatus, which is able to apply forces in a controlled manner and to monitor the material's corresponding deformation.<sup>50</sup> In the simplest case a normal force  $F_n$  is applied on an area  $A$ , referred to as normal stress  $\sigma_n$ . The corresponding deformation  $\delta$  is here measured as ratio between the measured elongation  $\Delta L$  of the material and its original length  $L$  is referred to as normal strain  $\varepsilon_n$ . The stress  $\sigma$  is expressed in Newton (N) per square meters ( $\text{m}^2$ ) or more common in Pascal (Pa). The strain  $\varepsilon$  is a dimensionless quantity and has no units.

$$\text{normal stress: } \sigma_n = \frac{F_n}{A}; [\sigma] = \frac{\text{N}}{\text{m}^2} \quad \text{normal strain: } \varepsilon_n = \frac{\Delta L}{L}; [\varepsilon] = \frac{\text{mm}}{\text{m}}$$

These equations are limited to homogeneous materials that experience a uniform deformation throughout the volume. Depending on the direction of the axial force acting on the material, stress and strain are specified as tensile or compressive.

The mechanical response of a material can be *elastic* or *plastic*. If the material recovers its original dimensions during unloading, it is a *reversible* and *elastic* deformation. If the deformation is permanent and the original shape is not recovered, it is named *irreversible* or *plastic*.

To describe the mechanical properties of materials, characteristic parameters are used: the Young's modulus  $E$  and the Poisson ratio  $\nu$ . The Young's modulus  $E$  can be described by Hooke's Law and refers to the proportionality constant of the linear relation between stress and strain. It is expressed as stress with the unit Pascal (Pa). The Poisson ratio  $\nu$  expresses the ratio between lateral  $\varepsilon_n^l$  and axial strains  $\varepsilon_n$  and is dimensionless.

$$\text{Young's modulus: } E = \sigma_n / \varepsilon_n \quad \text{Poisson ratio: } \nu = - \frac{\varepsilon_n^l}{\varepsilon_n}$$

Beside compression tests of materials, they can experience also tangential forces in shear experiments or compression forces in bulk experiments. If tangential forces  $F_t$

act on an area the ratio of shear stress  $\sigma_t$  to shear strain  $\varepsilon_t$  refers to the shear modulus  $G$ . For a three-dimensional compression of an object, the ratio between bulk stress  $\sigma_b$  and the volume change (bulk strain  $\varepsilon_b$ ) refers to the bulk modulus  $K$ . In Table 2-2 material constants of common materials are indicated.

Table 2-1: Young's modulus  $E$ , shear modulus  $G$ , bulk modulus  $K$  and Poisson's ratio  $\nu$  of common materials.

Material	$E$ [GPa]	$G$ [GPa]	$K$ [GPa]	$\nu$
Steel <sup>51</sup>	195	80	170	0.28
Glass <sup>51</sup>	76	33	38	0.17
Polystyrene <sup>52</sup>	3.8	1.0	4.7	0.4
Rubber <sup>52</sup>	0.003	0.001	0.006	0.49

To assess, mechanical properties of microcapsules the existing techniques can be differentiated in methods measuring an ensemble of microcapsules or methods measuring single microcapsules.

### 2.2.1 Ensemble Methods

The advantage of ensemble methods is the large number of capsules that is measured simultaneously. Such high-throughput methods are common in the industrial sector, because they yield good statistics in a short time and are due to this reason convenient for quality controls. The majority of these methods measure breaking forces<sup>53</sup> or the capsule strength<sup>54</sup> in compression or shearing experiments. Standard commercial available compression instruments - called texture analyzers - offer force ranges between 20 N and 10 kN.<sup>55</sup> In practice, this means that only capsules that survive the smallest breaking force can be measured with such an equipment. In addition, ensemble methods yield average values for the tested mechanical properties, which is limiting the correlation between the capsule's geometric features and its mechanical properties. Ensemble measurements and structural-mechanical correlations is only available for capsules systems with defined monodisperse size and shell thickness. By using shearing tests in turbine reactors lower forces become accessible, which allows for the measurement of softer microcapsules. Drochon and co-workers<sup>105, 106</sup>

used this method to study the cell membrane mechanics of red blood cells. Soft artificial microcapsules - e.g. nylon microcapsules - were also successfully studied with this technique<sup>56, 57</sup>.

### 2.2.2 Single-Microcapsule Methods

The understanding of structure-property-relations is of paramount importance in many disciplines. Consequently, also characterization techniques were developed over the last years that allow studying microcapsules on the single-particle-level. An analysis on the single-microcapsule-level is decisive to link e.g. the capsule's geometry to the capsule's mechanical response. This section will give an overview of available experimental approaches to access mechanical properties on the single-capsule-level. The methods presented are ordered according to their increasing force sensitivity as shown in Figure 2-2.

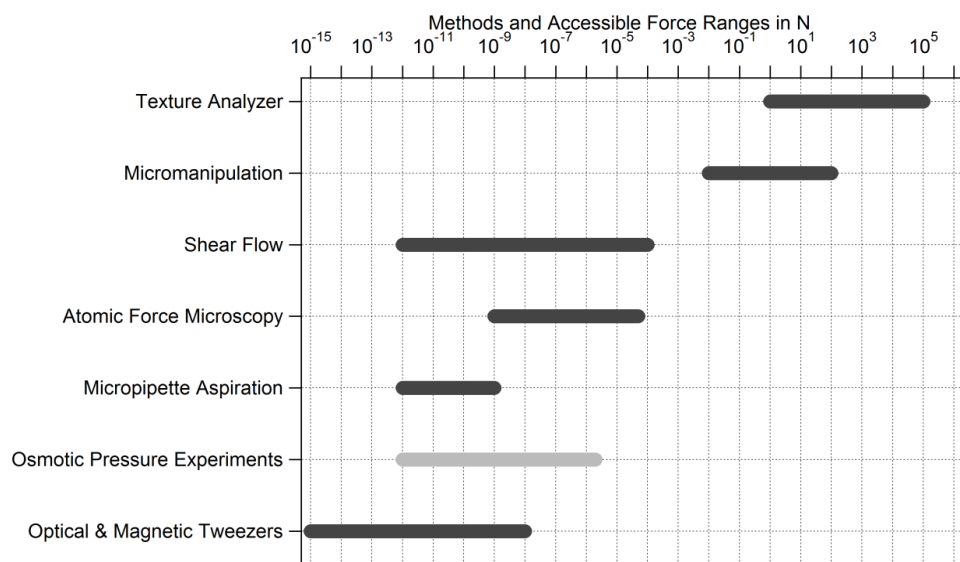


Figure 2-2 Schematic representation of single-capsule measurement techniques, each with typically available force range.

### Osmotic Pressure Method

An experimental approach that perfectly bridges the gap between ensemble and single microcapsule experiments is the osmotic pressure method introduced by Gao et al.<sup>58, 59</sup> With this experiment a batch of semi-permeable microcapsules experiences a bulk compression through osmotic pressure. However, shape changes of the microcapsules are analyzed on the single capsule level. Thus, a correlation between

dimensions and mechanics is possible. As characteristic value, the critical osmotic pressure  $\pi_c$  is determined, which refers to the pressure needed for the deformation of 50 % of the capsules. An example experiment is shown in Figure 2-3, where shape changes were followed with confocal microscopy.

The critical osmotic pressure  $\pi_c$  is proportional to the square of the shell thickness  $h$  and inversely proportional to the square of the capsule radius  $R_C$ . The proportionality constant is the elasticity modulus  $\mu$ , which can be easily transferred into the elastic modulus  $E$ .<sup>41</sup>

$$\pi_c = 4\mu \left(\frac{h}{R_C}\right)^2 = \frac{2E}{\sqrt{3(1-\nu)^2}} \left(\frac{h}{R_C}\right)^2 \quad E = 2\mu(\sqrt{3(1-\nu^2)})$$

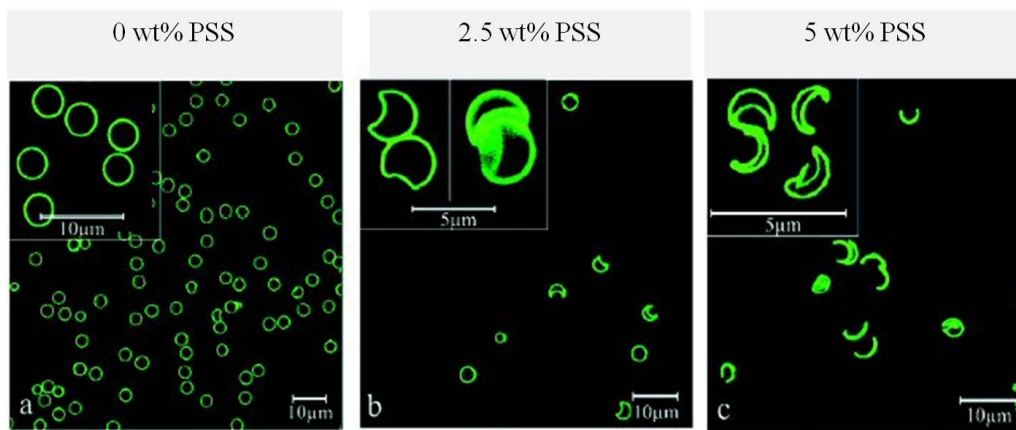


Figure 2-3 Confocal fluorescence micrographs of polyelectrolyte capsules exposed to increasing concentrations of polyelectrolyte in the solution. In the polyelectrolyte-free solution (a), the capsules are spherical in shape, whereas the addition of polyelectrolyte leads to buckling of the capsule membrane and indentations appear (b,c). Figure adapted from Fery et al., *Mechanics of Artificial Microcapsules*, *Journal of Physics*, Copyright (2004) IOP Science.<sup>41</sup>

As a drawback of this method the high concentrations of the solute have to be mentioned which are necessary to reach critical osmotic pressures. Therefore, typically polyelectrolytes are used as solutes because they possess many dissociable groups, which contribute to the concentration of the active species. Moreover, the control and measure of osmotic pressures represents an experimentally laborious approach.

Recently Datta et al.<sup>60, 61</sup> (Figure 2-4) presented an approach, which reminds one on the osmotic pressure experiments. Nanoparticle-shelled microcapsules showed buckling phenomena when the capsule's core volume is decreased in a controlled manner by adding a fixed amount of unsaturated continuous phase, where the core material was partially soluble. Future experiments could allow for a systematic study of the shrinking process and an evaluation of the mechanical properties.

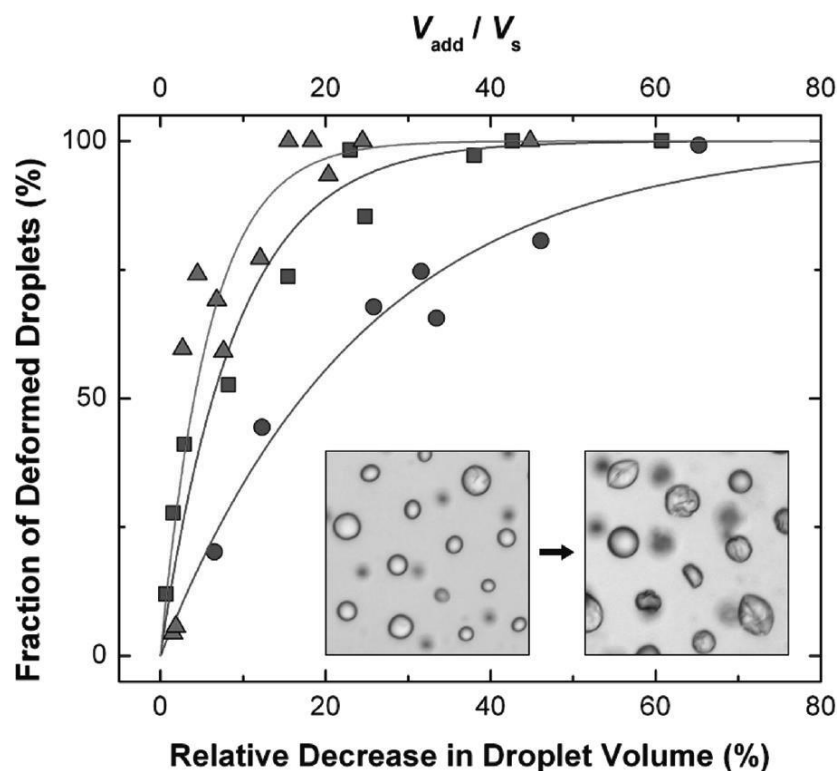


Figure 2-4 Plot of the fraction of buckled/crumpled droplets as a function of calculated relative change in droplet volume for samples of average droplet diameters  $d=14.7 \mu\text{m}$  (circles),  $34.7 \mu\text{m}$  (squares), and  $44.1 \mu\text{m}$  (triangles). Solid lines are guides to the eye. Inset shows optical micrographs of two different samples: left has undergone weak pumping, right has undergone stronger pumping. Reprinted with permission from Datta et al, Controlled Buckling and Crumpling of Nanoparticle coated Droplets, *Langmuir*, Copyright (2010) American Chemical Society.

### Parallel Plate Compression Experiments

Parallel plate compression experiments on the single-capsule-level were first performed by Cole et al., who studied in the 1930s the deformation behavior of arbutin eggs.<sup>62</sup> Today, parallel plate set-ups can be found in various hardware. Commercial available texture analyzers offer a resolution of about 1 mN. Bartkowiak and Hunkeler<sup>107, 10863-65</sup> studied with this technique alginate oligochitosan capsules

and the impact of the shell thickness on mechanical properties. More recently Mahou et al.<sup>66</sup> studied with this technique the mechanical resistance of alginate polyethylene glycol hybrid microspheres.

In addition, Liu and co-workers used self-built instruments similar to texture analyzers to study the deformation of single microcapsules as for example.<sup>67</sup> Later Keller and Sottos adopted this apparatus to study the mechanical properties of phase change materials<sup>68</sup> and self-healing materials<sup>69, 70</sup>.

With the start of the late 1990s resolutions in the range of 1  $\mu\text{N}$  became available with the micromanipulation technique introduced by Zhang and coworkers<sup>71</sup>. Thus, mechanical properties of smaller and softer microcapsules became accessible. Recent work by co-workers of Zhang focused on the mechanical stability of melamine formaldehyde resin capsules<sup>72</sup>, the impact of formaldehyde percentage<sup>73</sup> and the shell's self-healing properties<sup>74</sup>. Other systems investigated with this technique were soft hydrogel microcapsules<sup>75</sup> and silica-shell/oil-core microcapsules<sup>76</sup>.

### **Atomic Force Microscopy**

Atomic force microscopy (AFM) and particular force spectroscopy, works very similar to a parallel plate set-up. Here, microcapsules are exposed as well to uniaxial deformations. However, a smaller force range, with values between pN to  $\mu\text{N}$ , becomes accessible with this technique and the corresponding deformations are monitored with a much higher resolution in the range of Angstrom. This is an outstanding advantage for AFM when it comes to small deformation studies on the order of the shell thickness.<sup>6</sup> More details about the working principle can be found in section 2.4. As force sensor cantilevers are used, which can be tipless, with sharp tip or tips modified with colloidal particles, also called colloidal probes.<sup>77</sup> The first force spectroscopy experiments for the estimation of the shell's elastic modulus were performed for the first time independently from Vinogradova and co-workers<sup>78-80</sup> and from Fery and co-workers.<sup>38, 40, 81</sup> Both groups reported on the PEMCS shell's elastic modulus, which was found to be in the low GPa range. Moreover the colloidal probe technique was used to study mechanical properties of vesicles<sup>82</sup>, aminoresin capsules<sup>16</sup>, biopolymer capsules<sup>83</sup> or the salt softening of PEMCs<sup>84</sup>. Other groups used a sharp tip set-up for the characterization of artificial<sup>85-87</sup> and biological<sup>88-90</sup> capsule systems. Tip-less cantilever were also used to study the mechanical properties

of microcapsules<sup>91-95</sup>. However, sharp tips risk penetration into the shell material, and tipless cantilevers risk to be accompanied by shearing or sliding, because commercially available cantilevers are tilted about 10°. Small force loads and rather small capsules (with respect to cantilever dimensions) keep these effects acceptably low.

Furthermore, the combination of AFM with optics allows for monitoring the change of the microcapsule's contact area during compression. In particular reflection interference contrast microscopy (RICM) turned out to be advantageous because it allows for an reconstruction of the capsule's shape in undeformed and deformed state (during measurement).<sup>38</sup>

### Microcapsules in Shear Flow

Microcapsules cannot only be exposed to uniaxial deformations but also to tangential deformations by using shear flow experiments.<sup>57, 96-99</sup> The typical range of these stresses is from mPa to kPa, i.e. for capsules with a typical radius of 5  $\mu\text{m}$  the applied forces can be estimated to be between 0.1 pN to 0.1  $\mu\text{N}$ . Thus, single microcapsules are exposed to controlled hydrodynamic forces while their shape change is monitored optically. Typical set-ups which allow a controlled deformation of soft and large microcapsules are rheometers<sup>57, 96, 99</sup> or the spinning drop apparatus<sup>100-105</sup>.

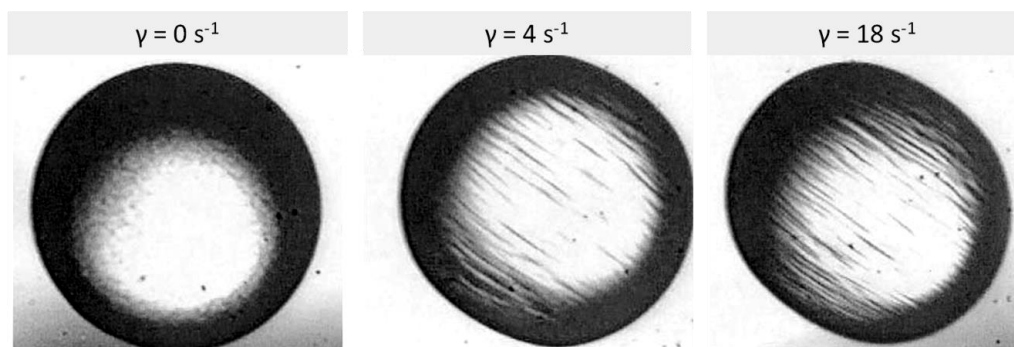


Figure 2-5 Reprinted from *Colloid and Surfaces A: Physicochemical and Engineering Aspects*, 183-185, Walter et al., Shear induced deformation of microcapsules: shape oscillations and membrane folding, 123-132, Copyright (2001) with permission from Elsevier.

In the case of rheological experiments<sup>99</sup>, shown in Figure 2-5, the applied force  $F$  is controlled by the shear rate  $\dot{\gamma}$  and the viscosity  $\eta$  of the sheared liquid. Walter<sup>99</sup> illustrates that the force is expressed by the shear stress  $\sigma$ , valid for Newtonian liquids.

$$\frac{F}{A} = \eta\gamma = \sigma \qquad \gamma = \frac{\Delta v}{\Delta x}$$

The shear rate is controlled via the velocity  $\Delta v$  of the two parallel plates and their separation distance  $\Delta x$ . Rehage and co-workers<sup>96</sup> reported on typical shear rates for swallowing of about  $10\text{-}100\text{ s}^{-1}$ , for stirring of about  $10\text{ to }1000\text{ s}^{-1}$  and for rubbing of about  $10^4\text{-}10^5\text{ s}^{-1}$ . The deformation  $\delta$  of the capsules from spherical to an elliptical shape is monitored optically. To describe the deformation the elliptic form is analyzed with the major axis  $l$  and the minor axis  $b$ .

$$\delta = \frac{l - b}{l + b}$$

In the range of small shear rates, a simple analytical relation can obtain the 2-dimensional elastic modulus  $E_s$ <sup>96</sup>:

$$E_s \sim \frac{\eta R_C}{\delta} \gamma$$

$E_s$  is then proportional to the viscosity  $\eta$ , the capsule radius  $R_C$ , the shear rate  $\gamma$  and the reciprocal of the observed deformation  $\delta$ .

Recently, microfluidic set-ups were used to study red blood cells<sup>106</sup> and artificial capsules<sup>107-110</sup> in confined shear flow. Barthès-Biesel and co-workers described the numerical evaluations and corresponding theoretical models for the description and interpretation of the microcapsules response towards shear forces.<sup>113,111, 112</sup>

### **Micropipette Aspiration**

Micropipette aspiration is a classic technique for the quantification of mechanical properties of soft biological (cells, vesicles) and soft artificial microcapsules. In the 1950s Mitchison and Swan determined the mechanical response of a cell monitoring its deformation during it is sucked by a negative hydrostatic pressure into the mouth of a micropipette.<sup>113, 114</sup>

The pressure  $\Delta P$  can be measured and the deformation  $\delta$  is observed with optical microscopy. The applied force  $F$  is then the suction pressure  $\Delta P$  times the cross sectional area of the pipette with a radius  $R_p$ <sup>115</sup>:

$$F = \Delta P \pi R_p^2$$

Pressure from 0.1 pN/ $\mu\text{m}^2$  to 96 nN/ $\mu\text{m}^2$  are accessible with micropipette aspiration corresponding to force ranges of 0.1 pN to 10  $\mu\text{N}$ . The Laplace's law is used to quantify from experimental data the 2-dimensional elastic modulus  $E_c$ <sup>116, 117</sup>.

$$\Delta P = 2E_c \left( \frac{1}{R_p} - \frac{1}{R_c} \right)$$

Where  $\Delta P$  is the applied pressure,  $E_c$  the cortical tension (2d-elastic modulus),  $R_p$  is the radius of the pipette and  $R_c$  the radius of the capsules. To interpret the measured force deformation relations in depths mechanical models are necessary. Evans<sup>118</sup> and Skalak<sup>119</sup> where the first proposing a membrane model which correlated the deformed shape with general stress and strain laws. Later theoretical variations were developed to model the elastic, solid like or viscous behavior of different cell types and vesicles. An overview of cell experiments with the micropipette aspiration technique and the different theoretical methods can be found in the review of Hochmuth and co-workers<sup>115</sup> and a comparison with AFM is provided by Dieluweit and co-workers<sup>120</sup>.

The limitations for the micropipette aspiration technique are:

- high sensitivity to evaporation and resultant data drifts<sup>115</sup>.
- limited force range, which is for synthetic capsules often too small to obtain bursting forces<sup>72</sup>. Typically, only soft and large microcapsules are accessible with this technique.
- quantitative analysis is complicated by plastic deformation of the capsule<sup>41</sup>.
- friction between the micropipette and the aspirated microcapsule is often neglected<sup>115</sup> as well as different stress concentration at the pipette edge.

Since these first pioneering contributions the technique has been further improved and applied to study both biological<sup>114-116, 121-123</sup> and artificial capsules<sup>120, 124-126</sup> and theoretical models have been developed to analyze micropipette aspiration experiments.<sup>118, 119, 121, 127-131</sup>

### **Optical, Magnetic and Electromagnetic Tweezers**

A relative new approach is the application of forces via optical or magnetic trapping. The advantage of these techniques is an extremely high sensitivity of the applied forces:

- Optical tweezers can assess a force range of about 0.1 pN to 100pN.
- Magnetic tweezers can assess a force range of about 0.001 pN to 100pN.
- Electromagnetic tweezers can assess a force range of about 0.01 pN to  $10^4$  pN.

For artificial microcapsules these techniques do not play a major role, because artificial microcapsules are often not soft enough (too hard shells) to be accessible with these optic techniques. Therefore the interested reader is referred to the review by Neuman et al <sup>132</sup> and other literature<sup>133-136</sup>.

### 2.3 Overview-Table - Mechanical Properties of Microcapsules

The following Table 2-2 gives an overview for mechanical properties of typical bulk materials and microcapsules -  $E$  and  $\nu$  values - reported in literature.

Table 2-2: The table indicates the elastic modulus  $E$  and Poisson ratio  $\nu$  for bulk materials and the microcapsule's shell material.

<b>Material</b>	<b><math>E</math></b>	<b><math>\nu</math></b>	<b>Method</b>	<b>Lit</b>
Steel	190-210 GPa	0.27-0.3	Tensile test	137
Glass	48-83 GPa	0.2-0.27	Tensile test	137
Melamine formaldehyde	6-7 GPa	0.34	Tensile test ESPI	138
Polystyrene	3-3.5 GPa	0.33-0.34	Tensile test	137
Poly lactide	1.4- 2.8 GPa		Tensile test	92
Rubber	0.007-0.04 GPa	0.45-0.49	Tensile test	137
<b>Microcapsules</b>	<b><math>E</math></b>	<b><math>\nu</math></b>	<b>Method</b>	<b>Lit</b>
Silica (Stöber)	18 GPa	0.17	AFM-sharp tip	85
Poly(urea-formaldehyde)	3.6 GPa	0.33	Micromanipulation	68
Poly lactide	2-18 GPa	0.42	AFM-tipless	92
Melamine Formaldehyde	1 – 2.5 GPa	0.5	Micromanipulation	139
Virus capsids	1-1.9 GPa	0.4	AFM & others	140
(PSS/PAH) <sub>5</sub>	1.6 GPa	0.33-0.66	AFM-colloidal probe	38
(PSS/PDADMAC) <sub>5</sub>	420 MPa	0.5	Osmotic pressure	59
(PSS/PAH) <sub>5</sub>	1.5-2.25 GPa	0.5	Osmotic pressure	58
(PSS/PAH) <sub>5</sub> PSS	60-400 MPa	0.66	AFM-colloidal probe	84
(PSS/PAH) <sub>4</sub>	1-100 MPa	-	AFM-colloidal probe	79

## Status of the Field

---

Colloidosomes (60 $\mu$ m PS particles)	1-10 MPa		Micropipette	35
Silica/Siloxane	200 MPa	0.3	AFM-sharp tip	86
DPPC Liposomes	110 MPa	0.5	AFM-sharp tip	89
Vesicle (PS403-b- PAA62)	45 MPa	0.5	AFM-sharp tip	141
Endothelial cells	0.5 kPa		Micropipette	115
Neutrophils (soft cells)	100 Pa		Micropipette	115

## 2.4 Atomic Force Microscopy - Working Principle

To clarify structure-property-relations of microcapsules on the single-particle-level AFM combined with optical microscopy proved suitable. Therefore, some more details about microcapsule compression using force spectroscopy will be discussed.

After 1986, when Binnig and co-workers<sup>142</sup> introduced the AFM, physical-chemical properties of surfaces became accessible with nanometer resolution. AFM is used for:

- Imaging of surfaces with a spatial resolution of about 20 nm (standard sharp tips).
- Force spectroscopy measurements with a force resolution in the range of pico-Newton. A detailed review about force spectroscopy is provided by Butt et al<sup>77</sup>.

### 2.4.1 AFM Components

AFM belongs to the family of scanning probe microscopes and thus contains the following components: a probe (cantilever), a piezo-scanner and a sensor for the detection of the vertical position of the probe. In Figure 2-6 the set-up used in this thesis is depicted.

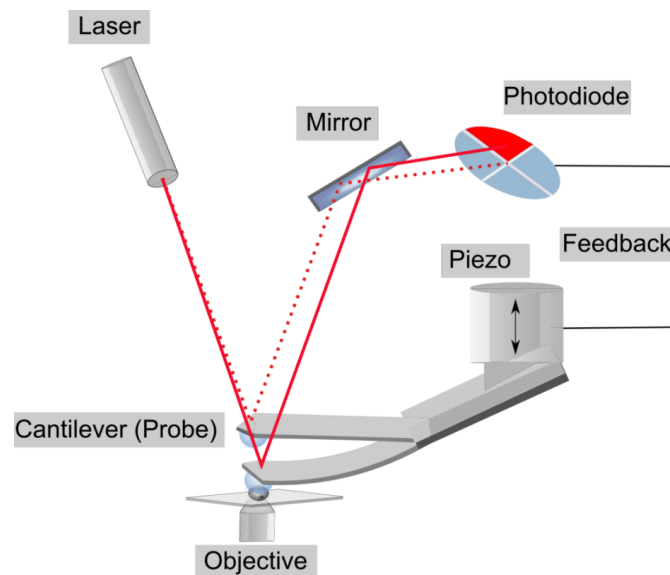


Figure 2-6 Components in an AFM: The cantilever is the probe interacting with the surface. A piezo-scanner moves the probe over the surface and controls the distance between probe and sample. The optical lever principle is used for the detection of the cantilever position. Here the AFM is displayed in combination with an optical microscope and cantilevers carrying a colloidal probe.

*Probe (Cantilever):* Commercial available cantilevers are typically made of silicon or silicon nitride and can be understood as micro-springs. They are characterized by the spring constant  $k_c$  and the resonance frequency  $\nu_0$ . Cantilevers can be ordered with sharp tips or tipless. Further modifications, where a colloidal probe is glued on the apex of the cantilever are of particular interest for experiments with microcapsules, because a sphere-sphere-geometry is obtained during compression. In view of the lateral resolution the probe is the limiting factor. Here the tip radius and the inclination angle of the cantilever -in general  $10^\circ$  - need to be considered. Thus, standard cantilevers with a sharp tip allow for a resolution of about 20 nm.

*Piezo-Scanner:* Control over the vertical movement of the cantilever is obtained via a piezo element. Thus, the height position  $Z_P$  of the cantilever is adjusted via the applied voltage and the piezoelectric translator. When the cantilever is approaching the surface, local attractive or repulsive forces, are detected, which lead to a bending of the cantilever.

*Optical Lever Technique:* The beam of a laser diode is positioned on the end of the cantilever. To increase the optical path length and allow for the measurement of small cantilever deflections the beam is then first reflected to a mirror before arriving on a position sensitive detector PSD system. The majority of instruments is using a four-quadrant photo diode, which allows the calculation of the vertical and lateral deflection  $\Delta PSD$  in Volt by comparing the signal detected on the four segments of the diode.

$$\Delta PSD = \frac{(A + B) - (C + D)}{(A + B) + (C + D)}$$

The vertical resolution, the determination of the cantilever position is in the range of Angstrom. This high resolution becomes accessible through the optical lever technique. Thus, the thermal or acoustic vibrations of the cantilever limit the vertical resolution. In practice, AFM imaging resolutions in the range of nm are obtained. Here often the surface roughness of the scanned material limits the vertical resolution. For example, the surface of glass substrate has a roughness of about ~4-6 nm.

### 2.4.2 Cantilever Calibration

In general, the accuracy of a force spectroscopy measurement depends on the accuracy of the calibration of the cantilever's spring constant. Cantilever suppliers estimate the spring constant most often from the cantilever's geometry<sup>77</sup>.  $E$  is the elastic modulus and  $\rho$  the density of the cantilever material;  $w$  the width,  $t_C$  the thickness and  $L$  the length of the cantilever.

$$k_C = \frac{Ewt_C^3}{4L^4} \quad \nu_0 = 0.1615 \frac{t_C}{L^2} \sqrt{\frac{E}{\rho}}$$

This obtained spring constant value is good for a first estimation and selection of an adequate cantilever, but is too imprecise for the evaluation of a force-deformation experiment. Uncertainty is caused because the method assumes a constant cantilever thickness  $t_C$  and a homogenous material<sup>77</sup>. Both is not realistic because cantilevers neither are made of homogeneous thickness  $t_C$  nor are composed of completely homogeneous material (oxidation layers and coating layers).<sup>77</sup> Thus, the calculated spring constant does not reflect the real spring constant,

Several methods have been developed in the last decades, to calibrate the vertical spring constant cantilevers in a simple, reproducible and accurate way<sup>77</sup>. In this thesis the thermal Sader-method<sup>143</sup> and the thermal noise method<sup>77</sup> were used for calibration. Critical unknown parameters, such as thickness, density and E-modulus are avoided by using the thermal vibration of a cantilever: the resonance frequency  $\omega_0$  and the quality factor  $Q$ . Further parameter constants which are needed are the density  $\rho_f$  of the fluid (air), the hydrodynamic function  $\Gamma$  and the Reynolds number  $Re$ . From the plane view the dimensions width  $w$  and length  $L$  are obtained.

$$k_C = 0.1906 \rho_f w^2 L Q \Gamma_i(Re) \omega_0^2$$

Today the thermal noise method is implemented in the majority of instruments and can be considered as standard calibration method. The method, developed by Hutter and Bechhofer<sup>144</sup>, measures the thermal fluctuations of the cantilever over time. Thus a frequency power spectrum is obtained, shown in Figure 2-7.<sup>144</sup>

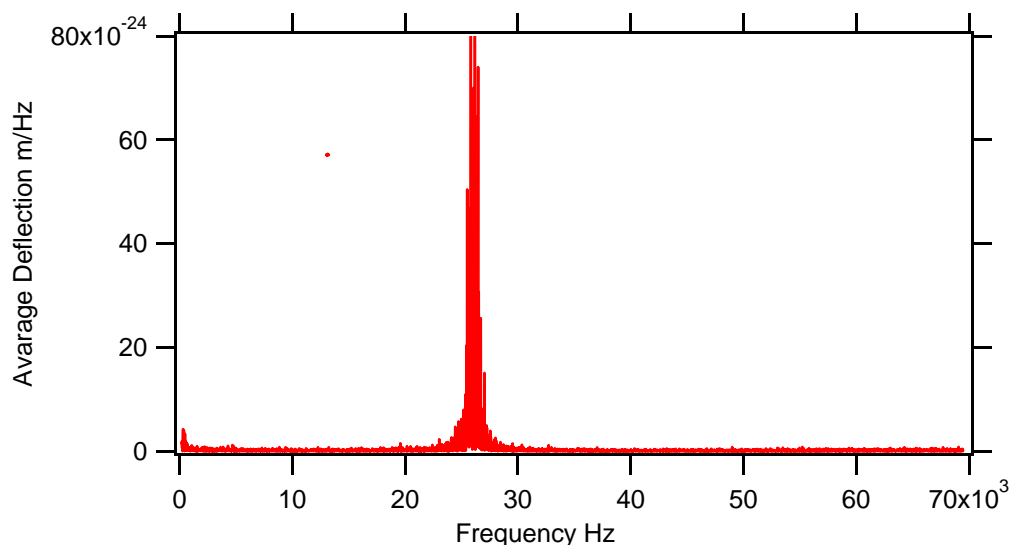


Figure 2-7 Thermal noise power spectrum.

Using the model of a harmonic oscillator, the thermal energy absorbed by the cantilever is obtained by an integration over the whole frequency range. Via the equipartition theorem, one can calculate from the mean square deflection  $\langle q^2 \rangle$ , the temperature  $T$  and the Boltzmann constant  $k_B$  the cantilever spring constant  $k_c$ .

$$k_c = k_B T / \langle q^2 \rangle$$

### 2.4.3 Colloidal Probe AFM

In the 1990s Ducker et al.<sup>145</sup> and Butt<sup>146</sup> introduced the colloidal probe technique, aiming on well-defined contact geometries. Sharp tip-cantilevers and tipless cantilevers both cannot provide information on the contact between probe and sample. For force spectroscopy experiments the contact area between support and sample, and sample and probe are of particular interest. By using colloidal particles - there is no limitation to the type of colloid probe<sup>147</sup> - interactions between probe and sample can thus be measured with the following advantages:

- Well-defined contact area between colloidal probe and sample.<sup>77</sup>
- *In situ* determination of contact area as a function of applied loads with soft colloidal probes, which offer outstanding sensitivity.<sup>148</sup>
- Large deformation of soft materials become accessible, without risking indentation events.<sup>6</sup>

- Theory from parallel plate systems can be used to describe large and small deformations.<sup>6</sup>

Various methods are available for the preparation of colloidal probes.<sup>77, 148, 149</sup>

#### 2.4.4 Force-Distance Curves

A typical force-distance curve recorded in a force spectroscopy experiment is shown in Figure 2-8. The cantilever deflection measured by the PSD in Volt is plotted versus the height position of the piezo-translator  $Z_P$ . The progression of the curve is typical for any force-distance curve on a hard substrate and should therefore be explained in few words.

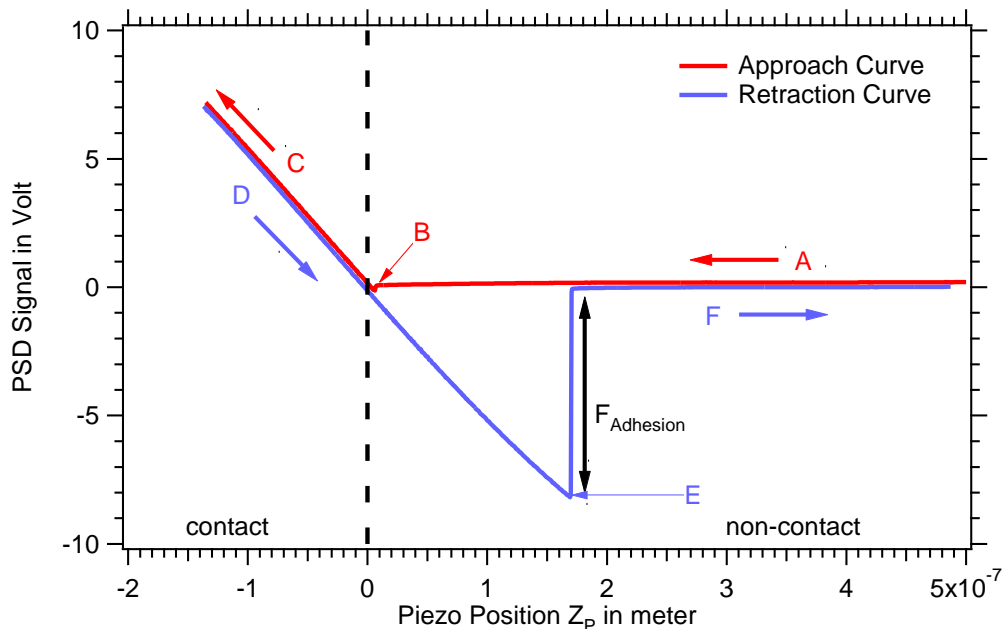


Figure 2-8 Typical force-distance curve obtained with AFM. The curve is divided in a contact and a non-contact regime.

A force distance measurements always consist of an approach curve (red) and a retraction curve (blue). The curve can be sectioned in significant parts and points illustrated in Figure 2-8. The first important part of the curve is the so-called “baseline” (A), here the approaching cantilever is not interacting with the sample surface and no signal change is detected by the PSD (0V). A first interaction between tip and surface is marked by the “jump-to-contact-point” (B). This is typical for attractive forces between tip and sample and marks the start of the contact between the cantilever and the hard substrate. Afterwards a linear increase of the deflection is

observed corresponding to the bending of the cantilever (C). During the retraction, the cantilever deflection follows ideally the same curve progression (D). Due to attractive forces between tip and sample, a sticking of the probe to the sample is observed leading to a longer contact between probe and sample. When the forces overcome the adhesive interaction, a “jump-out-off-contact-point” (E) is observed and the curve returns to the baseline (F).

To obtain a force-deformation curve several transformations are necessary. First, the y-axis has to be transformed from an electronic signal in Volt to the force applied on the sample. The slope (C) also referred to as inverse optical lever sensitivity (InvOLS) or in short form as sensitivity, gives the linear correlation between the deflection signal and the real movement of the cantilever. Thus, the deflection signal can be transformed with a known sensitivity in the actual cantilever displacement in nanometers.

$$[Z_C] = V ; [Z_C \times \text{InvOLS}] = V \times \frac{\text{nm}}{V} = \text{nm}$$

The force  $F$  is then calculated using Hooke’s Law and the spring constant of the cantilever  $k_c$ :

$$F = k_c Z_C$$

Finally, the x-axis has to be converted from the piezo-displacement into the real tip-sample distance  $D$ . Therefore, the measured cantilever deflection has to be subtracted from the piezo-displacement.

$$D = \frac{F}{k_c}$$

## 2.5 Capsule Mechanics – Models & Theory

To further interpret and analyze the results obtained from mechanical characterization physical models are needed. When the shell material is idealized as a continuum, no absolute length scale enters the theoretical description and mechanical properties and the response to applied loads are the same for objects of all length-scales. The basis to model the response of hollow spherical objects to applied loads are detailed mathematical descriptions that can be found in shell theory.<sup>150-153</sup> The broad range of descriptions available in shell theory was already reviewed in view of

microcapsule mechanics by Fery and Weinkammer<sup>6</sup>. Further information on theoretical models is provided in the article *Mechanics of Microcapsules: From function to stability*<sup>154</sup>, chapter 7 of the thesis.

Modeling capsule deformations is challenging compared to deformations of solid particles made of homogenous elastic material. The reason is the shell that is introducing a different deformation response. During the deformation of a microcapsule, a complex response is obtained caused by stretching and bending forces, which are acting simultaneously on the shell. Although both forces are always present, the dimension of the deformation has an influence if stretching or bending forces are dominant. This is useful to simplify the complex mathematical descriptions. Therefore, in particular the deformation compared to the length scales of the capsule - capsule radius and shell thickness- need to be considered. Thus, two type of deformations are distinguished:

- *small deformations* on the order of the shell thickness indicated in Figure 2-9 (left), used to probe the shell's mechanical properties, and
- *large deformations* on the order of the capsule radius indicated in Figure 2-9 (right), where mechanical failure, in other words burst properties of capsules can be tested.

### 2.5.1 Reissner -Thin Shells, Small Deformations

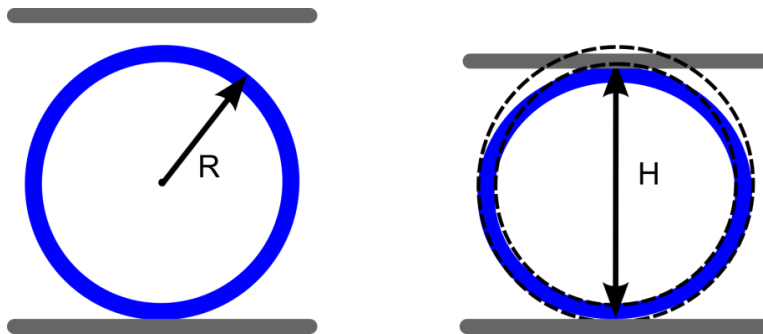


Figure 2-9 Small deformations of microcapsules in the range of the shell thickness. (Left) Non-deformed spherical microcapsule with radius  $R_C$  and shell thickness  $h$ . (Right) Small deformation of a microcapsule.

To simplify the theoretical treatment of shells, the problem is first restricted to thin shells with a shell thickness  $h$  to radius  $R$  ratio of less than  $1/20$ .<sup>155</sup> In thin shell theory, the shell material is supposed to be homogeneous and isotropic and to show linear

elastic behavior. By defining,  $R$  as the radius of curvature of the middle surface between the inner and outer surface of the capsule's shell, the 3D-shell-problem is reduced to a 2D-problem. This is also known as the Kirchhoff-Love assumptions, original used for thin plate theory.<sup>155</sup> In case of small deformations, Reissner<sup>156-159</sup> was one of the first scientists to present a first-order approximation, revealing a linear scaling of the applied force  $F$  and the resulting deformation  $\delta$ .

$$F = \frac{h^2}{R} \cdot \frac{4 E}{\sqrt{3 (1 - \nu^2)}} \cdot \delta$$

Further variables are the radius of curvature  $R$ , shell thickness  $h$  and the material elastic constants, elastic modulus  $E$  and Poisson's ratio  $\nu$ . Even though Reissner's theory was originally developed for point loads, it has been experimentally proved to be valid also for less concentrated loading situations, as for examples for deformations with a colloidal probe.<sup>6</sup> For microcapsules mechanics this result is of particular interest, because the shells' elastic modulus becomes directly accessible from small deformation experiments with parallel plate compression experiments using texture analyzers, micromanipulation or AFM force spectroscopy.

However, the simple description of microcapsules' response to small deformations shows constraints. In practice, the microcapsule' shell is an interface and will bring along surface tension, the shell is also a barrier to regulate permeability and the shell's surface shows adhesive properties. All these facts can result in pre-tensions - pre-deformations and pre-inflations - that have to be kept in mind, because they can lead to a Non-Hookean behavior. Examples for thin-shelled microcapsules where interfacial tension plays a dominate role are Pickering emulsion droplets<sup>160</sup> or droplets stabilized by clay particles<sup>161</sup>. Ferri and co-workers developed in a pioneering work, a model accounting for both contributions - surface tension and mechanical membrane tension - to the overall deformation behavior. Furthermore, their model considered the capsule's shape changes during compression.

### 2.5.2 Pogorelov - Thin Shells, Large Deformations

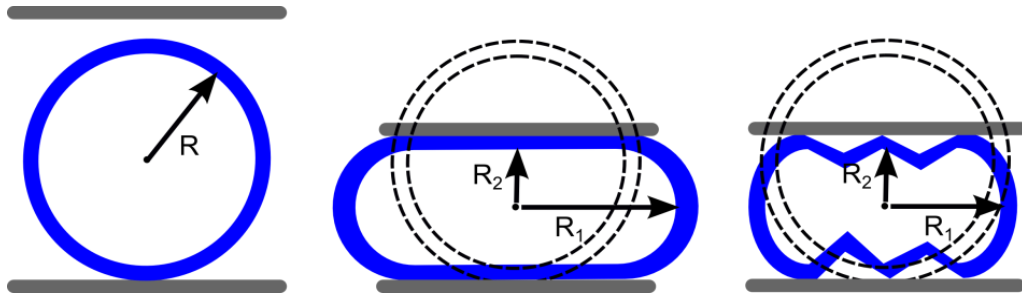


Figure 2-10 Large deformations can result in a non-linear elastic response or in plastic deformations which are dominated by buckling.

Pogorelov proposed a theoretical model for large deformations of microcapsules, assuming an infinite permeability as the simplest case. For a Hookean material under point load he assumed the following relationship<sup>162</sup>:

$$F = \frac{1.89Eh^2}{R(1-\nu)}\sqrt{h\delta}$$

In contrast to Reissner's formula, the force no longer scales linearly but with the square root of deformation. With this model, the onset of buckling, the formation of a surface with changed curvature is described. Several studies used Pogorelov's scaling behavior to estimate from the onset of buckling elastic properties of shells.<sup>163-167</sup> Further approaches to treat theoretically large deformations for non-Hookean models, such as Neo-Hookean or Mooney-Rivlin, can be found in literature<sup>67, 168</sup>.

The crux for treating large deformations is obviously the shells permeability, because during large deformations, permeability is not any more negligible and volume-constraint contributions become increasingly dominant. Therefore, capsule wall permeability has to be considered, when large deformations are modeled. In the following equations the deformation is always indicated as relative deformation, referring to the height of the deformed capsule ( $H$ ) in relation to the capsules original diameter ( $2R_C$ ), indicated in Figure 2-10:

$$\varepsilon = \frac{H}{2R_C}$$

In the following, we will compare the scaling laws of small compared to large deformations. While for small deformations, irrespective of permeability, the force  $F$  scales linearly with relative deformation  $\varepsilon$ .<sup>169</sup>

$$F \propto \frac{4}{3} E h^2 \varepsilon$$

In the case of large deformations and an impermeable shell an additional term accounting for the stretching of the shell is added. Then the force scales cubically with the deformation.<sup>79</sup>

$$F \propto \frac{16\pi}{3} E h R \varepsilon^3$$

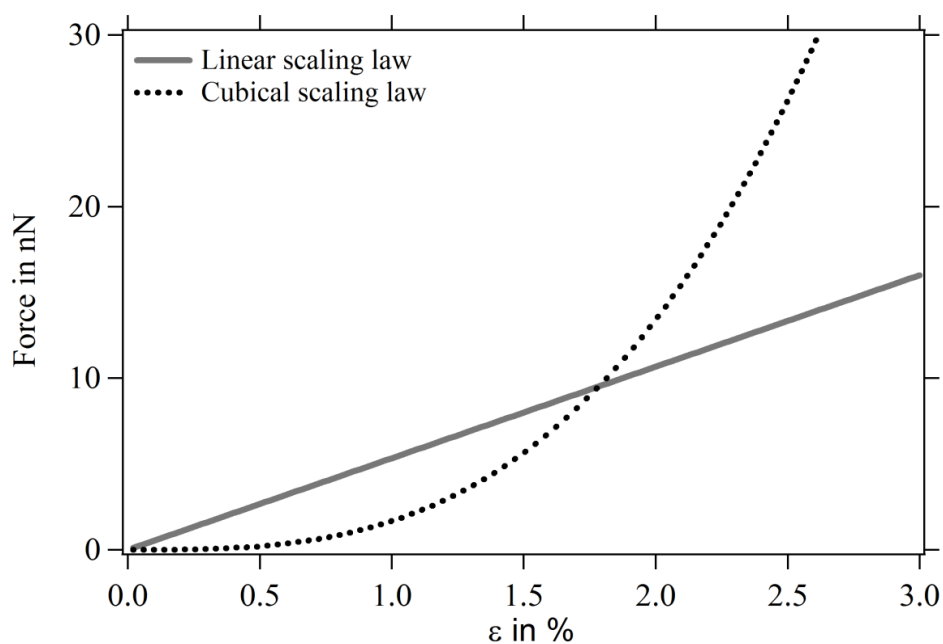


Figure 2-11 Linear elastic (continuous line) and volume-constraint (dotted line) contributions to forces  $F$  upon capsule deformation (relative deformation  $\varepsilon$ ), calculated for a capsule 10  $\mu\text{m}$  in diameter, shell thickness of 20 nm and Young's modulus of 1 GPa.

Plotting both scaling laws in a common graph (Figure 2-11) shows clearly that, as long as we restrict ourselves to small deformations on the order of the shell thickness, permeability issues are negligible. In this case, additional contributions arise particularly from edge bending at the sites of high curvature around the dimple and stretching caused by the rising fluid pressure.<sup>170</sup> Comparing both experimental data and theoretical calculations for the deformation of an empty and a water-filled racquetball Taber finds that deformations below 20% are dominated by bending. Only for larger compression the load-deflection curve of filled shells deviated from the square root like scaling and compared to the empty shells a stiffening was observed.<sup>170</sup>

### 2.5.3 Burst of Microcapsules

Finally, at very high loads capsule burst can occur. Experimentally, Zhang *et al.* found for melamine formaldehyde (MF) microcapsules a clear correlation with both bursting force and displacement at burst increasing in a linear fashion with capsule diameter.<sup>71</sup> Additionally, it was discovered that burst typically occurs at a critical relative deformation of 70%, irrespective of capsule size.<sup>171</sup> Mercadé-Prieto *et al.* carried out finite element modeling (FEM) to elucidate the failure behavior of MF microcapsules.<sup>172</sup> The compression behavior between two parallel plates is simulated up to bursting by applying an elastic-perfectly plastic model with strain hardening and comparison with experimental data shows very good agreement. Strain at rupture for this system was found to be approximately 0.48 and a failure stress of around 350 MPa was obtained.

## 2.6 Objective of the thesis

Concepts for the rational design of microcapsules are of enormous interest in research and in industry. Rational design is relevant for novel multifunctional microcapsules as well as for well-established microcapsule systems used in industrial large-scale processes.

Towards a general approach for the adjustment of mechanical properties, this thesis aims on developing a characterization concept, which allows for an understanding of fundamental structure-property-relations in microcapsules. Therefore, parameters that are critical for the microcapsules' mechanical properties need to be identified and characterized in a reproducible manner. Even though shell thickness and shell properties are known to be critical for the mechanical response of microcapsules less effort is recorded in the quantification of the shell thickness. In particular, a reproducible and statistical significant characterization method is rare. Therefore, this thesis aims on a characterization concept that allows for a reproducible and statistical significant assessment of critical parameters like e.g. shell thickness. By clarifying structure-property, relations the gaps between synthesis and application can be closed. To proof the general character of the approach, different microcapsule systems that aim on specific and different applications will be investigated.

## 2.7 References

1. Ghosh, S. K., Functional Coatings and Microencapsulation: A General Perspective. In *Functional Coatings: By Polymer Encapsulation*, Wiley-VCH Verlag GmbH & Co. KGaA: **2006**; 1-28.
2. Luzzi, L. A., *Journal of Pharmaceutical Sciences* **1970**, 59, (10), 1367-1376.
3. Nazzaro, F.; Orlando, P.; Fratianni, F.; Coppola, R., *Curr. Opin. Biotechnol.* **2012**, 23, (2), 182-186.
4. Loscertales, I. G.; Barrero, A.; Guerrero, I.; Cortijo, R.; Marquez, M.; Ganan-Calvo, A. M., *Science* **2002**, 295, (5560), 1695-1698.
5. Sliwka, W., *Angew Chem Int Ed Engl* **1975**, 14, (8), 539-50.
6. Fery, A.; Weinkamer, R., *Polymer* **2007**, 48, 7221-7235.
7. Mathapa, B. G.; Paunov, V. N., *Soft Matter* **2013**, 9, (19), 4780-4788.
8. Arshady, R.; George, M. H., *Polymer Engineering & Science* **1993**, 33, (14), 865-876.
9. Cui, J. W.; Wang, Y. J.; Postma, A.; Hao, J. C.; Hosta-Rigau, L.; Caruso, F., *Advanced Functional Materials* **2010**, 20, (10), 1625-1631.
10. Torini, L.; Argillier, J. F.; Zydowicz, N., *Macromolecules* **2005**, 38, (8), 3225-3236.
11. Kobaslija, M.; McQuade, D. T., *Macromolecules* **2006**, 39, (19), 6371-6375.
12. Akartuna, I.; Tervoort, E.; Studart, A. R.; Gauckler, L. J., *Langmuir* **2009**, 25, (21), 12419-12424.
13. Arshady, R., *Polym. Eng. Sci.* **1990**, 30, (15), 905-914.
14. Loxley, A.; Vincent, B., *J Colloid Interf Sci* **1998**, 208, (1), 49-62.
15. Yow, H. N.; Routh, A. F., *Soft Matter* **2006**, 2, (11), 940-949.
16. Pretzl, M.; Neubauer, M.; Tekaas, M.; Kunert, C.; Kuttner, C.; Leon, G.; Berthier, D.; Erni, P.; Ouali, L.; Fery, A., *ACS Appl. Mater. Interfaces* **2012**, 4, (6), 2940-2948.
17. Utada, A. S.; Lorenceau, E.; Link, D. R.; Kaplan, P. D.; Stone, H. A.; Weitz, D. A., *Science* **2005**, 308, (5721), 537-541.
18. Chen, P. W.; Erb, R. M.; Studart, A. R., *Langmuir* **2012**, 28, (1), 144-152.
19. Hennequin, Y.; Pannacci, N.; de Torres, C. n. P.; Tetradis-Meris, G.; Chapuliot, S.; Bouchaud, E.; Tabeling, P., *Langmuir* **2009**, 25, (14), 7857-7861.
20. Zhang, J.; Coulston, R. J.; Jones, S. T.; Geng, J.; Scherman, O. A.; Abell, C., *Science* **2012**, 335, (6069), 690-694.
21. Zhang, H.; Tumarkin, E.; Peerani, R.; Nie, Z.; Sullan, R. M. A.; Walker, G. C.; Kumacheva, E., *J Am Chem Soc* **2006**, 128, (37), 12205-12210.
22. Chu, L. Y.; Utada, A. S.; Shah, R. K.; Kim, J. W.; Weitz, D. A., *Angewandte Chemie-International Edition* **2007**, 46, (47), 8970-8974.
23. Kim, J. W.; Utada, A. S.; Fernandez-Nieves, A.; Hu, Z. B.; Weitz, D. A., *Angewandte Chemie-International Edition* **2007**, 46, (11), 1819-1822.
24. Bohmer, M. R.; Schroeders, R.; Steenbakkens, J. A. M.; de Winter, S.; Duineveld, P. A.; Lub, J.; Nijssen, W. P. M.; Pikkemaat, J. A.; Stapert, H. R., *Colloid Surf. A-Physicochem. Eng. Asp.* **2006**, 289, (1-3), 96-104.
25. Dohnal, J.; Stepanek, F., *Powder Technol.* **2010**, 200, (3), 254-259.

26. Decher, G., *Science* **1997**, 277, (5330), 1232-1237.
27. Sukhorukov, G. B.; Donath, E.; Davis, S.; Lichtenfeld, H.; Caruso, F.; Popov, V. I.; Möhwald, H., *Polymers for Advanced Technologies* **1998**, 9, (10-11), 759-767.
28. Sukhorukov, G. B.; Donath, E.; Davis, S.; Lichtenfeld, H.; Caruso, F.; Popov, V. I.; Mohwald, H., *Polymers for Advanced Technologies* **1998**, 9, (10-11), 759-767.
29. del Mercato, L. L.; Rivera-Gil, P.; Abbasi, A. Z.; Ochs, M.; Ganas, C.; Zins, I.; Sonnichsen, C.; Parak, W. J., *Nanoscale* **2010**, 2, (4), 458-467.
30. Skirtach, A. G.; Yashchenok, A. M.; Mohwald, H., *Chemical Communications* **2011**, 47, (48), 12736-12746.
31. Caruso, F.; Caruso, R. A.; Mohwald, H., *Science* **1998**, 282, (5391), 1111-1114.
32. Caruso, F.; Spasova, M.; Saigueirino-Maceira, V.; Liz-Marzan, L. M., *Adv. Mater.* **2001**, 13, (14), 1090-1094.
33. Müller, R.; Daehne, L.; Fery, A., *J. Phys. Chem. B* **2007**, 111, (29), 8547-8553.
34. Velev, O. D.; Furusawa, K.; Nagayama, K., *Langmuir* **1996**, 12, (10), 2374-2384.
35. Dinsmore, A. D.; Hsu, M. F.; Nikolaidis, M. G.; Marquez, M.; Bausch, A. R.; Weitz, D. A., *Science* **2002**, 298, (5595), 1006-1009.
36. Rossier-Miranda, F. J.; Schroen, C.; Boom, R. M., *Colloid Surf. A-Physicochem. Eng. Asp.* **2009**, 343, (1-3), 43-49.
37. Peyratout, C. S.; Dähne, L., *Angewandte Chemie International Edition* **2004**, 43, (29), 3762-3783.
38. Dubreuil, F.; Elsner, N.; Fery, A., *Eur. Phys. J. E* **2003**, 12, (2), 215-221.
39. Elsner, N. *Nanomechanik und Adhäsion von Polyelektrolytmultischicht-Hohlkapseln*. Monographie, Universität Potsdam, Potsdam, **2005**.
40. Elsner, N.; Dubreuil, F.; Fery, A., *Phys Rev E* **2004**, 69, (3), 6.
41. Fery, A.; Dubreuil, F.; Mohwald, H., *New J Phys* **2004**, 6, 18.
42. Fernandes, P. A. L.; Delcea, M.; Skirtach, A. G.; Mohwald, H.; Fery, A., *Soft Matter* **2010**, 6, (9), 1879-1883.
43. Skirtach, A. G.; Karageorgiev, P.; Bedard, M. F.; Sukhorukov, G. B.; Mohwald, H., *J Am Chem Soc* **2008**, 130, (35), 11572-11573.
44. De Geest, B. G.; Dejugnat, C.; Sukhorukov, G. B.; Braeckmans, K.; De Smedt, S. C.; Demeester, J., *Adv. Mater.* **2005**, 17, (19), 2357-2361.
45. Peyratout, C.; Dähne, L., *Angewandte Chemie-International Edition* **2004**, 43, (29), 3762-3783.
46. Bedard, M. F.; Braun, D.; Sukhorukov, G. B.; Skirtach, A. G., *Acs Nano* **2008**, 2, (9), 1807-1816.
47. Skirtach, A. G.; Yashchenok, A. M.; Mohwald, H., *Chem Commun (Camb)* **2011**, 47, (48), 12736-46.
48. Sukhorukov, G. B.; Mohwald, H., *Trends Biotechnol.* **2007**, 25, (3), 93-98.
49. Sukhorukov, G. B.; Fery, A.; Möhwald, H., *Prog. Polym. Sci.* **2005**, 30, (8-9), 885-897.
50. Gere, J. M.; Goodno, B. J., *Mechanics of materials*. Cengage Learning: **2009**.
51. Eichler, J., *Physik -Grundlagen für das Ingenieurstudium-kurz und prägnant*. Friedr. Vieweg & Sohn Verlag: **2007**.

52. ©<http://www.insula.com.au/physics/index.html>
53. Ohtsubo, T.; Tsuda, S.; Tsuji, K., *Polymer* **1991**, 32, (13), 2395-2399.
54. Bartkowiak, A.; Hunkeler, D., *Chemistry of Materials* **1999**, 11, (9), 2486-2492.
55. Kohler, B.; Bomas, H.; Zoch, H. W.; Stalkopf, J., *Mater. Test.-Mater. Compon. Techn. Appl.* **2010**, 52, (11-12), 759-764.
56. Poncelet, D.; Neufeld, R. J., *Biotechnol. Bioeng.* **1989**, 33, (1), 95-103.
57. Chang, K. S.; Olbricht, W. L., *J. Fluid Mech.* **1993**, 250, 609-633.
58. Gao, C.; Donath, E.; Moya, S.; Dudnik, V.; Mohwald, H., *Eur. Phys. J. E* **2001**, 5, (1), 21-27.
59. Gao, C. Y.; Leporatti, S.; Moya, S.; Donath, E.; Mohwald, H., *Langmuir* **2001**, 17, (11), 3491-3495.
60. Datta, S. S.; Shum, H. C.; Weitz, D. A., *Langmuir* **2010**, 26, (24), 18612-18616.
61. Datta, S. S.; Kim, S. H.; Paulose, J.; Abbaspourrad, A.; Nelson, D. R.; Weitz, D. A., *Phys. Rev. Lett.* **2012**, 109, (13), 5.
62. Cole, K. S., *Journal of Cellular and Comparative Physiology* **1932**, 1, (1), 1-9.
63. Bartkowiak, A.; Hunkeler, D., *Chemistry of Materials* **2000**, 12, (1), 206-212.
64. Bartkowiak, A.; Brylak, W., *Polimery* **2006**, 51, (7-8), 547-554.
65. Rehor, A.; Canaple, L.; Zhang, Z.; Hunkeler, D., *Journal of Biomaterials Science, Polymer Edition* **2001**, 12, (2), 157-170.
66. Mahou, R.; Wandrey, C., *Macromolecules* **2010**, 43, (3), 1371-1378.
67. Liu, K. K.; Williams, D. R.; Briscoe, B. J., *Phys Rev E* **1996**, 54, (6), 6673-6680.
68. Keller, M. W.; Sottos, N. R., *Exp. Mech.* **2006**, 46, (6), 725-733.
69. Caruso, M. M.; Blaiszik, B. J.; Jin, H. H.; Schelkopf, S. R.; Stradley, D. S.; Sottos, N. R.; White, S. R.; Moore, J. S., *ACS Appl. Mater. Interfaces* **2010**, 2, (4), 1195-1199.
70. Blaiszik, B. J.; Sottos, N. R.; White, S. R., *Compos. Sci. Technol.* **2008**, 68, (3-4), 978-986.
71. Zhang, Z.; Saunders, R.; Thomas, C. R., *Journal of Microencapsulation* **1999**, 16, (1), 117-124.
72. Liu, M. *Understanding the mechanical strength of microcapsules and their adhesion on fabric surfaces*. PhD Thesis, University of Birmingham, Birmingham, **2010**.
73. Long, Y.; York, D.; Zhang, Z. B.; Preece, J. A., *J. Mater. Chem.* **2009**, 19, (37), 6882-6887.
74. Hu, J. F.; Chen, H. Q.; Zhang, Z. B., *Mater. Chem. Phys.* **2009**, 118, (1), 63-70.
75. Kim, K.; Cheng, J.; Liu, Q.; Wu, X. Y.; Sun, Y., *J. Biomed. Mater. Res. Part A* **2010**, 92A, (1), 103-113.
76. O'Sullivan, M.; Zhang, Z. B.; Vincent, B., *Langmuir* **2009**, 25, (14), 7962-7966.
77. Butt, H. J.; Cappella, B.; Kappl, M., *Surface Science Reports* **2005**, 59, (1-6), 1-152.
78. Lulevich, V. V.; Radtchenko, I. L.; Sukhorukov, G. B.; Vinogradova, O. I., *J. Phys. Chem. B* **2003**, 107, (12), 2735-2740.
79. Lulevich, V. V.; Andrienko, D.; Vinogradova, O. I., *J Chem Phys* **2004**, 120, (8), 3822-3826.

80. Lebedeva, O. V.; Kim, B. S.; Vinogradova, O. I., *Langmuir* **2004**, 20, (24), 10685-10690.
81. Fery, A.; Dubreuil, F.; Mohwald, H., *New J. Phys.* **2004**, 6, 13.
82. Liang, X. M.; Mao, G. Z.; Ng, K. Y. S., *J Colloid Interf Sci* **2004**, 278, (1), 53-62.
83. Palankar, R.; Pinchasik, B. E.; Schmidt, S.; De Geest, B. G.; Fery, A.; Mohwald, H.; Skirtach, A. G.; Delcea, M., *J. Mat. Chem. B* **2013**, 1, (8), 1175-1181.
84. Heuvingh, J.; Zappa, M.; Fery, A., *Langmuir* **2005**, 21, (7), 3165-71.
85. Zhang, L.; D'Acunzi, M.; Kappl, M.; Auernhammer, G. K.; Vollmer, D.; van Kats, C. M.; van Blaaderen, A., *Langmuir* **2009**, 25, (5), 2711-2717.
86. Zoldesi, C. I.; Ivanovska, I. L.; Quilliet, C.; Wuite, G. J. L.; Imhof, A., *Phys Rev E* **2008**, 78, (5), -.
87. Jaskiewicz, K.; Makowski, M.; Kappl, M.; Landfester, K.; Kroeger, A., *Langmuir* **2012**, 28, (34), 12629-12636.
88. Cuellar, J. L.; Meinhoefel, F.; Hoehne, M.; Donath, E., *J. Gen. Virol.* **2010**, 91, 2449-2456.
89. Delorme, N.; Fery, A., *Phys Rev E* **2006**, 74, (3), 3.
90. Roos, W. H.; Gibbons, M. M.; Arkhipov, A.; Uetrecht, C.; Watts, N. R.; Wingfield, P. T.; Steven, A. C.; Heck, A. J. R.; Schulten, K.; Klug, W. S.; Wuite, G. J. L., *Biophys. J.* **2010**, 99, (4), 1175-1181.
91. Sboros, V.; Glynos, E.; Pye, S. D.; Moran, C. M.; Butler, M.; Ross, J. A.; McDicken, W. N.; Koutsos, V., *Ultrasonics* **2007**, 46, (4), 349-354.
92. Glynos, E.; Koutsos, V.; McDicken, W. N.; Moran, C. M.; Pye, S. D.; Ross, J. A.; Sboros, V., *Langmuir* **2009**, 25, (13), 7514-7522.
93. Grant, C. A.; McKendry, J. E.; Evans, S. D., *Soft Matter* **2012**, 8, (5), 1321-1326.
94. Santos, E. B.; Morris, J. K.; Glynos, E.; Sboros, V.; Koutsos, V., *Langmuir* **2012**, 28, (13), 5753-5760.
95. Chen, C. C.; Wu, S. Y.; Finan, J. D.; Morrison, B.; Konofagou, E. E., *IEEE Trans. Ultrason. Ferroelectr. Freq. Control* **2013**, 60, (3), 524-534.
96. Rehage, H.; Husmann, M.; Walter, A., *Rheol. Acta* **2002**, 41, (4), 292-306.
97. Walter, A.; Rehage, H.; Leonhard, H., *Colloid Polym Sci* **2000**, 278, (2), 169-175.
98. Koleva, I.; Rehage, H., *Soft Matter* **2012**, 8, (13), 3681-3693.
99. Walter, A.; Rehage, H.; Leonhard, H., *Colloid Surf. A-Physicochem. Eng. Asp.* **2001**, 183, 123-132.
100. Degen, P.; Leick, S.; Rehage, H., *Z. Phys. Chemie-Int. J. Res. Phys. Chem. Chem. Phys.* **2009**, 223, (9), 1079-1090.
101. Pieper, G.; Rehage, H.; Barthes-Biesel, D., *J Colloid Interf Sci* **1998**, 202, (2), 293-300.
102. Leick, S.; Kott, M.; Degen, P.; Henning, S.; Pasler, T.; Suter, D.; Rehage, H., *Phys Chem Chem Phys* **2011**, 13, (7), 2765-2773.
103. Husmann, M.; Rehage, H.; Dhenin, E.; Barthes-Biesel, D., *J Colloid Interf Sci* **2005**, 282, (1), 109-119.
104. Leick, S.; Kemper, A.; Rehage, H., *Soft Matter* **2011**, 7, (14), 6684-6694.

105. Leick, S.; Henning, S.; Degen, P.; Suter, D.; Rehage, H., *Phys Chem Chem Phys* **2010**, 12, (12), 2950-2958.
106. Tomaiuolo, G.; Simeone, M.; Martinelli, V.; Rotoli, B.; Guido, S., *Soft Matter* **2009**, 5, (19), 3736-3740.
107. Lefebvre, Y.; Leclerc, E.; Barthes-Biesel, D.; Walter, J.; Edwards-Levy, F., *Phys. Fluids* **2008**, 20, (12), 10.
108. She, S. P.; Xu, C. X.; Yin, X. F.; Tong, W. J.; Gao, C. Y., *Langmuir* **2012**, 28, (11), 5010-5016.
109. Leclerc, E.; Kinoshita, H.; Fujii, T.; Barthes-Biesel, D., *Microfluid. Nanofluid.* **2012**, 12, (5), 761-770.
110. Chu, T. X.; Salsac, A. V.; Leclerc, E.; Barthes-Biesel, D.; Wurtz, H.; Edwards-Levy, F., *J Colloid Interf Sci* **2011**, 355, (1), 81-88.
111. Lac, E.; Barthes-Biesel, D.; Pelekasis, N. A.; Tsamopoulos, J., *J. Fluid Mech.* **2004**, 516, 303-334.
112. Barthes-Biesel, D., *C. R. Phys.* **2009**, 10, (8), 764-774.
113. Mitchison, J. M.; Swann, M. M., *J. Exp. Biol.* **1954**, 31, (3), 443-460.
114. Rand, R. P.; Burton, A. C., *Biophys. J.* **1964**, 4, (2), 115-135.
115. Hochmuth, R. M., *J. Biomech.* **2000**, 33, (1), 15-22.
116. Kim, D. H.; Wong, P. K.; Park, J.; Levchenko, A.; Sun, Y., *Annu. Rev. Biomed. Eng.* **2009**, 11, 203-233.
117. Theret, D. P.; Levesque, M. J.; Sato, M.; Nerem, R. M.; Wheeler, L. T., *J. Biomech. Eng.-Trans. ASME* **1988**, 110, (3), 190-199.
118. Evans, E. A., *Biophys. J.* **1973**, 13, (9), 941-954.
119. Skalak, R.; Tozeren, A.; Zarda, R. P.; Chien, S., *Biophys. J.* **1973**, 13, (3), 245-280.
120. Dieluweit, S.; Csiszar, A.; Rubner, W.; Fleischhauer, J.; Houben, S.; Merkel, R., *Langmuir* **2010**, 26, (13), 11041-11049.
121. Chien, S.; Sung, K. L. P.; Skalak, R.; Usami, S., *Biophys. J.* **1978**, 24, (2), 463-487.
122. Evans, E.; Yeung, A., *Biophys. J.* **1989**, 56, (1), 151-160.
123. Shao, J. Y.; Hochmuth, R. M., *Biophys. J.* **1996**, 71, (5), 2892-2901.
124. Ratanabanangkoon, P.; Gropper, M.; Merkel, R.; Sackmann, E.; Gast, A. P., *Langmuir* **2003**, 19, (4), 1054-1062.
125. Rawicz, W.; Olbrich, K. C.; McIntosh, T.; Needham, D.; Evans, E., *Biophys. J.* **2000**, 79, (1), 328-339.
126. Mabrouk, E.; Cuvelier, D.; Pontani, L. L.; Xu, B.; Levy, D.; Keller, P.; Brochard-Wyart, F.; Nassoy, P.; Li, M. H., *Soft Matter* **2009**, 5, (9), 1870-1878.
127. Sohail, T.; Tang, T.; Nadler, B., *Z. Angew. Math. Phys.* **2012**, 63, (4), 737-757.
128. Heinrich, V.; Ounkomol, C., *Biophys. J.* **2007**, 93, (2), 363-372.
129. Baaijens, F. P. T.; Trickey, W. R.; Laursen, T. A.; Guilak, F., *Ann. Biomed. Eng.* **2005**, 33, (4), 494-501.
130. Theret, D. P.; Levesque, M. J.; Sato, M.; Nerem, R. M.; Wheeler, L. T., *J. Biomech. Eng.-Trans. ASME* **1988**, 110, (3), 190-199.
131. Discher, D. E.; Boal, D. H.; Boey, S. K., *Biophys. J.* **1998**, 75, (3), 1584-1597.

132. Neuman, K. C.; Nagy, A., *Nat Meth* **2008**, 5, (6), 491-505.
133. Ashkin, A., *Phys. Rev. Lett.* **1970**, 24, (4), 156-159.
134. Svoboda, K.; Block, S. M., *Annu. Rev. Biophys. Biomolec. Struct.* **1994**, 23, 247-285.
135. Noy, A., *Handbook of Molecular Force Spectroscopy*. Springer: New York, **2008**.
136. Zhang, H.; Liu, K. K., *J. R. Soc. Interface* **2008**, 5, (24), 671-690.
137. e-funda <http://www.efunda.com/home.cfm>
138. Konnerth, J.; Gindl, W.; Müller, U., *J. Appl. Polym. Sci.* **2007**, 103, (6), 3936-3939.
139. Mercadé-Prieto, R.; Nguyen, B.; Allen, R.; York, D.; Preece, J. A.; Goodwin, T. E.; Zhang, Z., *Chemical Engineering Science* **2011**, 66, 2042-2049.
140. Roos, W. H.; Bruinsma, R.; Wuite, G. J. L., *Nat Phys* **2010**, 6, (10), 733-743.
141. Chen, Q.; Schonherr, H.; Vancso, G. J., *Soft Matter* **2009**, 5, (24), 4944-4950.
142. Binnig, G.; Quate, C. F.; Gerber, C., *Phys. Rev. Lett.* **1986**, 56, (9), 930.
143. Sader, J. E., *J. Appl. Phys.* **1998**, 84, (1), 64-76.
144. Hutter, J. L.; Bechhoefer, J., *Rev. Sci. Instrum.* **1993**, 64, (7), 1868-1873.
145. Ducker, W. A.; Senden, T. J.; Pashley, R. M., *Nature* **1991**, 353, (6341), 239-241.
146. Butt, H. J., *Biophys. J.* **1991**, 60, (6), 1438-1444.
147. Max, E.; Hafner, W.; Bartels, F. W.; Sugiharto, A.; Wood, C.; Fery, A., *Ultramicroscopy* **2010**, 110, (4), 320-324.
148. Erath, J.; Schmidt, S.; Fery, A., *Soft Matter* **2010**, 6, (7), 1432-1437.
149. Kuznetsov, V.; Papastavrou, G., *The Review of scientific instruments* **2012**, 83, (11), 116103-116103.
150. Landau, L. D.; Lifschitz, E. M.; Ziesche, P., *Lehrbuch der theoretischen Physik, Band VII: Elastizitätstheorie*. Deutsch Harri GmbH: **2007**.
151. Timoshenko, S.; Woinowsky-Krieger, S., *Theory of plates and shells*. McGraw-Hill: **1959**.
152. Calladine, C. R., *Theory of Shell Structures*. Cambridge University Press: **1989**.
153. Pozrikidis, C., Shell theory for capsules and cells. In *Modeling and Simulation of Capsules and Biological Cells*, Chapman & Hall/Crc: Boca Raton, **2003**; 35-101.
154. Neubauer, M.; Poehlmann, M.; Fery, A., *Advances in Colloid and Interface Science* **2014**, 207, 65-80.
155. Ventsel, E.; Krauthammer, T., *Thin Plates and Shells*. Marcel Dekker: New York, **2001**.
156. Reissner, E., *Journal of Mathematics and Physics* **1946**, 25, (2), 80-85.
157. Reissner, E., *Commun. Pure Appl. Math.* **1959**, 12, (2), 385-398.
158. Reissner, E., *Journal of Mathematics and Mechanics* **1958**, 7, (2), 121-140.
159. Reissner, E.; Wan, F. Y. M., *Stud. Appl. Math.* **1969**, 48, (1), 1.
160. Ferri, J. K.; Carl, P.; Gorevski, N.; Russell, T. P.; Wang, Q.; Boker, A.; Fery, A., *Soft Matter* **2008**, 4, (11), 2259-2266.
161. Tan, S. Y.; Tabor, R. F.; Ong, L.; Stevens, G. W.; Dagastine, R. R., *Soft Matter* **2012**, 8, (11), 3112-3121.

162. Pogorelov, A. V.; Babenko, V. I., *Int. Appl. Mech.* **1992**, 28, (1), 1-17.
163. Arnoldi, M.; Fritz, M.; Bauerlein, E.; Radmacher, M.; Sackmann, E.; Boulbitch, A., *Phys Rev E* **2000**, 62, (1), 1034-1044.
164. Boulbitch, A., *J. Electron Microsc.* **2000**, 49, (3), 459-462.
165. Wan, K. T.; Chan, V.; Dillard, D. A., *Colloid Surf. B-Biointerfaces* **2003**, 27, (2-3), 241-248.
166. Yao, X.; Walter, J.; Burke, S.; Stewart, S.; Jericho, M. H.; Pink, D.; Hunter, R.; Beveridge, T. J., *Colloid Surf. B-Biointerfaces* **2002**, 23, (2-3), 213-230.
167. Zhongcan, O. Y.; Helfrich, W., *Phys. Rev. A* **1989**, 39, (10), 5280-5288.
168. Pujara, P.; Lardner, T. J., *Z. Angew. Math. Phys.* **1978**, 29, (2), 315-327.
169. Landau, L. D.; Lifschitz, E. M., *Elastizitätstheorie*. Akademie: Berlin, **1991**.
170. Taber, L. A., *Journal of Applied Mechanics-Transactions of the Asme* **1982**, 49, (1), 121-128.
171. Sun, G.; Zhang, Z., *Journal of Microencapsulation* **2001**, 18, (5), 593-602.
172. Mercade-Prieto, R.; Allen, R.; Zhang, Z. B.; York, D.; Preece, J. A.; Goodwin, T. E., *Aiche J.* **2012**, 58, (9), 2674-2681.

### 3. Overview of the thesis

In this cumulative thesis structure-property-relations on the single-particle-level were studied and used for a rational design of microcapsules. Four manuscripts have been published in the framework of this thesis, which are presented in the chapters 4 to 7.

#### 3.1 Mechanics of Microcapsules: From Stability to Function (Chapter 4)

The history of microcapsules is a real success story. After the first industrial production of carbon less copy paper in the 1950s, microcapsules have established in all kind of application fields: pharmacy, food industry, agriculture, cosmetics, textile industry, printing, biosensor engineering, active coatings and construction. Today innovate microcapsules aim on custom-made and multi-functional properties. Thus, scientific expertise is needed to understand the fundamental structure-property-relations of microcapsules and to tailor their mechanical properties with regard to functional aspects.

Microcapsule preparation methods and their potential to adjust geometrical features - diameter and shell thickness - are decisive for tuning mechanical properties. Therefore, different preparation methods are reviewed in this manuscript, which was structured according to the thesis' chapter 2 *Status of the Field*, where the preparation and characterization methods are described in detail. In brief, preparation methods can be distinguished in:

- Physico-mechanical processes are used for a large-scale production of encapsulated materials. Easy handling, low costs and a multi-tonne production brings along a large polydispersity in particle diameter and shell thickness.
- Template-assisted methods offer control over the microcapsule's diameter. Hard and soft templates can be distinguished.
- Self-assembly methods with e.g. lipids, blockcopolymers, or colloids offer very precise control over the shell thickness.
- A combination of both, template-assisted and self-assembly methods, offers the possibility to produce microcapsule with custom-made dimensions.

Examples are microcapsules produced via the layer-by-layer deposition technique or microfluidic approaches.

With an emphasis on the characterization of mechanical properties, ensemble and single-capsule techniques are discussed in the article. Methods for a characterization on the single-particle-level are discussed in depth, because they offer a correlation of morphological and mechanical properties.

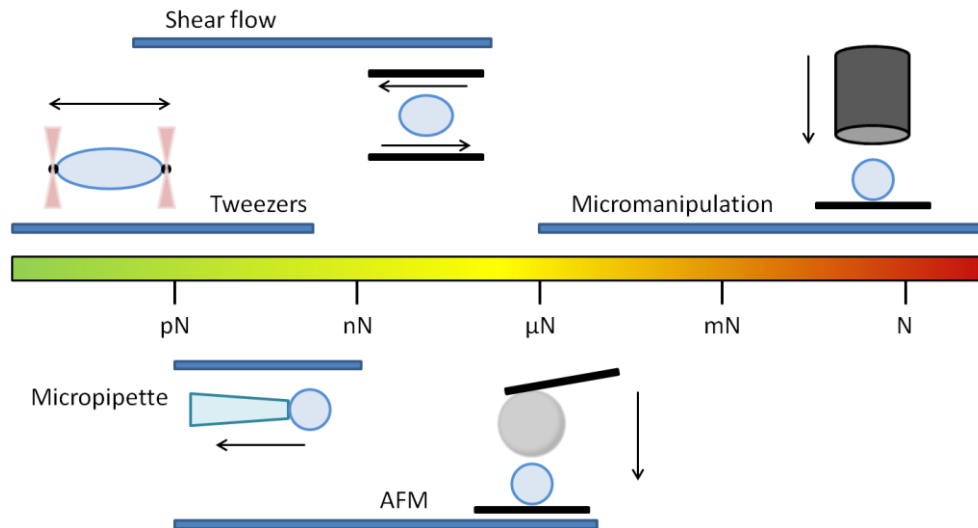


Figure 3-1 Schematic representation of single-capsule measurement techniques, each with typically available force range. Arrows indicate the directions in which forces are acting.

In detail the following techniques ordered according to their decreasing force sensitivity (Fig 3-1), are presented:

- Optical, magnetic and electromagnetic tweezers
- Micropipette aspiration
- Shear flow experiments (rheology, microfluidics)
- Force spectroscopy experiments (AFM)
- Micromanipulation techniques and
- Osmotic pressure experiments

Theoretical models are needed for the interpretation of the experimental results, obtained from static, quasi-static and dynamic characterization methods. Therefore an overview of the physics of capsule deformation is given, considering analytical and numerical methods. Of major interest is the thin shell theory, which

provides a useful approximation for small and large deformation scenarios. Analytical simple scaling laws from Reissner and Pogorelov are discussed and their limitations in view of a pre-tension caused by interfacial tension or pre-inflation of microcapsules.

A systematic design of micromechanical properties carries the potential to turn microcapsules into multi- functional devices that are of interest for:

- force sensors,
- the tailoring of an increased cellular uptake,
- specified release profiles,
- the development of analytical devices for quality control and fractionation of microcapsule with specific mechanical properties, or
- active motion of microcapsules.

### **3.2 Polymeric Air-Filled Microbubbles for Theranostic Applications: Burst Release of Therapeutic Gases (Chapter 5)**

Theranostic microbubbles (MB) have a polymeric shell made of poly(vinyl alcohol) (PVA), which is enveloping a gaseous core. The release of encapsulated therapeutic gases, *e.g.* NO, is triggered by a burst of the shell via high intensity ultrasound. The polymeric microbubbles are synthesized by cross-linking of telechelic PVA at the air-water interface of air-bubbles produced through vigorous stirring at room temperature. This reproducible and simple one-pot synthesis allows for up-scaling and commercialization.

Structure-property relations on the single-particle-level were required for the shell thickness, shell composition and the mechanical and adhesive properties. For polymeric gas-filled microbubbles a characterization on the single-particle-level was successfully established by using the following techniques: atomic force microscopy (AFM) combined with reflection interference contrast microscopy (RICM) and scanning transmission X-ray microscopy (STXM).

With force-spectroscopy experiments the mechanical properties of micron-sized microbubbles were determined in the small (100 nm) and large (1  $\mu\text{m}$ ) deformation regime as illustrated in Figure 3-2.

The obtained force-deformation curves indicated a microbubble's stiffness of about 0.1 N/m - 0.2 N/m and a critical burst force of about 0.5  $\mu\text{N}$  - 2.5  $\mu\text{N}$ . RICM proofed suitable to follow the event of burst *in situ*. RICM images in Figure 3-2 clearly indicate the loss of the gaseous core through a change of the refractive index ratio between inner and outer medium. The bright spot in the middle indicating the air/water interface vanishes abruptly during the burst of the MB and the formation of a water/water interface. RICM and optical microscopy further revealed that a burst does not lead to a fragmentation of MBs, but turns air-filled MBs into water-filled MBs.

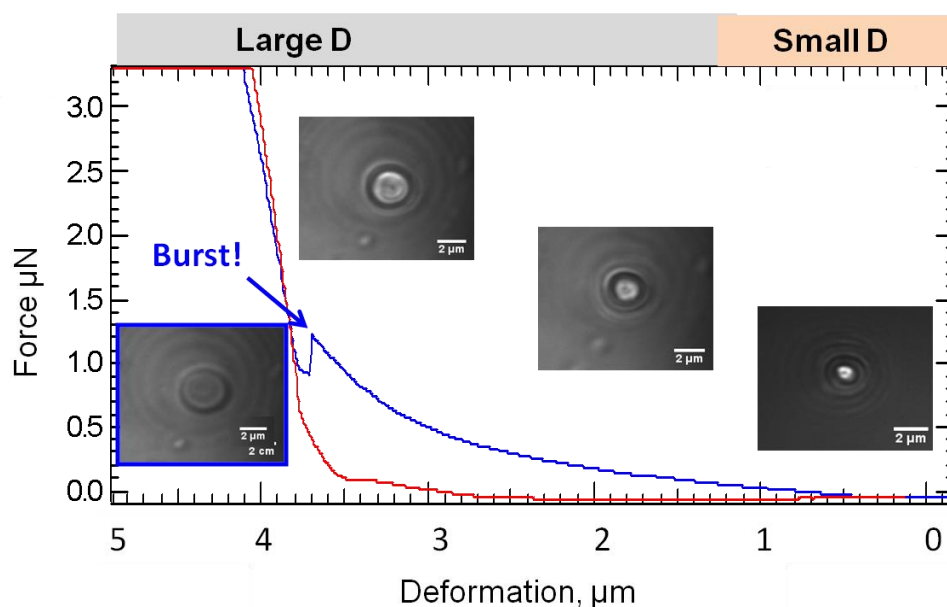


Figure 3-2: In this force-deformation graph the deformation of the microbubble under a force load up to 3  $\mu\text{m}$  is shown. The deformation of the microbubble can be followed with *in situ* RICM.

Force-spectroscopy measurements are feasible in air, under physiological conditions, as well as for a broad range of temperatures. Thus, the impact of an increased temperature - here the change from room to body temperature- was found to shift the microbubble's stiffness to values which are of about 10 % smaller (from 0.115 N/m to 0.098 N/m), as shown in Figure 3-3. In other words,

microbubbles will become softer and change their deformation behavior when injected in the human body.

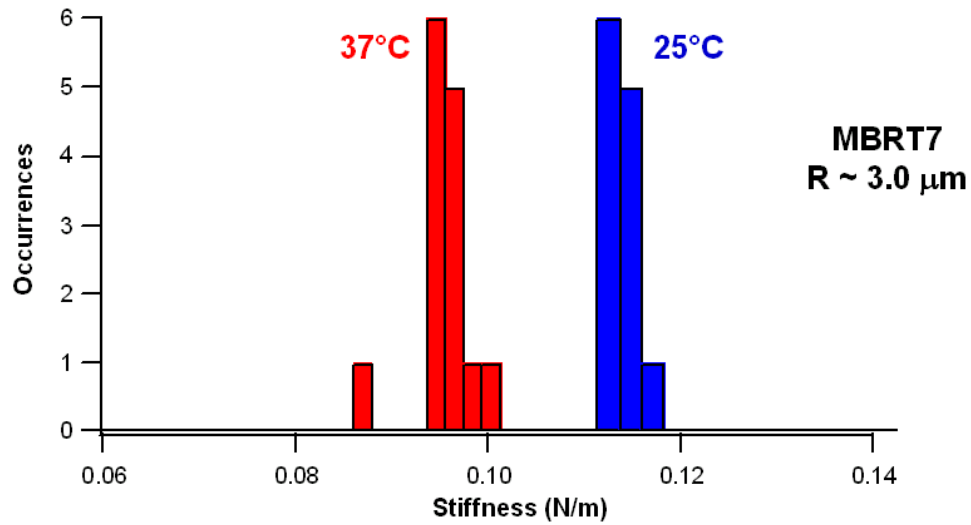


Figure 3-3: Histograms of MB stiffness at room and body temperature.

Moreover, the impact of aging was investigated. In particular, burst forces of fresh and one year old samples were compared with each other. The experiments showed that a storage of the samples at room temperature an increased scattering of the stiffness values is observed upon aging, indicating a structural change of the shell material through the aging process. Therefore, the storage under cool and dark conditions is recommended for the preservation of the MBs' mechanical properties.

An elegant way to determine adhesive properties of polymeric MBs qualitatively and quantitatively offers AFM combined with *in situ* RICM. This combination benefits on the one hand from the precise determination of the apparent contact area *in situ* (RICM) and a high resolution of the corresponding adhesion force in the range of pN (AFM). The theranostic particles showed burst upon deformations of about ~70 - 80% of their diameter before burst and weak adhesion with a max. adhesion force of ~4 nN. Adhesive properties were then used to control and direct MB adhesion into arrays (see Figure 3-4) by using chemical patterned substrates. Such arrays are of interest for *e.g.* serial testing of mechanical properties.

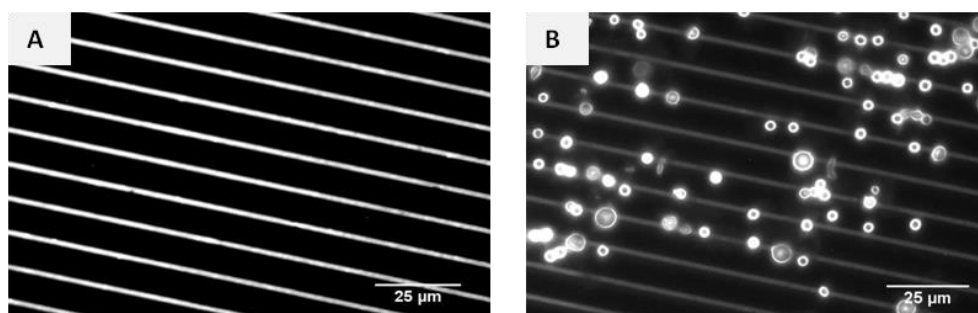


Figure 3-4: (A) Line pattern transferred with micro-contact printing to a polyelectrolyte multilayer. (B) Selective adhesion of microbubbles on a patterned substrate.

A novel spectro-microscopic characterization technique, which was developed in the group of Prof. Rainer Fink from the University of Erlangen, is scanning transmission X-ray microscopy (STXM). This characterization method allows for elemental and chemical imaging with a spatial resolution in the sub-40 nm regime and a spectral resolving power  $E/\Delta E > 5000$  (at the N K-edge, approx. 400 eV). In environmental studies (here in aqueous solution) structure and composition of MB and their shell were determined. In particular, the technique allowed for monitoring the interior of the MB and thus proofed the existence of the gaseous core as shown in Figure 3-5. Moreover, the obtained 2-D images with a high spatial resolution provided the basis to determine for the first the shell thickness (300 nm- 600 nm) of the MB dispersed in water and the chemical composition of the shell material (20% PVA and 80% water).

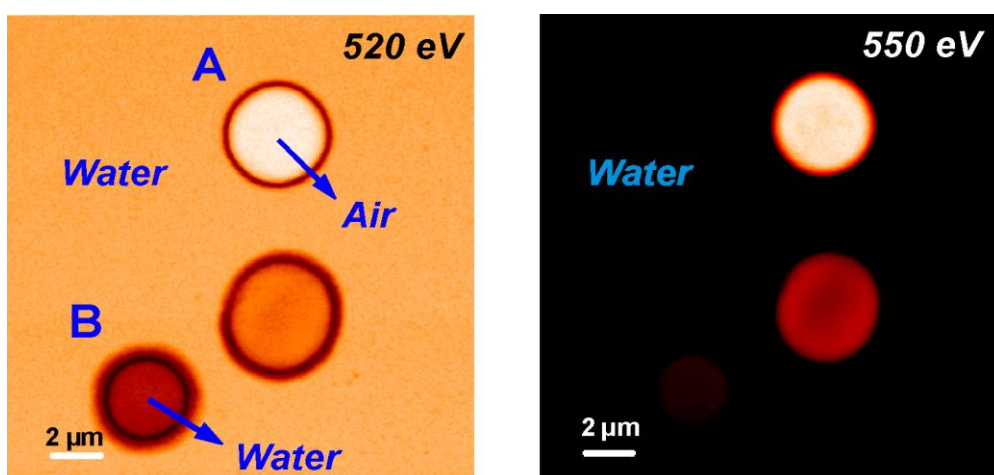


Figure 3-5: STXM transmission images of MBs in water environment recorded at  $h\nu = 520$  eV and  $h\nu = 550$  eV (scanned image size:  $20 \times 20 \mu\text{m}^2$ ).

In conclusion, the presented characterization techniques showed to be suitable for the characterization of microcapsules on the single particle level. In particular STXM proved to be of value for the shell thickness determination, which is for microcapsules in the range of nanometers and thus often difficult to assess. AFM and RICM showed to be in combination a powerful tool to study the deformation behavior and to retrieve reproducible mechanical and adhesive properties of single microcapsules. Thus, the presented techniques made clear that they play a key role towards a systematic design of MB by providing the basis for a thorough and straightforward characterization of structure-property relations of MB, which is also applicable for other microcapsule systems.

### **3.3 Hybrid Contrast Agents for Ultrasound and MRI Imaging: Impact of Nanoparticle Integration on Shell Properties in Low and High Frequency Mechanics (Chapter 6)**

Hybrid contrast agents gained enormous interest since the development of new hybrid scanners that promise to revolutionize the medical imaging market. Imaging techniques with new, more precise and complementary information already arrived in today's clinical routine. In this work hybrid contrast agents active in ultrasound and magnetic resonance imaging were studied. Polyvinyl-shelled microbubbles (US active) served as platform for the built-up of the hybrid contrast agents. Through the integration of super paramagnetic iron oxide nanoparticles (SPIONs) the microbubbles (ultrasound contrast agents) become magnetic and thus also active in magnetic resonance imaging. Two different pathways were tested to yield magnetic microbubbles: a physical approach to embed SPIONs inside the polymeric network and a chemical approach to couple nanoparticles to the shell surface.

For ultrasound contrast agents the mechanical properties of the shell are crucial, because they determine the performance during imaging. Thus, it is of fundamental interest to understand how the SPIONs' integration affects the shell's mechanical properties. The comprehensive study presents a pioneering work that links the synthesis straightforward to the performance of a US/MRI contrast agent. The critical parameters -shell thickness and microcapsule diameter- were in this study independently determined with two different techniques:

- AFM imaging of flat-folded dried and hydrated MBs.
- Transmission electron microscopy (TEM) imaging of ultrathin sections of embedded MBs.

AFM allowed to determine with relative high-throughput (compared to STXM and TEM) a good statistic of both parameters- shell thickness and diameter. In addition the single particle analysis allowed for a correlation of both parameters with each other (Figure 3-6). TEM also provided information about the location of integrated SPIONs and the homogeneity of the shell. However, shell thickness values measured with TEM need to be corrected from the random slicing process by a factor of 0.72, which was carried out during the sample preparation. The morphologic analysis clearly showed that both shell thickness and microbubble diameter are not affected through the integration of SPIONs, neither from the chemical nor from the physical approach (Figure 3-6).

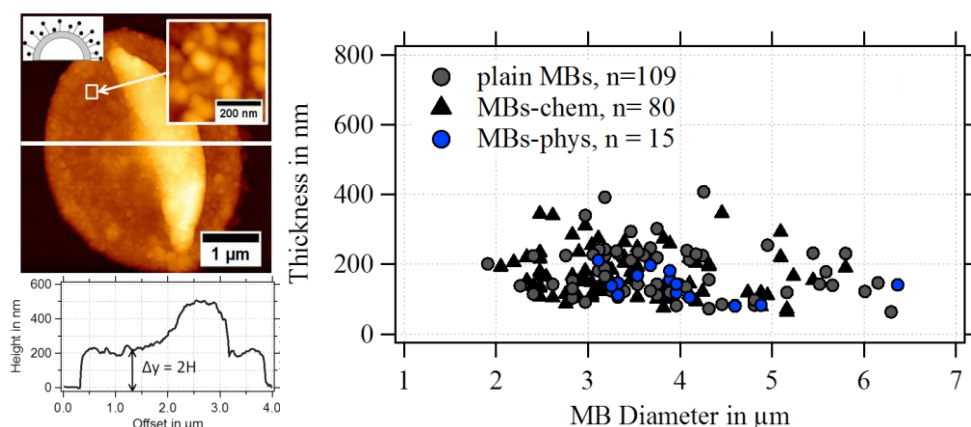


Figure 3-6 Thickness plotted versus the radius of the MBs imaged with AFM in dried conditions.

However, a change in the mechanical response was determined from force spectroscopy experiments (Figure 3-7). The quantification of the elastic modulus showed that properties of the shell material changed. In particular, magnetic MBs with SPIONs embedded in the polymeric network of the shell showed an increased elastic modulus (3.2 MPa), while magnetic MBs with SPIONs coupled to the shell surface showed even a lower elastic modulus (230 kPa) than the PVA shell of the original ultrasound contrast agents (1.3 MPa).

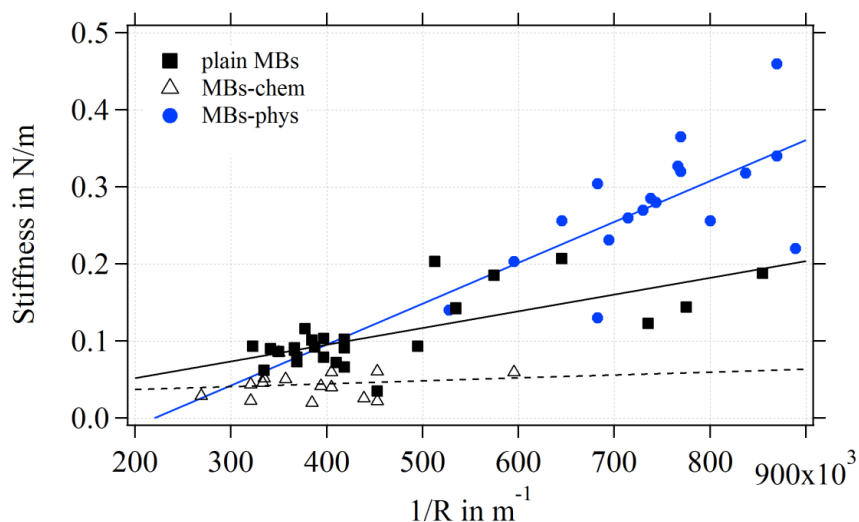


Figure 3-7: Scattering plot of the stiffness in N/m versus the inverse of the MB radius.

The reason for the increased elastic modulus is a reinforcement of the shell material and an increased density of the shell through the embedment of SPIONs. The reason for the softening observed for MBs treated by the chemical approach is a result of the shell's exposure to the reaction conditions of a reductive amination, which was needed to couple SPIONs to the shell surface.

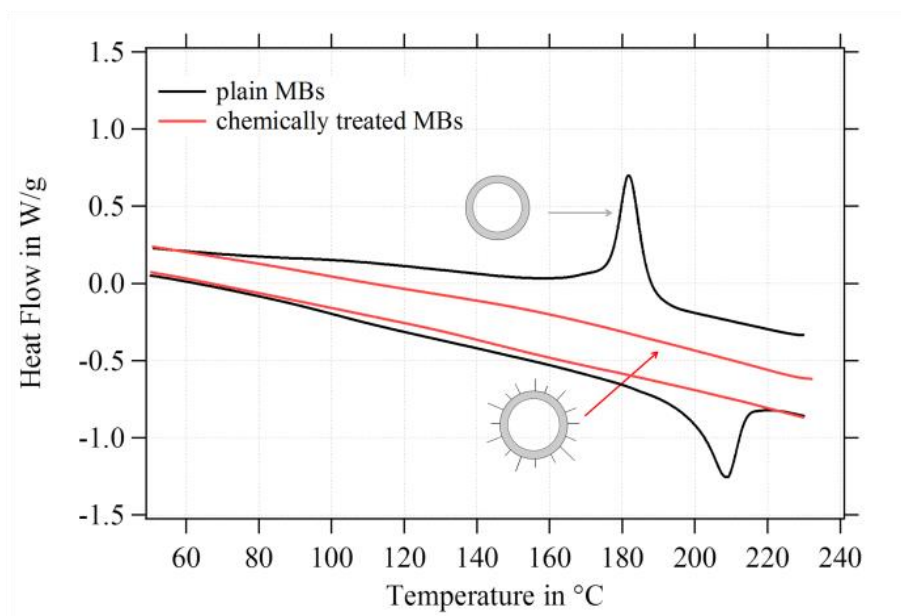


Figure 3-8: DSC results for plain MBs before and after chemical treatment without attaching SPIONs.

Differential scanning calorimetry showed that a decrease of physical cross-links (crystalline units) occurs within the PVA network through the chemical treatment (Figure 3-8).

Moreover, the study built a bridge from the nano/micro-scale to the macro-scale by showing that the changed properties of the shell material are not only reflected on the single-particle-level and for low-frequency experiments, but as well for an ensemble of MBs tested in the high frequency regime during ultrasound exposure. Theoretical treatment of the high-frequency results were used to estimate the shear modulus of the shell during dynamic oscillation, which showed the same trend. In conclusion, the presented strategy made clear that different structural designs of hybrid probes are important and can be used for their systematic design and optimization in view of the ultrasound performance.

### **3.4 Perfume-filled Aminoplast Microcapsules: Tuning Shell Properties for Controlled Release of Perfume in Fabric Softeners (Chapter 7)**

Perfume-filled aminoplast resin microcapsules represent a classical capsule systems used world-wide in industrial large scale productions for the encapsulation of fragrances. The studied aminoplast microcapsules are prepared by an emulsion-based process. The shell is built-up during a phase separation polymerization of melamine formaldehyde. The challenge in characterizing structure-property relations of industrial produced microcapsules is often the compensation of a size-dispersed system with an adequate number of experiments on the single-particle level to yield a significant statistic. For the studied microcapsules a diameter between 10  $\mu\text{m}$  to 50  $\mu\text{m}$  and a shell thickness between 50 nm and 200 nm was determined. The shell thickness was determined from ultrathin sections of embedded microcapsules imaged with TEM (Figure 3-9). The measured shell thickness was corrected from the random slicing process by a correction factor of 0.62.

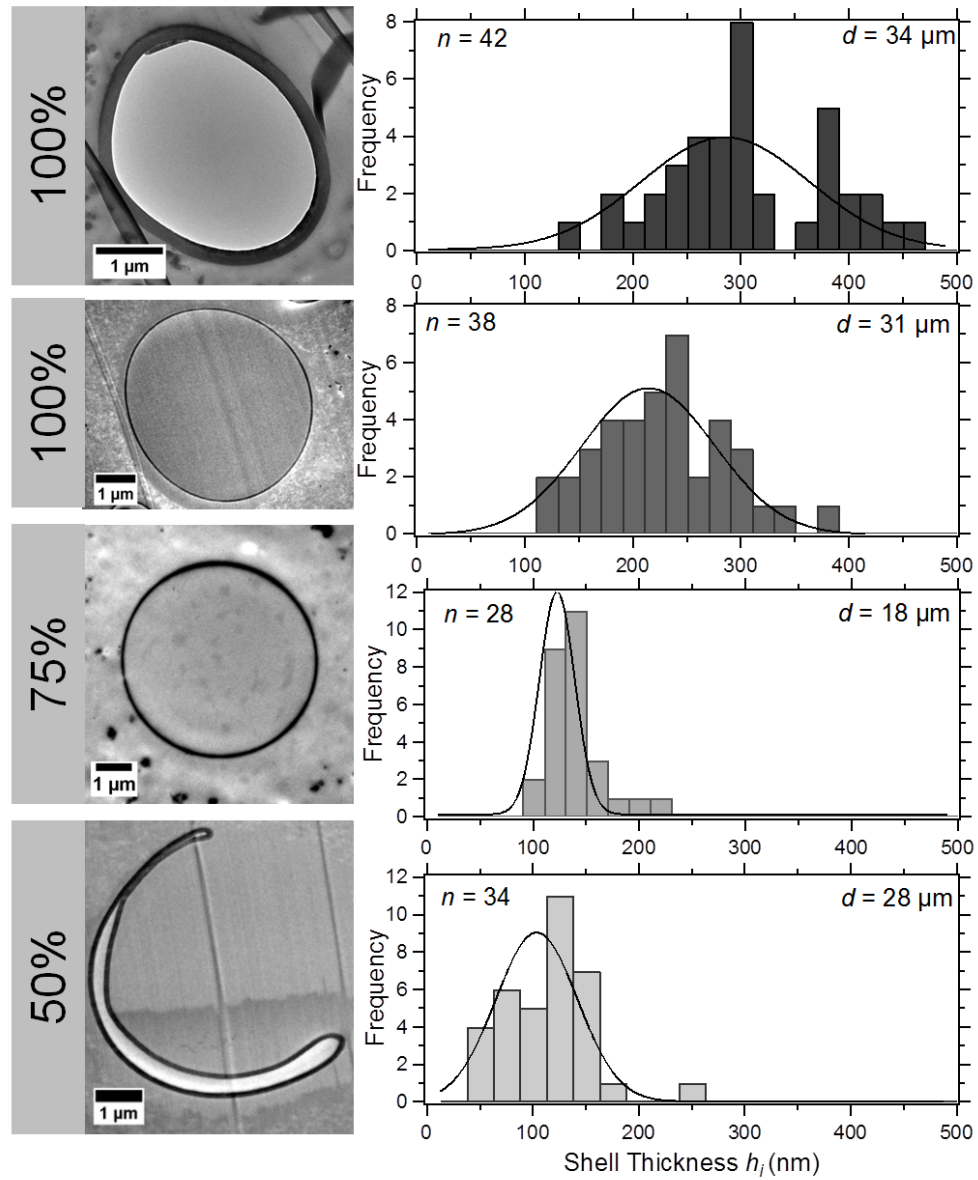


Figure 3-9: TEM images of embedded microcapsules sectioned with an ultra microtome and the quantified distribution of the measured shell thickness. The number of analyzed sections  $n$  is indicated along with the used amount of resin in percentage and the average diameter  $d$ .

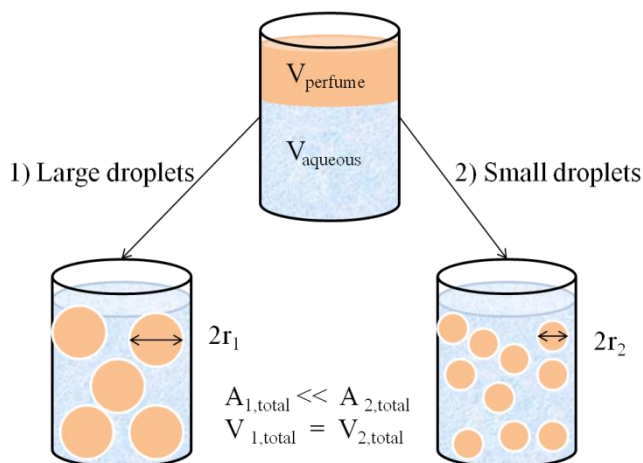


Figure 3-10: is illustrating the change of the surface area  $A$  for emulsions produced from a constant volume  $V$  of the dispersed phase and different radius  $r$  of the emulsion droplets.

As key parameter for the control of the shell thickness the amount of employed pre-polymer per total surface area of the dispersed phase was identified. Generally industrial processes use a defined amount of pre-polymer for the microcapsule preparation. In this case, the shell thickness becomes thinner with decreasing microcapsule diameters, which is reflecting an increased surface area as illustrated in Figure 3-10.

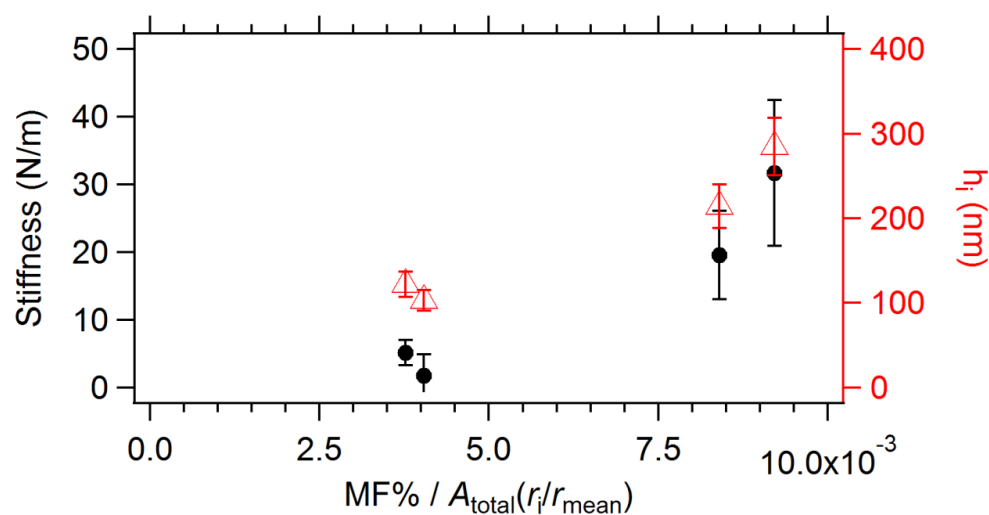


Figure 3-11: Summary of the morphological and mechanical characterization.

Within this study, mechanical properties of aminoresin capsules were studied for the first time in the small deformation regime using colloidal-probe force spectroscopy. Thus, it was possible to establish a link between the synthesis-controlled geometrical features and the capsule's mechanical response (Figure

3-7). With increasing shell thickness the stiffness of the microcapsules increased from 2 N/m to 30 N/m.

The elastic modulus for the melamine formaldehyde shell was estimated to be in the range of 1.7 GPa. Thus, thin-shelled microcapsules will reach the critical deformation for a burst release earlier than thick-shelled microcapsules.

### **3.5 Individual Contributions to Joint Publications**

The results of the thesis were obtained in collaboration with others. In the following, the contribution of the co-authors are specified.

**Chapter 4** is a reprint with permission from Elsevier. The manuscript was published in *Advances in Colloid and Interface Science* 2014, 207, 65-80, under the title:

#### **Microcapsule Mechanics: From Stability to Function**

*Martin Neubauer, Melanie Pöhlmann, Andreas Fery*

I structured the content of the first three sections of this article and provided the corresponding literature, which is basically the chapter 2 (*Status of the Field*) of this thesis. I was further involved in scientific discussions and the correction of the manuscript.

Martin Neubauer wrote most of the manuscript and carried out the rest of the literature research.

Andreas Fery wrote the last section of the article and was involved in scientific discussions and in the design and correction of the manuscript.

**Chapter 5** is reproduced with kind permission from Springer Science and Business Media, Copyright (2010). The manuscript was written in the framework of the FP6-IST-033700-project SIGHT-Systems for in-situ theranostics using micro-particles triggered by ultrasound. The European consortium contained experts for microbubble synthesis, ultrasound equipment producers, radiologists and medical engineers. The manuscript was published as a chapter in the book *Ultrasound contrast agents – Targeting and processing methods for theranostics* by the editors Gaio Paradossi, Paolo Pelegretti, Andrea Trucco under the title:

#### **Novel Characterization Techniques of Microballoon**

*Paulo Fernandes, Melanie Pretzl, Rainer Fink, Georg Tzvetkov, and Andreas Fery.*

I wrote the section on adhesion properties of microbubbles, performed the corresponding experimental work using AFM and RICM and carried out the

controlled and directed particle adhesion on patterned substrates, as well as the production of the corresponding patterned substrates.

Paulo Fernandes wrote most of the manuscript and carried out the AFM experiments (force spectroscopy experiments).

Georg Tzvetkov wrote the section about STXM and carried out all STXM experiments. Furthermore, he was involved in scientific discussions and in the correction of the manuscript.

Rainer Fink supervised Georg Tzvetkov and was involved in scientific discussions and in the correction of the book chapter.

Andreas Fery supervised the project and was involved in scientific discussions and in the correction of the manuscript.

**Chapter 6** is reprinted from *Soft Matter* 2014, 10 (1), 214 - 226 with permission of the Royal Chemical Society. This study was carried out in the framework of the FP7-NMP-2009-LARGE-245572-project 3MICRON-Three modality contrast imaging using multi-functionalized microballoons. The European consortium bundled experts for microbubble synthesis, ultrasound equipment producers, radiologists and medical engineers. The manuscript was published under the title:

**On the interplay of shell structure with low and high frequency mechanics  
of multifunctional magnetic microbubbles**

*Melanie Poehlmann, Dmitry Grishenkov, Satya V.V.N. Kothapalli, Johan Haermark, Hans Hebert, Alexandra Philipp, Roland Hoeller, Maximilian Seuss, Christian Kuttner, Silvia Margheritelli, Gaio Paradossi, Andreas Fery*

I coordinated the work between the different research groups and wrote the manuscript. Moreover, I performed all experimental work and the analysis, except that:

Alexandra Phillip and Maximilian Seuß contributed to the manuscript by investigating a statistically meaningful number of MBs to allow the quantitative analysis of the MBs dimensions. Both co-authors carried out some of the mechanical characterization using force-spectroscopy under my supervision in the framework of their bachelor thesis.

Roland Höller adopted the protocol provided by Johann Härmark and carried out the TEM characterization in Bayreuth. His work was performed under my supervision in the framework of his bachelor thesis.

Dmitry Grishenkov and Satya Kothapalli carried out the acoustic experiments and were responsible for the modeling of the MBs' acoustic response towards ultrasound exposure. In addition, they were writing parts of the acoustic section. Johann Härmark and Hans Hebert developed the TEM sample preparation for MBs. Moreover, they contributed with a significant number of TEM images to the quantitative evaluation of the shell thickness.

Christian Kuttner further modified the model for the correction of the shell thickness and determined the correction factor for all measured MBs.

Silvia Margheritelli and Gaio Paradossi synthesized the MBs and carried out the DSC measurements.

Andreas Fery supervised the project at the University of Bayreuth and was involved in scientific discussions and corrected the manuscript.

**Chapter 7** is reprinted with permission from ACS Applied Materials & Interfaces, 2012, 4(6), 2940-2948. Copyright (2012). American Chemical Society. The study was carried out in cooperation with the R&D division of the company Firmenich SA (Geneva, Switzerland). This work was published under the title

**Formation and Mechanical Characterization of Aminoplast Core/Shell  
Microcapsules**

*Melanie Pretzl, Martin Neubauer, Melanie Tekaas, Carmen Kunert, Christian Kuttner, Géraldine Leon, Damien Berthier, Philipp Erni, Lahoussine Ouali and  
Andreas Fery*

I planned and coordinated the experimental work carried out between the co-workers in this project and wrote the manuscript. I performed all experimental work and the corresponding analysis and interpretation of the results, except that:

Martin Neubauer carried out parts of the AFM experiments and the corresponding data analysis, was involved in scientific discussions and proofreading of the manuscript.

Melanie Tekaat participated in AFM experiments and the corresponding data analysis under my supervision and in the framework of her bachelor thesis "Characterization of Core/Shell Materials".

Carmen Kunert performed the TEM sample preparation - embedding and sectioning of microcapsules - and imaging of the thin sections with TEM.

Christian Kuttner applied a model proposed by Smith to correct the error of the shell thickness obtained through the random slicing process. Furthermore, he was involved in scientific discussions and proof-reading of the manuscript.

Géraldine Leon and Damien Berthier synthesized the MF microcapsules with different amount of MF and characterized the size distribution of the microcapsules. Both were involved in scientific discussions, were writing the corresponding experimental part in the manuscript and were proof-reading the manuscript.

Phillip Erni supervised the project at Firmenich SA, was involved in scientific discussions and corrected the manuscript.

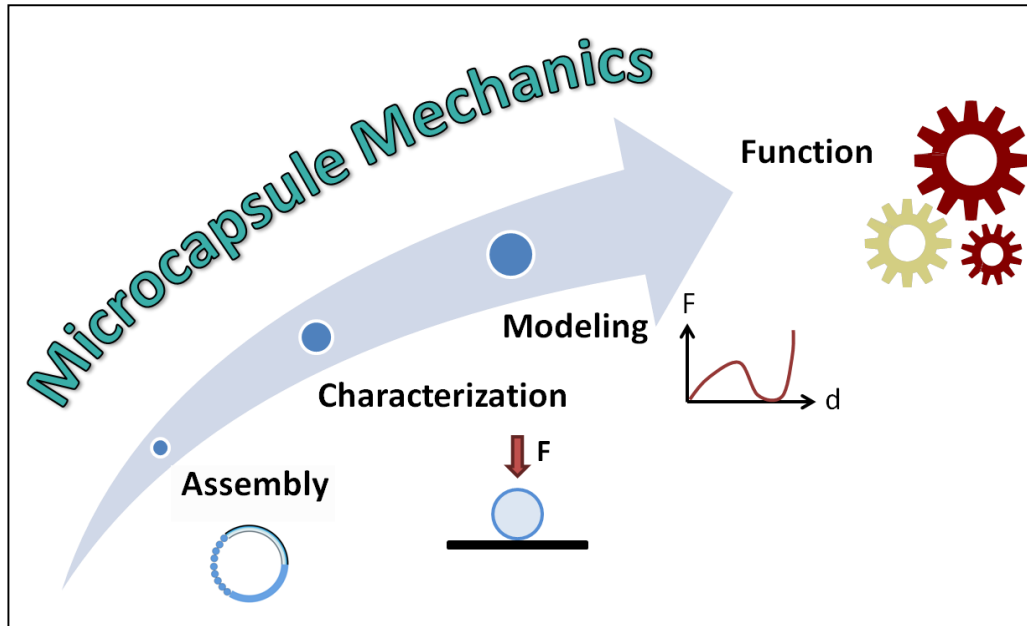
Andreas Fery supervised the project at the University Bayreuth, was involved in scientific discussions regarding the interpretation of the results and corrected the manuscript.



## 4. Mechanics of Microcapsules - From Stability to Function

Martin P. Neubauer<sup>a</sup>, Melanie Poehlmann<sup>a</sup>, Andreas Fery<sup>a,\*</sup>

<sup>a</sup>University of Bayreuth, Department of Physical Chemistry II, Universitätsstraße 30, 95440 Bayreuth, Germany



## **Abstract**

Microcapsules are reviewed with special emphasis on the relevance of controlled mechanical properties for functional aspects. At first, assembly strategies are presented that allow control over the decisive geometrical parameters, diameter and wall thickness, which both influence the capsule's mechanical performance. As one of the most powerful approaches the layer-by-layer technique is identified. Subsequently, ensemble and, in particular, single-capsule deformation techniques are discussed. The latter generally provide more in-depth information and cover the complete range of applicable forces from smaller than pN to N. In a theory chapter, we illustrate the physics of capsule deformation. The main focus is on thin shell theory, which provides a useful approximation for many deformation scenarios. Finally, we give an overview of applications and future perspectives where the specific design of mechanical properties turns microcapsules into (multi-)functional devices, enriching especially life sciences and material sciences.

## **4.1 Introduction**

Microcapsule-research is a classic example of a field, which has been driven and fueled by many disciplines ranging from biophysics, via fundamental colloid- and interface research in physical chemistry and synthesis – both organic and inorganic – up to applied sciences and engineering. Microcapsules have been an object of research in these areas for many decades. First studies date back as early as to the 1930s, when Bungenberg de Jong and co-workers investigated coacervates which can be seen as the first artificial, man-made microcapsules.<sup>1, 2</sup> At the same time Cole performed the first compression experiments on single microcapsules, i.e. on *Arbacia* eggs with a diameter around 75  $\mu\text{m}$ .<sup>3</sup> Especially the development of novel synthesis strategies, e.g., layer-by-layer assembly, and techniques to characterize capsules on a single-capsule level has stimulated scientific research in this area within the past twenty years. At the same time, microcapsules have been increasingly used in industry. The first large-scale production of microcapsules was established for carbonless copy paper already in the 1950s.<sup>4</sup> Today, microcapsules are designed for and employed in many different fields of application, such as pharmacy<sup>5-11</sup>, food industry<sup>12-21</sup>, agriculture<sup>22-25</sup>, cosmetics<sup>26, 27</sup>, textile industry<sup>28-30</sup>, printing<sup>31</sup>, biosensor engineering<sup>32-34</sup>, active coatings<sup>35, 36</sup> and construction<sup>37-39</sup>. For instance, in food technology active ingredients are protected from decomposition through environmental impacts or flavors are prevented from premature volatilization.<sup>20</sup> Textiles have been modified with microcapsules for long-term fragrance release, to introduce fire retardants and even to combat counterfeiting.<sup>28</sup> The interest in and the demand for intelligent, custom-made capsule systems is continuously rising. And scientific research plays a key role as the understanding of the fundamental properties of microcapsules is breaking ground for innovation.

## **4.2 Microcapsules: Definition and Assembly Strategies**

In view of the broad range of capsule systems and the different context in which they have been investigated, it is no surprise that there are various, sometimes at least partially diverging definitions of the term microcapsules and microencapsulation<sup>40-44</sup>. Therefore, let us first clarify the semantics for the purpose of this review: Generally, microencapsulation is understood as the process by which one material of microscopic dimensions is entirely coated by another. Hence, a core-shell-composite

or microcapsule is created where the core can take all aggregate states but the shell is solid. This fundamental definition already points out the two main components of microcapsules, core/interior/inner phase and shell/wall/membrane/outer phase, which can be tuned with respect to materials, permeability, size, shape etc. Out of this large zoo of possible microcapsules it is indispensable to introduce some further constraints. In the context of this review article we examine mechanical properties of microcapsules. These are particularly interesting when dominated by the shell. Therefore, we limit ourselves to microcapsules being composed of a fluid core wrapped by a solid shell. In contrast, capsules consisting of a solid core will be referred to as core/shell particles and will not be in the center of interest. In terms of the mechanical properties of the shell, we limit ourselves to non-fluid shells. The broad class of vesicles formed from lipids or in general low-molecular weight species will thus not be covered. The microcapsules considered in this review will always be spherical, if not stated differently, and their size will range from several hundreds of nanometers to some tens (in few cases to some hundreds) of micrometers, with the restriction that the shell thickness is small as compared to the diameter.

The focus will finally be on artificial microcapsules, which naturally lets us start from reviewing the various approaches for the formation of microcapsules meeting the aforesaid definitions. As stated above, microcapsules find already various usages in industry. The industrially relevant encapsulation techniques are typically based on physicochemical processes that allow for large scale production. These include spray drying<sup>45</sup>, co-extrusion, spinning disk, multiple-nozzle spraying, fluidized-bed coating and vacuum encapsulation.<sup>40, 44</sup> Among the advantages of these methods are the easy handling, upscalability and low costs. On the other hand, the obtained microcapsules are often polydisperse in diameter and shell thickness. In other words, current approaches allow for comparatively little control over the particles morphology and the possibilities of capsule design are rather restricted.

A far better control over capsule core and shell dimensions and a selective introduction of functionality is provided by template-assisted and/or self-assembly approaches. Both soft and hard template-assisted methods offer fine-tuning of the core size and can be combined with a self-assembly process which allows excellent control over shell thickness, down to molecular level. Soft template-assisted methods are mostly emulsion-based, such as microfluidic processes<sup>46-52</sup>, polymerosomes<sup>6, 53-</sup>

<sup>58</sup> (which are typically nm-sized), colloidosomes <sup>59-61</sup>, interfacial polymerization <sup>62-65</sup>, interfacial assembly <sup>66</sup>, inkjet printing <sup>67, 68</sup> or phase separation processes <sup>69, 70</sup>. A special case is the soft colloid templated multilayer assembly which offers control over all geometric parameters.<sup>71, 72</sup> The underlying principle was first exploited using hard templates, namely the layer-by-layer deposition technique <sup>73-78</sup>. Combining templates and self-assembly permits precise adjustment of geometry, diameter <sup>79</sup>, shell thickness and shell material <sup>80</sup>. Furthermore, such methods allow for introduction of multifunctionality.<sup>26</sup> That means, in addition to enclosing their content until desired delivery, microcapsules are designed which, for example in medical applications, can be tracked within the human body, directed to a specific site and, finally, specifically triggered to release their cargo. A schematic overview of microcapsule designs obtained from template-assisted and self-assembly methods is given in Figure 4-1. It becomes clear that the synthesis process strongly determines the choice of core and shell material, and the design possibilities.

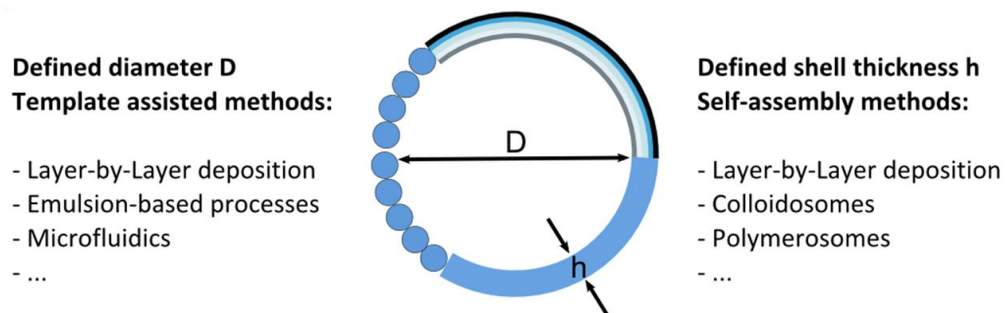


Figure 4-1: Template-assisted and self-assembly methods for a controlled capsule design. The scheme shows typical wall materials (particles, multilayers, homogeneous film) and the crucial geometric parameters, diameter  $D$  and wall thickness  $h$ .

### **4.3 Mechanical Characterization of Microcapsules**

Mechanical properties of microcapsules become accessible through a variety of experimental techniques. These can be divided into two general categories: ensemble methods and methods on a single-capsule level. Ensemble methods measure a batch of capsules simultaneously, yielding average values. These measurements can often be performed in an automated, high-throughput fashion and a large number of capsules are captured. In contrast, single capsule measurements provide generally more detailed information on deformation properties, but require a sequential measurement of capsules.

One possibility of determining mechanical properties of microcapsule ensembles is to make use of shear forces. A slurry or suspension of capsules can be measured, for instance, in a turbine reactor.<sup>81</sup> Here, rather high forces are acting provoking breakage of capsules. Therefore, such a method is mainly relevant for studying large deformation behavior and release under high stresses. A more sensitive approach is given by rheological investigations. Drochon *et al.* measured the viscosity of a diluted suspension of red blood cells and calculated the shear elastic modulus of the cell membrane.<sup>82, 83</sup> The underlying model has been derived by the same authors and other groups.<sup>84-87</sup> Suspensions of microcapsules under shear have been further studied experimentally by Bredimas *et al.*<sup>88</sup> and theoretically by the groups of Misbah<sup>89-93</sup> and Kalluri<sup>94, 95</sup>.

Another means to obtain information about mechanical parameters of a multitude of capsules is to perform osmotic pressure experiments. With the upcoming of polyelectrolyte multilayer capsules (PEMCs) Gao and co-workers used this method to extract mechanical data.<sup>96, 97</sup> Upon increase of osmotic pressure the capsules started to deform and assumed a buckled shape. The onset of this buckling was associated with a critical osmotic pressure which was shown to depend on capsule wall thickness and elastic modulus as well as on the size of the capsule. The established theoretical model allows for the calculation of the shells' elastic modulus from the measured critical pressure. In a later study Datta *et al.* examined the buckling behavior of Pickering emulsion droplets by continuously reducing their volume.<sup>98</sup> The results show that these kinds of capsules undergo similar buckling transitions as known for typical polymer based thin shell systems.

In the following, single capsule measurement techniques will be presented, ordered according to increasing force sensitivity. Figure 4-2 gives a schematic overview. First, we focus on parallel plate compression where the capsule is deformed between two approaching plates with a typical force range between  $\mu\text{N}$  and  $\text{N}$ . Such studies date back to the early 1930s when Cole examined surface forces of the arbutia egg with a flat gold wire.<sup>3</sup> Starting from the late 1990s well defined compression of micron scale capsules was introduced. Zhang *et al.* developed a micromanipulation technique to measure burst forces of melamine formaldehyde (MF) microcapsules in a controlled fashion.<sup>99</sup>

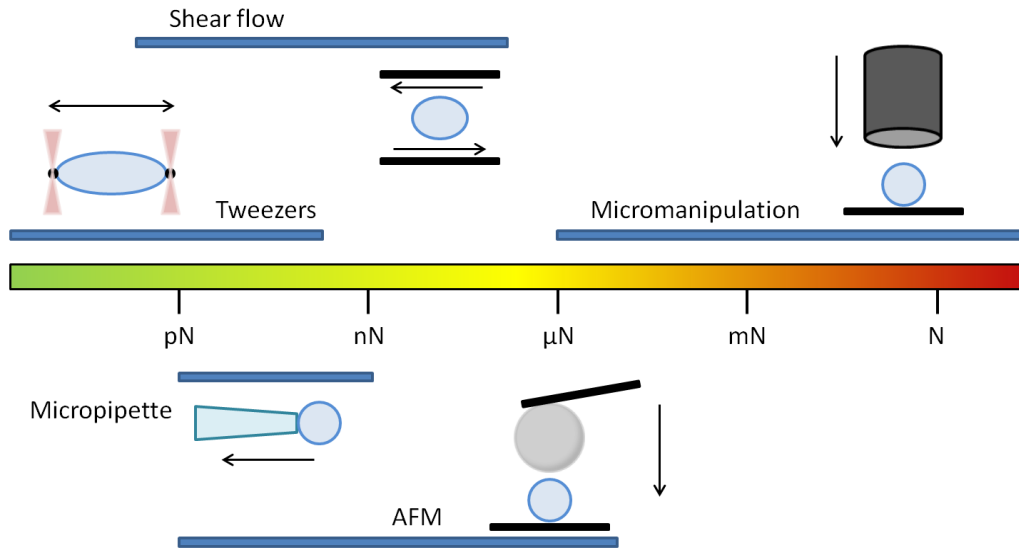


Figure 4-2: Schematic representation of single-capsule measurement techniques, each with typically available force range. Arrows indicate the directions in which forces are acting.

Figure 4-3 shows pictures from a similar deformation experiment. The immobilized microcapsule is deformed by the flat end of a cylindrical probe connected to a force transducer. The optical microscope allows for alignment and observation of the deformation in situ. As a result of approaching and retracting the probe a force versus deformation characteristic is obtained. Bursting of the capsule is associated with a sharp drop in the recorded force. Similar plate compression experiments on MF microcapsules were conducted by Hu et al.<sup>100</sup>, Keller and Sottos investigated poly(urea-formaldehyde) microcapsules.<sup>101</sup> Theoretical treatment and simulations can be found in <sup>102-104</sup>.

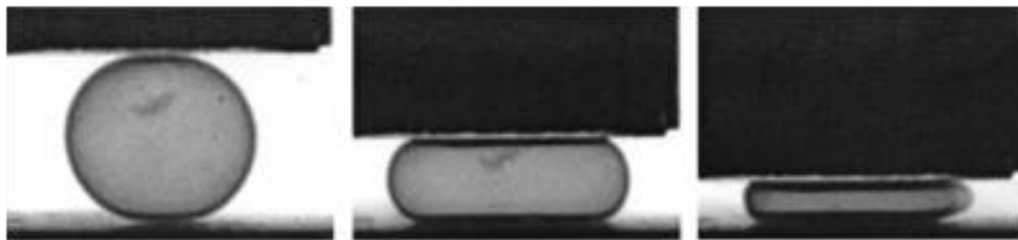


Figure 4-3: Sequence of images of an alginate capsule under parallel plate compression with a micromanipulator. Image adapted from <sup>105</sup>. Copyright 2003 Wiley. Used with permission from Carin et al., Compression of biocompatible liquid-filled HSA-alginate capsules: Determination of the membrane mechanical properties, *Biotechnology & Bioengineering*, John Wiley and Sons.

A technique closely related to plate compression testing is atomic force microscopy (AFM). Similar to the situation in a micromanipulator uniaxial deformations are effected, however, the accessible force range is shifted to smaller values (pN to  $\mu\text{N}$ ) accompanied with higher resolution.<sup>106</sup> Therefore, it is a suitable tool for capsule systems to study shell mechanical properties in the small deformation regime on the order of the shell thickness. Often, the colloidal probe setup is used, where a particle of colloidal dimensions is attached to a tip-less cantilever to achieve well defined sphere-sphere deformation geometry. In analogy to plate compression AFM can be combined with optics and measurements in air and in liquid are feasible. Figure 4-4 depicts a typical force vs. deformation characteristic from a colloidal probe AFM measurement. First studies with this technique to characterize PEMCs were reported independently from Vinogradova and co-workers<sup>107-109</sup> and from Fery and co-workers<sup>110-112</sup>. The elastic modulus of PSS/PAH multilayer capsules was determined to be in the low GPa range. It was shown that the shell thickness has a drastic influence on the mechanical properties. Further, by using an optical microscope in RICM mode it was possible to reconstruct the actual capsule shape both in undeformed state and during measurement. Other groups have employed the colloidal probe technique to study mechanical properties of vesicles<sup>113</sup>, MF capsules<sup>114</sup> and biopolymer capsules<sup>115</sup> or the salt softening of PEMCs<sup>116</sup>. Shell mechanical properties of capsule systems can equally be investigated by AFM when using a cantilever with a sharp tip at its apex. However, measurements have to be performed carefully avoiding penetration of the shell. Consequently, the applicable force range is typically lower than with a colloidal probe. A variety of systems has been tested with this method, such as vesicles<sup>117, 118</sup>, polymeric capsules<sup>119</sup>, capsules with a silica shell<sup>120</sup>, viral shells<sup>121, 122</sup> and polymersomes<sup>123</sup>. A third option for capsule deformation with AFM is to employ a tip-less cantilever. Here, the major constraint arises from the fact that commercially available cantilever holders are tilted by several degrees; a typical inclination angle is  $10^\circ$ . Therefore, compression will always be accompanied by some shearing or sliding, which can lead to pushing away the capsule in extreme cases. Yet, for moderate loads and small capsules (with respect to cantilever dimensions) these effects should be acceptably low. With this method a range of microcapsules and –bubbles have been investigated.<sup>124-128</sup>

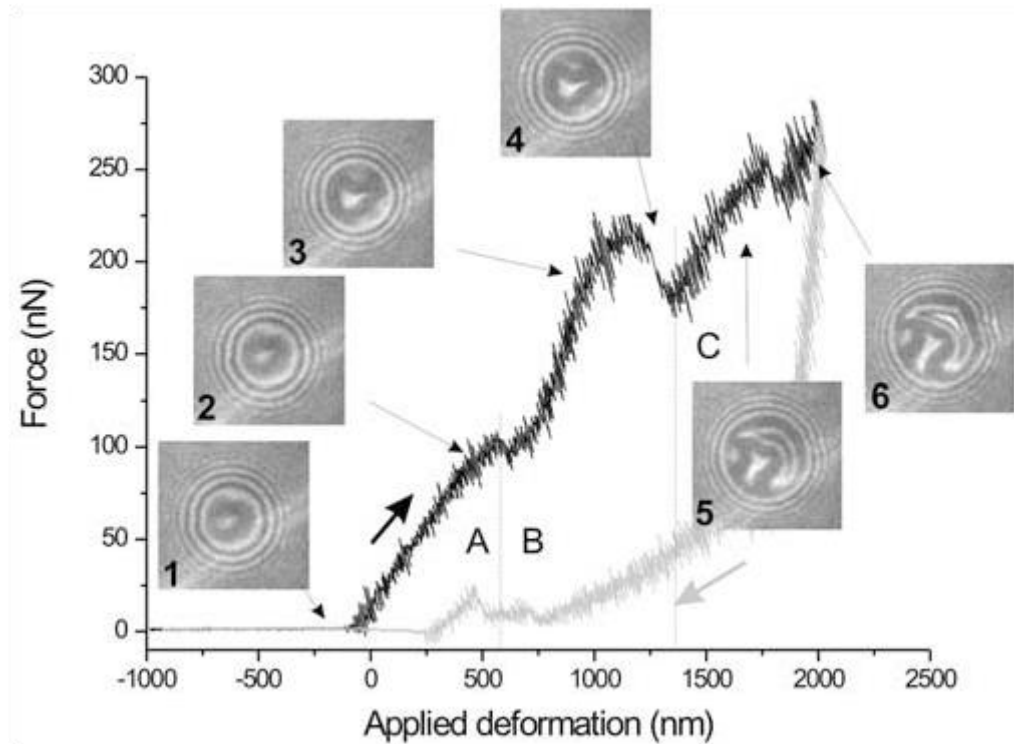


Figure 4-4: Force-deformation characteristic of a polyelectrolyte multilayer microcapsule, 10  $\mu\text{m}$  in radius. Insets show corresponding RICM micrographs. A clear correlation can be observed between applied loads and apparent contact area.<sup>110</sup> Buckling of the shell is evidenced by discontinuities in the curve and, correspondingly, abrupt changes in contact geometry. With kind permission from Springer Science and Business Media: Springer, the European Physical Journal E, 12 (2), 2003, p.215, Elastic properties of polyelectrolyte capsules studied by atomic force microscopy and RICM, F. Dubreuil, Fig 4.

A conceptually completely different approach is to apply shear stresses. The typical range of these stresses is from mPa to kPa, i.e. for capsules with a typical radius of 5  $\mu\text{m}$  the applied forces can be estimated to be in between 0.1 pN to 0.1  $\mu\text{N}$ . Several studies have been performed in Couette flow, i.e. the microcapsules are exposed to shear flow created by two concentric cylinders rotating in opposite direction.<sup>129-133</sup> The outer cylinder of the rheoscope is optically transparent, thus enabling observation of capsule shape and orientation with a microscope. An example is given in Figure 4-5, where the shear rate has been increased until capsule break. A similar setup is used for spinning drop experiments.<sup>134-139</sup> Here, the microcapsule is placed within a liquid filled rotating tube and shape changes are again followed via microscope. In both methods, the shear modulus is determined, based on the change in capsule shape as a function of applied shear forces. Theoretical models for different shear and flow conditions have been developed.<sup>140-146</sup> A related method is based on microfluidics.

The microcapsules mechanical properties are studied by guiding them through narrow channels and following the change in shape. Such an approach has been reported both for biological cells<sup>147</sup> and artificial capsules<sup>148-151</sup>. Corresponding theoretical descriptions have been worked out.<sup>152-159</sup>

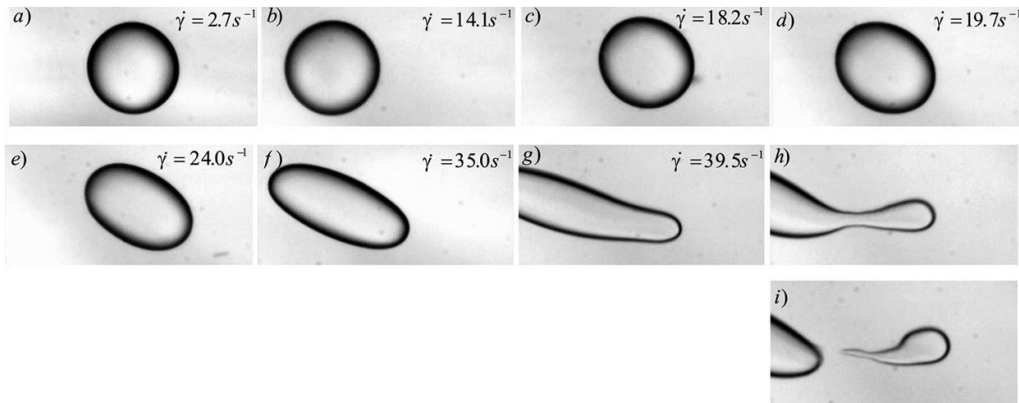


Figure 4-5: Series of images of an initially spherical polysiloxane microcapsule in shear flow at different shear rates  $\dot{\gamma}$  until break. Reproduced from<sup>133</sup> with permission of The Royal Society of Chemistry (RSC).

A more sensitive technique is micropipette aspiration. It has originally been developed by Mitchison and Swann to examine elastic properties of living cells and the setup was therefore termed “cell elastimeter”.<sup>160</sup> A glass micropipette is connected to a movable reservoir which effects slight suction when lowered. This way a single cell can be aspirated, held and depending on the position of the reservoir suction pressure can be systematically varied and capsules can be released after the experiments. Normally, applied pressures range between 1 Pa and 1 kPa. This means, with typical inner diameters of the capillary of 1-5  $\mu\text{m}$ , forces in between pN to nN are exerted. Shape changes of the capsule are followed with an optical microscope (see Figure 4-6). The observed bulging of the cell membrane is used to extract information about mechanical properties such as stiffness, Young’s modulus or internal pressure. Since these first pioneering contributions the technique has been improved further and applied to study both biological samples<sup>161-166</sup> and artificial capsules<sup>167-170</sup>. Theoretical models have been developed to accurately describe and evaluate micropipette aspiration experiments.<sup>164, 171-177</sup>

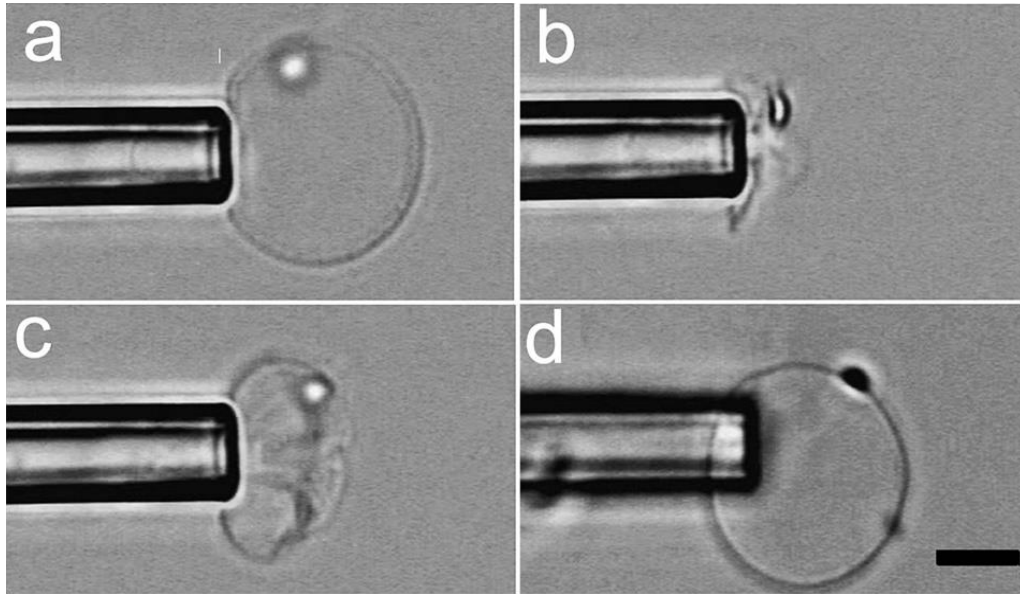


Figure 4-6: Micropipette suction experiment with a polymersome. After aspiration (a) and collapse (b) a positive pressure is applied (c), finally leading to full recovery of the capsule (d). Scale bar is 5  $\mu\text{m}$ . Reproduced from <sup>170</sup> with permission of The Royal Society of Chemistry (RSC).

Finally, a class of methods is discussed which enables the exertion of very low forces (several tens of fN to some hundreds of pN): optical and magnetic tweezers. Though mainly used to study biological samples (e.g., cells) we still add this paragraph to round out the picture concerning single-capsule deformation techniques. Generally, optical tweezers exploit the forces arising from a light source such that a dielectric particle can be trapped and manipulated. Detailed information about this technique and theoretical background can be found in <sup>178-182</sup>. In a classical experiment two beads which are attached to opposite sides of a cell are trapped with optical tweezers and then pulled apart to investigate the cells mechanical properties and determine elastic parameters such as the shear modulus of the cell membrane.<sup>183-185</sup> An example is given in Figure 4-7, where the experimental observations are accompanied by numerical simulations. Non-symmetric systems with only one traceable particle attached to a cell have been studied by Titushkin *et al.* <sup>186</sup> and by Frases and co-workers <sup>187</sup>. Calibration of optical tweezers has been treated in the group of Nussenzveig.<sup>188, 189</sup> A special case of optical tweezers is given in the optical stretcher where microcapsules can be directly trapped and deformed without additional particles. This method was introduced by Guck *et al.* <sup>190</sup>, theoretical considerations can be found in <sup>191-193</sup>. The working principle of magnetic tweezers is similar to

optical tweezers. Magnetic beads attached to a cell wall are trapped in a magnetic field and then moved to perform a microrheology experiment.<sup>194-196</sup>

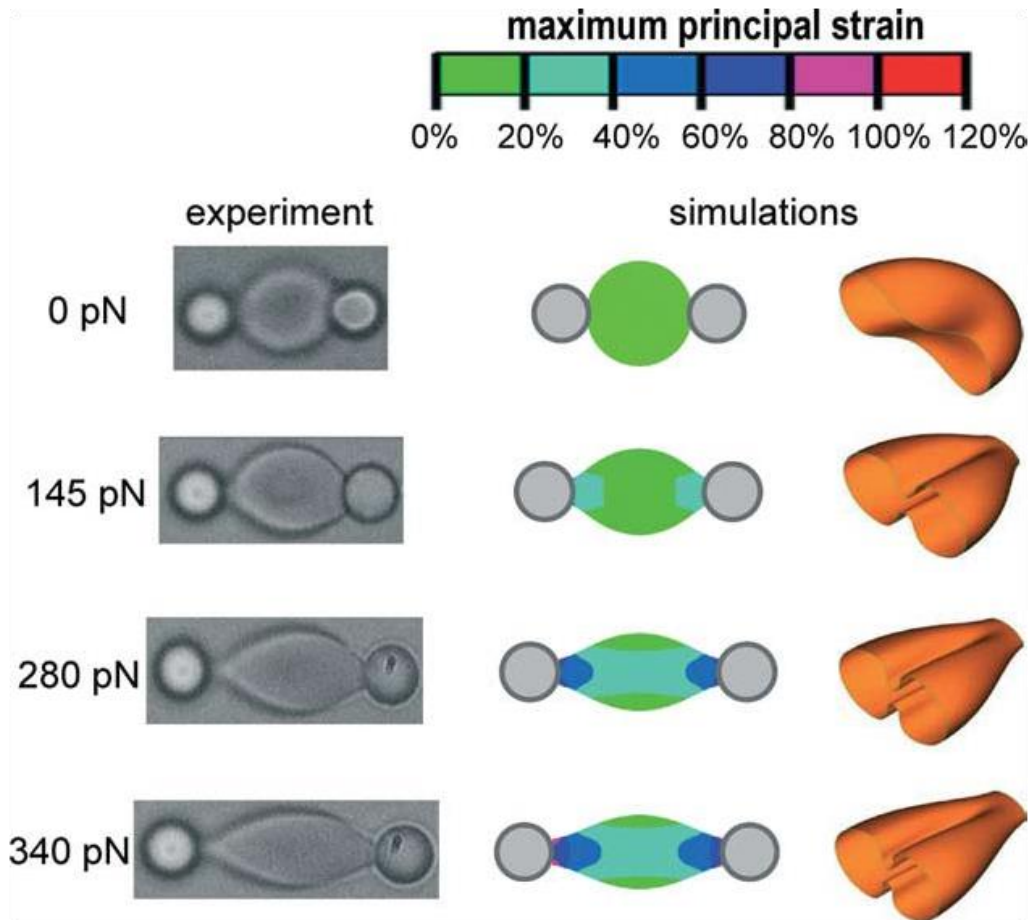


Figure 4-7: Cell deformation experiments with optical tweezers at increasing loads. Left, optical micrographs, right, corresponding simulations revealing strain distributions and 3D-shape changes.

<sup>197</sup> Reprinted from *Acta Materialia*, 52, C.T. Lim et al., Large deformation of living cells using laser traps, Copyright (2004) with permission from Elsevier.

#### **4.4 Modeling – Physics of capsule deformation**

As it was shown in the previous part a wide range of techniques has been established to characterize mechanical properties of capsule systems. There are static, quasi-static and dynamic methods which all need to be evaluated with a suitable physical model to extract meaningful quantities out of the obtained data. As compared to the deformation of massive particles made from an elastically homogenous medium, modeling capsule deformation is intrinsically more challenging and qualitatively new features arise, which are often linked to nonlinear effects. In addition, several qualitatively different deformation regimes are found. Deformations can be on the

same range or small as compared to the capsules' typical length scales such as wall thickness or radius, and capsules can be permeable or not, to mention only the most important aspects. In the following we first focus on the (more general) modeling of capsule deformation within the framework of shell theory before comparing to membrane approach and discussing more complex deformation scenarios.

Shell structures are widely and successfully used in nature, architecture and technology, covering all length scales in-between biological cells and dome constructions.<sup>198</sup> However, the underlying physical concepts to describe their mechanical properties and to predict response to applied loads are the same. One of the major advantages of shells is that, despite often being very thin and thereby saving material, extreme stability and protection of the interior is nevertheless guaranteed. This brings us to a first important (and for many systems valid) simplification concerning theoretical treatment: the restriction to thin shells, i.e. structures with a shell thickness  $h$  to radius  $R$  ratio of less than  $1/20$ .<sup>199</sup> Here,  $R$  corresponds to the radius of curvature of the middle surface between the inward and outward faces of the shell. In the course of this section shells will always be considered as thin. Further assumptions in thin shell theory are linear elasticity of the shell material (which is supposed to be homogeneous and isotropic), small deformation with respect to the shell thickness, and the Kirchhoff hypotheses, together known as the Kirchhoff-Love assumptions. Additionally, the 3D-shell-problem is reduced to a 2D-problem by focusing on the middle surface of the shell.<sup>199</sup> One of the first scientists to present such a first-order approximation was Reissner.<sup>200-204</sup> His analysis revealed a linear scaling of applied force  $F$  and resulting deformation  $d$ .

$$F = \frac{h^2}{R} \cdot \frac{4E}{\sqrt{3(1-\nu^2)}} \cdot d$$

Further variables in equation 1 are the radius of curvature  $R$ , shell thickness  $h$  and the material elastic constants, Young's modulus  $E$  and Poisson's ratio  $\nu$ . Originally developed for point loads, Reissner's theory has been experimentally proved to be valid also for less concentrated loading situations, e.g., deformations with a colloidal probe.<sup>106</sup> In the context of microcapsules this simple result is particularly interesting as the shells' elasticity modulus becomes directly accessible from small deformation experiments, e.g., parallel plate compression or AFM force spectroscopy. An overview over further first- and higher-order approximations is provided in <sup>199</sup>.

A constraint to the simple description of small deformations can arise from membrane pre-tensions which become important for very thin shells. In a pioneering work, Ferri and co-workers tried to separate the contributions of surface tension and mechanical membrane tension to the overall deformation behavior of Pickering emulsion droplets.<sup>205</sup> A model was developed accounting for both tension contributions and including the shape changes of the capsule during compression. Based on experimental data, stress-strain relations are calculated and compared to the predictions of continuum mechanical shell models. Significant differences are found which are attributed to strong influence of surface tension effects originating from the oil-particle-water interface. Tan *et al.* built up on this work and investigated mechanical properties of droplets stabilized by clay particles.<sup>206</sup> Predictions from Ferri's work are in good agreement with their experiments. As the determined surface Young's modulus depends on the applied strain, it is clear that the shells' elasticity cannot be described by a pure Hooke law. This non-Hookean behavior is, again, suggested to result from interfacial tensions.

Pre-inflation as it can arise from swelling has been identified as another source of pre-tension. It has been shown that the shape of capsules in axisymmetric flow is largely influenced by such additional mechanic tension.<sup>159</sup> A corresponding trend was found for capsules in shear flow. Here, the deformation characteristic is significantly altered and, for high pre-stresses, the validity of small deformation theory is passed.<sup>145</sup>

Remaining under thin shell assumptions we now focus on larger deformations. For the simplest case, a capsule with infinite permeability, Pogorelov proposed the following relationship for a Hookean material under point load.<sup>207</sup>

$$F = \frac{1.89Eh^2}{R(1-\nu)}\sqrt{hd}$$

In this scenario, a dimple is forming and, in contrast to Reissner's formula, the force no longer scales linearly but with the square root of deformation. Theoretical solutions of the large deformation problem under assumption of non-Hookean models, such as Neo-Hookean or Mooney-Rivlin, are presented in <sup>208, 209</sup>.

Several studies have used the onset of buckling, as described by Pogorelov, as a means for estimating elastic properties of shells.<sup>210-214</sup> Experimentally, this can be addressed by using osmotic pressure effects. For instance, Gao and co-workers made

use of the osmotic pressure to calculate the elastic modulus of PSS/PAH polyelectrolyte capsules (see also Figure 4-8).<sup>96</sup> Following earlier argumentations<sup>215, 216</sup> a model is presented where the critical osmotic pressure is related to the elastic modulus of the shell.

$$p_c = \frac{2E}{\sqrt{3(1-\nu^2)}} \left(\frac{h}{R}\right)^2$$

Here,  $p_c$  is the critical pressure when buckling of the shell starts. This pressure scales directly with the shell thickness squared and indirectly with the square of radius, or, in other words,  $p_c$  scales indirectly with the Föppl-von Kármán number  $\gamma$ .

$$\gamma = 12(1 - \nu^2) \left(\frac{R}{h}\right)^2$$

The experimental data clearly confirmed this relation and the determined modulus is in good agreement with independent measurements.<sup>110</sup> Vliegenthart and Gompper analyzed the problem of capsule buckling under external pressure by means of simulations.<sup>217</sup> They found that the shape of the capsules in the deformed state is determined by three variables, deformation rate, reduced volume and, again, the Föppl-von Kármán number  $\gamma$ .

The simulations reveal two energy regimes. The first, for small indentations with circular dimple, follows the classic prediction after Landau and Lifshitz with the energy scaling like  $E \propto \gamma^{1/4}$ .<sup>218</sup> When the shell is deformed to a larger extent leading to polygonal shape of the dimple, the scaling exponent changes to less than 1/6.

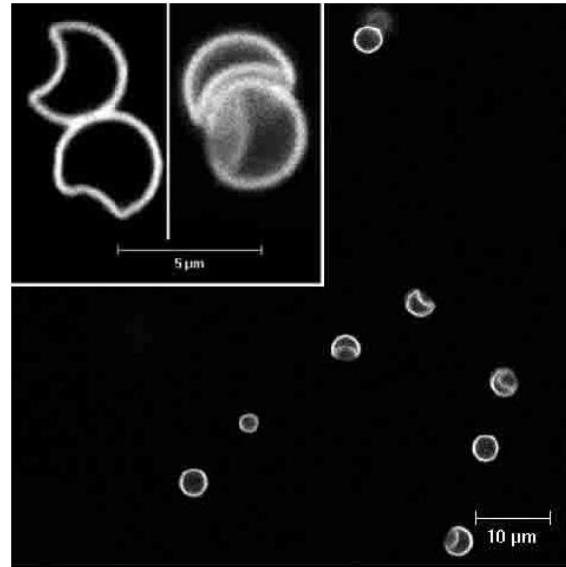


Figure 4-8: Buckling of polyelectrolyte multilayer capsules induced by osmotic pressure <sup>96</sup>. With kind permission from Springer Science and Business Media: Springer, the European Physical Journal E, 5 (1), 2001, p.21, Elasticity of hollow polyelectrolyte capsules prepared by the layer-by-layer technique, C. Dubreuil, Fig 2b.

Generally, the formation of a dimple or invagination upon large deformation of capsules has received much attention in the literature. Buckling instabilities have been observed and described in both experimental and theoretical studies.<sup>219-237</sup> A special case are pressurized shells which show wrinkling under point load conditions.<sup>238</sup> The same group has also studied the mechanical properties of pressurized shells under point loads.<sup>239</sup> In addition to the initial linear regime as predicted by Reissner for small deformations a second linear regime was found for large indentations.

It is obvious that for a range of systems, particularly for large deformations, permeability is not negligible and, therefore, needs to be considered. For small deformations of a capsule, irrespective of permeability, the force  $F$  scales linearly with relative deformation  $\varepsilon$  (deformation divided by capsule radius  $R$ ).<sup>240</sup>

$$F \propto \frac{4}{3} E h^2 \varepsilon$$

This is the basis for Reissner's reasoning. In the case of an impermeable membrane a second term has to be considered. This term accounts for the stretching of the shell while being deformed. Here, the force scales cubically with deformation.<sup>108</sup>

$$F \propto \frac{16\pi}{3} E h R \varepsilon^3$$

Plotting both scaling laws in a common graph (Figure 4-9) shows clearly that, as long as we restrict ourselves to small deformations on the order of the shell thickness, permeability issues are negligible. In contrast, for large deformations volume-constraint contributions become increasingly dominant. Therefore, capsule wall permeability has to be considered in modeling of large deformations.

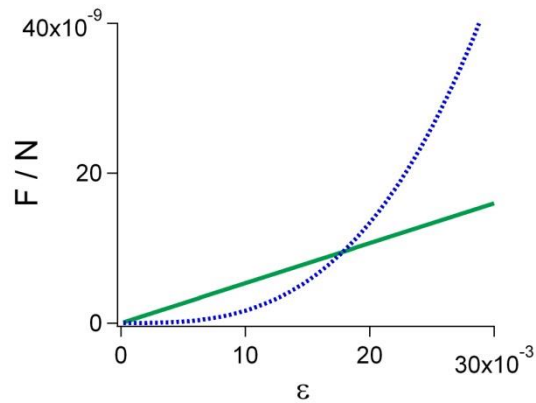


Figure 4-9: Linear elastic (continuous line) and volume-constraint (dotted line) contributions to forces  $F$  upon capsule deformation (relative deformation  $\varepsilon$ ), calculated for a capsule 10  $\mu\text{m}$  in diameter, shell thickness of 20 nm and Young's modulus of 1 GPa.

In this case, additional contributions arise particularly from edge bending at the sites of high curvature around the dimple and stretching caused by the rising fluid pressure.<sup>241</sup> Comparing both experimental data and theoretical calculations for the deformation of an empty and a water-filled racquetball Taber finds that deformations below 20% are dominated by bending. Only for larger compression the load-deflection curve of filled shells deviated from the square root like scaling and compared to the empty shells a stiffening was observed.<sup>241</sup>

Finally, at very high loads capsule burst can occur. Experimentally, Zhang *et al.* found for melamine formaldehyde (MF) microcapsules a clear correlation with both bursting force and displacement at burst increasing in a linear fashion with capsule diameter.<sup>99</sup> Additionally, it was discovered that burst typically occurs at a critical relative deformation of 70%, irrespective of capsule size.<sup>242</sup> Mercadé-Prieto *et al.* carried out finite element modeling (FEM) to elucidate the failure behavior of MF microcapsules.<sup>103</sup> The compression behavior between two parallel plates is simulated up to bursting by applying an elastic-perfectly plastic model with strain hardening

and comparison with experimental data shows very good agreement. Strain at rupture for this system was found to be approximately 0.48 and a failure stress of around 350 MPa was obtained.

After going through thin shell theory it is worth comparing with membrane models. What is the main difference between these two approaches for describing capsule systems? Generally, shell structures support externally applied loads in two ways: in-plane (stretching and shear) and out-of-plane (bending and twisting).<sup>106, 199</sup> The much vaunted stability of many solid shells originates from the high resistance to bending.<sup>199</sup> Accordingly, thin shells carry axial loads mainly by in-plane action. In contrast, in the membrane scenario bending and twisting moments are small, i.e. the main characteristic of a fluid membrane is its flexibility. It supports external loads only by its tension and deforms in pure bending.<sup>199, 243</sup> Such conditions are often fulfilled in biological systems. Surely, the prototypes of fluid membranes are cell membranes or lipid bilayers. The bending resistance of such membranes has been treated in a range of publications.<sup>243-249</sup> The key variable to describe mechanical properties of membranes is the bending rigidity  $k_{bend}$ . It is related to the area elastic modulus  $K_A$  by a simple expression<sup>245, 250</sup>:

$$k_{bend} = \beta K_A h^2$$

Here,  $\beta$  is a constant and  $h$  is again the membrane thickness. However, there is also a class of membrane-like systems with finite shear modulus, i.e. in-plane elastic energy has to be considered. In the literature, these are commonly referred to as tethered or polymerized membranes.<sup>243, 244, 247</sup> Here, the shell consists of an interconnected network instead of a loose assembly of individual molecules. Several studies described such membrane-like systems including both bending and shear contributions.<sup>248, 249, 251</sup> Hence, we see that, when a membrane is “properly” modified (cross-linked, strengthened), a transition takes place towards more shell-like mechanical properties. In conclusion, thin shell and membrane approaches are each special or limiting cases of the comprehensive, general shell theory. Simmonds *et al.* suggest in their theoretical analysis that the exact description of a spherical shell under load is given by the sum of a membrane-like, a shell-like and a slab-like solution.<sup>252</sup> An example of a system that is characterized as being located in-between the state of fluid membranes and solid shells are polymer vesicles.<sup>253</sup>

While mainly axial deformation has been considered so far we now turn to a more complex scenario, namely capsules in (shear) flow. A recent overview of this topic can be found in <sup>143</sup>. In the simplest case, a homogeneous thin elastic shell is modeled following Hooke's law for small deformations. It is characterized by its surface shear modulus  $G_S$  and area dilation modulus  $K_S$ , with  $K_S = G_S(I + \nu_S)/(I - \nu_S)$  and  $\nu_S$  being the surface Poisson ratio. The principle tensions  $T_{1,2}$  and extension ratios  $\lambda_{1,2}$  are correlated to give the subsequent equations:

$$T_1 = \frac{G_S}{1-\nu_S} [\lambda_1^2 - 1 + \nu_S(\lambda_2^2 - 1)]$$

$$T_2 = \frac{G_S}{1-\nu_S} [\lambda_2^2 - 1 + \nu_S(\lambda_1^2 - 1)]$$

More details on freely suspended microcapsules in simple shear flow can be found in a range of publications <sup>84-86, 140</sup> covering also tumbling <sup>142, 144, 254</sup>, large deformations <sup>87</sup> or the effect of pre-stresses <sup>145</sup>. A closely related topic is the motion of capsules in channels, e.g., blood cells or delivery vehicles in arteries. Several groups have addressed this issue.<sup>152-159</sup> When a capsule flows through a constriction it assumes a certain shape depending on its mechanical properties, flow rate, channel size <sup>152</sup> and geometry <sup>154, 155</sup>.

To conclude this section we would like to draw the readers' attention to some examples of non-spherical capsules. Delorme and co-workers studied the mechanical properties of polyhedrons.<sup>255</sup> Both the elastic modulus (Reissner approximation for thin shells) and bending modulus (membrane theory) were determined and found to be in a reasonable range compared to independent measurements. Additionally, a distinct difference in stiffness between facets and vertexes could be shown. The mechanical properties of ellipsoidal shells are studied in <sup>256</sup> and <sup>257</sup>. It is clearly shown how geometry, namely the curvature, influences the stiffness of a given shell, e.g., that a hen's egg supports higher loads at its poles than around the equator. Additionally, the stiffening effect of internal pressure is examined (Figure 4-10).

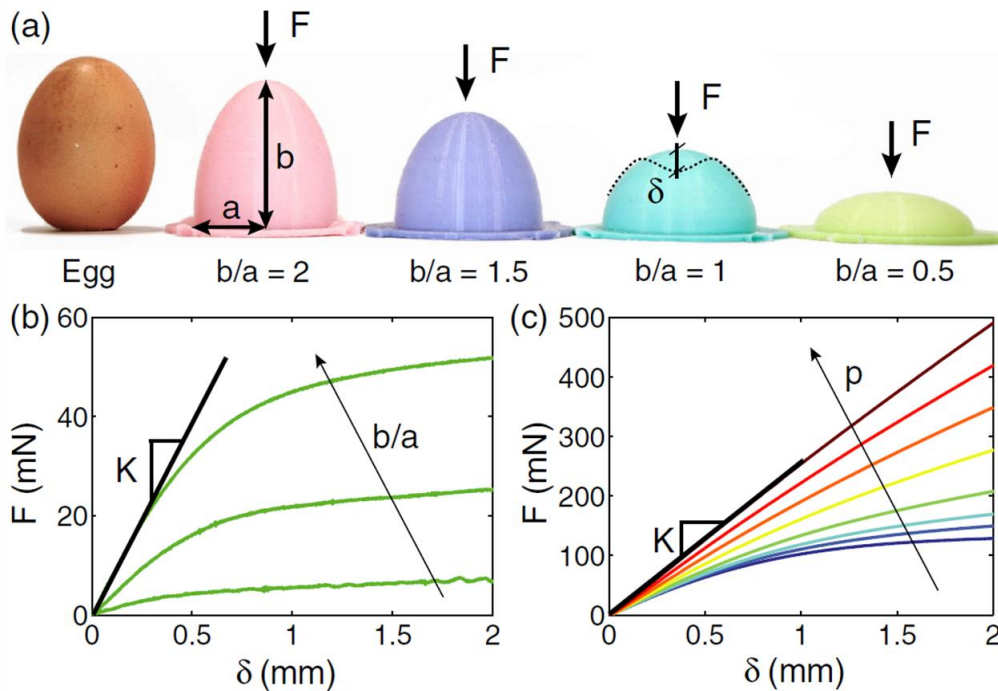


Figure 4-10: a) Ellipsoidal shells with different aspect ratios  $b/a$ . b) Effect of aspect ratio on force-deformation characteristic for axial loads on non-pressurized shells. c) Effect of internal pressure for a given aspect ratio (1.5). Pressure ranges from 0-10 kPa. <sup>256</sup> Copyright (2012) by the American Physical Society.

Another class of non-spherical microcontainers, capsids, is investigated in <sup>258</sup>. The authors present a corresponding elasticity theory and reveal the interrelation between energy and shape. This finally leads to a shape phase diagram, where the transitions from spherical to spherocylindrical to icosahedral geometries are given as a function of the spontaneous curvature and the Föppl-von Kármán number. Mechanical properties of hollow tubes have been characterized and evaluated by Mueller et al. <sup>79, 259</sup>, based on a model developed earlier for microtubules <sup>260</sup>. The scaling of the tube wall materials' stiffness with wall thickness and radius is similar to the Reissner relation for spherical shells, yet with slightly higher exponents. Anisotropic microcapsules assuming cubic or pyramidal shapes were constructed *via* a layer-by-layer approach by Shchepelina and co-workers. <sup>261</sup> With the help of computer simulations it is demonstrated that these geometries provide enhanced mechanical properties compared to spherical capsules. Simulating osmotic pressure, the edges and corners, i.e. the regions of high curvature, act as a kind of intrinsic frame which stabilizes the whole structure, whereas the hollow spheres show the typical buckling instabilities. In a later work, hollow cubic capsules are investigated with regard to

pH-induced shape changes.<sup>262</sup> While (PMAA)<sub>20</sub> capsules show a shape transition to spherical structures, the (PMAA-PVPON)<sub>5</sub> capsules retain their morphology. This difference is attributed to a change in materials' stiffness. The more rigid composite better withstands the stresses due to pH triggered swelling, whereas the softer single-component capsule is subject to bending of its side faces.

Generally, numerical methods such as finite element modeling (FEM) can help to understand experimental observations and to predict system response, particularly when more complex morphologies are investigated (e.g., the anisotropic capsules discussed before) and when deformation regimes beyond linear elasticity are probed (e.g., capsule burst). In these cases analytical treatment is often not possible. In FEM simulations the shell is modeled as consisting of a finite number of discrete elements.<sup>263-265</sup> With this approach several capsule systems have been studied, e.g., artificial spherical capsules<sup>102-104, 266-269</sup> and icosahedral viral capsids<sup>270-273</sup>. An alternative way to reduce complexity is to model the shell structures as spring networks. Here, the continuous shell is replaced by a grid with a set mesh size where the links between the nodes represent springs obeying a predefined elasticity law. This model has been shown to apply well to both icosahedral<sup>232, 274-276</sup> and spherical shells<sup>217</sup>. A related approach is coarse-grained simulation techniques<sup>277-280</sup> and meso-scale modeling<sup>281, 282</sup>. Instead of considering every single atom or molecule as in classical molecular dynamics simulations (which is far too time-consuming for micron-sized systems) several molecules or polymer segments are grouped and represented by one bead. Neighboring beads are connected by a bond to which a certain potential is attributed. Several groups employed this technique to examine mechanical properties of microcapsules<sup>281, 283-285</sup> and viral capsids<sup>273, 286-288</sup>.

#### **4.5 Functionality and Application Perspectives**

As has been outlined in the introductory section microencapsulation is already today an important processing method in industry and bears great potential for a wide range of applications. Mechanics of microcapsules plays a critical role for the ultimate purpose of most encapsulation applications: *controlling release* of the encapsulated material. Depending on the specific application, desired release scenarios range from prolonged release by diffusion through the capsule wall to quick burst release. For the first scenario, mechanical failure of microcapsules will result in premature release

and has to be avoided by designing microcapsules in a way that they withstand the wear and tear associated to storage, transport and administration. For the second scenario, mechanical failure can become a powerful release mechanism, if mechanical properties can be designed such, that instabilities occur under the desired conditions. Thus it is no surprise, that recent patent literature puts strong emphasis on mechanical properties.<sup>289, 290</sup>

In the light of the previous chapters, it is evident that especially controlling mechanical instabilities requires excellent control over relevant geometrical parameters of the microcapsules. For spherical systems these are radius and wall thickness. Therefore, template assisted methods like LbL greatly extend the possibilities, since the radius can be well adjusted using monodisperse templates and wall thicknesses can be controlled on the molecular scale. In the following we will illustrate this using some examples from recent literature focusing on PEMCs without claiming complete coverage of the broad field of microcapsules.

While mechanical experiments on PEMCs have first focused on estimating the Young's modulus and its responsiveness towards external parameters like temperature<sup>291, 292</sup>, pH<sup>293, 294</sup> and salt-concentration<sup>116, 294, 295</sup>, so far the correlation between mechanical properties and release of encapsulated material has received little attention in this field. Fernandes *et al.* studied the release of a fluorescent dye from microcapsules as a function of deformation by colloidal probe AFM (Figure 4-11).<sup>296</sup> The change of fluorescence intensity within the microcapsule was followed and a clear correlation between deformation and fluorescence intensity of encapsulated dye was observed. Interestingly, a sharp drop in intensity occurred at a relative deformation around 20 %, which could be attributed to a transition from an elastic to a plastic deformation regime indicating mechanical failure at this point.

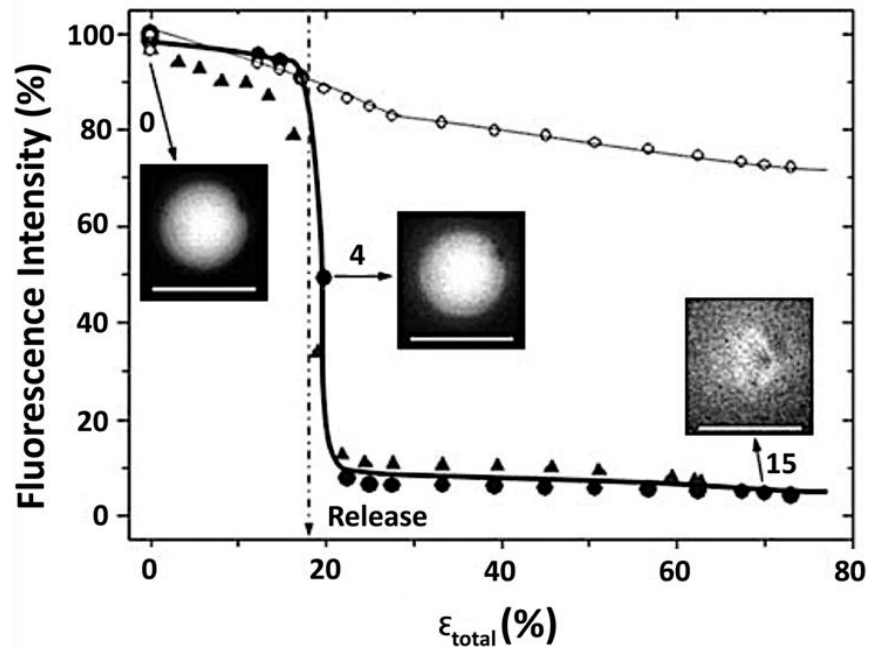


Figure 4-11: Fluorescence intensity as a function of relative deformation  $\epsilon$  of a microcapsule (filled symbols) and control experiment (open symbols) with a microcapsule not subjected to deformation. Insets show corresponding images of a microcapsule at different degrees of deformation as indicated by arrows. Scale bar is 5  $\mu\text{m}$ . Reproduced from <sup>296</sup> with permission of The Royal Society of Chemistry.

Similar studies were carried out by Palankar *et al.* who investigated the release of biodegradable polymer microcapsules upon mechanical deformation *ex situ* and their uptake by HeLa cells *in vivo*.<sup>115</sup> The technique opens the possibility to quantify forces for mechanical failure in a force regime several orders of magnitude below conventional indentation tests. An example for the relevance of this force regime can be found in recent studies of cellular uptake of microcapsules: <sup>297</sup>, <sup>298</sup>. The uptake process is accompanied by forces that are exerted on the microcapsule. If these forces are high enough to induce mechanical instability, encapsulated material will be released prematurely and not enter the intracellular area. The authors showed, using a series of microcapsules with varying deformability, that there is a clear correlation between microcapsule mechanics and the probability of release during the uptake process (see Figure 4-12). Apart from the relevance for intra-cellular delivery it was possible to estimate the forces that the cell wall exerts during incorporation. Thus mechanically well-defined microcapsules could serve as probes.

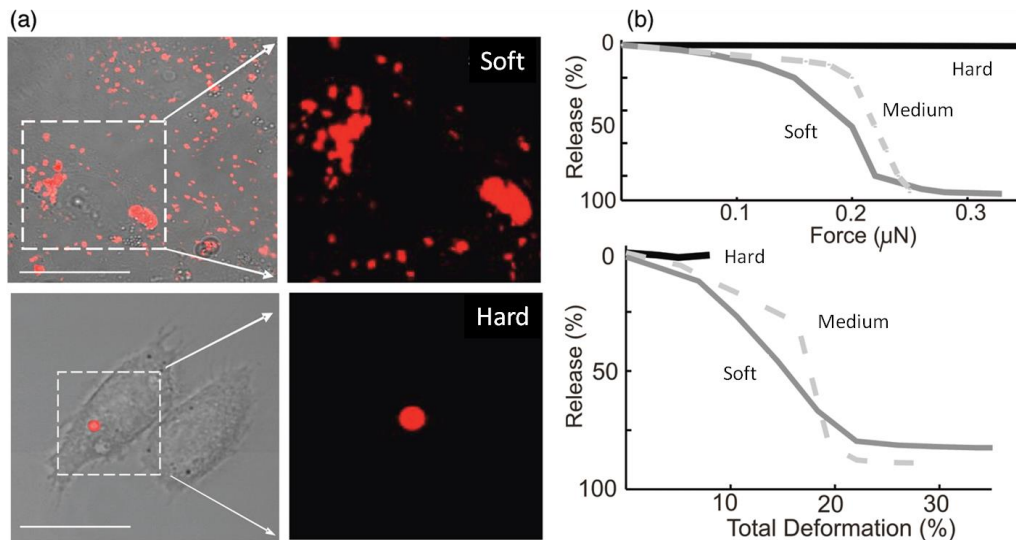


Figure 4-12: Release from microcapsules with different mechanical strength depending on annealing temperature. (a) Soft capsules release the fluorescently labeled encapsulate prematurely, i.e. outside the cell. The more rigid capsule is entirely uptaken without rupturing. (b) Release as a function of applied force and deformation from single capsule measurements <sup>299</sup>. Copyright (2010) Wiley. Used with permission from Delcea et al., *Mechanobiology: Correlation Between Mechanical Stability of Microcapsules Studied by AFM and Impact of Cell-Induced Stresses*, Small, John Wiley and Sons.

However, the relevance of deformation properties for cellular uptake goes beyond these stability considerations. Several studies show that mechanical properties as well influence the uptake probability significantly; yet, these studies investigated full instead of hollow spheres. Beningo *et al.* found that bone-marrow-derived macrophages from mice preferred harder particles to softer ones.<sup>300</sup> Here, the stiffness of polyacrylamide beads was tuned by changing the amount of crosslinker resulting in a more than threefold difference in modulus (absolute values were not given). In contrast, Liu *et al.* found that HepG2 cells internalized softer particles faster and to a greater extent than the stiffer ones.<sup>301</sup> Here, particles consisted of poly(2-hydroxyethyl methacrylate) (HEMA) and, again, the modulus was tuned by varying crosslinker content (compressive modulus from 15-156 kPa). Banquy *et al.* discovered that the stiffness of particles from the same material and similar modulus range had an influence on the pathway how they are taken up by murine macrophage cells.<sup>302</sup> In a theoretical study Yi *et al.* show the wrapping of a vesicle by a cell membrane.<sup>303</sup> It is stated that due to energetical reasons, uptake of stiffer particles is preferred. While the different findings suggest that there is no simple design criterion for all cell types, the significance of deformability is central. Generally, the possibility to now prepare microcapsules with well-defined mechanics, study their

properties on single particle level and correlate them with cellular uptake should provide the basis for gaining understanding of this behavior and for examining mechanical responsiveness for the uptake.

While in the above examples, mechanical instability was due to an external force, PEMCs have as well been used to show burst release due to internal forces: Since their shells are semi-permeable, osmotic pressure provides a means for causing tension and eventually collapse or bursting of microcapsules.<sup>97</sup> This has been taken advantage of for programming the mechanical instability of microcapsules: De Geest and coworkers deposited a LbL shell onto hydrolyzable hydrogel-cores.<sup>304, 305</sup> The system is designed such, that the shell is impermeable for degradation products of the dextran-based gels. Thus increasing osmotic pressure can build up in the course of gel hydrolysis and trigger capsule-burst.<sup>306</sup> Mechanical stability and resistance toward osmotic pressure can be tuned by adjusting the composition and thickness of the capsule wall. Thus tailored release can be achieved covering timescales between seconds and days (see example of fast response in Figure 4-13<sup>307</sup>

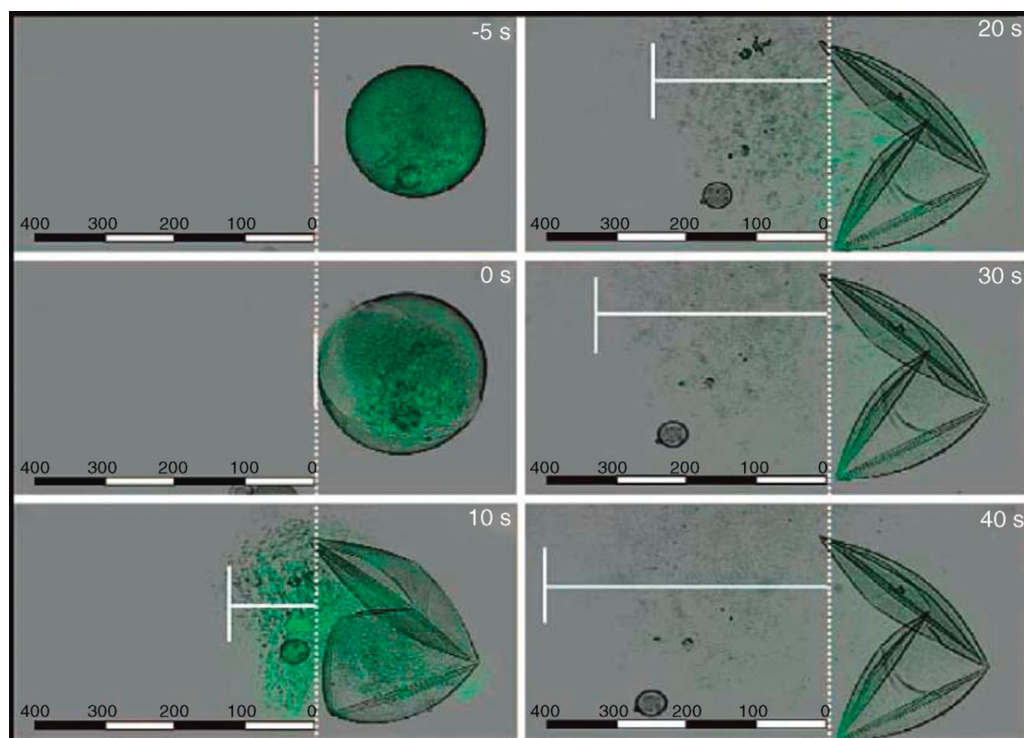


Figure 4-13: Confocal microscopy images of LbL-coated microgels at different times. At 0 s sodium hydroxide is added leading to capsule burst and release of fluorescent dye after 10 s. Scale bar unit is  $\mu\text{m}$ .<sup>307</sup> Reprinted with permission from the Journal of the American Chemical Society, 130, 14480, De Geest et.al, Microcapsules ejecting nanosized species into the environment. Copyright (2008) American Chemical Society.

This is particularly useful for pharmaceutical applications like vaccination, where a sustained delivery of vaccines is desired. This can now be realized by a single vaccination with a cocktail of microcapsules displaying different, temporally tuned release profiles.<sup>308</sup> An interesting aspect of the burst release that is visible in Figure 4-14 is its directionality. Membrane failure occurs usually at a single point only, and the expulsion of the encapsulate is driven by the flows induced by the relaxation of the pressure difference. Therefore, release is not a diffusion controlled process in this case. Knowing the weak points of the membrane where mechanical instability occurs, the location of release can be predetermined; experimentally, defects or destabilizing elements can be included and addressed externally.<sup>309</sup> Deformation experiments have been carried out to elucidate the mechanical properties and their relevance for release for this class of microcapsules.<sup>310</sup> In this context, using non-spherical microcapsules offers interesting perspectives. As shown by Tsukruk et *al.*, cubic or tetrahedral microcapsules exhibit “non-trivial rupture spots” at the edges/corners where strains are localized.<sup>261</sup> This opens the way towards directed release applications.

While in the previous examples mechanical stability was investigated in a quasi-static deformation regime at low frequencies, high frequency mechanics of microcapsules have also caught much attention recently: Especially Ultrasound (US) is of broad interest, since ultrasound is widely used in medical diagnostics and therapies. Thus, microcapsules carrying therapeutic gases could – depending on US intensity – do both enhance contrast and systematically release of therapeutically active gases. The applied US intensities strongly determine the microcapsules response. For gas-filled microcapsules the acoustic response can typically be divided in three regimes: 1) linear oscillations for low-ultrasound intensities 2) non-linear oscillations also called harmonics for increased US intensities and 3) the fragmentation of microcapsules when a certain pressure threshold is reached.<sup>311</sup> Theoretical descriptions of the dynamic linear and non-linear deformation observed in experiments are discussed with regard to shell properties and the microcapsule length scales, radius and shell thickness for example in <sup>312</sup> and <sup>313</sup>. Recently, we showed for polymeric gas-filled microcapsules the change of low and high frequency mechanics upon integration of nanoparticles in the shell.<sup>314</sup> Theranostic concepts such as US diagnosis combined with the release of therapeutic NO gases by high-intensity ultrasound or alternating magnetic fields were recently reported by different authors.<sup>315, 316</sup> However,

oscillations of microcapsules during ultrasound exposure is restricted to gas-filled microcapsules with thin soft shells. For other designs of microcapsules, effects such as cavitation, the formation of small bubbles in the liquid medium, and thermal effects can be used to release therapeutics stored in liquid-filled microcapsules.<sup>317</sup>

Shchukin and co-workers were among the first to investigate US-triggered release from PEMCs.<sup>318</sup> It could be shown that embedding of nanoparticles into the shell increases the sensitivity towards US. This effect could be attributed to both nanoparticle induced shell stiffening<sup>319</sup> raising the brittleness of the material and a higher density gradient which locally enhances US action. In later studies the correlation between shell thickness, amount of embedded nanoparticles and resistance against ultrasonic treatment was elucidated to more detail for PEMCs and polymer-shelled microcapsules.<sup>320-322</sup> Interestingly, while theory suggests and earlier studies on PEMCs found an increase of capsule stiffness with shell thickness<sup>110, 320</sup>, Kolesnikova *et al.* observed a decrease in stiffness and elastic modulus with increasing shell thickness and amount of included nanoparticles.<sup>320</sup> Obviously, in this system the introduction of NPs makes the shell fragile, which is reflected by an increased sensitivity towards US.

The mechanical instability of microcapsules can also be used to induce shape changes / break the spherical symmetry of capsules. As has been shown in the previous chapter capsule deformations are often accompanied by buckling, particularly for large compressions. Control over this process offers an elegant and simple way for the production of anisotropic particles with a multiplicity of available geometries. This is of great interest especially in the field of materials science, e.g., with regard to plasmonics or meta-materials, when tailored morphology is combined with directed assembly. Quilliet and co-workers present experimental and theoretical studies on non-trivial buckling.<sup>235</sup> They show that buckling can be easily induced by the removal of solvent from the capsules' interior in order to give a variety of anisotropic shapes. These geometries depend mainly on the shell properties, in particular the Föppl-von-Kármán number. A similar approach was adopted by Datta *et al.* for particle coated droplets.<sup>98</sup> The same group illustrated the drastic influence of inhomogeneities on the buckling process which could provide another means for tuning shapes.<sup>226</sup> Combining both buckling and assembly of sub-micron sized polymeric capsules was described by Yang and co-workers.<sup>323</sup> First, hexagonally packed 2D-arrays were

created by convective self-assembly and then shape changes were induced via solvent evaporation. A similar approach has been reported recently by Zhang *et al.* for core-shell particles.<sup>324</sup> An interesting advancement for the application of non-spherical capsules has been published recently by Wilson and co-workers.<sup>325</sup> Bowl-shaped micro-containers were produced by the controlled buckling of polymer vesicles to serve as moveable “artificial stomatocytes”. Softer anisotropic capsules were formed using osmotic pressure induced buckling, and their cavity was filled with catalytically active platinum nanoparticles turning hydrogen peroxide (which is present in the medium around the capsules) into oxygen and water. The oxygen produced inside the cavity escapes through the opening of the stomatocyte and, thereby, creates a pressure that is sufficient to propel the capsule in the opposite direction (Figure 4-14).

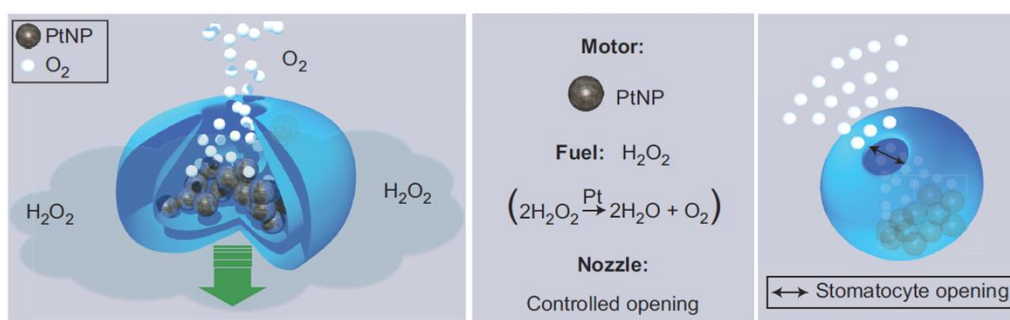


Figure 4-14: The anisotropic shape of polymer vesicles after a buckling transition is exploited for forming “artificial stomatocytes” and facilitating active motion on the colloidal scale: Catalytic platinum nanoparticles are introduced into the cavity and oxygen generated by decomposition of hydrogen peroxide results in propulsion. Reprinted by permission from Macmillian Publishers Ltd: Nature Chemistry,<sup>325</sup> copyright (2012).

Finally, adhesion is a crucial parameter for many applications of capsule systems. In the biological or medical domain it is important to know, understand, and eventually, modify or trigger adhesive interactions. For example, the adhesion between a capsular delivery container and target cells supposed to take up the cargo should be promoted specifically. On the other hand, adhesion may also not be desired, for instance, when capsules are intended to circulate for a longer period of time in blood vessels (e.g., for purposes of imaging or sustained release). Elsner *et al.* investigated the influence of shell thickness on adhesion.<sup>111</sup> It turned out that with increasing number of PE layers (which also means an increase in mechanical stability) adhesion of the capsules to the substrate decreased as monitored by the contact radius. Two deformation scenarios were distinguished based on which the scaling of contact

radius along with shell thickness and radius could be predicted. Hence, tuning of shell thickness offers one convenient way of adjusting adhesion properties. A more general theory on the adhesion of vesicles is presented by Seifert and co-workers.<sup>326</sup> They mainly focused on shape/shape changes and transitions from free to bound state. In a later publication shape equations were solved numerically.<sup>327</sup> An expression for a critical adhesion energy is derived and theoretical results are compared to the experimental data obtained from Elsner *et al.* showing good agreement. Wan and Liu worked out a model for adhesive contact mechanics of a thin-walled capsule to a flat substrate within linear elastic theory.<sup>328</sup> It is demonstrated that an increase of osmotic pressure can reduce contact area and even provoke detachment of the capsule from the substrate. Nolte and Fery introduced a method to align polyelectrolyte capsules on patterned substrates making use of electrostatic interactions.<sup>329</sup> This approach has been developed further to covalently bind the assembled capsules to the substrate.<sup>330</sup> By computational modeling, Alexeev *et al.* examined the fluid driven motion of a capsule on a substrate.<sup>281, 284, 331</sup> They found that besides stiffness and pattern of the substrate the mechanical properties of the microcapsules play an important role for the tuning of mutual adhesion. Based on these results concepts are introduced to selectively trap and burst the capsules<sup>332</sup> as well as to sort and guide them in a predetermined manner<sup>333-335</sup>. This opens an application perspective for, e.g., analytical devices for quality control regarding capsule mechanics or for a fractionation device allowing the extraction of capsules with desired mechanical properties from a given batch. Lastly, for an in-depth study of shell adhesion, an exhaustive treatment of the topic can be found in<sup>336</sup>.

#### 4.6 Conclusions

Microcapsule mechanics is a fascinating topic, which has attracted attention from various scientific communities for many decades. Still, we are currently witnessing the dawn of a new era: Modern synthetic approaches like the layer-by-layer technique or other template-assisted self-assembly methods allow unprecedented control over geometrical parameters of capsules as well as on the composition of wall and interior. Consequently, mechanical properties like capsule stiffness in the small deformation range, buckling forces/pressures or burst forces / fracture strength can be adjusted accurately. This allows not only tailoring mechanical properties such that sufficient stability to withstand wear and tear in applications is ensured - rather mechanical

properties and instabilities can be taken advantage of for introducing functionality. The present review focuses on novel possibilities and illustrates them by some selected examples from literature, without aiming for completeness of this highly dynamic field. Gaining control and further understanding of microcapsule mechanics requires a truly interdisciplinary approach. Therefore, the foundations in terms of suitable synthesis / assembly are introduced together with theoretical basics of microcapsules mechanics as well as an overview of experimental characterization techniques with special emphasis on single microcapsule measurements. Thus, we hope to provide an entry point for interested researchers into this interdisciplinary field.

**References:**

1. Jong, H. G. B., *Protoplasma* **1932**, 15, (1), 110-173.
2. Bungenberg de Jong, H. G.; Bon-Ner, J., *Protoplasma* **1935**, 24, ((2)), 198-218.
3. Cole, K. S., *Journal of Cellular and Comparative Physiology* **1932**, 1, (1), 1-9.
4. Green, B. K.; Lowell, S. **1953**.
5. Youan, B. B. C.; Jackson, T. L.; Dickens, L.; Hernandez, C.; Owusu-Ababio, G., *J. Control. Release* **2001**, 76, (3), 313-326.
6. Kataoka, K.; Harada, A.; Nagasaki, Y., *Adv. Drug Deliv. Rev.* **2001**, 47, (1), 113-131.
7. Bae, Y.; Kataoka, K., *Adv. Drug Deliv. Rev.* **2009**, 61, (10), 768-784.
8. Discher, D. E.; Eisenberg, A., *Science* **2002**, 297, (5583), 967-973.
9. Langer, R., *Nature* **1998**, 392, (6679), 5-10.
10. De Geest, B. G.; De Koker, S.; Sukhorukov, G. B.; Kreft, O.; Parak, W. J.; Skirtach, A. G.; Demeester, J.; De Smedt, S. C.; Hennink, W. E., *Soft Matter* **2009**, 5, (2), 282-291.
11. Tong, W. J.; Gao, C. Y., *J. Mater. Chem.* **2008**, 18, (32), 3799-3812.
12. Madene, A.; Jacquot, M.; Scher, J.; Desobry, S., *International Journal of Food Science & Technology* **2006**, 41, (1), 1-21.
13. Rokka, S.; Rantamaki, P., *Eur. Food Res. Technol.* **2010**, 231, (1), 1-12.
14. Gharsallaoui, A.; Roudaut, G.; Chambin, O.; Voilley, A.; Saurel, R., *Food Res. Int.* **2007**, 40, (9), 1107-1121.
15. Onwulata, C. I., Encapsulation of New Active Ingredients. In *Annual Review of Food Science and Technology*, Annual Reviews: Palo Alto, **2012**; Vol. 3, 183-202.
16. Ezhilarasi, P. N.; Karthik, P.; Chhanwal, N.; Anandharamkrishnan, C., *Food Bioprocess Technol.* **2013**, 6, (3), 628-647.
17. Kandansamy, K.; Somasundaram, P. D., *Int. J. Food Eng.* **2012**, 8, (2), 1-15.
18. Shahidi, F.; Han, X. Q., *Crit. Rev. Food Sci. Nutr.* **1993**, 33, (6), 501-547.
19. Champagne, C. P.; Fustier, P., *Curr. Opin. Biotechnol.* **2007**, 18, (2), 184-190.
20. Desai, K. G. H.; Park, H. J., *Dry. Technol.* **2005**, 23, (7), 1361-1394.
21. Gouin, S., *Trends Food Sci. Technol.* **2004**, 15, (7-8), 330-347.
22. Tsuji, K., *Journal of Microencapsulation* **2001**, 18, (2), 137-147.
23. Salem, M. A.; Al-Zayadneh, W.; Cheruth, A. J., *Water Resources Management* **2010**, 24, (10), 2237-2246.
24. Sopena, F.; Maqueda, C.; Morillo, E., *Cienc. Investig. Agrar.* **2009**, 36, (1), 27-42.
25. Hack, B.; Egger, H.; Uhlemann, J.; Henriët, M.; Wirth, W.; Vermeer, A. W. P.; Duff, D. G., *Chem. Ing. Tech.* **2012**, 84, (3), 223-234.
26. Sukhorukov, G. B.; Mohwald, H., *Trends Biotechnol.* **2007**, 25, (3), 93-98.
27. Ammala, A., *International Journal of Cosmetic Science* **2013**, 35, (2), 113-124.
28. Nelson, G., *Int. J. Pharm.* **2002**, 242, (1-2), 55-62.

29. Sanchez, L.; Lacasa, E.; Carmona, M.; Rodriguez, J. F.; Sanchez, P., *Ind. Eng. Chem. Res.* **2008**, 47, (23), 9783-9790.
30. Teixeira, C.; Martins, I. M. D.; Mata, V. L. G.; Barreiro, M. F. F.; Rodrigues, A. E., *J. Text. Inst.* **2011**, 103, (3), 269-282.
31. Akers Jr, C. E.; Sun X, J. US 7354962, **2008**.
32. Park, B. W.; Yoon, D. Y.; Kim, D. S., *Biosens. Bioelectron.* **2010**, 26, (1), 1-10.
33. Roitman, D. B. US 07312040, Dec 26 **2007**.
34. Chaudhary, A.; McShane, M. J.; Srivastava, R., *Analyst* **2010**, 135, (10), 2620-2628.
35. Shchukin, D. G.; Grigoriev, D. O.; Mohwald, H., *Soft Matter* **2010**, 6, (4), 720-725.
36. Shchukin, D. G.; Mohwald, H., *Chemical Communications* **2011**, 47, (31), 8730-8739.
37. Raj, V. A. A.; Velraj, R., *Renew. Sust. Energ. Rev.* **2010**, 14, (9), 2819-2829.
38. Waqas, A.; Din, Z. U., *Renew. Sust. Energ. Rev.* **2013**, 18, 607-625.
39. Boh, B. S., Bostjan, *RMZ - Materials and Geoenvironment* **2008**, 55, (3), 329-344.
40. Ghosh, S. K., Functional Coatings and Microencapsulation: A General Perspective. In *Functional Coatings: By Polymer Encapsulation*, Wiley-VCH Verlag GmbH & Co. KGaA: **2006**; 1-28.
41. Luzzi, L. A., *Journal of Pharmaceutical Sciences* **1970**, 59, (10), 1367-1376.
42. Nazzaro, F.; Orlando, P.; Fratianni, F.; Coppola, R., *Curr. Opin. Biotechnol.* **2012**, 23, (2), 182-186.
43. Loscertales, I. G.; Barrero, A.; Guerrero, I.; Cortijo, R.; Marquez, M.; Ganan-Calvo, A. M., *Science* **2002**, 295, (5560), 1695-1698.
44. Sliwka, W., *Angew Chem Int Ed Engl* **1975**, 14, (8), 539-50.
45. Re, M. I., *Dry. Technol.* **1998**, 16, (6), 1195-1236.
46. Utada, A. S.; Lorenceau, E.; Link, D. R.; Kaplan, P. D.; Stone, H. A.; Weitz, D. A., *Science* **2005**, 308, (5721), 537-541.
47. Chen, P. W.; Erb, R. M.; Studart, A. R., *Langmuir* **2012**, 28, (1), 144-152.
48. Hennequin, Y.; Pannacci, N.; de Torres, C. n. P.; Tetradis-Meris, G.; Chapuliot, S.; Bouchaud, E.; Tabeling, P., *Langmuir* **2009**, 25, (14), 7857-7861.
49. Zhang, J.; Coulston, R. J.; Jones, S. T.; Geng, J.; Scherman, O. A.; Abell, C., *Science* **2012**, 335, (6069), 690-694.
50. Zhang, H.; Tumarkin, E.; Peerani, R.; Nie, Z.; Sullan, R. M. A.; Walker, G. C.; Kumacheva, E., *J Am Chem Soc* **2006**, 128, (37), 12205-12210.
51. Chu, L. Y.; Utada, A. S.; Shah, R. K.; Kim, J. W.; Weitz, D. A., *Angewandte Chemie-International Edition* **2007**, 46, (47), 8970-8974.
52. Kim, J. W.; Utada, A. S.; Fernandez-Nieves, A.; Hu, Z. B.; Weitz, D. A., *Angewandte Chemie-International Edition* **2007**, 46, (11), 1819-1822.
53. Discher, D. E.; Ahmed, F., Polymersomes. In *Annu. Rev. Biomed. Eng.*, Annual Reviews: Palo Alto, **2006**; Vol. 8, 323-341.
54. Peer, D.; Karp, J. M.; Hong, S.; Farokhzad, O. C.; Margalit, R.; Langer, R., *Nat Nano* **2007**, 2, (12), 751-760.
55. Li, M. H.; Keller, P., *Soft Matter* **2009**, 5, (5), 927-937.

56. Meng, F. H.; Zhong, Z. Y.; Feijen, J., *Biomacromolecules* **2009**, 10, (2), 197-209.
57. Onaca, O.; Enea, R.; Hughes, D. W.; Meier, W., *Macromolecular Bioscience* **2009**, 9, (2), 129-139.
58. Lee, J. S.; Feijen, J., *J. Control. Release* **2012**, 161, (2), 473-483.
59. Velev, O. D.; Furusawa, K.; Nagayama, K., *Langmuir* **1996**, 12, (10), 2374-2384.
60. Dinsmore, A. D.; Hsu, M. F.; Nikolaides, M. G.; Marquez, M.; Bausch, A. R.; Weitz, D. A., *Science* **2002**, 298, (5595), 1006-1009.
61. Rossier-Miranda, F. J.; Schroen, C.; Boom, R. M., *Colloid Surf. A-Physicochem. Eng. Asp.* **2009**, 343, (1-3), 43-49.
62. Arshady, R.; George, M. H., *Polymer Engineering & Science* **1993**, 33, (14), 865-876.
63. Cui, J. W.; Wang, Y. J.; Postma, A.; Hao, J. C.; Hosta-Rigau, L.; Caruso, F., *Advanced Functional Materials* **2010**, 20, (10), 1625-1631.
64. Torini, L.; Argillier, J. F.; Zydowicz, N., *Macromolecules* **2005**, 38, (8), 3225-3236.
65. Kobaslija, M.; McQuade, D. T., *Macromolecules* **2006**, 39, (19), 6371-6375.
66. Akartuna, I.; Tervoort, E.; Studart, A. R.; Gauckler, L. J., *Langmuir* **2009**, 25, (21), 12419-12424.
67. Bohmer, M. R.; Schroeders, R.; Steenbakkers, J. A. M.; de Winter, S.; Duineveld, P. A.; Lub, J.; Nijssen, W. P. M.; Pikkemaat, J. A.; Stapert, H. R., *Colloid Surf. A-Physicochem. Eng. Asp.* **2006**, 289, (1-3), 96-104.
68. Dohnal, J.; Stepanek, F., *Powder Technol.* **2010**, 200, (3), 254-259.
69. Arshady, R., *Polym. Eng. Sci.* **1990**, 30, (15), 905-914.
70. Loxley, A.; Vincent, B., *J Colloid Interf Sci* **1998**, 208, (1), 49-62.
71. Li, J. A.; Stover, H. D. H., *Langmuir* **2010**, 26, (19), 15554-15560.
72. Grigoriev, D. O.; Bukreeva, T.; Mohwald, H.; Shchukin, D. G., *Langmuir* **2008**, 24, (3), 999-1004.
73. Decher, G., *Science* **1997**, 277, (5330), 1232-1237.
74. Sukhorukov, G. B.; Donath, E.; Davis, S.; Lichtenfeld, H.; Caruso, F.; Popov, V. I.; Mohwald, H., *Polymers for Advanced Technologies* **1998**, 9, (10-11), 759-767.
75. del Mercato, L. L.; Rivera-Gil, P.; Abbasi, A. Z.; Ochs, M.; Ganas, C.; Zins, I.; Sonnichsen, C.; Parak, W. J., *Nanoscale* **2010**, 2, (4), 458-467.
76. Skirtach, A. G.; Yashchenok, A. M.; Mohwald, H., *Chemical Communications* **2011**, 47, (48), 12736-12746.
77. Caruso, F.; Caruso, R. A.; Mohwald, H., *Science* **1998**, 282, (5391), 1111-1114.
78. Caruso, F.; Spasova, M.; Saigueirino-Maceira, V.; Liz-Marzan, L. M., *Adv. Mater.* **2001**, 13, (14), 1090-1094.
79. Müller, R.; Daehne, L.; Fery, A., *J. Phys. Chem. B* **2007**, 111, (29), 8547-8553.
80. Peyratout, C. S.; Dähne, L., *Angewandte Chemie International Edition* **2004**, 43, (29), 3762-3783.
81. Poncelet, D.; Neufeld, R. J., *Biotechnol. Bioeng.* **1989**, 33, (1), 95-103.
82. Drochon, A., *Eur. Phys. J.-Appl. Phys* **2003**, 22, (2), 155-162.

83. Drochon, A.; Barthesbiesel, D.; Lacombe, C.; Lelievre, J. C., *J. Biomech. Eng.-Trans. ASME* **1990**, 112, (3), 241-249.
84. Barthesbiesel, D., *J. Fluid Mech.* **1980**, 100, (OCT), 831-853.
85. Barthesbiesel, D.; Rallison, J. M., *J. Fluid Mech.* **1981**, 113, (DEC), 251-267.
86. Barthesbiesel, D.; Sgaier, H., *J. Fluid Mech.* **1985**, 160, (NOV), 119-135.
87. Ramanujan, S.; Pozrikidis, C., *J. Fluid Mech.* **1998**, 361, 117-143.
88. Bredimas, M.; Veyssie, M.; Barthesbiesel, D.; Chhim, V., *J Colloid Interf Sci* **1983**, 93, (2), 513-520.
89. Danker, G.; Biben, T.; Podgorski, T.; Verdier, C.; Misbah, C., *Phys Rev E* **2007**, 76, (4), 10.
90. Danker, G.; Misbah, C., *Phys. Rev. Lett.* **2007**, 98, (8), 4.
91. Danker, G.; Verdier, C.; Misbah, C., *J. Non-Newton. Fluid Mech.* **2008**, 152, (1-3), 156-167.
92. Farutin, A.; Misbah, C., *J. Fluid Mech.* **2012**, 700, 362-381.
93. Ghigliotti, G.; Biben, T.; Misbah, C., *J. Fluid Mech.* **2010**, 653, 489-518.
94. Bagchi, P.; Kalluri, R. M., *J. Fluid Mech.* **2011**, 669, 498-526.
95. Bagchi, P.; Kalluri, R. M., *Phys Rev E* **2010**, 81, (5), 11.
96. Gao, C.; Donath, E.; Moya, S.; Dudnik, V.; Mohwald, H., *Eur. Phys. J. E* **2001**, 5, (1), 21-27.
97. Gao, C. Y.; Leporatti, S.; Moya, S.; Donath, E.; Mohwald, H., *Langmuir* **2001**, 17, (11), 3491-3495.
98. Datta, S. S.; Shum, H. C.; Weitz, D. A., *Langmuir* **2010**, 26, (24), 18612-18616.
99. Zhang, Z.; Saunders, R.; Thomas, C. R., *Journal of Microencapsulation* **1999**, 16, (1), 117-124.
100. Hu, J. F.; Chen, H. Q.; Zhang, Z. B., *Mater. Chem. Phys.* **2009**, 118, (1), 63-70.
101. Keller, M. W.; Sottos, N. R., *Exp. Mech.* **2006**, 46, (6), 725-733.
102. Rachik, M.; Barthes-Biesel, D.; Carin, M.; Edwards-Levy, F., *J Colloid Interf Sci* **2006**, 301, (1), 217-226.
103. Mercade-Prieto, R.; Allen, R.; Zhang, Z. B.; York, D.; Preece, J. A.; Goodwin, T. E., *Aiche J.* **2012**, 58, (9), 2674-2681.
104. Mercade-Prieto, R.; Nguyen, B.; Allen, R.; York, D.; Preece, J. A.; Goodwin, T. E.; Zhang, Z. B., *Chemical Engineering Science* **2011**, 66, (10), 2042-2049.
105. Carin, M.; Barthes-Biesel, D.; Edwards-Levy, F.; Postel, C.; Andrei, D. C., *Biotechnol. Bioeng.* **2003**, 82, (2), 207-212.
106. Fery, A.; Weinkamer, R., *Polymer* **2007**, 48, (25), 7221-7235.
107. Lulevich, V. V.; Radtchenko, I. L.; Sukhorukov, G. B.; Vinogradova, O. I., *J. Phys. Chem. B* **2003**, 107, (12), 2735-2740.
108. Lulevich, V. V.; Andrienko, D.; Vinogradova, O. I., *J Chem Phys* **2004**, 120, (8), 3822-3826.
109. Lebedeva, O. V.; Kim, B. S.; Vinogradova, O. I., *Langmuir* **2004**, 20, (24), 10685-10690.
110. Dubreuil, F.; Elsner, N.; Fery, A., *Eur. Phys. J. E* **2003**, 12, (2), 215-221.

111. Elsner, N.; Dubreuil, F.; Fery, A., *Phys Rev E* **2004**, 69, (3), 6.
112. Fery, A.; Dubreuil, F.; Mohwald, H., *New J. Phys.* **2004**, 6, 13.
113. Liang, X. M.; Mao, G. Z.; Ng, K. Y. S., *J Colloid Interf Sci* **2004**, 278, (1), 53-62.
114. Pretzl, M.; Neubauer, M.; Tekaas, M.; Kunert, C.; Kuttner, C.; Leon, G.; Berthier, D.; Erni, P.; Ouali, L.; Fery, A., *ACS Appl. Mater. Interfaces* **2012**, 4, (6), 2940-2948.
115. Palankar, R.; Pinchasik, B. E.; Schmidt, S.; De Geest, B. G.; Fery, A.; Mohwald, H.; Skirtach, A. G.; Delcea, M., *J. Mat. Chem. B* **2013**, 1, (8), 1175-1181.
116. Heuvingh, J.; Zappa, M.; Fery, A., *Langmuir* **2005**, 21, (7), 3165-71.
117. Delorme, N.; Fery, A., *Phys Rev E* **2006**, 74, (3), 3.
118. Chen, Q.; Schonherr, H.; Vancso, G. J., *Soft Matter* **2009**, 5, (24), 4944-4950.
119. Zoldesi, C. I.; Ivanovska, I. L.; Quilliet, C.; Wuite, G. J. L.; Imhof, A., *Phys. Rev. E* **2008**, 78, (5), 8.
120. Zhang, L.; D'Acunzi, M.; Kappl, M.; Auernhammer, G. K.; Vollmer, D.; van Kats, C. M.; van Blaaderen, A., *Langmuir* **2009**, 25, (5), 2711-2717.
121. Cuellar, J. L.; Meinhoevel, F.; Hoehne, M.; Donath, E., *J. Gen. Virol.* **2010**, 91, 2449-2456.
122. Roos, W. H.; Bruinsma, R.; Wuite, G. J. L., *Nat. Phys.* **2010**, 6, (10), 733-743.
123. Jaskiewicz, K.; Makowski, M.; Kappl, M.; Landfester, K.; Kroeger, A., *Langmuir* **2012**, 28, (34), 12629-12636.
124. Sboros, V.; Glynos, E.; Pye, S. D.; Moran, C. M.; Butler, M.; Ross, J. A.; McDicken, W. N.; Koutsos, V., *Ultrasonics* **2007**, 46, (4), 349-354.
125. Glynos, E.; Koutsos, V.; McDicken, W. N.; Moran, C. M.; Pye, S. D.; Ross, J. A.; Sboros, V., *Langmuir* **2009**, 25, (13), 7514-7522.
126. Grant, C. A.; McKendry, J. E.; Evans, S. D., *Soft Matter* **2012**, 8, (5), 1321-1326.
127. Santos, E. B.; Morris, J. K.; Glynos, E.; Sboros, V.; Koutsos, V., *Langmuir* **2012**, 28, (13), 5753-5760.
128. Chen, C. C.; Wu, S. Y.; Finan, J. D.; Morrison, B.; Konofagou, E. E., *IEEE Trans. Ultrason. Ferroelectr. Freq. Control* **2013**, 60, (3), 524-534.
129. Chang, K. S.; Olbricht, W. L., *J. Fluid Mech.* **1993**, 250, 609-633.
130. Walter, A.; Rehage, H.; Leonhard, H., *Colloids and Surfaces A: Physicochemical and Engineering Aspects* **2001**, 183-185, 123-132.
131. Rehage, H.; Husmann, M.; Walter, A., *Rheol. Acta* **2002**, 41, (4), 292-306.
132. Walter, A.; Rehage, H.; Leonhard, H., *Colloid Polym Sci* **2000**, 278, (2), 169-175.
133. Koleva, I.; Rehage, H., *Soft Matter* **2012**, 8, (13), 3681-3693.
134. Degen, P.; Leick, S.; Rehage, H., *Z. Phys. Chemie-Int. J. Res. Phys. Chem. Chem. Phys.* **2009**, 223, (9), 1079-1090.
135. Pieper, G.; Rehage, H.; Barthes-Biesel, D., *J Colloid Interf Sci* **1998**, 202, (2), 293-300.
136. Leick, S.; Kott, M.; Degen, P.; Henning, S.; Pasler, T.; Suter, D.; Rehage, H., *Phys Chem Chem Phys* **2011**, 13, (7), 2765-2773.
137. Husmann, M.; Rehage, H.; Dhenin, E.; Barthes-Biesel, D., *J Colloid Interf Sci* **2005**, 282, (1), 109-119.

138. Leick, S.; Kemper, A.; Rehage, H., *Soft Matter* **2011**, 7, (14), 6684-6694.
139. Leick, S.; Henning, S.; Degen, P.; Suter, D.; Rehage, H., *Phys Chem Chem Phys* **2010**, 12, (12), 2950-2958.
140. Lac, E.; Barthes-Biesel, D.; Pelekasis, N. A.; Tsamopoulos, J., *J. Fluid Mech.* **2004**, 516, 303-334.
141. Barthes-Biesel, D., *C. R. Phys.* **2009**, 10, (8), 764-774.
142. Finken, R.; Kessler, S.; Seifert, U., Micro-capsules in shear flow. In 2011; Vol. 23, 184113.
143. Barthes-Biesel, D., *Curr. Opin. Colloid Interface Sci.* **2011**, 16, (1), 3-12.
144. Kessler, S.; Finken, R.; Seifert, U., *J. Fluid Mech.* **2008**, 605, 207-226.
145. Lac, E.; Barthes-Biesel, D., *Phys. Fluids* **2005**, 17, (7), 8.
146. Viades-Trejo, J.; Gracia-Fadrique, J., *Colloid Surf. A-Physicochem. Eng. Asp.* **2007**, 302, (1-3), 549-552.
147. Tomaiuolo, G.; Simeone, M.; Martinelli, V.; Rotoli, B.; Guido, S., *Soft Matter* **2009**, 5, (19), 3736-3740.
148. Lefebvre, Y.; Leclerc, E.; Barthes-Biesel, D.; Walter, J.; Edwards-Levy, F., *Phys. Fluids* **2008**, 20, (12), 10.
149. She, S. P.; Xu, C. X.; Yin, X. F.; Tong, W. J.; Gao, C. Y., *Langmuir* **2012**, 28, (11), 5010-5016.
150. Leclerc, E.; Kinoshita, H.; Fujii, T.; Barthes-Biesel, D., *Microfluid. Nanofluid.* **2012**, 12, (5), 761-770.
151. Chu, T. X.; Salsac, A. V.; Leclerc, E.; Barthes-Biesel, D.; Wurtz, H.; Edwards-Levy, F., *J Colloid Interf Sci* **2011**, 355, (1), 81-88.
152. Coupier, G.; Farutin, A.; Minetti, C.; Podgorski, T.; Misbah, C., *Phys. Rev. Lett.* **2012**, 108, (17), 5.
153. Farutin, A.; Misbah, C., *Phys. Rev. Lett.* **2013**, 110, (10), 5.
154. Hu, X. Q.; Salsac, A. V.; Barthes-Biesel, D., *J. Fluid Mech.* **2012**, 705, 176-194.
155. Kuriakose, S.; Dimitrakopoulos, P., *Phys Rev E* **2011**, 84, (1), 22.
156. Li, H.; Ma, G., *Phys Rev E* **2010**, 82, (2), 14.
157. Ma, G.; Hua, J. S.; Li, H., *Phys Rev E* **2009**, 79, (4), 17.
158. Queguiner, C.; Barthes-Biesel, D., *J. Fluid Mech.* **1997**, 348, 349-376.
159. Lefebvre, Y.; Barthes-Biesel, D., *J. Fluid Mech.* **2007**, 589, 157-181.
160. Mitchison, J. M.; Swann, M. M., *J. Exp. Biol.* **1954**, 31, (3), 443-460.
161. Rand, R. P.; Burton, A. C., *Biophys. J.* **1964**, 4, (2), 115-135.
162. Hochmuth, R. M., *J. Biomech.* **2000**, 33, (1), 15-22.
163. Kim, D. H.; Wong, P. K.; Park, J.; Levchenko, A.; Sun, Y., *Annu. Rev. Biomed. Eng.* **2009**, 11, 203-233.
164. Chien, S.; Sung, K. L. P.; Skalak, R.; Usami, S., *Biophys. J.* **1978**, 24, (2), 463-487.
165. Evans, E.; Yeung, A., *Biophys. J.* **1989**, 56, (1), 151-160.
166. Shao, J. Y.; Hochmuth, R. M., *Biophys. J.* **1996**, 71, (5), 2892-2901.

167. Dieluweit, S.; Csiszar, A.; Rubner, W.; Fleischhauer, J.; Houben, S.; Merkel, R., *Langmuir* **2010**, 26, (13), 11041-11049.
168. Ratanabanangkoon, P.; Gropper, M.; Merkel, R.; Sackmann, E.; Gast, A. P., *Langmuir* **2003**, 19, (4), 1054-1062.
169. Rawicz, W.; Olbrich, K. C.; McIntosh, T.; Needham, D.; Evans, E., *Biophys. J.* **2000**, 79, (1), 328-339.
170. Mabrouk, E.; Cuvelier, D.; Pontani, L. L.; Xu, B.; Levy, D.; Keller, P.; Brochard-Wyart, F.; Nassoy, P.; Li, M. H., *Soft Matter* **2009**, 5, (9), 1870-1878.
171. Evans, E. A., *Biophys. J.* **1973**, 13, (9), 941-954.
172. Skalak, R.; Tozeren, A.; Zarda, R. P.; Chien, S., *Biophys. J.* **1973**, 13, (3), 245-280.
173. Sohail, T.; Tang, T.; Nadler, B., *Z. Angew. Math. Phys.* **2012**, 63, (4), 737-757.
174. Heinrich, V.; Ounkomol, C., *Biophys. J.* **2007**, 93, (2), 363-372.
175. Baaijens, F. P. T.; Trickey, W. R.; Laursen, T. A.; Guilak, F., *Ann. Biomed. Eng.* **2005**, 33, (4), 494-501.
176. Theret, D. P.; Levesque, M. J.; Sato, M.; Nerem, R. M.; Wheeler, L. T., *J. Biomech. Eng.-Trans. ASME* **1988**, 110, (3), 190-199.
177. Discher, D. E.; Boal, D. H.; Boey, S. K., *Biophys. J.* **1998**, 75, (3), 1584-1597.
178. Ashkin, A., *Phys. Rev. Lett.* **1970**, 24, (4), 156-159.
179. Svoboda, K.; Block, S. M., *Annu. Rev. Biophys. Biomolec. Struct.* **1994**, 23, 247-285.
180. Neuman, K. C.; Nagy, A., *Nat. Methods* **2008**, 5, (6), 491-505.
181. Noy, A., *Handbook of Molecular Force Spectroscopy*. Springer: New York, **2008**.
182. Zhang, H.; Liu, K. K., *J. R. Soc. Interface* **2008**, 5, (24), 671-690.
183. Henon, S.; Lenormand, G.; Richert, A.; Gallet, F., *Biophys. J.* **1999**, 76, (2), 1145-1151.
184. Sleep, J.; Wilson, D.; Simmons, R.; Gratzner, W., *Biophys. J.* **1999**, 77, (6), 3085-3095.
185. Dao, M.; Lim, C. T.; Suresh, S., *J. Mech. Phys. Solids* **2003**, 51, (11-12), 2259-2280.
186. Titushkin, I.; Cho, M., *Biophys. J.* **2006**, 90, (7), 2582-2591.
187. Frases, S.; Pontes, B.; Nimrichter, L.; Rodrigues, M. L.; Viana, N. B.; Casadevall, A., *Biophys. J.* **2009**, 97, (4), 937-945.
188. Viana, N. B.; Rocha, M. S.; Mesquita, O. N.; Mazolli, A.; Neto, P. A. M.; Nussenzveig, H. M., *Phys Rev E* **2007**, 75, (2), 14.
189. Dutra, R. S.; Viana, N. B.; Neto, P. A. M.; Nussenzveig, H. M., *Appl. Phys. Lett.* **2012**, 100, (13), 3.
190. Guck, J.; Ananthakrishnan, R.; Mahmood, H.; Moon, T. J.; Cunningham, C. C.; Kas, J., *Biophys. J.* **2001**, 81, (2), 767-784.
191. Bareil, P. B.; Sheng, Y.; Chen, Y. Q.; Chiou, A., *Opt. Express* **2007**, 15, (24), 16029-16034.
192. Ekpenyong, A. E.; Posey, C. L.; Chaput, J. L.; Burkart, A. K.; Marquardt, M. M.; Smith, T. J.; Nichols, M. G., *Appl. Optics* **2009**, 48, (32), 6344-6354.
193. Skelton, S. E.; Sergides, M.; Memoli, G.; Marago, O. M.; Jones, P. H., *J. Opt.* **2012**, 14, (7), 10.

194. Bausch, A. R.; Ziemann, F.; Boulbitch, A. A.; Jacobson, K.; Sackmann, E., *Biophys. J.* **1998**, 75, (4), 2038-2049.
195. Bausch, A. R.; Moller, W.; Sackmann, E., *Biophys. J.* **1999**, 76, (1), 573-579.
196. Kamgoue, A.; Ohayon, J.; Tracqui, P., *J. Biomech. Eng.-Trans. ASME* **2007**, 129, (4), 523-530.
197. Lim, C. T.; Dao, M.; Suresh, S.; Sow, C. H.; Chew, K. T., *Acta Materialia* **2004**, 52, (7), 1837-1845.
198. Ramm, E.; Wall, W. A., *International Journal for Numerical Methods in Engineering* **2004**, 60, (1), 381-427.
199. Ventsel, E.; Krauthammer, T., *Thin Plates and Shells*. Marcel Dekker: New York, **2001**.
200. Reissner, E., *Journal of Mathematics and Physics* **1946**, 25, (2), 80-85.
201. Reissner, E., *Journal of Mathematics and Physics* **1946**, 25, (4), 279-300.
202. Reissner, E., *Commun. Pure Appl. Math.* **1959**, 12, (2), 385-398.
203. Reissner, E., *Journal of Mathematics and Mechanics* **1958**, 7, (2), 121-140.
204. Reissner, E.; Wan, F. Y. M., *Stud. Appl. Math.* **1969**, 48, (1), 1.
205. Ferri, J. K.; Carl, P.; Gorevski, N.; Russell, T. P.; Wang, Q.; Boker, A.; Fery, A., *Soft Matter* **2008**, 4, (11), 2259-2266.
206. Tan, S. Y.; Tabor, R. F.; Ong, L.; Stevens, G. W.; Dagastine, R. R., *Soft Matter* **2012**, 8, (11), 3112-3121.
207. Pogorelov, A. V.; Babenko, V. I., *Int. Appl. Mech.* **1992**, 28, (1), 1-17.
208. Liu, K. K.; Williams, D. R.; Briscoe, B. J., *Phys Rev E* **1996**, 54, (6), 6673-6680.
209. Pujara, P.; Lardner, T. J., *Z. Angew. Math. Phys.* **1978**, 29, (2), 315-327.
210. Arnoldi, M.; Fritz, M.; Bauerlein, E.; Radmacher, M.; Sackmann, E.; Boulbitch, A., *Phys Rev E* **2000**, 62, (1), 1034-1044.
211. Boulbitch, A., *J. Electron Microsc.* **2000**, 49, (3), 459-462.
212. Wan, K. T.; Chan, V.; Dillard, D. A., *Colloid Surf. B-Biointerfaces* **2003**, 27, (2-3), 241-248.
213. Yao, X.; Walter, J.; Burke, S.; Stewart, S.; Jericho, M. H.; Pink, D.; Hunter, R.; Beveridge, T. J., *Colloid Surf. B-Biointerfaces* **2002**, 23, (2-3), 213-230.
214. Zhongcan, O. Y.; Helfrich, W., *Phys. Rev. A* **1989**, 39, (10), 5280-5288.
215. Landau, L. D.; Lifschitz, E. M., *Course of Theoretical Physics*. 3. ed.; Butterworth-Heinemann: Oxford, **1997**; Vol. 7.
216. Pogorelov, A. V., *Bending of Surface and Stability of Capsules*. American Mathematical Society: **1988**.
217. Vliegthart, G. A.; Gompper, G., *New J Phys* **2011**, 13, 24.
218. Landau, L. D.; Lifschitz, E. M., *Theory of Elasticity*. Butterworth-Heinemann: Oxford, **1986**.
219. Pauchard, L.; Pomeau, Y.; Rica, S., *Comptes Rendus Acad. Sci. Ser. II-B* **1997**, 324, (7), 411-418.
220. Vaziri, A.; Mahadevan, L., *Proc. Natl. Acad. Sci. U. S. A.* **2008**, 105, (23), 7913-7918.

221. Yildirim, B.; Yukseler, R. F., *J. Elastomer Plast.* **2011**, 43, (2), 167-187.
222. Pauchard, L.; Rica, S., *Philos. Mag. B-Phys. Condens. Matter Stat. Mech. Electron. Opt. Magn. Prop.* **1998**, 78, (2), 225-233.
223. Parker, K. H.; Winlove, C. P., *Biophys. J.* **1999**, 77, (6), 3096-3107.
224. Shorter, R.; Smith, J. D.; Coveney, V. A.; Busfield, J. J. C., *J. Mech. Mater. Struct.* **2010**, 5, (5), 693-705.
225. Knoche, S.; Kierfeld, J., *Phys Rev E* **2011**, 84, (4), 13.
226. Datta, S. S.; Kim, S. H.; Paulose, J.; Abbaspourrad, A.; Nelson, D. R.; Weitz, D. A., *Phys. Rev. Lett.* **2012**, 109, (13), 5.
227. Komura, S.; Tamura, K.; Kato, T., *Eur. Phys. J. E* **2005**, 18, (3), 343-358.
228. Bauer, L.; Reiss, E. L.; Keller, H. B., *Commun. Pure Appl. Math.* **1970**, 23, (4), 529.
229. Reboux, S.; Richardson, G.; Jensen, O. E., *Eur. J. Appl. Math.* **2009**, 20, 479-518.
230. Helfer, E.; Harlepp, S.; Bourdieu, L.; Robert, J.; MacKintosh, F. C.; Chatenay, D., *Phys. Rev. Lett.* **2001**, 87, (8), 4.
231. Quilliet, C., *Phys Rev E* **2006**, 74, (4), 6.
232. Siber, A., *Phys Rev E* **2006**, 73, (6), 10.
233. Preston, S. P.; Jensen, O. E.; Richardson, G., *Q. J. Mech. Appl. Math.* **2008**, 61, 1-24.
234. Siber, A.; Podgornik, R., *Phys Rev E* **2009**, 79, (1), 5.
235. Quilliet, C.; Zoldesi, C.; Riera, C.; van Blaaderen, A.; Imhof, A., *Eur. Phys. J. E* **2008**, 27, (1), 13-20.
236. Quemeneur, F.; Quilliet, C.; Faivre, M.; Viallat, A.; Pepin-Donat, B., *Phys. Rev. Lett.* **2012**, 108, (10), 5.
237. Quilliet, C., *Eur. Phys. J. E* **2012**, 35, (6), 9.
238. Vella, D.; Ajdari, A.; Vaziri, A.; Boudaoud, A., *Phys. Rev. Lett.* **2011**, 107, (17), 5.
239. Vella, D.; Ajdari, A.; Vaziri, A.; Boudaoud, A., *J. R. Soc. Interface* **2012**, 9, (68), 448-455.
240. Landau, L. D.; Lifschitz, E. M., *Elastizitätstheorie*. Akademie: Berlin, **1991**.
241. Taber, L. A., *Journal of Applied Mechanics-Transactions of the Asme* **1982**, 49, (1), 121-128.
242. Sun, G.; Zhang, Z., *Journal of Microencapsulation* **2001**, 18, (5), 593-602.
243. Gompper, G.; Kroll, D. M., *J. Phys.-Condes. Matter* **1997**, 9, (42), 8795-8834.
244. Evans, E.; Rawicz, W., *Phys. Rev. Lett.* **1990**, 64, (17), 2094-2097.
245. Evans, E. A., *Biophys. J.* **1974**, 14, (12), 923-931.
246. Gompper, G.; Kroll, D. M., *J. Phys.-Condes. Matter* **2000**, 12, (8A), A29-A37.
247. Helfer, E.; Harlepp, S.; Bourdieu, L.; Robert, J.; MacKintosh, F. C.; Chatenay, D., *Phys Rev E* **2001**, 63, (2), 021904.
248. Kwak, S.; Pozrikidis, C., *Phys. Fluids* **2001**, 13, (5), 1234-1242.
249. Pozrikidis, C., *J. Fluid Mech.* **2001**, 440, 269-291.
250. Bermudez, H.; Hammer, D. A.; Discher, D. E., *Langmuir* **2004**, 20, (3), 540-543.

251. Barthes-Biesel, D.; Diaz, A.; Dhenin, E., *J. Fluid Mech.* **2002**, 460, 211-222.
252. Simmonds, J. G.; Wan, F. Y. M., *Int. J. Solids Struct.* **2001**, 38, (38-39), 6869-6887.
253. Tu, Z. C.; Ge, L. Q.; Li, J. B.; Ou-Yang, Z. C., *Phys Rev E* **2005**, 72, (2), 7.
254. Zhou, H.; Pozrikidis, C., *J. Fluid Mech.* **1995**, 283, 175-200.
255. Delorme, N.; Dubois, M.; Garnier, S.; Laschewsky, A.; Weinkamer, R.; Zemb, T.; Fery, A., *J. Phys. Chem. B* **2006**, 110, (4), 1752-1758.
256. Lazarus, A.; Florijn, H. C. B.; Reis, P. M., *Phys. Rev. Lett.* **2012**, 109, (14), 5.
257. Vella, D.; Ajdari, A.; Vaziri, A.; Boudaoud, A., *Phys. Rev. Lett.* **2012**, 109, (14), 5.
258. Nguyen, T. T.; Bruinsma, R. F.; Gelbart, W. M., *Phys Rev E* **2005**, 72, (5), 19.
259. Mueller, R.; Daehne, L.; Fery, A., *Polymer* **2007**, 48, (9), 2520-2525.
260. de Pablo, P. J.; Schaap, I. A. T.; MacKintosh, F. C.; Schmidt, C. F., *Phys. Rev. Lett.* **2003**, 91, (9), 4.
261. Shchepelina, O.; Kozlovskaya, V.; Kharlampieva, E.; Mao, W. B.; Alexeev, A.; Tsukruk, V. V., *Macromol. Rapid Commun.* **2010**, 31, (23), 2041-2046.
262. Kozlovskaya, V.; Wang, Y.; Higgins, W.; Chen, J.; Chen, Y.; Kharlampieva, E., *Soft Matter* **2012**, 8, (38), 9828-9839.
263. Zienkiewicz, O. C.; Taylor, R. L., *The finite element method for solid and structural mechanics*. Elsevier Butterworth-Heinemann: Oxford, **2005**; 15, 631.
265. Reddy, J. N., *An introduction to the finite element method*. McGraw-Hill Higher Education: New York, **2006**; Vol. 16, 766.
266. Lim, T. J.; Smith, B.; McDowell, D. L., *Acta Materialia* **2002**, 50, (11), 2867-2879.
267. MacMeccan, R. M.; Clausen, J. R.; Neitzel, G. P.; Aidun, C. K., *J. Fluid Mech.* **2009**, 618, 13-39.
268. Kruger, T.; Varnik, F.; Raabe, D., *Comput. Math. Appl.* **2010**, 61, (12), 3485-3505.
269. Walter, J.; Salsac, A. V.; Barthes-Biesel, D.; Le Tallec, P., *International Journal for Numerical Methods in Engineering* **2010**, 83, (7), 829-850.
270. Gibbons, M. M.; Klug, W. S., *Phys Rev E* **2007**, 75, (3), 11.
271. Ahadi, A.; Colomo, J.; Evilevitch, A., *J. Phys. Chem. B* **2009**, 113, (11), 3370-3378.
272. Ahadi, A.; Johansson, D.; Evilevitch, A., *J. Biol. Phys.* **2013**, 39, (2), 183-199.
273. Roos, W. H.; Gibbons, M. M.; Arkhipov, A.; Uetrecht, C.; Watts, N. R.; Wingfield, P. T.; Steven, A. C.; Heck, A. J. R.; Schulten, K.; Klug, W. S.; Wuite, G. J. L., *Biophys. J.* **2010**, 99, (4), 1175-1181.
274. Lidmar, J.; Mirny, L.; Nelson, D. R., *Phys Rev E* **2003**, 68, (5), 10.
275. Vliegthart, G. A.; Gompper, G., *Biophys. J.* **2006**, 91, (3), 834-841.
276. Buenemann, M.; Lenz, P., *Phys Rev E* **2008**, 78, (5), 21.
277. Arkhipov, A.; Freddolino, P. L.; Imada, K.; Namba, K.; Schulten, K., *Biophys. J.* **2006**, 91, (12), 4589-4597.
278. Arkhipov, A.; Freddolino, P. L.; Schulten, K., *Structure* **2006**, 14, (12), 1767-1777.
279. Arkhipov, A.; Yin, Y.; Schulten, K., *Biophys. J.* **2008**, 95, (6), 2806-2821.
280. Yin, Y.; Arkhipov, A.; Schulten, K., *Structure* **2009**, 17, (6), 882-892.

281. Alexeev, A.; Verberg, R.; Balazs, A. C., *Macromolecules* **2005**, 38, (24), 10244-10260.
282. Buxton, G. A.; Verberg, R.; Jasnow, D.; Balazs, A. C., *Phys Rev E* **2005**, 71, (5), 16.
283. Maresov, E. A.; Kolmakov, G. V.; Yashin, V. V.; Van Vliet, K. J.; Balazs, A. C., *Soft Matter* **2012**, 8, (1), 77-85.
284. Alexeev, A.; Verberg, R.; Balazs, A. C., *Soft Matter* **2006**, 2, (6), 499-509.
285. Zhu, G. D.; Alexeev, A.; Kumacheva, E.; Balazs, A. C., *J Chem Phys* **2007**, 127, (3), 10.
286. Arkhipov, A.; Roos, W. H.; Wuite, G. J. L.; Schulten, K., *Biophys. J.* **2009**, 97, (7), 2061-2069.
287. Cieplak, M.; Robbins, M. O., *J Chem Phys* **2010**, 132, (1), 12.
288. Carrasco, C.; Luque, A.; Hernando-Perez, M.; Miranda, R.; Carrascosa, J. L.; Serena, P. A.; de Ridder, M.; Raman, A.; Gomez-Herrero, J.; Schaap, I. A. T.; Reguera, D.; de Pablo, P. J., *Biophys. J.* **2011**, 100, (4), 1100-1108.
289. Smets, J.; Sands, P. D.; Guinebretiere, S. J.; Pintens, A.; Dihora, J. O. **2013**.
290. Guinebretiere, S. J.; Smets, J.; Sands, P. D.; Pintens, A.; Dihora, J. O. **2012**.
291. Mueller, R.; Kohler, K.; Weinkamer, R.; Sukhorukov, G.; Fery, A., *Macromolecules* **2005**, 38, (23), 9766-9771.
292. Kim, B. S.; Fan, T. H.; Vinogradova, O. I., *Soft Matter* **2011**, 7, (6), 2705-2708.
293. Elsner, N.; Kozlovskaya, V.; Sukhishvili, S. A.; Fery, A., *Soft Matter* **2006**, 2, (11), 966-972.
294. Lulevich, V. V.; Vinogradova, O. I., *Langmuir* **2004**, 20, (7), 2874-2878.
295. Lebedeva, O. V.; Kim, B. S.; Vasilev, K.; Vinogradova, O. I., *J Colloid Interf Sci* **2005**, 284, (2), 455-462.
296. Fernandes, P. A. L.; Delcea, M.; Skirtach, A. G.; Mohwald, H.; Fery, A., *Soft Matter* **2010**, 6, (9), 1879-1883.
297. Delcea, M.; Schmidt, S.; Palankar, R.; Fernandes, P. A. L.; Fery, A.; Mohwald, H.; Skirtach, A. G., *Small* **2010**, 6, (24), 2858-2862.
298. Bedard, M. F.; Munoz-Javier, A.; Mueller, R.; del Pino, P.; Fery, A.; Parak, W. J.; Skirtach, A. G.; Sukhorukov, G. B., *Soft Matter* **2009**, 5, (1), 148-155.
299. Fery, A.; Tsukruk, V. V., Tailoring the Mechanics of Freestanding Multilayers. In *Multilayer Thin Films: Sequential Assembly of Nanocomposite Materials*, 2 ed.; Decher, G.; Schlenoff, J., Eds. Wiley: Weinheim, **2012**; Vol. 1.
300. Beningo, K. A.; Wang, Y. L., *J. Cell Sci.* **2002**, 115, (4), 849-856.
301. Liu, W. J.; Zhou, X. Y.; Mao, Z. W.; Yu, D. H.; Wang, B.; Gao, C. Y., *Soft Matter* **2012**, 8, (35), 9235-9245.
302. Banquy, X.; Suarez, F.; Argaw, A.; Rabanel, J. M.; Grutter, P.; Bouchard, J. F.; Hildgen, P.; Giasson, S., *Soft Matter* **2009**, 5, (20), 3984-3991.
303. Yi, X.; Shi, X. H.; Gao, H. J., *Phys. Rev. Lett.* **2011**, 107, (9), 5.
304. De Geest, B. G.; Dejughnat, C.; Sukhorukov, G. B.; Braeckmans, K.; De Smedt, S. C.; Demeester, J., *Adv. Mater.* **2005**, 17, (19), 2357-2361.
305. De Geest, B. G.; Dejughnat, C.; Prevot, M.; Sukhorukov, G. B.; Demeester, J.; De Smedt, S. C., *Advanced Functional Materials* **2007**, 17, (4), 531-537.

306. Stubbe, B. G.; Horkay, F.; Amsden, B.; Hennink, W. E.; De Smedt, S. C.; Demeester, J., *Biomacromolecules* **2003**, 4, (3), 691-695.
307. De Geest, B. G.; McShane, M. J.; Demeester, J.; De Smedt, S. C.; Hennink, W. E., *J Am Chem Soc* **2008**, 130, (44), 14480.
308. De Cock, L. J.; De Koker, S.; De Geest, B. G.; Grooten, J.; Vervaeke, C.; Remon, J. P.; Sukhorukov, G. B.; Antipina, M. N., *Angewandte Chemie-International Edition* **2010**, 49, (39), 6954-6973.
309. Bedard, M. F.; De Geest, B. G.; Moehwald, H.; Sukhorukov, G. B.; Skirtach, A. G., *Soft Matter* **2009**, 5, (20), 3927-3931.
310. Schmidt, S.; Fernandes, P. A. L.; De Geest, B. G.; Delcea, M.; Skirtach, A. G.; Mohwald, H.; Fery, A., *Advanced Functional Materials* **2011**, 21, (8), 1411-1418.
311. Qin, S. P.; Caskey, C. F.; Ferrara, K. W., *Phys Med Biol* **2009**, 54, (14), 4621.
312. De Jong, N.; Bouakaz, A.; Frinking, P., *Echocardiography* **2002**, 19, (3), 229-240.
313. Marmottant, P.; van der Meer, S.; Emmer, M.; Versluis, M.; de Jong, N.; Hilgenfeldt, S.; Lohse, D., *J Acoust Soc Am* **2005**, 118, (6), 3499-3505.
314. Poehlmann, M.; Grishenkov, D.; Kothapalli, S. V. V. N.; Harmark, J.; Hebert, H.; Philipp, A.; Hoeller, R.; Seuss, M.; Kuttner, C.; Margheritelli, S.; Paradossi, C.; Fery, A., *Soft Matter* **2014**, 10 (1), 214 - 226.
315. Cavaliere, F.; Finelli, I.; Tortora, M.; Mozetic, P.; Chiessi, E.; Polizio, F.; Brismar, T. B.; Paradossi, G., *Chemistry of Materials* **2008**, 20, (10), 3254-3258.
316. Yang, F.; Chen, P.; He, W.; Gu, N.; Zhang, X. Z.; Fang, K.; Zhang, Y.; Sun, J. F.; Tong, J. Y., *Small* **2010**, 6, (12), 1300-1305.
317. Kiessling, F.; Fokong, S.; Koczera, P.; Lederle, W.; Lammers, T., *J. Nucl. Med.* **2012**, 53, (3), 345-348.
318. Shchukin, D. G.; Gorin, D. A.; Moehwald, H., *Langmuir* **2006**, 22, (17), 7400-7404.
319. Dubreuil, F.; Shchukin, D. G.; Sukhorukov, G. B.; Fery, A., *Macromol. Rapid Commun.* **2004**, 25, (11), 1078-1081.
320. Kolesnikova, T. A.; Gorin, D. A.; Fernandes, P.; Kessel, S.; Khomutov, G. B.; Fery, A.; Shchukin, D. C.; Mohwald, H., *Advanced Functional Materials* **2010**, 20, (7), 1189-1195.
321. Lensen, D.; Gelderblom, E. C.; Vriezema, D. M.; Marmottant, P.; Verdonchot, N.; Versluis, M.; de Jong, N.; van Hest, J. C. M., *Soft Matter* **2011**, 7, (11), 5417-5422.
322. Pavlov, A. M.; Saez, V.; Cogley, A.; Graves, J.; Sukhorukov, G. B.; Mason, T. J., *Soft Matter* **2011**, 7, (9), 4341-4347.
323. Yang, Q. Y.; Chen, J. F.; Wang, L. B.; Xu, Q.; He, L. H., *J Colloid Interf Sci* **2011**, 358, (2), 437-443.
324. Zhang, Y. F.; Lu, T.; Zeng, X. P.; Zhou, H. J.; Guo, H. X.; Bonaccorso, E.; Butt, H. J.; Wang, J.; Song, Y. L.; Jiang, L., *Soft Matter* **2013**, 9, (9), 2589-2592.
325. Wilson, D. A.; Nolte, R. J. M.; van Hest, J. C. M., *Nat. Chem.* **2012**, 4, (4), 268-274.
326. Seifert, U.; Lipowsky, R., *Phys. Rev. A* **1990**, 42, (8), 4768-4771.
327. Graf, P.; Finken, R.; Seifert, U., *Langmuir* **2006**, 22, (17), 7117-7119.
328. Wan, K. T.; Liu, K. K., *Medical & Biological Engineering & Computing* **2001**, 39, (5), 605-608.
329. Nolte, M.; Fery, A., *Langmuir* **2004**, 20, (8), 2995-2998.

330. Yang, J.; Gao, C. Y., *Macromol. Rapid Commun.* **2010**, 31, (12), 1065-1070.
331. Alexeev, A.; Verberg, R.; Balazs, A. C., *Journal of Polymer Science Part B-Polymer Physics* **2006**, 44, (18), 2667-2678.
332. Alexeev, A.; Balazs, A. C., *Soft Matter* **2007**, 3, (12), 1500-1505.
333. Smith, K. A.; Alexeev, A.; Verberg, R.; Balazs, A. C., *Langmuir* **2006**, 22, (16), 6739-6742.
334. Alexeev, A.; Verberg, R.; Balazs, A. C., *Langmuir* **2007**, 23, (3), 983-987.
335. Usta, O. B.; Alexeev, A.; Balazs, A. C., *Langmuir* **2007**, 23, (22), 10887-10890.
336. Springman, R. M. *Mechanical and chemical effects in adhesion of thin shell structures with applications in wafer bonding and adhesion of living cells*. University of Pennsylvania, Philadelphia, **2009**.



## 5. Novel Characterization Techniques of Microballoons

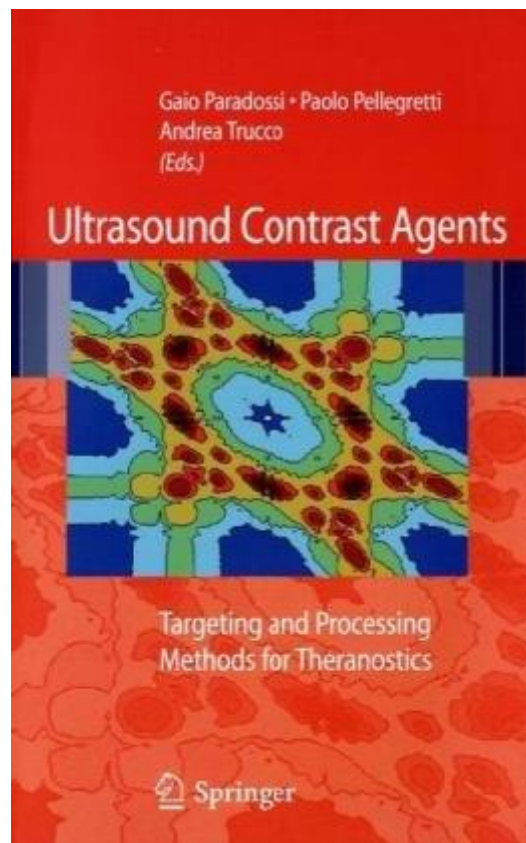
*Fernandes, P. A. L.<sup>1</sup>; Pretzl, M.<sup>1</sup>; Fery, A.<sup>1</sup>; Tzvetkov, G.<sup>2</sup>; Fink, R. H.<sup>2</sup>*

1) Department of Physical Chemistry II, University of Bayreuth, Universitätsstraße 30, D-95447 Bayreuth, Germany

2) Department of Physical Chemistry II, Friedrich-Alexander Universität Erlangen, Egerlandstraße 3, 91058 Erlangen

Published as Bookchapter in Ultrasound contrast agents – Targeting and processing methods for theranostics , Springer Science and Business Media

Editors: Gaio Paradossi, Paolo Pelegretti, Andrea Trucco





## 5.1 Characterization of MBs by AFM

Mechanical properties of microbubbles (MB) are obviously important as they determine stability. As targeted drug delivery agents triggered by ultrasound the microbubbles have to possess enough robustness to avoid membrane rupture and enough elasticity to favor targeted adhesion while still susceptible to ultrasound induced membrane rupture. There is therefore a complicated interplay of different interaction processes that closely depend on the mechanical properties of the MBs and that need to be understood in order to better control their behavior in applications.

Several techniques exist to study mechanical properties of microbubbles<sup>1</sup>. The atomic force microscope (AFM)<sup>2</sup> offers several advantages as it can apply a wide range of forces (from tens of pico to microNewtons) and detect deformations smaller than 1 nm on individual microbubbles in solution and at different temperatures. This renders the technique very attractive to study the mechanical properties of microbubbles. In addition this technique has been successfully used to study mechanical properties of polyelectrolyte multilayer capsules (PEM,<sup>3-8</sup>) and vesicles<sup>9, 10</sup>.

In this section the mechanical experiments performed on MBs (prepared at room temperature and pH 5) will be presented. In a first part the AFM force spectroscopy technique is introduced followed by the most important results obtained.

## 5.2 Experimental setup

An AFM mounted on an inverted optical microscope was used to probe the mechanical properties of individual MBs (Figure 5-1). During force spectroscopy AFM experiments an individual MB is compressed by a cantilever (moving a piezo) while the deflection of the cantilever is measured by an optical lever (detection of a laser reflected on the tip of the cantilever). With a calibrated cantilever the deflection versus piezo displacement data can be transformed into a force versus deformation curve which gives the mechanical response of the particular MB to the applied force. Force spectroscopy measurements were carried out under water using commercial AFM setups: a Nanowizard I (JPK Instruments, Germany) used for the experiments at body temperature and an MFP 1D (Asylum Research) for most of the experiments at room temperature. In both setups the AFMs were placed on top of an inverted

optical microscopes (Zeiss Axiovert 200 for the first and Olympus IX71 for the second) to control the alignment and monitor the MBs during the compression. A colloidal probe <sup>11, 12</sup> (glass bead, diameter  $\sim 50 \mu\text{m}$ , PolyScience inc.) was glued to a tipless cantilever (MikroMash, Spain) with two component epoxy glue (UHU Plus endfest 300, UHU GmbH & Co. KG, Germany) using a micromanipulator (Suttner Instrument Co.). The spring constants of the cantilevers were determined using the thermal noise method <sup>13</sup> or the Sader method <sup>14</sup> (for stiffer cantilevers). To perform a force spectroscopy measurement the MBs have to be reasonably attached to the substrate to avoid slippage during compression. To promote this adhesion a droplet of MBs solution was applied to a PEI coated thin glass slide. The experiments revealed that slippage can still occur if the MBs and probe are not aligned (this should be carefully monitored by use of the inverted optical microscope). Typical compression/retraction cycles were done in 1 second.

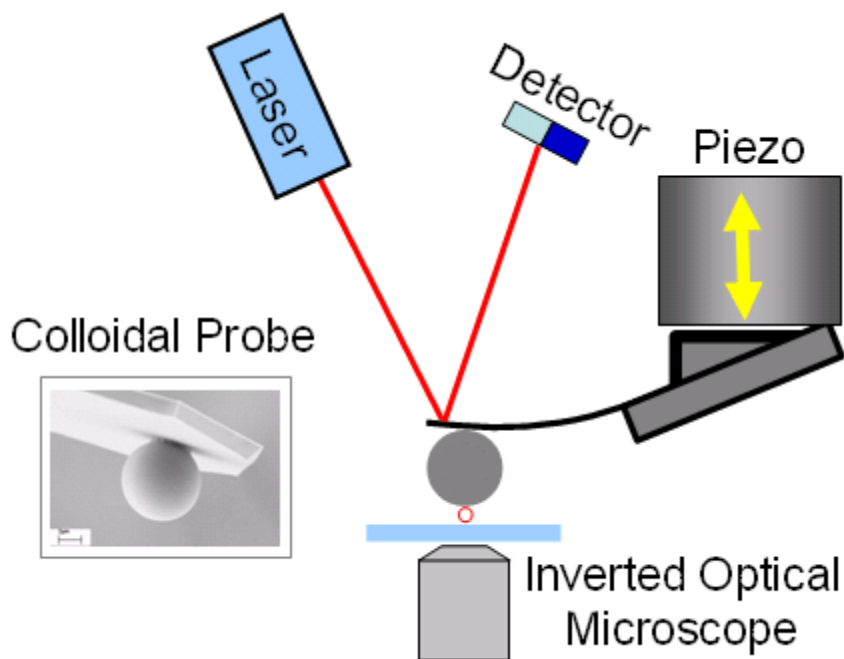


Figure 5-1: Schematic of the AFM setup used with an inverted optical microscope. A colloidal probe (silica bead) was glued to a tip-less cantilever and the measurements were done under water.

### 5.3 Bubble bursting

In Figure 5-2 the force-deformation curve obtained for a typical MB is presented (the force-deformation curves should be read from right to left). The compression curve (trace, blue) presents a first zone where the force increases with the deformation of

the sample until a point where there is a peak followed by a decrease in the measured force. Next the effect of the substrate is observed by an almost vertical increase of the force. The red retraction curve shows that after such deformation the MB does not behave elastically, as expected. We interpret the force peak as the bubble bursting. This scenario is compatible with the optical microscopy images observed (Figure 5-3) before and after the bursting event: before bursting the air-filled MB has larger index of refraction gradients (between air and polymer) so it scatters more light (Figure 5-3, right) than after the bursting where water replaces air and, consequently the water-filled MB presents smaller index of refraction gradients (only between water and polymer) so it scatters less light (Figure 5-3, left).

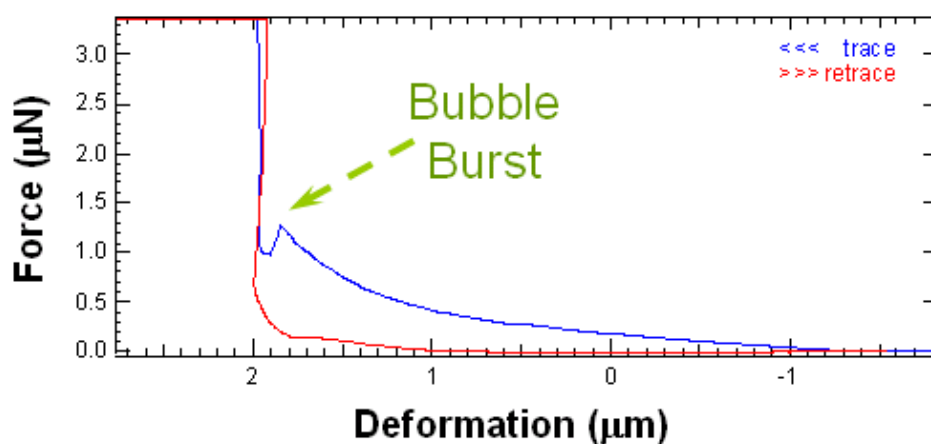


Figure 5-2: AFM force-deformation curve of a MB ( $R \sim 2.36 \mu\text{m}$ ), where the bubble burst can be observed.

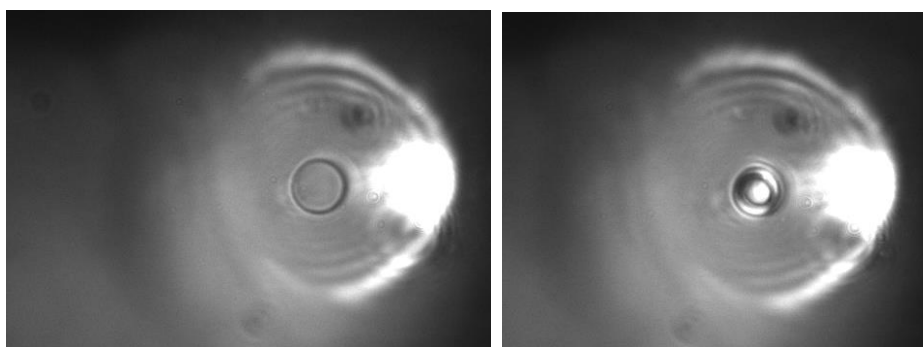


Figure 5-3: Inverted optical microscope images of a MB, after (left) and before (right) bursting.

Several MBs were analyzed and presented similar bursting profiles, from which a burst force (peak force in the force-deformation curve) could be measured. In Figure 5-4 a graph of the burst as a function of bubble radius is presented. There is some

dispersion, as expected, since we are analyzing individual MBs that can present an important polydispersity in wall thickness and composition, air pressure. Nevertheless the data seems to indicate an increase of the burst force with bubble radius. One more point regarding the bursting phenomenon: experiments performed with slower compression/retraction cycles lower burst forces were observed. This is also compatible with the bursting scenario due possibly to crack propagation kinetics.

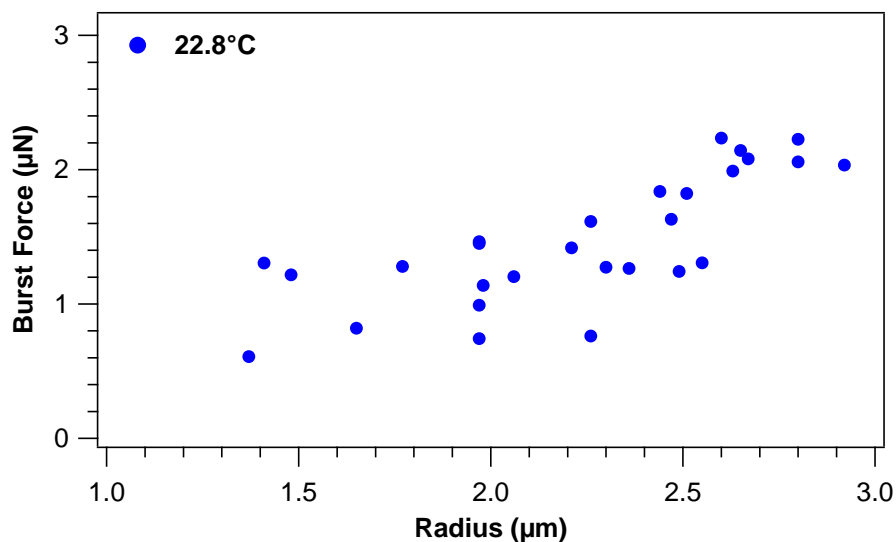


Figure 5-4: Burst force versus bubble radius at room temperature.

## 5.4 Bubbles after bursting

An important question regarding the bubble bursting is what happens to the bubble afterwards? To elucidate this point force spectroscopy measurements (compression/retraction cycles) were made after the MB bursting was observed. In Figure 5-5 the force versus piezo displacement curves of a MB during (left) and after (right) bursting are presented. In the force curve after bursting we can notice that the force response of the MB starts at approximately the same piezo displacement as in the bursting curve. This means that the MB does not fragment into pieces after burst but actually recovers almost completely its previous shape. We note further that the behavior after burst is reproducible for at least 10 compression/retraction cycles.

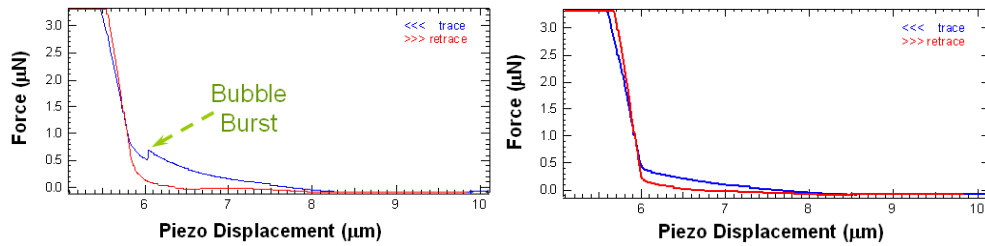


Figure 5-5: AFM force-deformation curve of a MB ( $R \sim 2.26 \mu\text{m}$ ), during (left) and after (right) bursting.

## 5.5 Bubbles' stiffness cycle dependence

AFM force spectroscopy can provide much more information about the sample than just the burst force. In particular, the linear slope of the force curve at small deformations can be used as a measure of the stiffness of the MBs wall. By performing several push-pull cycles on the same MB we observed that its stiffness changes. Two different typical behaviors were identified:

- For soft cycles (with low applied forces, smaller than 50 nN, corresponding to small bubble deformations) the bubble wall stiffness increased (Figure 5-6 left).
- For hard cycles (with high applied forces, higher than 1  $\mu\text{N}$ , corresponding to large bubble deformations) the bubble wall stiffness decreased (Figure 5-6, right).

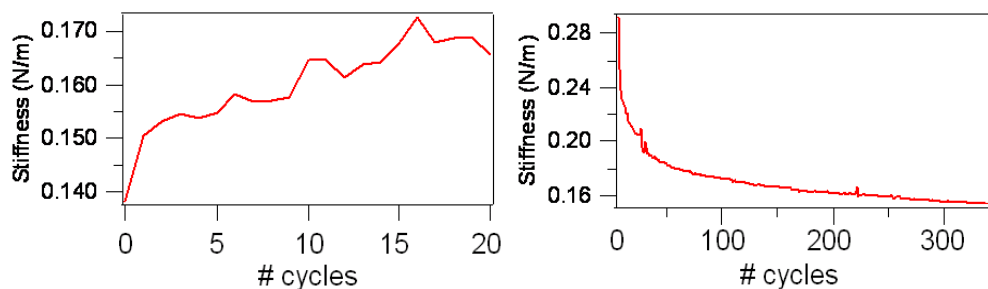


Figure 5-6: Typical stiffness response of MBs versus number of push-pull cycles under low applied forces (small deformations, left) and high applied forces (large deformations, right).

We note that in both cases the total cycle time was identical (one second). Several factors can play a role in this phenomenon like water displacement kinetics, visco-elastic effects, introduction of structural defects. Further experiments will be performed to understand this interesting and reproducible behavior.

## 5.6 Bubbles stiffness

Since the stiffness of the MBs changes with the number of push-pull cycles it has been subjected to, in order to obtain the stiffness dependence as a function of bubble radius (Figure 5-7) only the first push-pull cycle was considered. A relatively linear dependence is observed, the dispersion is quite reasonable taking into account the polydispersity of the samples (wall thickness, wall composition) and the fact that the stiffness depends also on the past mechanical history of the bubbles. To determine the Young's modulus of the MB wall from these data an appropriate model would have to be developed, taking into account the wall thickness and composition gradient. Nevertheless, preliminary estimation can be given by using the Reissner model<sup>15, 16</sup> (applicable for thin shells<sup>17</sup>, already successfully used to determine the Young's modulus of polymeric microcapsules<sup>3-8</sup>). Therefore, by considering an effective wall thickness of 600 nm the effective Young's modulus of the wall material according to the Reissner model is approximately 400 kPa.

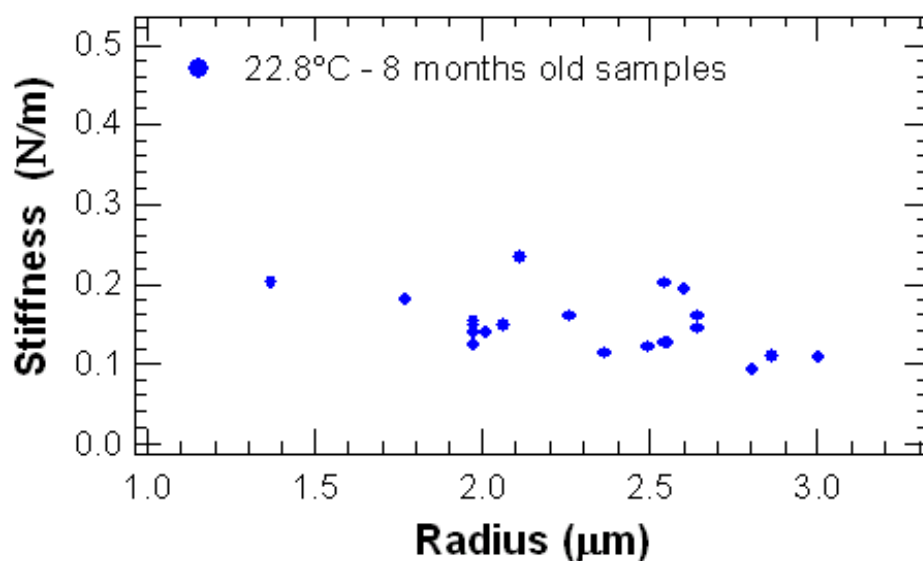


Figure 5-7: Stiffness versus MB radius at room temperature.

## 5.7 Bubbles temperature dependence

Taking into account the projected application of the MBs it is important to study their mechanical properties dependence with temperature. To this effect several compression/retraction cycles were performed on the same air-filled MB at room temperature and afterward at body temperature. To avoid bursting only small

deformations were imposed on the MB by using a softer cantilever. Several force-deformation curves were collected and from each one the stiffness (or slope) of the curve in the small deformation (linear) regime were determined. The results at room and body temperature are presented in the histogram of Figure 5-8 and clearly show that the MBs became softer at body temperature. We remark that, as seen before a sequence of soft push-pull cycles (as the ones made during this experiment) should increase the stiffness of the MB. Since we observed a stiffness decrease from room to body temperature it must be due to the temperature change and not to the push cycle sequence. The temperature softening effect (of around 10%) might be underestimated as there is probably some stiffening due to the consecutive push cycles.

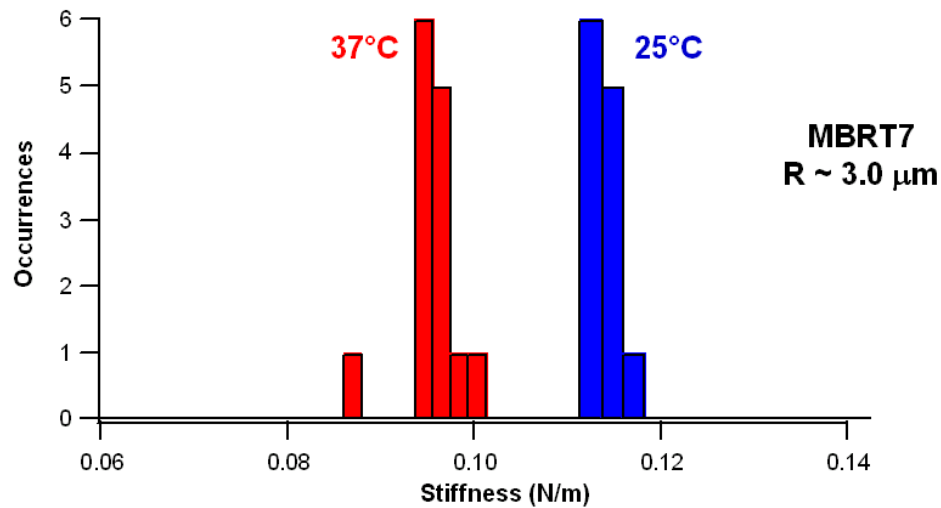


Figure 5-8: Histograms of MB stiffness at room and body temperature.

In Figure 5-9 we present the burst force versus MB radius at different temperatures. The dispersion is again expected, but it is interesting to note that the bursting force seems to be rather independent from temperature. Since a temperature induced softening of the wall material has been put into evidence (and the softness of the wall material should influence its bursting point) there might be an interplay of two effects that cancel each other out.

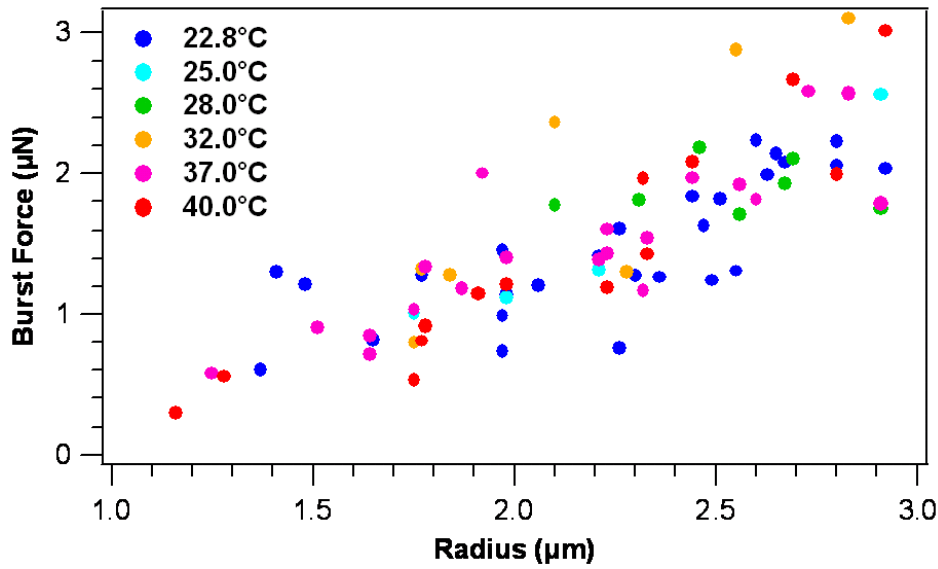


Figure 5-9: Burst force versus MB radius at different temperatures.

### 5.8 Samples age

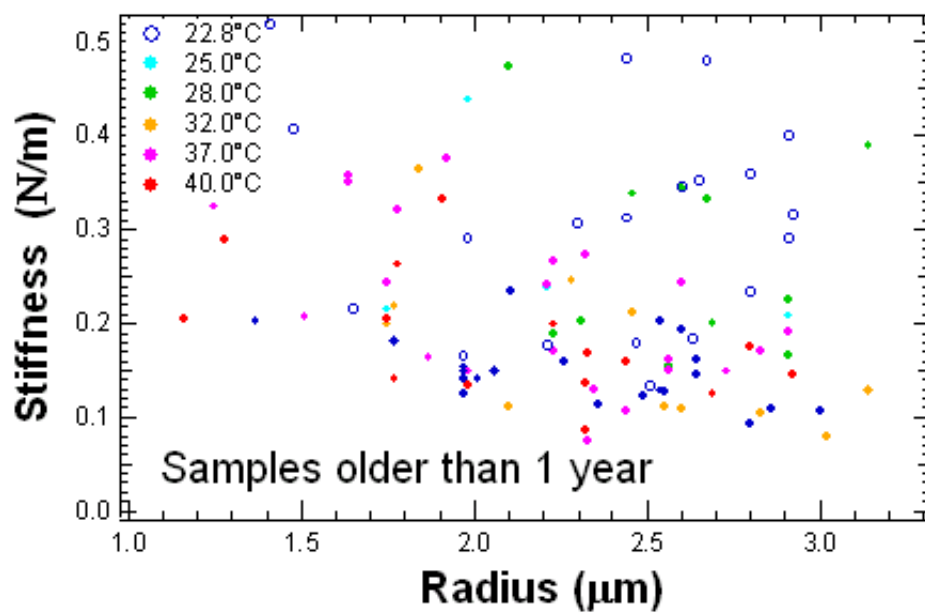


Figure 5-10: Stiffness versus MB radius at different temperatures for MB samples older than 1 year.

The stiffness of the MBs was also measured at different temperatures for samples prepared more than one year before the experiment (Figure 5-10). Instead of a linear behavior as in Figure 5-7 a more or less random distribution is observed. This result suggests that the polydispersity is significantly increased with sample age (this is compatible also with the fact that the stiffness of the bubbles depends on its previous

history: the older the samples the more history it has and less predictable are the stiffness values).

## 5.9 Adhesion forces

In addition to the mechanical properties of the microbubbles it is of course essential for their application to study the interactions between microbubbles and surfaces. Their application as theranostics, ultrasound enhanced contrast agents for diagnostic and drug delivery agents for therapeutic applications, they will be injected into the human bloodstream. An important task is then to control the interactions between the MBs and the surrounding tissue. An excellent tool to study adhesion properties between microbubbles and substrates is the colloidal-probe AFM combined with an optical microscope<sup>18, 19</sup>, that was already introduced for the measurements of the mechanical properties (Figure 5-1).

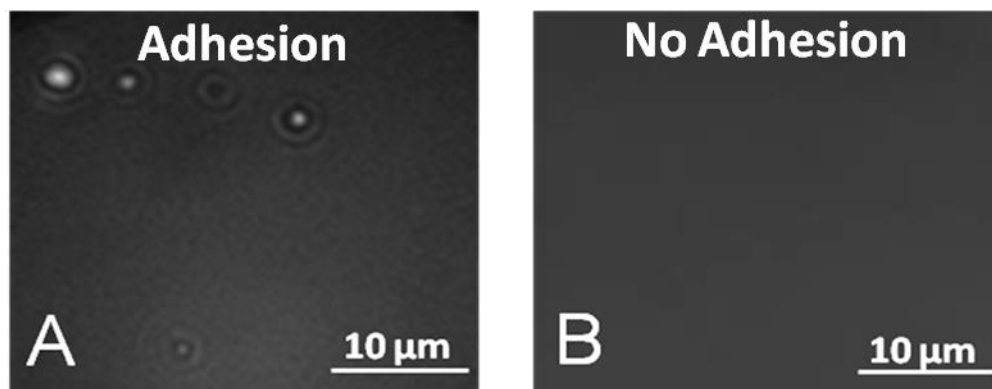


Figure 5-11: (A) Typical RICM result of adhered MBs: Bright spots and Newton fringes (B) MBs exposed to a repulsive substrate: No adhesion in the RICM visible.

The optical microscope is for these measurements used in the reflection interference contrast microscopy mode (RICM). This technique developed by Sackmann and co-workers<sup>20</sup> is very useful to investigate adhesion areas of particles based on the interference of reflected light. Microbubbles that are adhered to a glass substrate show in the RICM mode typical bright spots surrounded by an interference pattern. This pattern originates from reflected light from the microbubble shell and the substrate surface that is interfering constructively or destructively. In Figure 5-11 A typical interference pattern of adhered MBs with a size of about 4  $\mu\text{m}$  is displayed. In this experiment the polymer shell of the microbubbles is modified with

hyaluronic acid, thus the zeta potential increases to  $-20 \text{ mV} \pm 1.5 \text{ mV}$ . The negative charged MBs stick to positive charged substrates and adhesion is observed. If the same microbubbles are exposed to negative charged substrates (Figure 5-11 B) no adhesion and no bright spots are visible with RICM.

To quantify adhesion forces with RICM in detail, an apparent contact area between MB and substrate can be calculated. The contact or adhesion area for MB is considered as the constant grey region in the RICM images. For the determination of the area an intensity profile is extracted and the diameter of the contact region can be determined. The potential of the RICM technique is its combination with colloidal probe AFM. External forces can be applied onto the MB in liquid environment and the adhesion forces measured with AFM can be correlated with the change of the contact area followed by RICM.

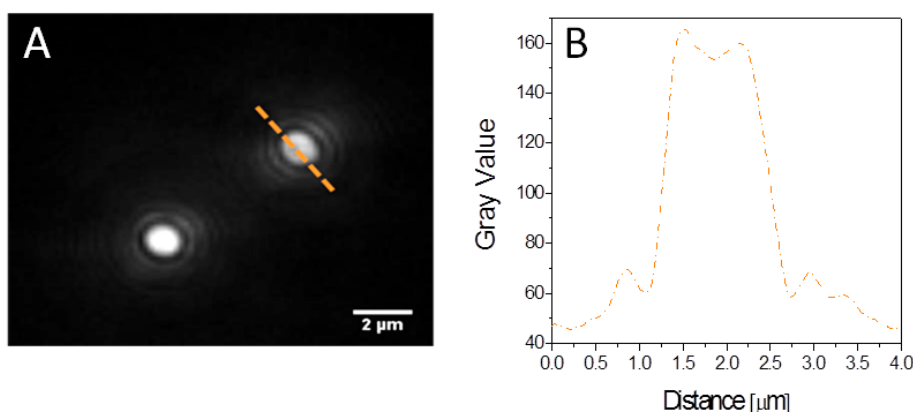


Figure 5-12: (A) The adhesion area of the microbubbles is the bright spot that is surrounded by an interference pattern (B) Extracted intensity profile of the interference pattern.

With AFM force–distance curves different external force loads between the colloidal probe and the MB can be measured. When the colloidal probe detaches from the MB a pull-off force (adhesion force) can be determined, shown Figure 5-13 A. For increasing external force loads an increase in the observed pull-off forces is displayed in Figure 5-13 B, due to the enlarged adhesion area.

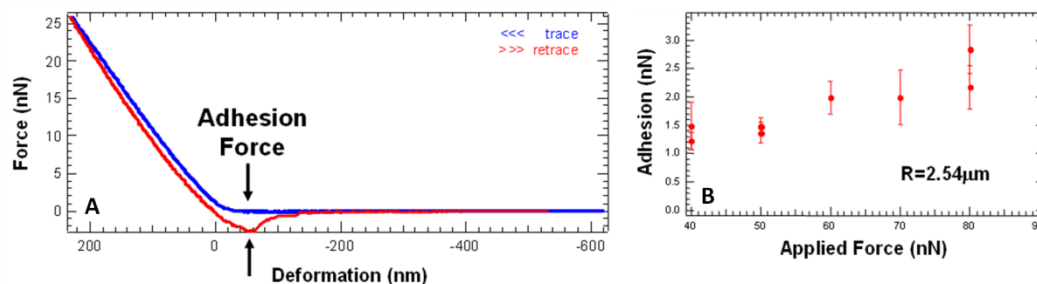


Figure 5-13: (A) AFM force-deformation curve, adhesion between probe and MB can be measured, (B) Adhesion between MB and probe versus applied force

With this technique several individual microbubbles can be tested. The observed adhesion forces are influenced by the size of the particles, the shell thickness and the air/water content of the MB. These results show that the MBs adhesion forces can be measured with the used AFM setup and that it is a very interesting and versatile technique to probe this system.

### 5.10 Adhesion arrays

The directed particle adhesion onto patterned substrates is interesting for a wide range of applications in the field of combinatorial chemistry, the buildup of sensor arrays or optical materials. The self assembly of MBs on structured substrates is of great interest, because it is an inexpensive approach to set up controlled arrangements of MB over a large area that can be used for serial testing of microbubbles or used as test substrates for cell exposure experiments. The observation and quantification of microbubbles adhesion to specific substrates allowed us to progress towards this goal. For the preparation of patterned substrates in addition to lithographic methods there are also various “soft lithographic” techniques available: micro-contact printing<sup>21-23</sup> polymer on polymer stamping<sup>24</sup>, wrinkling<sup>25,26</sup>. Several studies have been devoted to the selective deposition of polyelectrolytes<sup>27</sup>, cells<sup>28</sup>, proteins<sup>29</sup> and microcapsules<sup>30-32</sup>.

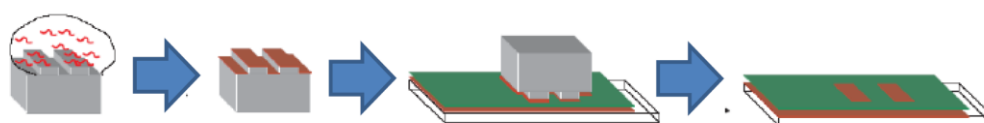


Figure 5-14: Schematic of the micro-contact printing process: (1) incubation of the elastomeric stamp with an aqueous solution of a fluorescent- labeled polyelectrolyte, (2) after rinsing and drying a thin monolayer is obtained on the stamp surface. (3) Transfer of the stamp onto a polyelectrolyte multilayer coated substrate (4) After remove of the stamp a patterned the substrate is obtained.

To direct the adhesion of negative charged MB (modified with hyaluronic acid) a patterned substrate with different charge densities can be used. In Figure 5-15 A line pattern was transferred via micro-contact printing (Figure 5-14) onto a multilayer coated glass substrate. This process is relatively easy to use, reproducible and allows the production of very well defined and broad range of patterns.

The bright lines in Figure 5-15 A are positively charged, while the dark background exhibits a negative charge. Negative charged MB adhere preferential to the line pattern (Figure 5-15 B). Due to the used polyelectrolyte a strong or weak adhesion of the MB onto the pattern can be controlled.

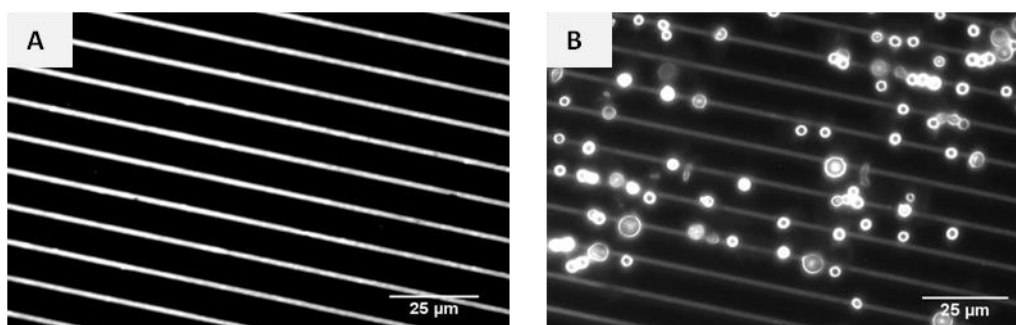


Figure 5-15: (A) Line pattern transferred with micro-contact printing to a polyelectrolyte multilayer. (B) Selective adhesion of microbubbles on patterned substrate.

### 5.11 Conclusion and perspectives

The AFM setup used allows not only the observation (through force curves corroborated with optical microscopy images) of individual MBs bursting but also and quite interestingly the quantification of the burst force. Both wall stiffness and burst force seem to depend linearly on the MB radius. Measurements at both room and body temperature revealed that the MBs became softer at body temperature but the burst force is relatively temperature independent. A significant increase in the wall stiffness polydispersity with samples age was put into evidence.

The presented set up, colloidal probe AFM and an optical microscope in RICM mode, offers a versatile technique to study adhesion forces on different substrates and under external forces. Adhesion forces increase with increasing external applied forces and the dependence on the deformation of the soft particles and the resulting change of the contact area can be studied with the set up in detail. The adhesion forces are influenced by various parameters like the size of the MB, the shell thickness and the MB air/water content. The quantification of adhesion energies between MB and different substrates was crucial for the set-up of MB arrays. These arrays are interesting substrates for the serial testing of microbubbles and cell exposure experiments.

## 5.12 Characterization of MBs with STXM

Zone-plate based scanning transmission soft X-ray microspectroscopy (STXM) is a rapidly developing analysis technique which makes use of the advantages of high brilliance synchrotron radiation<sup>33-36</sup>. In STXM synchrotron X-ray radiation is focused by a Fresnel zone plate and the sample is raster-scanned through the focal point while recording the intensity of transmitted X-rays. Thus, a 2D image is formed like in other scanning probe techniques.

A schematic of the STXM set-up is shown in Figure 5-16. The Fresnel zone plate (FZP) serves as demagnifying/focusing diffractive element. FZP is a circular diffraction grating of alternate transparent and opaque zones. Higher diffraction order beams are blocked by a pinhole, which serves as order-sorting aperture (OSA). Based on the near-edge X-ray absorption fine structure (NEXAFS) contrast STXM can be used for elemental and chemical imaging to determine the molecular composition in the sample. Thus, by measuring the energy dependent transmission in the focus of the X-ray beam the experiment provides chemical and sub-40 nm structural data which can be directly correlated. Furthermore, by operating in the “water window” spectral region between the carbon and oxygen *K*-edge absorption edges (about 285 eV to 535 eV), one can study samples in up to 10 mm of water or ice. STXM provides higher spatial resolution than the confocal laser scanning microscope (CLSM), at present a widely used technique for the investigation of microcapsule systems, which makes the X-ray microscopy very advantageous for obtaining new insights into the nanoscale assemblage of such materials. Besides, additional sample

preparation like, e.g., fluorescence labeling, is not used in STXM, since it utilizes the spectroscopic contrast which allows for quantitative chemical analysis.

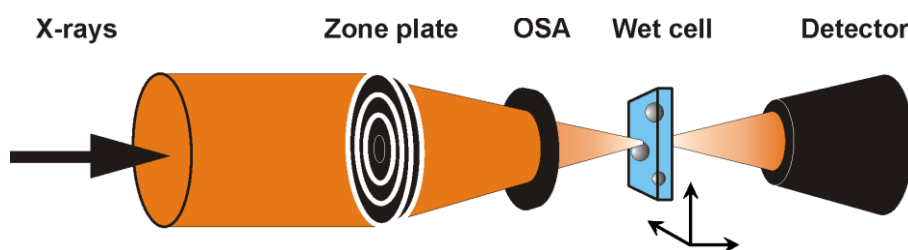


Figure 5-16: Scheme of a scanning transmission X-ray microscope (STXM) showing Fresnel zone plate (FZP) producing a diffraction limited focus, order selecting aperture (OSA) selecting only the first order focus, the wet cell and the detector measuring the transmitted intensity.

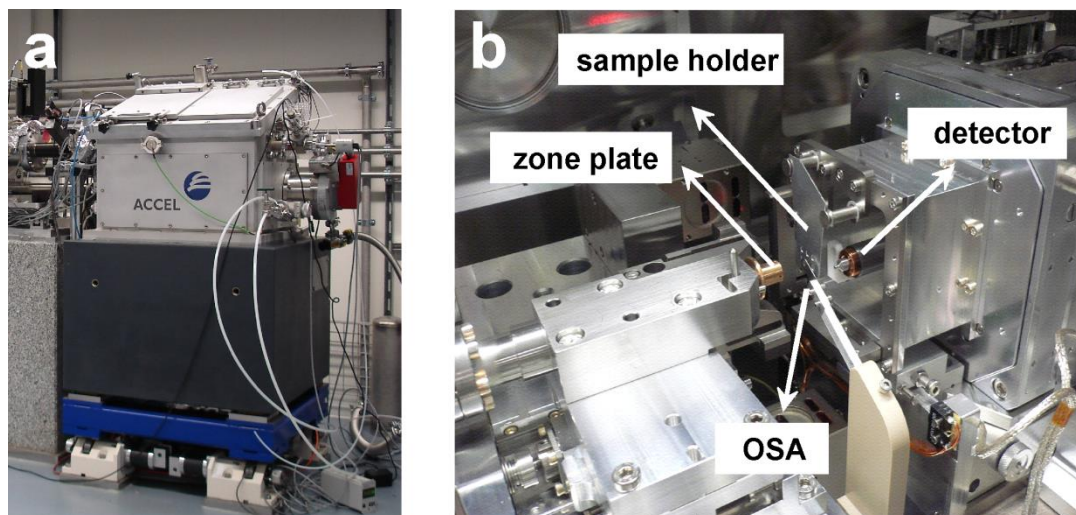


Figure 5-17: Photographs of the PolLux-STXM at beamline X07DA at the Swiss Light Source: (a) microscope chamber in the experimental hutch and (b) main elements of the set-up<sup>37</sup>.

For STXM measurements we used the so-called "wet cells" where approximately 1  $\mu\text{L}$  of well homogenized microbubbles (MBs) water suspension was sandwiched between two 100 nm thick  $\text{Si}_3\text{N}_4$  membranes (Silson Ltd, UK), which were then sealed with silicone high-vacuum grease to maintain the water environment during the experiment. The MBs were imaged in transmission mode in helium atmosphere using the PolLux-STXM microscope at the Swiss Light Source (SLS), Paul Scherrer Institute (Figure 5-17). The transmitted photon flux was measured using a photomultiplier tube (Hamamatsu 647P). SLS storage ring runs at 2.4 GeV and "top-up" operation mode which guarantees a constant electron beam current of  $400 \pm 1.5$  mA. The PolLux-STXM uses linearly polarized x-rays from a bending magnet in

the photon energy range between 200 eV and 1200 eV and it provides a spatial resolution better than 40 nm and spectral resolving power  $E/\Delta E > 5000$  (at the N *K*-edge, approx. 400 eV)<sup>37</sup>. Images were recorded at selected energies through the O 1s region (510–560 eV). Oxygen *K*-edge NEXAFS spectra were acquired in the so-called line-scan mode, i.e. the transmitted intensity signal was recorded while a line trajectory was scanned across a part of the sample for each photon energy through the spectrum. The line scans were performed with 0.1 eV energy steps from 520 eV to 560 eV and the NEXAFS spectra were normalized to unity at 560 eV.

So far, we have concentrated on two aspects: first, STXM was used to monitor the interior of the microbubbles, since the absorption contrast close to the O *K*-edge is superior to distinguish between air and water-filled MBs. The second aspect is concerned with the stabilizing shell of the MBs: from the 2D projection of spherical MBs the thickness profile of the shell can be quantitatively estimated.

Two STXM transmission images of three PVA-based microbubbles in water environment recorded at 520 eV and 550 eV (i.e. below and above the 1s absorption threshold of oxygen) are presented in Figure 5-18. STXM microscopy is based on the contrast given by the absorption coefficients of the species; the transmitted photon intensity through the material depends on the thickness, density and atomic number of each component according to Lambert-Beer's law. Taking into account the calculated transmission curves in the oxygen *K*-edge region of water, PVA and air components<sup>38</sup>, it becomes clear that the STXM image at  $h\nu = 520$  eV shows the PVA shells of the MBs while the water and air absorption is weak compared to the carbonaceous material. Above the oxygen *K*-edge ( $h\nu = 550$  eV) water environment and PVA strongly absorb the x-rays while air shows approximately one order of magnitude higher transmission of the x-rays. Consequently the gas-filled cores of the particles appear brighter due to detector intensity. Additionally, the core of the MB B shows essentially no contrast compared to the water background. This unambiguously suggests that air was released through the membrane and the particle is water-filled. Thus, the contrast variations in the STXM transmission images below and above the O *K*-edge provide a direct evidence of the MB gas interior.

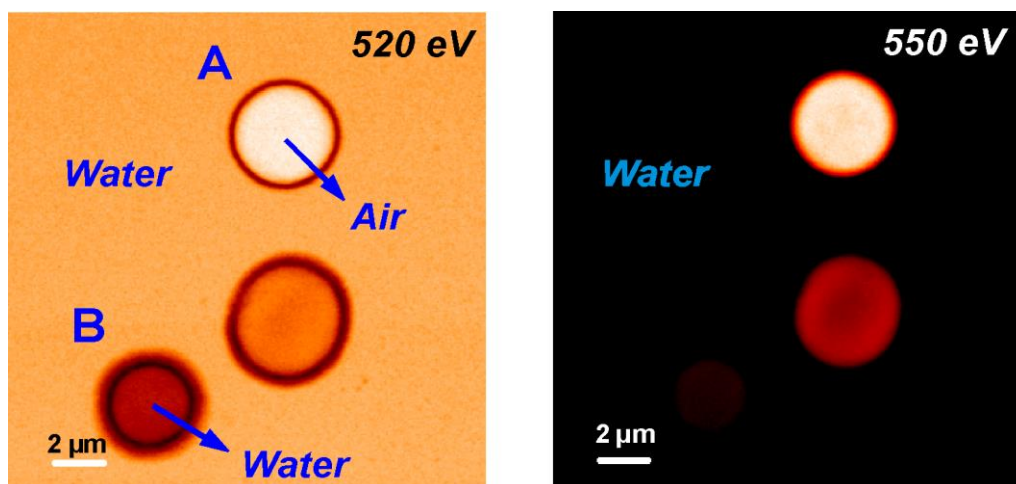


Figure 5-18: STXM transmission images of MBs in water environment recorded at  $h\nu = 520$  eV and  $h\nu = 550$  eV (scanned image size:  $20 \times 20 \mu\text{m}^2$ ).

In order to gain insight into the chemical composition of the interior of the MBs, oxygen *K*-edge NEXAFS spectroscopy was applied. Absorption spectra extracted from line-scans across the inner part of the particles A and B are compared in Figure 5-19. A NEXAFS spectrum taken from a water reference is also shown in Figure 5-19. A reference spectrum of the "water-free" polymeric shell was also obtained after drying the wet cell in the STXM chamber overnight. The oxygen *K*-edge NEXAFS spectrum taken from a microbubble-free volume of the sample exhibits the typical absorption features of liquid water. The water spectrum starts at 535.4 eV followed by the characteristic two-peak broad structure in the energy range of 537–543 eV<sup>39</sup>. The presence of a small feature at about 532 eV is most probably due to some organic contamination in the water (see below). The O *K*-edge spectrum from MB B shows essentially the same resonances as the water spectrum except a small intensity decrease of the feature at 535.4 eV and an intensity increase of the peak at 532.1 eV. This result unambiguously underlines the presence of water inside particle B. In contrast to the spectra of water and particle B, the NEXAFS spectrum of microbubble A demonstrates a line shape which is very similar to the one of a particle in a dry state (see Figure 5-19). The latter two spectra show a strong resonance at 532.1 eV which is assigned to the  $\text{O}1s \rightarrow \pi^*_{(\text{C}=\text{O})}$  transition originating from the carbonyl groups of the telechelic PVA shell. Furthermore, the water peak at 535.4 eV is absent in these spectra while the main  $\text{O}1s \rightarrow \sigma^*$  resonance appears at around 537 eV. Hence, the NEXAFS spectrum of MB A shows only the resonances typical for the telechelic PVA shell. This result strongly suggests that MB A is air-filled. The

STXM images presented in Figure 5-18 corroborate this conclusion. The air in the microbubbles appears much lighter than the water background in the STXM image at 550 eV while the water-filled particle B is indistinguishable at this energy.

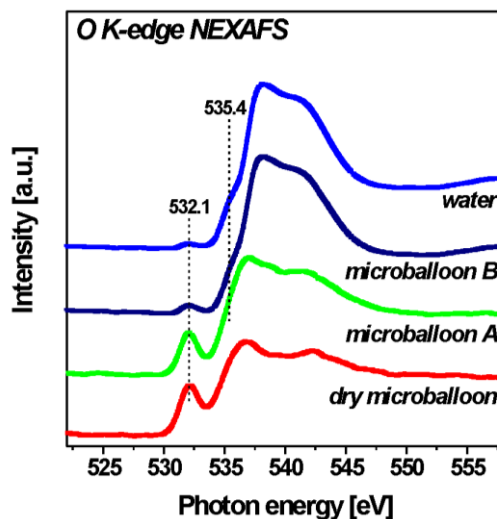


Figure 5-19: Oxygen *K*-edge NEXAFS spectra of the surrounding water, the interior parts of MBs A and B (Figure 5-18), and of another MB analyzed in the completely dehydrated state.

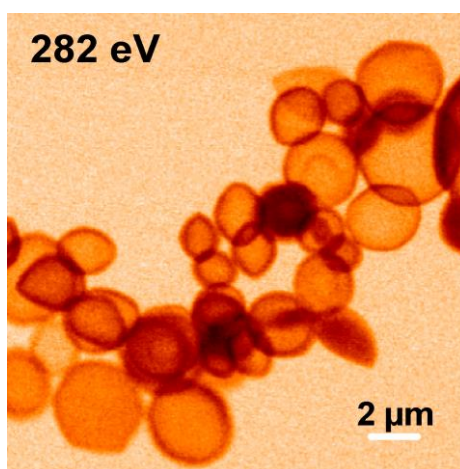


Figure 5-20: STXM transmission image at  $h\nu = 282$  eV of the freeze-dried MBs.

Very recently, a quantitative analysis of the STXM transmittance profiles of the MBs where the X-ray beam resolution and a third order polynomial radial membrane absorption function were taken into account, was reported<sup>40</sup>. In summary, the model is based on the Lambert-Beer expression for the transmitted monochromatic X-rays through a three-component system (encapsulated air, PVA-based shell and the surrounding water in the wet cell) and extends the previous quantitative studies of

water-filled polymeric microcapsules using full-field transmission X-ray microscopy (TXM) <sup>41, 42</sup>. From the proposed fitting procedure the MBs' physical parameters like radius, wall thickness and wall absorption can be determined with unprecedented high resolution. This analytical model opens new applications for quantitative characterization of multicomponent microcapsule materials by means of STXM.

STXM transmission image at 282 eV of freeze-dried PVA-based MBs deposited onto a Si<sub>3</sub>Ni<sub>4</sub> membrane is depicted in Figure 5-20. At this photon energy (below the C1s absorption edge) the contrast in the image originates from the topographical (thickness) differences in the microcapsules. As one see, the image clearly shows the deformed polymeric shells of the dry particles. The MBs were spectromicroscopically characterized after suspending the freeze-dried material in water. STXM images taken at 520 eV and 550 eV of the MBs suspension in a wet cell are shown in Figure 5-21. The changes in the freeze-dried MBs morphology are noticeable as one can see in the image at 520 eV. Furthermore, the contrast variations in the STXM images below and above the O *K*-edge (Figure 5-21) explicitly demonstrates the gas interior of the MBs. There are also several broken shells present (indicated with arrows in Figure 5-21) which are indistinguishable from the water medium in the STXM image at 550 eV.

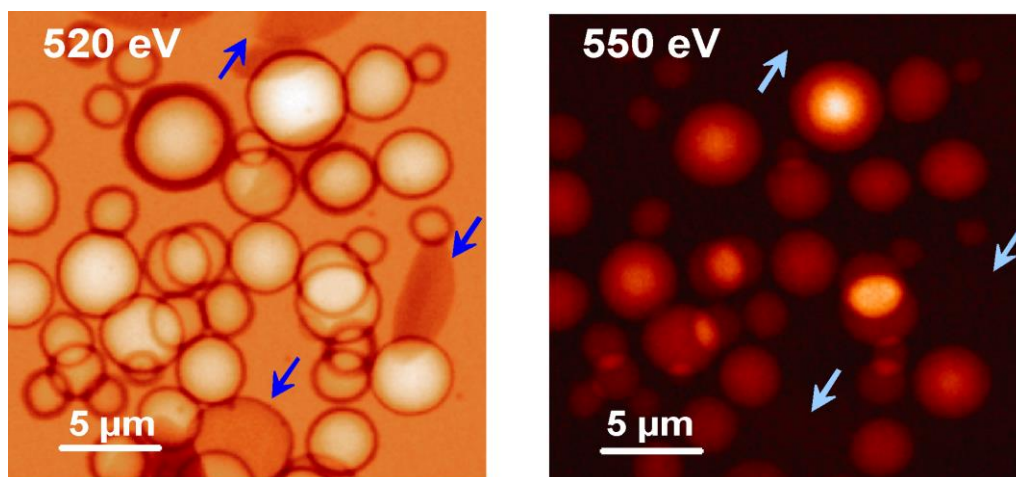


Figure 5-21: STXM transmission images recorded at  $h\nu = 520$  eV and  $h\nu = 550$  eV of freeze-dried MBs suspended in water. The statistical analysis has shown that approx. 80 % of the MBs in the wet cells are air-filled.

The present examples demonstrate the potential of the STXM technique for characterization of microbubble and microcapsule systems. STXM imaging below

and above the oxygen *K*-edge (520 eV and 550 eV) and NEXAFS spectroscopy can provide unique information on the composition of the MBs in water. Furthermore, with STXM it is possible to gain more detailed information on the variations in chemical structure of MBs subjected to external stimuli like temperature, mechanical forces or light irradiation. Thus, the analytical X-ray microscopy might be vital for the development of modern biochemical devices and applications in drug delivery and as ultrasound contrast agents. These first results will be extended to different types of hollow and solvent-filled therapeutic microcapsules.

## References

1. Fery, A.; Weinkamer, R., *Polymer* **2007**, 48, 7221-7235.
2. Binnig, G.; Quate, C. F.; Gerber, C., *Phys. Rev. Lett.* **1986**, 56, (9), 930.
3. Mueller, R.; Kohler, K.; Weinkamer, R.; Sukhorukov, G.; Fery, A., *Macromolecules* **2005**, 38, (23), 9766-9771.
4. Dubreuil, F.; Elsner, N.; Fery, A., *Eur. Phys. J. E* **2003**, 12, (2), 215-221.
5. Elsner, N.; Dubreuil, F.; Weinkamer, R.; Fischer, F. D.; Wasicek, F.; Fery, A., *Prog. Coll. Polym. Sci.* **2006**, 132, 117-132.
6. Fery, A.; Dubreuil, F.; Mohwald, H., *New J Phys* **2004**, 6, 18.
7. Dubreuil, F.; Shchukin, D. G.; Sukhorukov, G. B.; Fery, A., *Macromol. Rapid Commun.* **2004**, 25, (11), 1078-1081.
8. Heuvingh, J.; Zappa, M.; Fery, A., *Langmuir* **2005**, 21, (7), 3165-71.
9. Delorme, N.; Fery, A., *Phys Rev E* **2006**, 74, (3), 3.
10. Delorme, N.; Dubois, M.; Garnier, S.; Laschewsky, A.; Weinkamer, R.; Zemb, T.; Fery, A., *J. Phys. Chem. B* **2006**, 110, (4), 1752-1758.
11. Ducker, W. A.; Senden, T. J.; Pashley, R. M., *Nature* **1991**, 353, (6341), 239-241.
12. Butt, H. J., *Biophys. J.* **1991**, 60, (6), 1438-1444.
13. Hutter, J. L.; Bechhoefer, J., *Rev. Sci. Instrum.* **1993**, 64, (7), 1868-1873.
14. Sader, J. E., *J. Appl. Phys.* **1998**, 84, (1), 64-76.
15. Reissner, E., *Journal of Mathematics and Physics* **1946**, 25, (2), 80-85.
16. Reissner, E., *Journal of Mathematics and Physics* **1946**, 25, (4), 279-300.
17. Koiter, W. T., *A spherical shell under point loads at its poles*. Defense Technical Information Center: **1962**.
18. Raichur, A.; Vorös, J.; Textor, M.; Fery, A., *Biomacromolecules* **2006**, 7, (8), 2331-2336.
19. Elsner, N.; Dubreuil, F.; Fery, A., *Phys Rev E* **2004**, 69, (3), 6.
20. Raedler, J.; Sackmann, E., *Langmuir* **1992**, 8, (3), 848-853.
21. Xia, Y. N.; Whitesides, G. M., *Angewandte Chemie-International Edition* **1998**, 37, (5), 551-575.
22. Wong, C. P., *Polymers for electronic and photonic applications*. Academic Press: **1993**.
23. Kumar, A.; Biebuyck, H. A.; Whitesides, G. M., *Langmuir* **1994**, 10, (5), 1498-1511.
24. Hammond, P. T.; Whitesides, G. M., *Macromolecules* **1995**, 28, (22), 7569-7571.
25. Pretzl, M.; Schweikart, A.; Hanske, C.; Chiche, A.; Zettl, U.; Horn, A.; Boker, A.; Fery, A., *Langmuir* **2008**, 24, (22), 12748-12753.
26. Lu, C. H.; Mohwald, H.; Fery, A., *Soft Matter* **2007**, 3, (12), 1530-1536.
27. Kane, R. S.; Takayama, S.; Ostuni, E.; Ingber, D. E.; Whitesides, G. M., *Biomaterials* **1999**, 20, (23-24), 2363-2376.

28. Kam, L.; Boxer, S. G., *Journal of Biomedical Materials Research* **2001**, 55, (4), 487-495.
29. Howell, S. W.; Inerowicz, H. D.; Regnier, F. E.; Reifenberger, R., *Langmuir* **2003**, 19, (2), 436-439.
30. Saravia, V.; Kupcu, S.; Nolte, M.; Huber, C.; Pum, D.; Fery, A.; Sleytr, U. B.; Toca-Herrera, J. L., *Journal of Biotechnology* **2007**, 130, (3), 247-252.
31. Krol, S.; Nolte, M.; Mazza, D.; Magrassi, R.; Diaspro, A.; Gliozzi, A.; Fery, A., *Langmuir* **2005**, 21, 705.
32. Nolte, M.; Fery, A., *Ieee T Nanobiosci* **2004**, 3, (1), 22-26.
33. Kirz, J.; Rarback, H., *Rev. Sci. Instrum.* **1985**, 56, (1), 1-13.
34. Ade, H.; Hitchcock, A. P., *Polymer* **2008**, 49, (3), 643-675.
35. Ade, H.; Hsiao, B., *Science* **1993**, 262, (5138), 1427-1429.
36. Ade, H.; Zhang, X.; Cameron, S.; Costello, C.; Kirz, J.; Williams, S., *Science* **1992**, 258, (5084), 972-975.
37. Raabe, J.; Tzvetkov, G.; Flechsig, U.; Boege, M.; Jaggi, A.; Sarafimov, B.; Vernooij, M. G. C.; Huthwelker, T.; Ade, H.; Kilcoyne, D.; Tyliczszak, T.; Fink, R. H.; Quitmann, C., *Rev. Sci. Instrum.* **2008**, 79, (11), 113704.
38. Tzvetkov, G.; Graf, B.; Fernandes, P.; Fery, A.; Cavalieri, F.; Paradossi, G.; Fink, R. H., *Soft Matter* **2008**, 4, (3), 510-514.
39. Zubavichus, Y.; Zharnikov, M.; Yang, Y. J.; Fuchs, O.; Heske, C.; Umbach, E.; Tzvetkov, G.; Netzer, F. P.; Grunze, M., *J. Phys. Chem. B* **2005**, 109, (2), 884-891.
40. Fernandes, P. A. L.; Delcea, M.; Skirtach, A. G.; Moehwald, H.; Fery, A., *Soft Matter* **2010**, 6, (9), 1879-1883.
41. Dejugnat, C.; Koehler, K.; Dubois, M.; Sukhorukov, G. B.; Moehwald, H.; Zemb, T.; Guttman, P., *Adv. Mater.* **2007**, 19, (10), 1331-1336.
42. Koehler, K.; Dejugnat, C.; Dubois, M.; Zemb, T.; Sukhorukov, G. B.; Guttman, P.; Moehwald, H., *J. Phys. Chem. B* **2007**, 111, (29), 8388-8393.



## 6. On the interplay of shell structure with low and high frequency mechanics of multifunctional magnetic microbubbles

*Melanie Poehlmann<sup>a</sup>, Dmitry Grishenkov<sup>b,c</sup>, Satya V.V.N. Kothapalli<sup>b</sup>, Johan Härmärk<sup>d,e</sup>, Hans Hebert<sup>d,e</sup>, Alexandra Philipp<sup>a</sup>, Roland Hoeller<sup>a</sup>, Maximilian Seuss<sup>a</sup>, Christian Kuttner<sup>a</sup>, Silvia Margheritelli<sup>f</sup>, Gaio Paradossi<sup>f</sup>, Andreas Fery<sup>\*a</sup>*

<sup>a\*</sup> Department of Physical Chemistry II, University of Bayreuth, Universitätsstraße 30, DE-95440 Bayreuth, Germany. Fax: +49 (0)921 552059; Tel: +49 (0)921 552751; E-mail: andreas.fery@uni-bayreuth.de

<sup>b</sup> Division of Medical Engineering, School of Technology and Health, KTH, Royal Institute of Technology, Sweden.

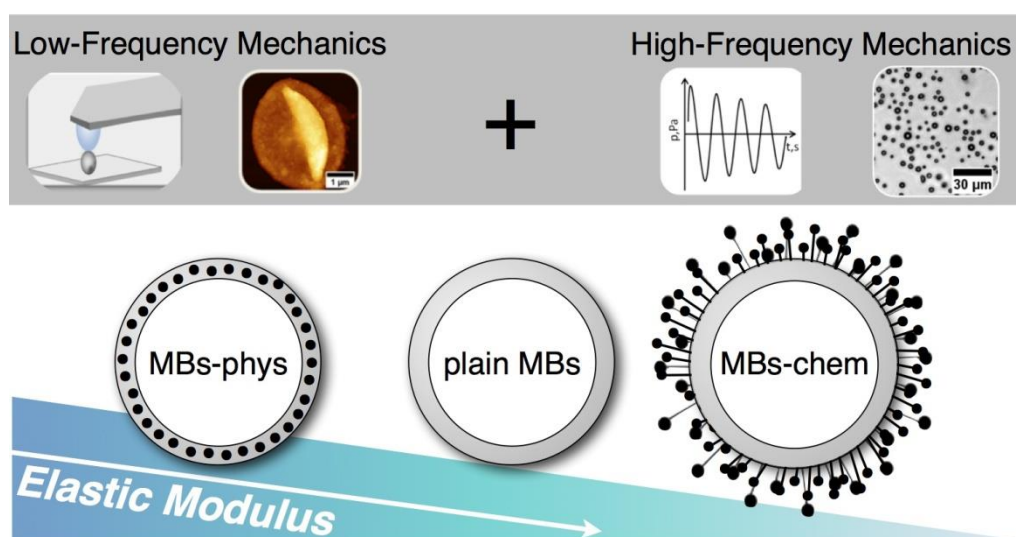
<sup>c</sup> Karolinska Institute, Department of Clinical Science, Intervention and Technology, Huddinge, Sweden.

<sup>d</sup> Division of Structural Biotechnology, School of Technology and Health, KTH, Royal Institute of Technology, Sweden.

<sup>e</sup> Karolinska Institute, Department of Biosciences and Nutrition, Huddinge, Sweden.

<sup>f</sup> Department of Chemical Sciences and Technologies, University of Rome Tor Vergata, Rome, Italy.

Published in Soft Matter



## **Abstract**

Polymer-shelled magnetic microbubbles have great potential as hybrid contrast agents for ultrasound and magnetic resonance imaging. In this work, we studied US/MRI contrast agents based on air-filled poly(vinyl alcohol)-shelled microbubbles combined with superparamagnetic iron oxide nanoparticles (SPIONs). The SPIONs are integrated either physically or chemically into the polymeric shell of the microbubbles (MBs). As a result, two different designs of a hybrid contrast agent are obtained. With the physical approach, SPIONs are embedded inside the polymeric shell and with the chemical approach SPIONs are covalently linked to the shell surface. The structural design of hybrid probes is important, because it strongly determines the contrast agent's response in the considered imaging methods. In particular, we were interested how structural differences affect the shell's mechanical properties, which play a key role for the MBs' US imaging performance. Therefore, we thoroughly characterized the MBs' geometric features and investigated low-frequency mechanics by using atomic force microscopy (AFM) and high-frequency mechanics by using acoustic tests. Thus, we were able to quantify the impact of the used SPIONs integration method on the shell's elastic modulus, shear modulus and shear viscosity. In summary, the suggested approach contributes to an improved understanding of structure–property relations in US-active hybrid contrast agents and thus provides the basis for their sustainable development and optimization.

## 6.1 Introduction

Hybrid imaging offers new diagnostic and therapeutic procedures and pushes the development of novel multifunctional contrast agents.<sup>1-10</sup> The successive use of ultrasound (US) and magnetic resonance imaging (MRI) is standard in today's clinical routine, because they show complementary information and operate without ionizing radiation. Hence, it is not surprising that a combination of both modalities for hybrid imaging is in sight.<sup>11-14</sup>

There exist difficult and specific imaging situations where conventional US and/or MRI imaging is limited and enhanced contrast is required.<sup>15</sup> Therefore, contrast agents are used such as gas-filled microbubbles (MBs) to enhance the US signal<sup>15-17</sup> and paramagnetic complexes or superparamagnetic nanoparticles to enhance the MRI signal<sup>18-20</sup>. Novel emerging diagnostics and therapies plus well-established imaging procedures give good reasons for the growing interest in producing adequate hybrid contrast agents visible in both modalities.<sup>21-26</sup> The major challenges in developing new US/MRI contrast agents are the different functional requirements that hybrid probes need to match. For US/MRI imaging hybrid probes need a sufficient stability during the circulation in the cardiovascular system<sup>27</sup>, an adequate US echo signal<sup>28</sup> and a reasonable reduced relaxation time of nearby located protons<sup>29</sup>. All these requirements have a direct impact on the structural design of the probes. For example, the upper size is limited to about 7  $\mu\text{m}$ <sup>27</sup>, because the contrast agent needs to pass capillary beds within the cardiovascular system. As lower size limit 100 nm are recommended to avoid any leakage through the endothelium and a response from the immune system.<sup>30-33</sup> However, the particle diameter or more precise the gas volume trapped inside the particles also matters for the acoustic response.<sup>27</sup> For basic applications like Doppler imaging a backscatter signal value of about 20 dB is needed.<sup>34</sup> Moreover, the contrast agent requires enough stability to cross the pulmonary capillary bed and facilitate adequate imaging times. A common solution to increase the MBs' stability is the use of water-low-soluble gases that are encapsulated by shells made of lipids, proteins or polymers.<sup>35-37</sup> On the one hand, the shell provides the platform for further functionalizations of ultrasound responsive MBs to hybrid probes and thus is a crucial design element. For US/MRI contrast, the shell is used for the integration of magnetic complexes or nanoparticles.<sup>10, 26, 38, 39</sup> On the other hand, the shell is also a well-known drawback for the acoustic response,

because it decreases of the backscatter signal, depending on the shell material and shell thickness.<sup>28, 40</sup> With regard to the final imaging performance of multimodal contrast agents all these different structural elements need to be considered and adjusted during the production of the probes. Therefore, we believe that a straightforward analysis of structure-property relations is essential when hybrid contrast agents are developed or optimized

In the focus of this study are recently presented<sup>23</sup> US/MRI contrast agents, which have as common feature a 3  $\mu\text{m}$  sized air-bubble stabilized by a shell made of poly(vinyl alcohol) (PVA).<sup>41, 42</sup> In this article a microbubble without any magnetic nanoparticles is referred to as *plain MB* as sketched in Figure 6-1.

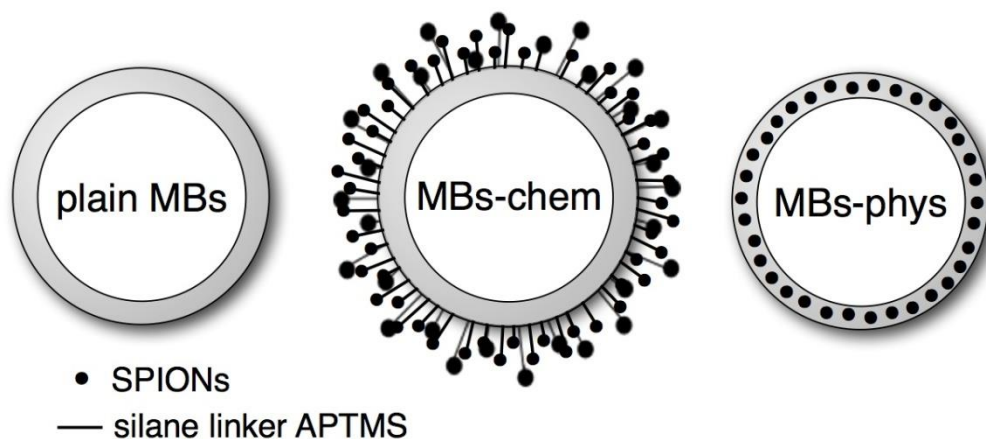


Figure 6-1: Schematic of plain MBs (MBs without SPIONs), MBs-chem with SPIONs covalently attached to the shell surface and MBs-phys with SPIONs physically embedded inside the shell.

Plain MBs are already well characterized regarding the option to carry therapeutic gases<sup>42, 43</sup> and the possibility to introduce molecules relevant for targeting or drug delivery<sup>44</sup>. Moreover, for plain MBs the echogenicity<sup>45-48</sup>, the biocompatibility<sup>49</sup> and cytotoxicity<sup>50</sup> were studied. Magnetic MBs were obtained either by physical or chemical integration of superparamagnetic iron oxide nanoparticles (SPIONs) to the plain MBs. The physical method<sup>51</sup> yields MBs with SPIONs embedded inside the shell, which are referred in this work as *MBs-phys*. The chemical approach<sup>23</sup> yields MBs with SPIONs attached covalently to the shell surface, referred to as *MBs-chem*. Recently, we reported on the synthesis process, weight percent of integrated SPIONs and US- and MR-imaging properties of these particles.<sup>23</sup> The magnetic properties of the particles were studied in vitro using a SQUID system showing a higher net

magnetization for MBs-phys compared to MBs-chem. The change in magnetization was attributed to different aggregation states of the SPIONs in the two samples. In vivo, magnetic properties were tested in rats for proof of concept by using clinical MRI equipment. These experiments were analyzed regarding spin-spin relaxation times and rates for different tissues.

This work focuses on mechanical properties of the MBs, which play a key role for their final performance in ultrasound imaging. In particular, we were interested if the SPIONs-integration method has an impact on the MB's low and high frequency mechanics. To bridge the gap between the contrast agents' synthesis and its final performance, a straightforward analysis of structure-property relations is crucial. Therefore, we first studied the influence of the methods on basic geometric properties, such as MB diameter and shell thickness. In the next step, the mechanical properties in the low and high frequency regime (low:2 Hz, high: 2-14 MHz) were studied. Low frequency experiments were performed with quasi-static force measurements of single microbubbles using atomic force microscopy (AFM). Sboros and co-workers<sup>52-55</sup> already showed that AFM is a useful tool to study the mechanical properties of hard-shelled ultrasound contrast with a bilayer shell made of albumin and polylactide. Recently, AFM force spectroscopy experiments were successfully used for the characterization of phospholipids-shelled MBs.<sup>56-58</sup> High frequency mechanics of the US/MRI contrast agent were investigated by exposure of an ensemble of MBs to an acoustic field.<sup>59, 60</sup> As a results we obtained the elastic modulus of the shell materials from low frequency mechanics and the shear modulus of the shell material from high frequency mechanics. This straightforward characterization of ultrasound contrast agents contributes to an improved understanding of structure/property relations and offers the possibility for a sustainable design of hybrid contrast agents.

## 6.2 Materials and methods

**Materials.** Iron chloride hexahydrate ( $\text{FeCl}_3 \cdot 6\text{H}_2\text{O}$ , purity>99%), iron chloride tetrahydrate ( $\text{FeCl}_2 \cdot 4\text{H}_2\text{O}$ , purity>99%), rhodamine B isothiocyanate (RBITC), (3-aminopropyl) trimethoxysilane (APTMS), sodium cyanoborohydride ( $\text{NaBH}_3\text{CN}$ ), and sodium (meta)periodate ( $\text{NaIO}_4$ ) were products from Sigma Aldrich, Milan, Italy. Low molecular weight chitosan (CHIT), with a Brookfield viscosity of 20,000 cP,

number-average molecular weight of  $50,000 \pm 5,000$  g/mol, and poly(vinyl alcohol) (PVA) with a number-average molecular weight of  $30,000 \pm 5,000$  g/mol determined by membrane osmometry and mass-average molecular weight of  $70,000 \pm 10,000$  g/mol determined by static light scattering, were purchased from Sigma-Aldrich, Milan, Italy. An acetylation degree of chitosan of 15% (mol/mole repeating units) was determined by  $^1\text{H}$  NMR at 300 MHz (Bruker Advance, Germany). Inorganic acids and bases were reagent grade products from Carlo Erba, Milan, Italy. Milli-Q water with purity grade 18.2 M $\Omega$ /cm was produced with a deionization apparatus (PureLab, Steroglass, PG, Italy).

**Synthesis of SPIONs.** SPIONs ( $\text{Fe}_3\text{O}_4$ ) with an average particle diameter of 8-10 nm were prepared using controlled co-precipitation described previously.<sup>23</sup> Briefly, 5 ml of an aqueous solution of 1 M  $\text{FeCl}_3 \cdot 6\text{H}_2\text{O}$ , 0.5 M  $\text{FeCl}_2 \cdot 4\text{H}_2\text{O}$ , and 0.4 M HCl were added under vigorous mechanical stirring (2,000 rpm) to 50 ml of 0.5 M NaOH. After heating the alkaline solution to 80°C, the reaction was carried out for 30 min under  $\text{N}_2$  atmosphere to prevent oxidation. The particles were collected by sedimentation with the help of a large magnetic stirring bar, washed with degassed water and ethanol, and dried in vacuum. For the coupling of SPIONs with non-reacted aldehyde groups available on the MB surface, amino groups were introduced to the SPIONs' surface via silanization. Therefore, 100 mg of SPIONs were washed with methanol (20 ml), then with a mixture of methanol and toluene (20 ml; 1:1, v/v), and finally with toluene alone (20 ml). SPIONs were then dispersed into 20 ml toluene. APTMS [0.5 ml, 3 mM, in a methanol/toluene (1:1, v/v) mixture] was added to the SPION suspension, followed by a further reflux of the suspension at 110°C for 24 h under a  $\text{N}_2$  flow and vigorous stirring. The modified particles were magnetically collected, washed three times with methanol and vacuum dried.

**Synthesis of plain MBs.** The synthesis was already previously reported by Cavalieri et al.<sup>41</sup> Briefly, sodium metaperiodate was added to an aqueous PVA solution (2% w/v) to selectively split vicinal hydroxyl groups. Shorter chains of PVA with aldehydes as terminal groups were obtained. An acetalization reaction between aldehyde and hydroxyl groups present in the PVA chains was carried out at a pH of 5.5 and room temperature under high shear stirring, using an Ultra-Turrax T-25 (IKA, Germany) equipped with a Teflon tip, at 8,000 rpm for 2 hours. Master concentration received for evaluation is  $1.4 \times 10^8$  MB/mL.

**Synthesis of magnetic *MBs-chem*.** For the coupling of SPIONs to the plain MBs' shell typically a weight ratio between plain MBs and silanized SPIONs of 1:2 (w/w) was used. First SPIONs were sonicated for 90 min in an US bath ("Ultrasound cleaner", CP104, CEIA, Italy). Then 20 mg/ml SPIONs were added to 10 mg of plain MBs. The reductive amination was carried out at a pH of 5.0 with NaBH<sub>3</sub>CN. The suspension was gently shaken for five days and washed with Milli-Q water. Chitosan oxidation was carried out by dissolving the polymer in water at a concentration of 1% (w/v) at pH 5.5, oxidizing the C2 and C3 carbons of the chitosan-repeating unit for 1 day with NaIO<sub>4</sub> (feed molar ratio GlcN/NaIO<sub>4</sub> 1:0.5, where GlcN indicates the glucosamine-repeating unit in the chitosan chain). Following conjugation with silanized SPIONs, the oxidized-repeating units of chitosan are coupled to hydroxyl groups of the PVA shells by mixing a dispersion of 5 mg of MBs with 13 mL of the chitosan solution. Master concentration received for evaluation is  $1.75 \times 10^8$  MB/ml. The amount of SPIONs was analyzed with thermogravimetric analysis (TGA) and found to be 29 w/w% for MBs-chem.<sup>23</sup>

**Synthesis of magnetic *MBs-phys*.** Unmodified SPIONs were physically embedded in the shell by exploiting the favorable interaction between iron oxide nanoparticles and PVA.<sup>51</sup> Briefly, SPIONs were suspended in water at a concentration of 5 mg/ml and sonicated 90 min in an ultrasonic bath (see above). 20 mg/ml SPIONs were added during the PVA shell formation. The rest of the synthesis is according the synthesis of plain MBs. Master concentration received for evaluation is  $4 \times 10^8$  MB/ml. The amount of SPIONs was analyzed with TGA and found to be 15 w/w% for MBs-phys.<sup>23</sup>

**Optical Microscopy.** A sample of MBs was inserted in a Neubauer Chamber improved from Carl Roth, Germany. Images of the floating MBs were obtained under Koehler illumination with an Axiovert 200 (Plan Neofluar Objective, 20x/0,50 Ph2) using high-resolution monochrome camera (AxioCam HRm) from Carl Zeiss AG, Germany. The resolution of the pictures was 1300 x 1030 pixels. To determine the size distribution the images were further analyzed with ImageJ software<sup>61</sup>. First, the brightness and contrast of the images were automatically corrected and then a binary with automated threshold was made. To analyze the particle distribution without

particles and to neglect bigger PVA residuals from the synthesis, for the analysis of particles a diameter range between 0.5  $\mu\text{m}$  and 8  $\mu\text{m}$  was chosen for the further evaluation.

**Transmission Electron Microscopy.** With TEM (CEM 902, Carl Zeiss AG, Germany) thin sections of about 50 nm to 60 nm, produced by an ultracut microtome (EM UC7, Leica Mikrosysteme Vertrieb GmbH, Germany), were imaged at 80 kV. The shell thickness was obtained from TEM images by extracting cross-sectional gray value profiles that were analyzed with ImageJ software<sup>61</sup>. The start/end of the shell was determined at 50% decrease/increase of the gray value intensity. TEM samples were prepared by mixing the capsule solution in a 1:1 ratio with 2% aqueous solution of agar (Agar Noble, Difco, USA). After curing, the flexible gel was cut with a scalpel into small cubes. Next, the agar-embedded capsules were solidified by one hour incubation with a 2% glutaraldehyde solution (Serva Electrophoresis GmbH, Germany) in phosphate buffer (0.05 M phosphate buffer, pH 7.4 Merck KGaA, Germany). Afterwards three washing steps with phosphate buffer were used to remove the excess of glutaraldehyde. Then the samples were dehydrated in ethanol-water mixtures with increasing ethanol content (30%/ 50%/ 70%/ 95%) and three times to plain ethanol (VWR International GmbH, Germany). The dehydration exposure time was 15 minutes for each step. The dried samples were then mixed with Epon 812 (Serva Electrophoresis GmbH, Germany): Epon 812/ethanol mixture (1:1) for 12 hours, followed by an Epon 812/ethanol mixture (3:1) for 3-4 hours and finished with three immersion steps (3-4 hours) in 100% Epon 812.

**Atomic Force Microscopy-imaging.** Gas-filled polymer MBs was imaged with an AFM Nanowizard I (JPK Instruments AG, Germany) mounted on a transmission microscope (Axiovert 200, Carl Zeiss AG, Germany). Prior to the measurement MBs were exposed 20 min to an ultrasonic bath at room temperature. This treatment leads to a replacement of the gas-filled core by the surrounding water. Water-filled particles will fold flat upon drying on a substrate. MBs were dried for 15 minutes in vacuum at 60°C. After the sample preparation, MBs were directly imaged with AFM. Dried MBs were imaged in intermittent modus with rectangular cantilevers purchased from Atomic Force, Germany (Olympus, OMCL-AC160TS (OTESPA),  $f=300$  kHz,  $k=42$  N/m). To determine the shell thickness of hydrated MBs, the dried and imaged MBs were immersed for 30 minutes in purified water (Millipore Advantage, Merck

AG, Germany). 30 min were enough to ensure a hydration state that did not affect any more the measured height of the MBs. Hydrated MBs were imaged in aqueous solution and in contact mode (CSC17, Mikromasch, Estonia,  $f= 12$  kHz,  $k= 0,15$  N/m). The height images were used to extract four cross section profiles by a standardized analysis with the commercial available AFM software JPK Data Processing.

**Atomic Force Microscopy-Force Spectroscopy.** The deformation behaviour of MBs was measured in force spectroscopy experiments with the same AFM used for imaging (Nanowizard I, JPK Instruments AG, Germany). Prior to calibration tipless cantilevers (CSC12, MikroMasch, Estonia,  $f= 75$  kHz,  $k = 0.60$  N/m) were cleaned in air plasma (5 min, Mini Flecto, Plasma Technology GmbH, Germany). Then the inverse optical lever sensitivity (InvOLS) was determined on a hard substrate at least at three different spots with a reasonable displacement of the cantilever ( $\sim 1$   $\mu\text{m}$ ), which is needed to fit the linear regime and read out the InvOLS in V/nm. With thermal noise<sup>62</sup> the spring constant of the cantilevers were determined. Colloidal probes<sup>63</sup> ( $\sim 40$   $\mu\text{m}$ , glass beads, Polyscience Europe GmbH, Germany) were attached with the help of a micromanipulator (MP-285, Sutter Instrument Co., CA, USA) to the cantilever tip with an epoxy glue (UHU plus endfest 300, UHU GmbH & Co KG, Germany). Prior to the MB deformation experiments, the colloidal probe cantilevers were cleaned for 5 minutes in air-plasma.

**Acoustic characterization.** The experimental setup used to assess the acoustic properties of the MBs suspension was already described elsewhere<sup>46</sup>. In brief, a flat transducer with nominal frequency  $f= 10$  MHz and -20 dB bandwidth ranges between 2.55 MHz and 14.5 MHz is used. An aluminium block, which is positioned 1 cm after the sample container, is used as a reflector. Within the near-field length ( $D^2/(4\lambda)=280$  mm, where  $D$  is the diameter of the transducer crystal, and  $\lambda$  is the ultrasound wavelength in the medium of propagation), this transducer produced a pressure field with a peak negative pressure not larger than 20 kPa. The peak negative pressure was assessed by PVdF 75  $\mu\text{m}$  needle hydrophone (Precision Acoustics Ltd., Dorchester, Dorset, UK). More information on the determination of the attenuation coefficient can be found in the supplementary information.

**Microbubble concentration.** It was previously reported<sup>23</sup> that acoustic efficiency, i.e. backscattered power, is proportional to the number of scatterers (here MBs) in the suspension if the excitation is performed below the resonance frequency and multiple scattering is disregarded. As a result, we propose to evaluate all types of MBs at three different concentrations: low, intermediate and high concentration. For plain MBs the concentrations were  $1.75 \times 10^5$  MB/ml,  $8.75 \times 10^5$  MB/ml and  $1.75 \times 10^6$  MB/ml. For MBs MBs-chem concentrations of  $4.37 \times 10^5$  MB/ml,  $8.75 \times 10^5$  MB/ml and  $1.75 \times 10^6$  MB/ml were used. And for MBs Type B concentrations of  $5 \times 10^5$  MB/ml,  $1 \times 10^6$  MB/ml,  $2 \times 10^6$  MB/ml were considered. Minor discrepancies between the number of bubbles taken for each investigation is attributed to the fact that dilution rate was kept constant among all tests while the master solution arrived at different initial concentrations.

**Differential scanning calorimetry.** The crystallinity of PVA was investigated using a TAQ200 (Waters, Milan, Italy) differential scanning calorimeter (DSC). A known amount of 2-3 mg of lyophilized MBs was sealed in an aluminum pan. The scans were performed from 50 °C to 250 °C at heating and cooling rates of 10 °C/min under a flux of 50 mL/min of dry N<sub>2</sub>. Data were collected after the first reference thermal cycle.

## 6.3 Results and Discussion

### 6.3.1 Geometrical dimensions of magnetic MBs

PVA-shelled MBs have a diameter of about 3  $\mu\text{m}$  as shown in the optical micrograph and the corresponding size distribution in Figure 6-2. Optical micrographs are useful for quality control and to estimate roughly the average diameter of the MBs.

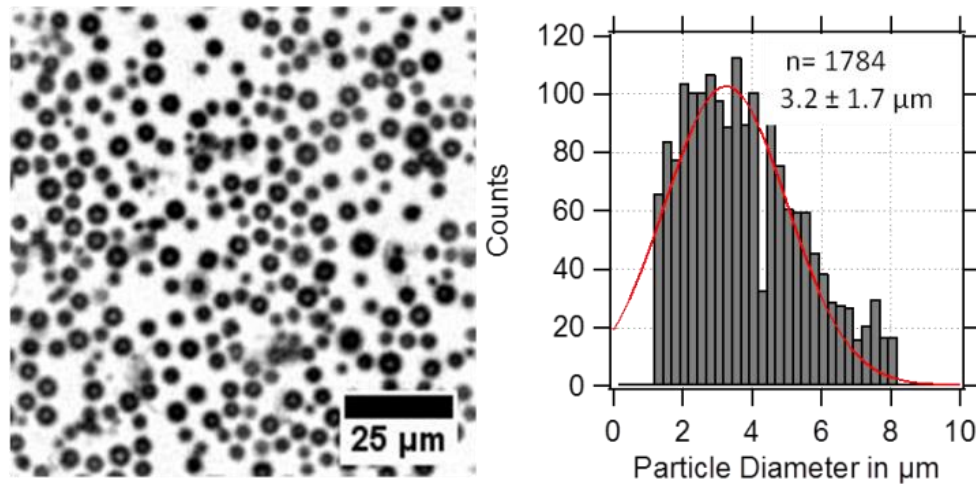


Figure 6-2: Optical micrograph of US/MRI contrast agent (MBs-phys) dispersed in water with the corresponding size distribution.

However, the obtained size distributions do not only represent the MBs' size dispersity but as well include the deviation caused by the error of the method. In the case of gas-filled MBs, the particles are floating at the water-air interface and can move in  $x$ ,  $y$  and  $z$ -direction. Thus, the obtained standard deviation broadens due to MBs that appear smaller by moving out of the focusing plane or appear bigger by overlapping with other MBs in different planes.

To model low- and high-frequency mechanics the MBs' diameter, shell thickness and the corresponding standard deviations are of paramount importance. Therefore, a method is required that enables precise information about the dispersity of both parameters. With AFM imaging the simultaneous characterization of diameter and shell thickness is possible, with a sufficient high resolution in the relevant micrometer and nanometer range.

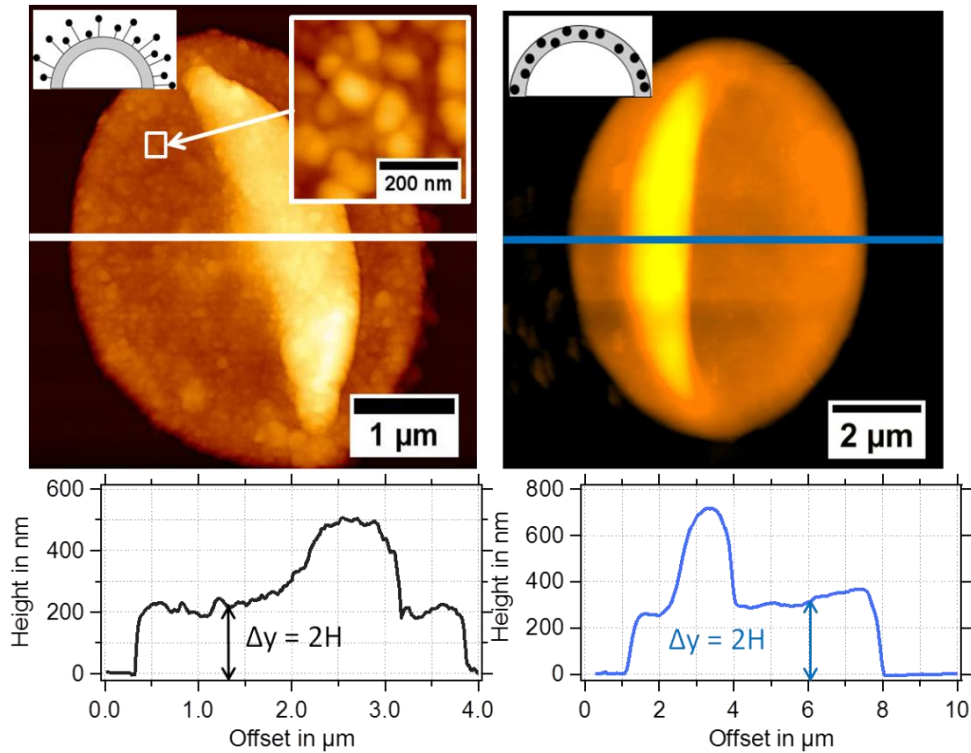


Figure 6-3: AFM height images of magnetic MBs with the corresponding extracted height profiles: (left) MBs-chem with SPIONs on the shell surface and (right) MBs-phys with SPIONs inside the shell.

In Figure 6-3 typical AFM height images of dried magnetic MBs are shown. Important for the determination of the shell thickness is a flat folded topography of the MB. This is realized by removal of the gas-core through a vacuum drying process, which is described in detail in the experimental part. For flat folded MBs we expect the shell thickness  $h$  to refer to half of the measured height  $y$ , as depicted in the cross sectional profiles in Fig 6-3. The diameter  $d_s$  of the spherical MBs was estimated from the surface area  $A_f$  of the flat folded MBs by assuming that the surface area of the spherical MB  $A_s$  is approximately twice the surface area of the flat folded MB  $A_f$  and twice the area of the folds  $A_{\text{fold}}$ .

$$A_s \approx 2A_f + 2A_{\text{fold}}; \quad d_s = \sqrt{\frac{2A_f + 2A_{\text{fold}}}{\pi}}$$

In Figure 6-4 the shell thickness of the individual studied MBs is plotted against their corresponding diameter. The scatter plot illustrates that the thickness does not depend on the MB diameter. The obtained shell thicknesses scatter around a mean value. Based on this result we conclude that the geometric dimensions of the magnetic MBs

did not change through the modification with magnetic nanoparticles and are the same for all three samples.

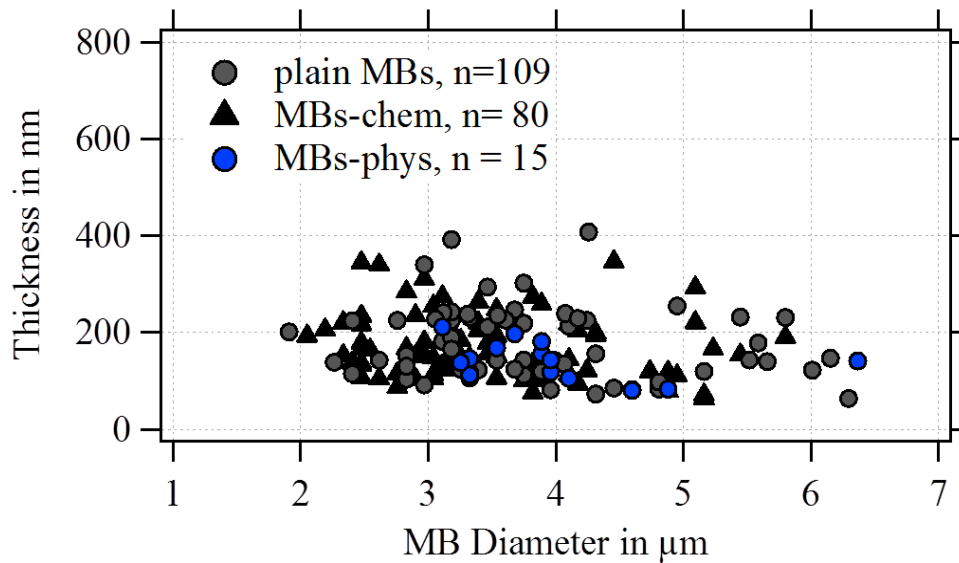


Figure 6-4: Thickness plotted versus the radius of the MBs imaged with AFM in dried conditions.

Thus, plain MBs, MBs-chem and MBs-phys were summarized for the statistical analysis of the shell thickness and the diameter, shown in the histogram in Figure 6-5. The average diameter of the MBs is of about  $3.5 \mu\text{m} \pm 0.8 \mu\text{m}$  and the average shell thickness of about  $150 \text{ nm} \pm 60 \text{ nm}$  for the dried shell. Detailed values for the statistical median and the peak value of the gauss distribution with their corresponding standard deviations are given in Table 6-1. An important result from the analysis of the geometrical parameters is that both shell thickness and diameter have a certain polydispersity. To interpret realistically force spectroscopy results and minimize uncertainties during analysis the in situ determination of the MBs on the single particle with optical microscopy during force spectroscopy experiments is essential. However, the shell thickness is not accessible in situ and an average value needs to be considered.

In addition to geometric parameters, the AFM images contain information about the MBs' surface structure. The inset in Figure 6-3 indicates an increased roughness of the shell surface for MBs-chem compared to MBs-phys, caused by the SPIONs and SPIONs aggregates on the shell surface.

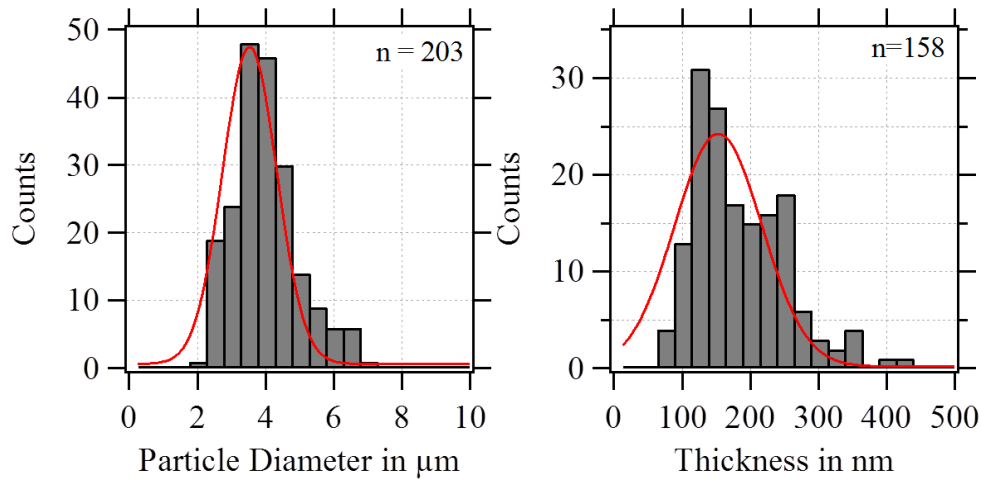


Figure 6-5: Diameter and shell thickness distribution of plain, MBs-chem and MBs-phys

Shells made of telechelic PVA are known to be responsive towards water and are described as hydrogel-like material. Previous studies with Scanning Transmission X-ray Microscopy (STXM) indicate a shell composition of 20% PVA and 80% water.<sup>64, 65</sup> STXM images were also used to estimate the shell thicknesses of three individual MBs in water. As a result, the authors found thickness values of 380 nm, 560 nm and 630 nm.<sup>66, 67</sup> Tzvetkov et al<sup>68</sup> showed that the both thickness and shell composition were maintained after the MBs experienced a drying step. In this study, we analyzed the change of the MBs' shell thickness from dried to hydrated condition. Therefore, dried MBs were exposed to aqueous solution and subsequent imaged with AFM in solution as described in the experimental part. A percental increase of the shell thickness  $H_{\text{increase}}$  of about 45% was observed, which refers to a shell thickness of about  $250 \text{ nm} \pm 127 \text{ nm}$  calculated with the Equation 2:

$$H_{\text{increase}} = 100 \frac{(H_{\text{H}_2\text{O}} - H_{\text{dried}})}{H_{\text{H}_2\text{O}}} \quad (2)$$

This result is in very good agreement with reported STXM<sup>67</sup> and cryo-TEM<sup>68, 69</sup> results. A summary of diameter and shell thickness values measured with different methods in this study and in previous work is reported in Table 6-1

Table 6-1: Diameter and shell thickness values determined with different methods.

<i>Method (diameter)</i>	<i>AFM</i>	<i>Optical</i>	<i>Confocal</i>	
dried-state ( $\mu\text{m}$ )	$3.5 \pm 1.1$	-	-	
in solution ( $\mu\text{m}$ )	$3.6 \pm 1.3$	$3.2 \pm 1.7$	$4.1 \pm 0.6^*$	
<i>Method(shell thickness)</i>	<i>AFM</i>	<i>STXM</i> <sup>67</sup>	<i>Cryo-TEM</i>	<i>TEM</i>
Dried-state (nm)	$152 \pm 90$	-	-	-
In solution (nm)	$215 \pm 133$	$523 \pm 128$	$200^{68}, 400^{69}$	206

Because the shell thickness is a very important parameter for the MBs' mechanical properties and the acoustic behavior, we used TEM as a complementary method to validate the results obtained from AFM. In our previous paper<sup>23</sup> TEM was successfully used to localize the SPIONs within the thin sections of magnetic MBs. SPIONs can be easily recognized as dark spots in the TEM images, because iron atoms have a high electron density. In Figure 6-6, SPIONs are located around the shell surface of MBs-chem and inside the polymer shell for MBs-phys. In addition, the spherical PVA shell can be clearly differentiated from the surrounding resinous matrix (EPON) in which MBs were embedded.

From contrast-corrected images, as described in Figure 6-13, cross sectional radial profiles of the gray value intensity were used to determine the shell thickness (see Figure 6-6). The edges of the shell are assumed to be at  $\pm 50\%$  change of the gray scale value of the PVA/EPON interface. However, the random slicing process will affect the measured shell thickness  $h_i$  and the measured radii  $r_i$ . Hence sections, which are derived from an increasing distance from the MB's center, will provide larger shell thicknesses and smaller radii compared to the true values. A model based on Smith's correction approach<sup>70</sup> was used to derive a correction factor for the measured shell thickness. The correction considers the diameter and thickness distributions

obtained from the TEM images and the probability of the slicing angle. Further details can be found in the Supporting Information.

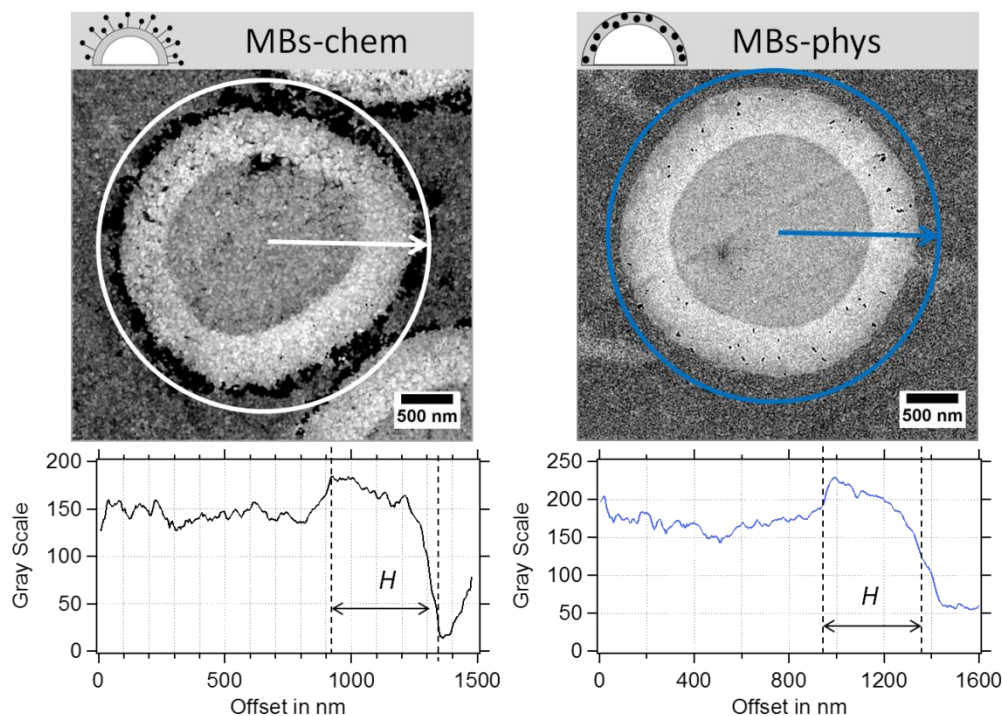


Figure 6-6: Ultrathin sections of magnetic MBs MBs-chem and MBs-phys imaged with TEM and the corresponding radial profiles of the gray value intensity.

MBs with a plain PVA shell indicated a mean thickness of about 300 nm. For the magnetic MBs very similar thickness distributions were obtained that did not significantly differ from plain MBs. As correction factor, we calculated a value of 0.72 for the investigated samples. Based on the found correction factor the true shell thickness is expected to be about 190 nm to 230 nm, which is in good accordance with the results obtained in the AFM experiments and the results reported in literature.

In conclusion, we know that the shell thickness ranges between 120 nm and 380 nm and that we have to expect a certain dispersity in the shell thickness.

### 6.3.2 Mechanical characterization with AFM

Sboros and co-workers<sup>52-55</sup> already made clear that the geometric dimensions and mechanical properties of MBs are crucial for the prediction of the MBs' acoustic behaviour, and that AFM is a useful tool to study the mechanical properties of

ultrasound contrast agents (UCAs) in force-deformation experiments. Their focus was mainly on hard-shelled UCAs with a shell made of a bilayer of albumin and polylactide. Recently, AFM force spectroscopy experiments were successfully used for the characterization of phospholipids-shelled MBs.<sup>56-58</sup> One distinctive feature compared to previous mechanical studies on UCAs is the detailed characterization of our investigated system regarding the mechanical key parameters: diameter, shell thickness, and size dispersity. Furthermore, the probe used for the quasi-static deformation of UCAs in the low frequency regime differs. Instead of a sharp tip we used a colloidal probe setup<sup>63</sup>, which is well established for mechanical tests on artificial microcapsules<sup>71-74</sup>. One practical advantage of a colloidal probe setup for mechanical tests of core/shell particles is an easy and optimal alignment of probe and sample. In addition, a defined contact area is obtained and local probing or indentation is avoided. In Figure 6-7, the inset sketches the used setup. The colloidal probe' diameter is about 30  $\mu\text{m}$  and thus about one magnitude larger than the investigated MBs. To test the mechanical response of the MB's shell material we carried out small deformations on the order of the hydrated shell thickness, referring to deformations smaller than 250 nm. For larger deformations, we expect a stretching and thinning of the shell due to an increasing gas volume within the gas-tight MBs, which will lead to additional restoring forces.<sup>72, 75</sup>

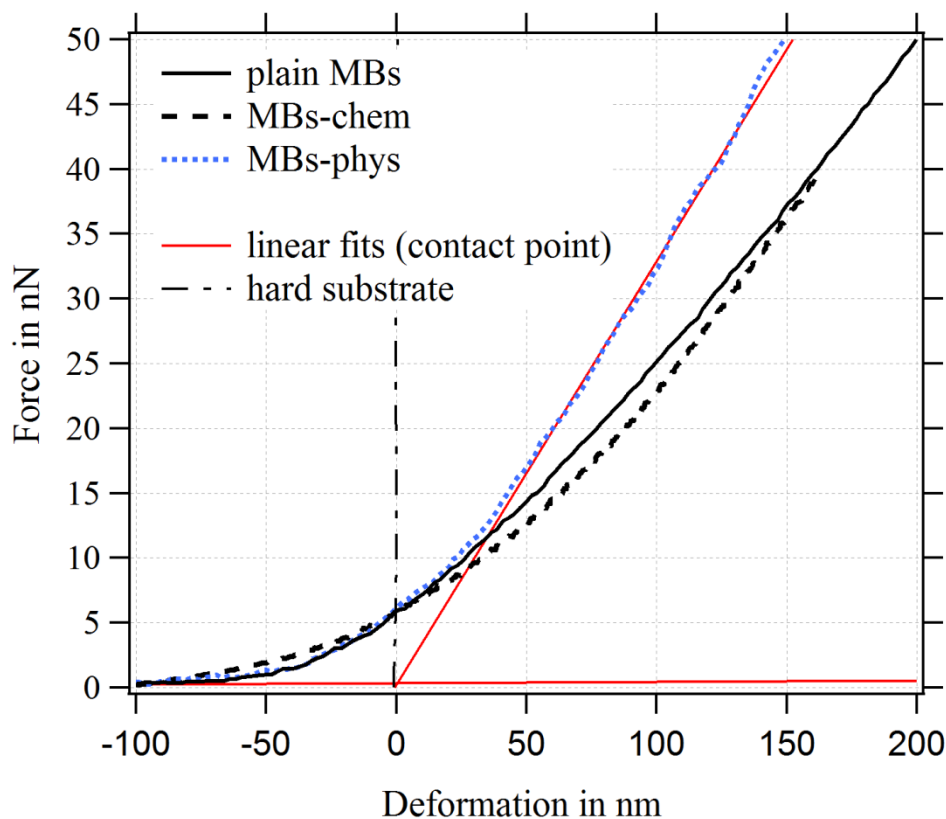


Figure 6-7: Force-deformation curves of plain MBs, MBs-chem, and MBs-phys.

To identify the relative deformation  $\varepsilon$ , where volume forces start to dominate the MBs deformation behavior Fery et al.<sup>72</sup> suggested a simple scaling argument for capsules that considers the shell thickness  $h$  and the radius  $r$ :

$$\varepsilon = \sqrt{\frac{h}{4\pi r}}; \quad D = \frac{\varepsilon}{2r} \quad (3)$$

For the investigated MBs with a radius of  $\sim 1.75 \mu\text{m}$  and an average hydrated shell thickness of 215 nm, we expect the crossover of these two regimes for a deformation  $D$  of about 350 nm. Figure 6-7 shows typical force deformation curves of plain MBs, MBs-chem and MBs-phys. The maximum applied force load was 50 nN that resulted in deformations up to 250 nm. The curve progression is very similar for all three samples and shows after a small non-linear onset a characteristic linear elastic deformation behavior. We believe that the onset observed in the force deformation curves is caused by various surface interactions such as steric repulsion of the PVA chains. The interface between gas core and the aqueous solution is the PVA shell, which is described as a hydrogel-like material of 20% polymer and 80% water. From previous published freeze fracture images<sup>68</sup> we distinguish the shell in a polymer rich

zone around the core and a polymer poor zone close to the aqueous phase, where PVA chains can also penetrate the aqueous phase. Differences of the MBs' deformation behavior are observed when we compare the force loads needed for a deformation of 200 nm. MBs with a comparable diameter were chosen for this graph to exclude size effects. The force load needed for a 200 nm deformation of MBs-chem was with 26 nN much lower compared to a force of 41 nN needed for MBs-phys. The corresponding stiffness  $F/D$  of the MBs is given in N/m, shown as red linear fit in the force-deformation curve.

The used AFM is combined with an optical microscope, thus the diameter is obtained for each deformed MB. In Figure 6-8, the statistical analysis of the observed diameter and the stiffness of the studied particles are displayed. All MBs had a diameter between 1  $\mu\text{m}$  and 3  $\mu\text{m}$ . MBs-chem showed average stiffness values of about 0.03 N/m which were smaller than the stiffness values of 0.08 N/m for plain MBs. Much larger stiffness values with much broader distributions were observed for MBs-phys with an average stiffness value of about 0.26 N/m. Thus we can conclude that MBs-chem are much softer than MBs-phys.

If the observed change in the stiffness is a result of changed material properties of the shell was further analyzed with a model proposed by Reissner<sup>76,77</sup>. With this model the deformation behavior of single MBs can be related to their geometry properties and the shell's material properties can be estimated. The stiffness  $F/D$  depends on shell thickness  $h$  radius  $R$ , elastic modulus  $E$  and the Poisson's ratio  $\nu$  as described in Equation 4:

$$\frac{F}{D} = \frac{h^2}{R} \frac{4E}{\sqrt{3(1-\nu^2)}} \quad (4)$$

As expected from the Reissner model we observe an increase of the measured stiffness values for MBs with smaller radius as shown in Figure 6-9. The scattering of the stiffness around the proposed linear trend can be attributed to the dispersity that we expect for the shell thickness. MBs-chem are softer compared to plain MBs and surface-modified MBs-phys. To estimate the elastic modulus of the shell's material, we used an approximated average shell thickness of 249 nm for the hydrated state.

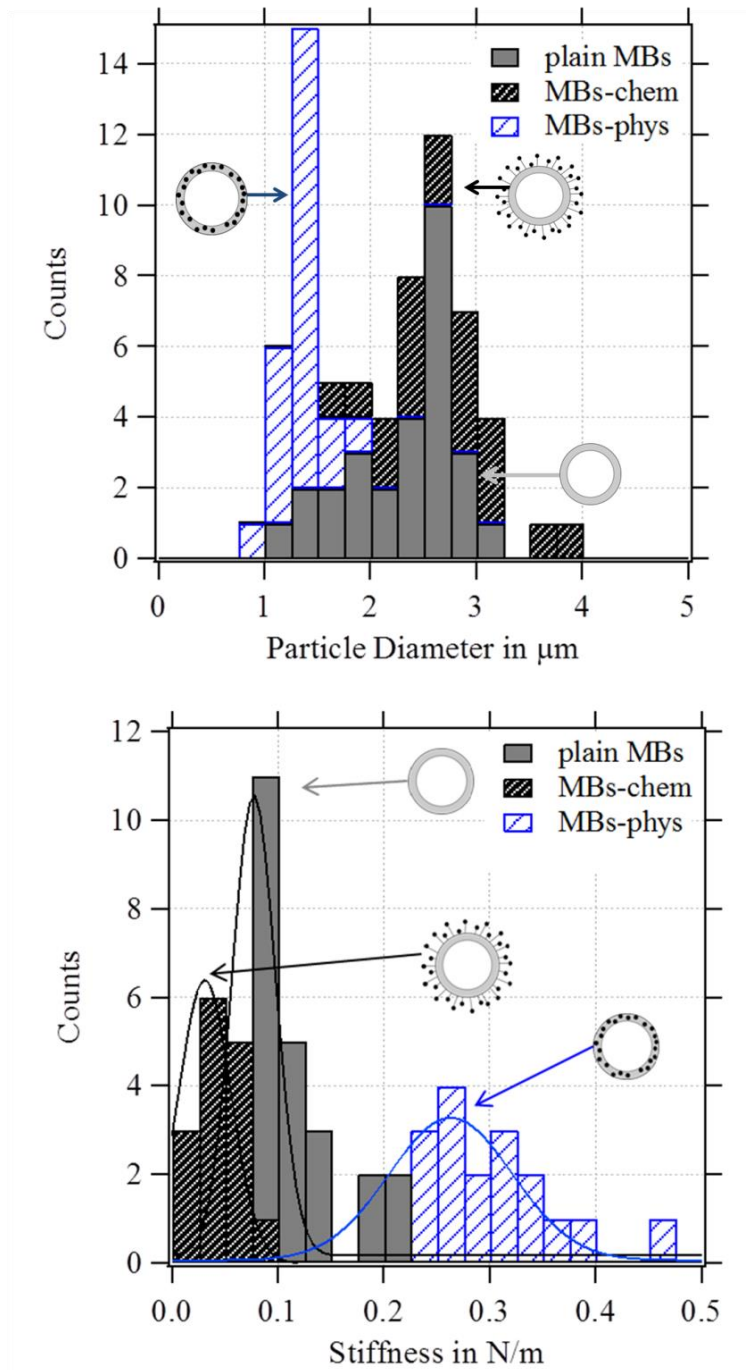


Figure 6-8: Histogram of the MBs stiffness and the particle diameter of the measured MBs.

The Poisson's ratio ranges for materials between 0.49 for rubber-like materials and 0.33 for solid materials. For the calculation of the elastic modulus of the rather soft polymer shell, we used a reasonable Poisson's ratio of 0.49. As a result, we obtained an elastic modulus of 230 kPa for MBs-chem, 1.3 MPa for plain MBs and about 3.2 MPa for MBs-phys. These results clearly indicate that the material properties have changed through the modification by SPIONs. As shown by the Equation 4 the value

of the Poisson ratio has a minor effect on the elastic modulus compared to the direct measured parameters such as the shell thickness and the radius. Here the change of the stiffness results in an increase of the elastic modulus. The reinforcement of the polymeric shell observed for MBs-phys is based on an higher density of the shell material. This has been already observed for other core/shell systems where nanoparticles were integrated into the shell.<sup>78, 79</sup>

For MBs-chem the decrease of the elastic modulus is based on a reduced number of cross-links within the shell's PVA network. The original shell, the polymeric shell of plain MBs, is stabilized by chemical and physical cross-links. Both cross-links are relevant for the mechanical stability of the shell and contribute to its stiffness. The chemical cross-links originate from the acetalization reaction carried out during the MBs synthesis, where telechelic PVA chains react with hydroxyl groups of the PVA chains. Non-covalent or physical cross-links refer to crystalline domains within the polymeric network, which are typical for PVA. The amount of crystalline units in the polymeric network is quantified by DSC measurements<sup>[23]</sup>. According to DSC, plain MBs, not exposed to a chemical treatment, retain about 50 % of the crystalline domains of the starting PVA material, used for their fabrication as shown in Figure 6-10. For MBs-chem the crystalline regions are lost after the post-production treatment, which was performed to couple SPIONs to the shell surface. Consequently, MBs chem are softer than plain MBs, because the number of physical cross-links has decreased compared to plain MBs.

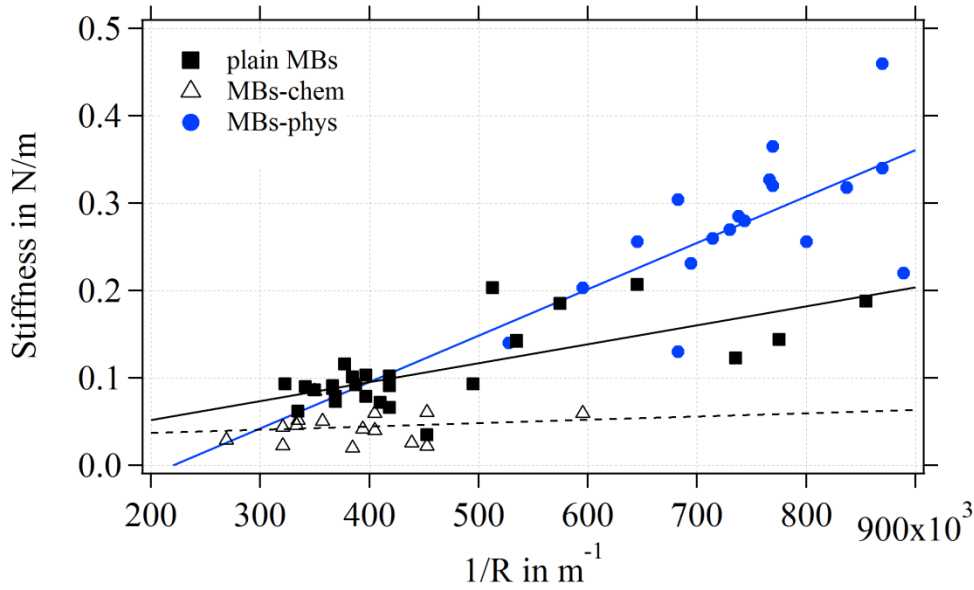


Figure 6-9: Scattering plot of the stiffness in N/m versus the inverse of the MB radius.

### 6.3.3 Internal Shell Structure

For the MBs' mechanical properties, the shell's structure and in particular the density of crosslinks inside the polymeric network are crucial. Both types of crosslinks - chemical and physical - need to be considered for a shell made of poly(vinyl alcohol).<sup>80</sup> For the MBs' polymeric shell, chemical crosslinks originate from the acetalization reaction carried out during the MBs synthesis, where aldehyde groups of the telechelic PVA react with hydroxyl groups. Non-covalent or physical crosslinks refer to crystalline domains within the polymeric network, which are typical for the semicrystalline polymer PVA.<sup>81, 82</sup>

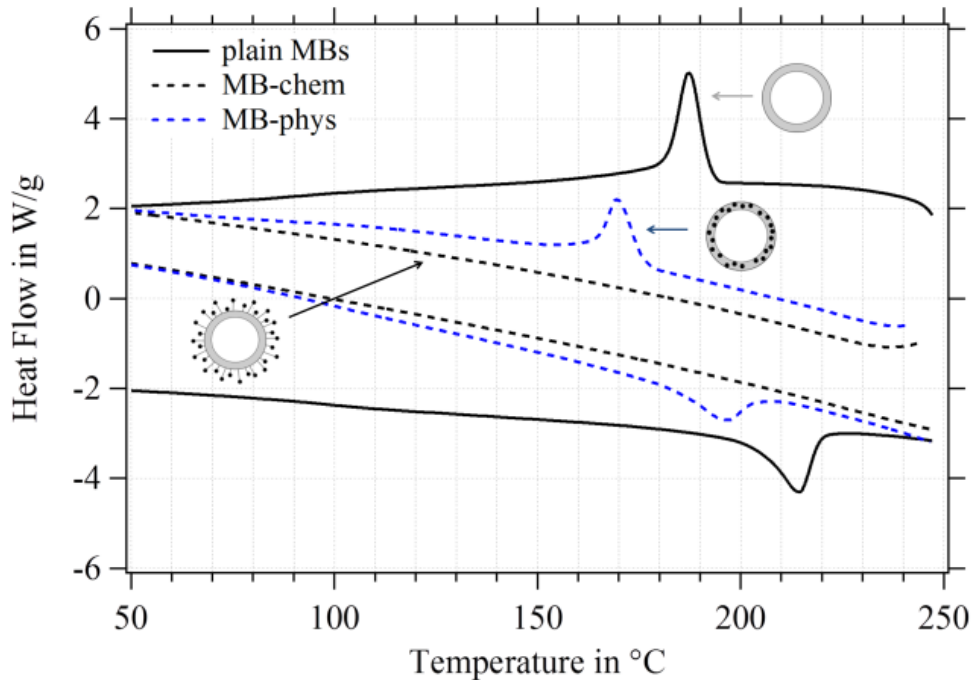


Figure 6-10: Differential scanning calorimetry of plain MBs (full line), MB-chem (dashed black line) and MB-phys (dashed blue line). Diagram adapted with permission from Brismar et al., *Magnetic Nanoparticles can be coupled to Support Multimodal Imaging*, *Biomacromolecules* 13(5), 1390. Copyright (2012) American Chemical Society.

The degree of crystallinity, referring to the crystalline domains present in the polymeric network, was determined with differential scanning calorimetry (DSC). Endothermic and exothermic peaks in the DSC diagram refer to the melting and recrystallization of the crystalline domains in the polymeric network. Thus, the degree of crystallinity is accessible, which is an indicator for the number of physical crosslinks inside the PVA shell. Recently,<sup>23</sup> we observed differences in the degree of crystallinity between plain MBs, MBs-chem, and MBs-phys as shown in Figure 6-10, adapted from Brismar et al.<sup>23</sup> Plain MBs showed the highest degree of crystallinity with typical endothermic and exothermic peaks. A major change of the number of physical crosslinks was found for SPIONs conjugated to the shell surface (MBs-chem). The typical peak profile is lost indicating the absence of crystalline domains in the PVA network and a complete loss of the physical crosslinks, which is reducing the overall crosslinking density. In contrast, the embedding of SPIONs (MB-phys) resulted in slight changes of the shell structure. Here, a decrease of peak signals was observed, referring to a lower degree of crystallinity and a reduced number of physical crosslinks.

Further experiments were performed in this study to understand the reason for the change of the shell structure and the MBs' mechanical stability. Therefore, we analyzed the degree of crystallinity of plain MBs before and after the chemical treatment. SPIONs were excluded from the chemical treatment, in other words, MBs were solely exposed to the corresponding chemicals and reaction conditions without using any nanoparticles. As Figure 6-11 shows, plain MBs indicate the typical peaks referring the crystalline domains in the network. After exposing the MBs to the reaction conditions and corresponding chemicals the peaks (crystalline domains) are lost. Plain MBs with APTMS attached to the surface show the same internal shell structure as MBs-chem. Thus, we can conclude from these experiments that the chemical treatment is the crucial factor for changes in the internal shell structural.

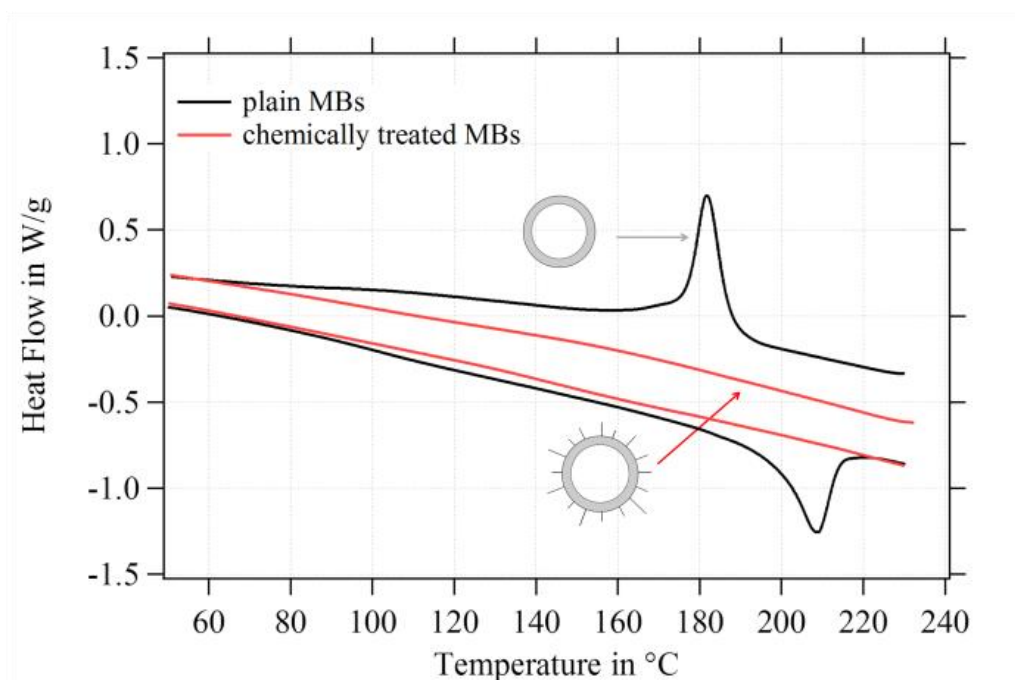


Figure 6-11: DSC results for plain MBs before and after chemical treatment without attaching SPIONs.

In view of the mechanical properties of MBs\_chem, the reduced number of physical crosslinks in the PVA shell is an explanation for the reduced elastic modulus of the shell.<sup>80</sup> However, the DSC result for MBs-phys, indicating a reduced amount of physical crosslinks, cannot explain the shell's increased elastic modulus. MBs-phys showed the highest elastic modulus of all three MB types. Here, the impact of nanoparticle embedment inside a polymeric network needs to be considered as well. For polymeric nanocomposites, reinforcement upon nanoparticles integration is well-

known.<sup>83,84,85, 86</sup> For PVA hydrogels reinforcement was observed for the addition of graphene,<sup>87</sup> silvernanoparticles<sup>87</sup> and silicaparticles,<sup>88</sup> which all resulted in an increase of the elastic modulus. For other capsule systems, the reinforcement of e.g. polyelectrolyte multilayer shells after incorporated of gold nanoparticles<sup>78</sup> or yttrium fluoride<sup>79</sup> nanoparticles was reported.

#### **6.3.4 Acoustical characterization – experiments and modeling.**

The acoustical characterization of MBs in vitro is crucial to bridge the gap between structure-property relations obtained from AFM studies and the application-relevant performance of the MBs during ultrasound imaging. While we concentrated in the AFM experiments on low-frequency mechanics of single MBs, we refocused in the acoustic tests on high-frequency mechanics of an ensemble of MBs. In particular, we were interested if the MB's mechanical properties observed during quasi-static AFM deformation experiments set the trend for the MB's dynamic oscillation during ultrasound exposure. As already previously reported on plain MBs<sup>46</sup> and magnetic MBs<sup>23</sup>, both demonstrate a backscatter enhancement of about 20 dB at concentrations approved for commercial available UCAs<sup>89</sup>. An interesting outcome of this previous study was the finding that MBs-chem reach the 20 dB backscatter enhancement already for a lower concentration ( $4.4 \times 10^5$  MB/ml) compared to MBs-phys ( $2 \times 10^6$  MB/ml). Moreover, the attenuation coefficient was smaller for MBs-chem than for MBs-phys. Based on the results of the structural characterization and low-frequency mechanics, we expect that the different mechanical properties of the shell are decisive for the changes in the MBs' acoustic behaviour. In other words, we think that the different SPIONs integration methods used for the production of MBs-chem and MBs-phys alter shell mechanics and the corresponding acoustic behaviour.

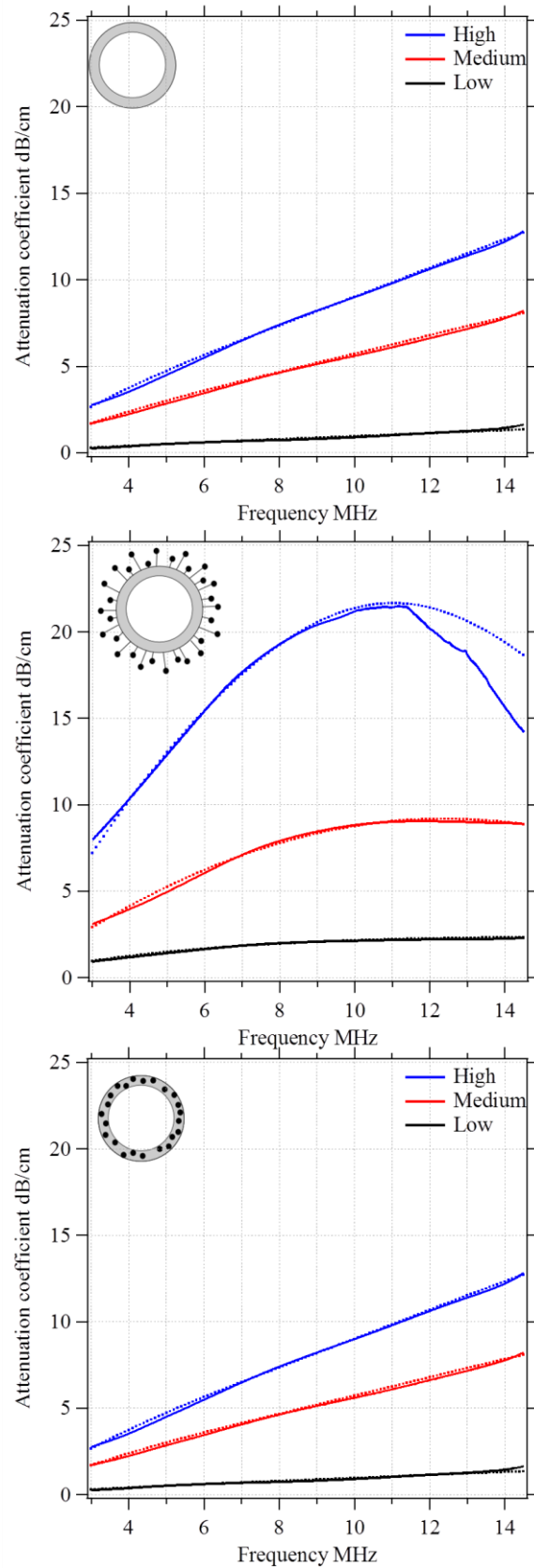


Figure 6-12: Attenuation coefficient versus frequency for three types of MBs: (a) plain, (b) MBs-chem and (c) MBs-phys; at three different concentrations. Solid lines in each plot indicate the experimental data, while dotted lines shows the theoretical predictions a

To understand the impact of the low frequency mechanics on the MBs behaviour in the high frequency regime we performed further acoustic studies. Moreover, we used the acoustic experiments to estimate the viscoelastic properties of the polymeric shell. In particular, we were interested in the shell's shear modulus  $G_{eq}$  and the shear viscosity  $\mu_0$ . The ultrasound experiments were carried out in-vitro and under controlled conditions as explained in the experimental section.

First, we measured the frequency dependence of the attenuation coefficient Figure 6-12 a, b and c show the observed results for plain, MBs-chem and MBs- phys. For each MB sample, we acquired data from a low, intermediate and high MB concentration. As expected the attenuation coefficient shifts to higher values with an increasing MB concentration, because the number of scatterers is increased in the suspension.<sup>23, 46</sup> In general, a monotonically increase of the attenuation coefficient is expected when the frequency is raised from 3 to 14 MHz. We identified the following changes in the curve progression with regard to the slope and the maximum absolute value of the attenuation coefficient.

Plain MBs show an almost linear frequency dependency of the attenuation coefficient for all studied concentrations. The incremental growth is about 4 dB/cm at 10 MHz and we observe a maximum value of about 12 dB/cm for the highest MB concentration. MBs-chem show a sigmoid-like frequency dependency of the attenuation coefficient, with an incremental growth of about 6 dB/cm to 12 dB/cm at 10 MHz. The highest absolute value for MBs-chem was about 22 dB/cm for the highest MB concentration. On the contrary, MBs-phys show an exponential-growth-like frequency dependency of the attenuation coefficient. The incremental growth is about 1 dB/cm to 2 dB/cm at 10 MHz and the MBs -phys lowest absolute value was of about 6 dB/cm. Based on this results we expect the lowest resonance frequency for MBs-chem and the highest value for the resonance frequency for MBs—phys.

By using a mathematical description, which not only considers size distribution and density but also the viscoelastic properties of the shell material we were able to model the MBs response in the high frequency regime. The acoustic tests are performed in MHz frequency range where MBs are exposed to a dynamic load. Thus, the viscoelastic material properties should be seen as dynamic or time dependant characteristics.<sup>90</sup> In general, the mechanism of the MB oscillation during ultrasound

exposure is described by a nonlinear Rayleigh-Plesset-like equation.<sup>59, 60, 91-93</sup> At low incident pressure, typically below 100kPa, the equation is simplified to the description of a harmonic oscillator (Equation 5) with a resonance frequency  $\omega_0(\omega)$  and a damping factor  $\delta(\omega)$ , which depends on the viscoelastic properties of the MBs shell. All parameters used in the following equations are explained in Table 6-2.

Table 6-2 Explanation of nomenclature used in Equations 5 to 8.

$x$	radial displacement
$R_{01}$	internal shell radius
$R_{02}$	external shell radius
$\mu_L$	viscosity of the surrounding liquid
$\rho_S$	density of the shell
$\rho_L$	density of surrounding liquid
$\kappa$	polytropic exponent of a gas
$P_{G,eq}$	equilibrium pressure gas in the MB core
$P_\infty(t)$	equilibrium pressure far from the bubble surface
$G(t)$	relaxation function
$G'(\omega)$	storage modulus
$G''(\omega)$	loss modulus
$\alpha$	$1 + (\rho_L - \rho_S) R_{01} / \rho_S R_{02}$
$V_S$	$R_{02}^3 - R_{01}^3$

$$\ddot{x} + \frac{4R_{01}\mu_L}{\alpha\rho_S R_{02}^2} \dot{x} + \frac{1}{\alpha\rho_S R_{01}^2} \left( 3\kappa P_{G,eq} x + \frac{4V_S}{R_{02}^3} \int_{-\infty}^t G(t-\tau) \dot{x}(\tau) d\tau \right) = \frac{1}{\alpha\rho_S R_{01}^2} (P_{G,eq} - P_\infty(t)) \quad (5)$$

$$\omega_0(\omega) = \frac{1}{R_{01}} \sqrt{\frac{1}{\alpha\rho_S} \left( 3\kappa P_{G,eq} + \frac{4V_S}{R_{02}^3} G'(\omega) \right)} \quad (6)$$

$$\delta(\omega) = \frac{4}{\alpha \rho_S R_{01}^2 R_{02}^3} \left( R_{01}^3 \mu_L + V_S \frac{G''(\omega)}{\omega} \right) \quad (7)$$

The total loss of energy, including absorption and scattering, from the acoustic wave propagating through the suspension of the MBs can be assessed using the extinction cross section,  $\sigma_e$  given in Eq. 8. <sup>60, 91</sup>

$$\sigma_e = 4\pi R_{01}^2 \frac{\Omega^4}{(1-\Omega^2)^2 + (\Omega\delta)^2} \frac{\delta}{\delta_c}, \quad (8)$$

where  $\Omega = \omega/\omega_0$  is the normalized frequency and  $\delta$  is the total damping, which is the sum of the following four terms:

$$\delta_c = \frac{\omega^2 R_{01}}{c}, \text{ damping from radiation resistance, }^{60, 91}$$

$$\delta_L = \frac{4\mu_L R_{01}^3}{\alpha \rho_S R_{01}^2 R_{02}^2}, \text{ damping from viscosity in the embedding liquid }^{59}$$

$$\delta_{Th} = \frac{3P_e}{\omega \rho R_{01}^2} \text{Im} \left( \frac{1}{\Phi} \right), \text{ thermal damping }^{60, 91}$$

$$\delta_S = \frac{4V_S}{\alpha \rho_S R_{01}^2 R_{02}^2} \frac{G''(\omega)}{\omega}, \text{ damping from the shell}^{46}$$

Two extra terms, namely damping from radiation resistance and thermal damping, are added to the Church model to its original formulation in Equation 7. The attenuation coefficient,  $\alpha(\omega)$  in dB/unit length can now be recalculated from the extinction cross section:

$$\alpha(\omega) = 10 (\log e) \int_0^\infty \sigma_e(R_{01}, \omega) f(R_{01}) dR_{01} \quad (9)$$

where  $f(R_{01})dR_{01}$  is the number of MBs in unit volume having radius between  $R_{01}$  and  $R_{01}dR_{01}$ . Using the following expressions for the storage and loss moduli<sup>46</sup>:

$$G'(\omega) = G_{eq} + G_1 \omega^{3/4} \quad (10)$$

$$G''(\omega) = \omega(\mu_0 - \mu_1 \omega) \quad (11)$$

Additional parameters used for the modelling are the speed of sound in pure water at 24 °C,  $c = 1493$  m/s; the viscosity of the surrounding liquid,  $\mu_L = 1 \times 10^{-3}$  Pas; the density of the surrounding liquid  $\rho_L = 1000$  kg/m<sup>3</sup> and the atmospheric pressure  $P_0 = 10^5$  Pa.

With the above-described modified Church model that accommodates the frequency dependence of the dynamic viscoelastic module, we were able to fit the experimental data of the frequency-dependant attenuation coefficient. Dotted lines in Figure 6-12 demonstrate the results of the theoretical modelling for each type of MBs.

Table 6-3: Parameters used for modelling the frequency dependent attenuation coefficient.

	<b>Plain</b>	<b>Type A</b>			<b>Type B</b>
<b>c, x10<sup>6</sup></b> <b>[MB/ml]</b>	0.2;0.9;1.8	0.4	0.9	2	0.5;1;2
<b>G<sub>eq</sub></b> <b>[MPa]</b>	10.5	4.0	3.8	4.0	28.0
<b>G<sub>1</sub></b> <b>[Pa/ (rad/s)<sup>3/4</sup>]</b>	5.5	10.7	4.2	0.1	10.0
<b>μ<sub>0</sub></b> <b>[Pa·s]</b>	0.6	0.3	0.2	0.2	0.7
<b>μ<sub>1</sub> x 10<sup>-9</sup></b> <b>[Pa·s<sup>2</sup>/rad]</b>	3.2	0.01	0.9	2.0	2.0
<b>F<sub>resonance</sub></b> <b>[MHz]</b>	12-14	11-16	10-12	9-10	18-20

The main idea of the fitting procedure, is the variation of four coefficients: the storage  $G'(\omega)$  and loss module  $G''(\omega)$ , the resonance frequency and the damping of the harmonic oscillator. As a result, the extinction cross section  $\sigma_e$  for each bubble will alter. Taking into account the distribution and concentration of the bubbles in a suspension one obtains the attenuation profile with respect to the driving frequency. Based on the diameter and shell thickness that were determined in the MBs' structural characterization in the first part of this paper, we were able to reconstruct the viscoelastic modulus of the shell. In Table 6-3 the four coefficients are indicated, which were used to determine the storage  $G'(\omega)$  and loss modulus  $G''(\omega)$ . A comparison between the two magnetic MBs shows that lower values for the static terms of both viscoelastic moduli,  $G_{eq}$  and  $\mu_0$ , were observed for MBs-chem. In

addition, MBs-chem have a lower resonance frequency of about 10 MHz than MBs phys with a resonance frequency of about 25 MHz. From these results, we conclude that MBs-chem are less rigid, are driven easier to oscillation and are more echogenic than MBs-phys. Thus, the trend observed for the mechanical shell properties in the high frequency regime, the acoustic tests, are in agreement with the shells' mechanical properties measured in the low-frequency regime. For both frequency regimes, MBs-chem showed a significant lower stiffness than MBs-phys.

#### **6.4 Conclusion**

In this interdisciplinary work, we presented strategies for a rational design of multimodality contrast agents. In particular, we provided a quantitative characterization of polymeric US/MRI contrast agents and their mechanical properties in the low and high frequency regime. The presented hybrid probes were produced with two different manufacturing processes leading to structural different magnetic MBs. The first process, a one-pot synthesis, SPIONs were physically embedded inside the polymeric network of the PVA shell (MBs-phys). In the second process, a 2-step synthesis, SPIONs were covalently attached to the shell surface (MBs-chem). Both SPIONs integration methods did not alter diameter or shell thickness of the magnetic MBs compared to plain MBs. However, we observed significant differences in the mechanical properties of the polymeric shell. The elastic modulus of MBs-chem, studied with quasi-static force measurements, was reduced from 1.3MPa (plain MBs) to 0.23MPa (MBs-chem). For plain MBs the polymeric shell is stabilized by chemical and physical cross-links within the PVA network. Through the chemical treatment physical cross-links are lost, which leads to a softening of the shell. In particular, crystalline domains in the PVA shell that serve as physical cross-links were lost by the postproduction treatment as demonstrated by DSC measurements. For MBs-phys that contain SPIONs embedded inside the polymer shell, we observed a reinforcement of the PVA shell. This is reflected in an increase of the elastic modulus from 1.3MPa (plain MBs) to 3.2 MPa (MBs-phys). Further acoustic experiments showed that the mechanical properties characterized in the quasi-static deformations experiments (AFM) set the trend for the MBs behaviour during ultrasound exposure. In the acoustic experiments, the frequency-dependency of the attenuation coefficient was analyzed with Church's modified model, which not only considers size distribution and density but also the viscoelastic properties of the

shell's material. Thus, we were able to reconstruct the dynamic viscoelastic modulus of the PVA shell. The trend of the results is in agreement with the AFM experiments and provided evidence that the shell of MBs-chem are characterized by a much softer shell compared to MBs-phys. Thus, we can conclude that shell properties analyzed on the single particle level, were crucial to understand the more complex behaviour of an ensemble of MBs exposed to an acoustic field. In summary, the presented work contributes to understand structure property relations relevant for the performance of UCA and provides an approach for the sustainable design and optimization of US/MRI contrast agents

### **6.5 Acknowledgements:**

M.P. thanks Lars Dähne and Gabriella Egri from Surflay Nanotec GmbH, Berlin for fruitful discussions and helpful critics on the characterization of MBs dimensions. M.P. and R. H. thank Carmen Kunert for her help with the sample preparation and acquisition of TEM images. The authors want to acknowledge the financial support from the European Commission within the 7<sup>th</sup> framework program of the FP7 Project 245572 3MICRON-Three modality contrast imaging using multi-functionalized microballoons.

## 6.6 Electronic Supplementary Information

### 6.6.1 Determination of the attenuation coefficient:

The attenuation coefficient of the ultrasound wave propagating through the MBs suspension is determined using a two-time-domain signals. The first signal is acquired from the ultrasound pulse propagating through the cell filled with pure water. The second signal is collected from the cell filled with the suspension of the MBs. The Fourier analysis reveals the harmonic decomposition of the time-domain signals to be equal:

$$f_{\text{ref}}(t) = \frac{1}{2\pi} \int_{-\infty}^{\infty} |F_{\text{ref}}(\omega)| e^{-jk_{\text{ref}}z} e^{-j\omega t} d\omega \quad (1)$$

Where  $|F_{\text{ref}}(\omega)|$  and  $k_{\text{ref}}z$  are modulus and phase of the spectra acquired from pure water. If the dissipation of energy is added, due to wave propagation through the MBs suspension, the only effect it cause is that the wave vector  $\vec{k}$  becomes complex, *i.e.*  $k_{\text{MB}}(\omega) = k_1(\omega) - jk_2(\omega)$ . Thus, the spectrum of the signal from MBs can be rewritten as:

$$\begin{aligned} f_{\text{MB}}(t) &= \frac{1}{2\pi} \int_{-\infty}^{\infty} |F_{\text{MB}}(\omega)| e^{-jk_{\text{MB}}(\omega)z} e^{-j\omega t} d\omega = \\ &= \frac{1}{2\pi} \int_{-\infty}^{\infty} |F_{\text{ref}}(\omega)| e^{-[k_2(\omega) - jk_1(\omega)]z} e^{-j\omega t} d\omega \end{aligned} \quad (2)$$

Where  $k_2(\omega)$  should be seen as attenuation coefficient  $\alpha(\omega)$ , and wave number  $k_1(\omega)$  represents the phase shift. Taking into account the “round-trip” propagation of the beam through the cell of length  $L$ , the harmonic decomposition of the signal from MBs on its final form is:

$$f_{\text{MB}}(t) = \frac{1}{2\pi} \int_{-\infty}^{\infty} |F_{\text{ref}}(\omega)| e^{-[\alpha(\omega) - jk_1(\omega)]2L} e^{-j\omega t} d\omega \quad (3)$$

Substituting the scale from Np to dB, the attenuation coefficient  $\alpha(\omega)$ , can be calculated from:

$$\alpha(\omega) = -\frac{20}{2L} \log \left( \frac{|F_{\text{MB}}(\omega)|}{|F_{\text{ref}}(\omega)|} \right) \text{ dB/unit length} \quad (4)$$

### 6.6.2 Atomic force microscopy - Characterization of diameter and shell thickness

Table 6-4: Summary of the results from the statistical analysis of the AFM height images: diameter  $d$ , shell thickness  $H$  with the corresponding standard deviation (SD), and half-width at half maximum (HWHM).

Parameter	$n$	Median $\pm$ SD	Gauss $\pm$ HWHM	SD Gauss = HWHM/ $\sqrt{2}$
$d_{\text{AFM,dry}} (\mu\text{m})$	203	$3.7 \pm 0.9$	$3.5 \pm 1.12$	0.8
$H_{\text{AFM,dry}} (\text{nm})$	158	$171 \pm 68$	$152 \pm 90$	63
$H_{\text{AFM,water}} (\text{nm})$	36	$249 \pm 127$	$215 \pm 133$	94

### 6.6.3 Transmission electron microscopy - characterization of shell thickness

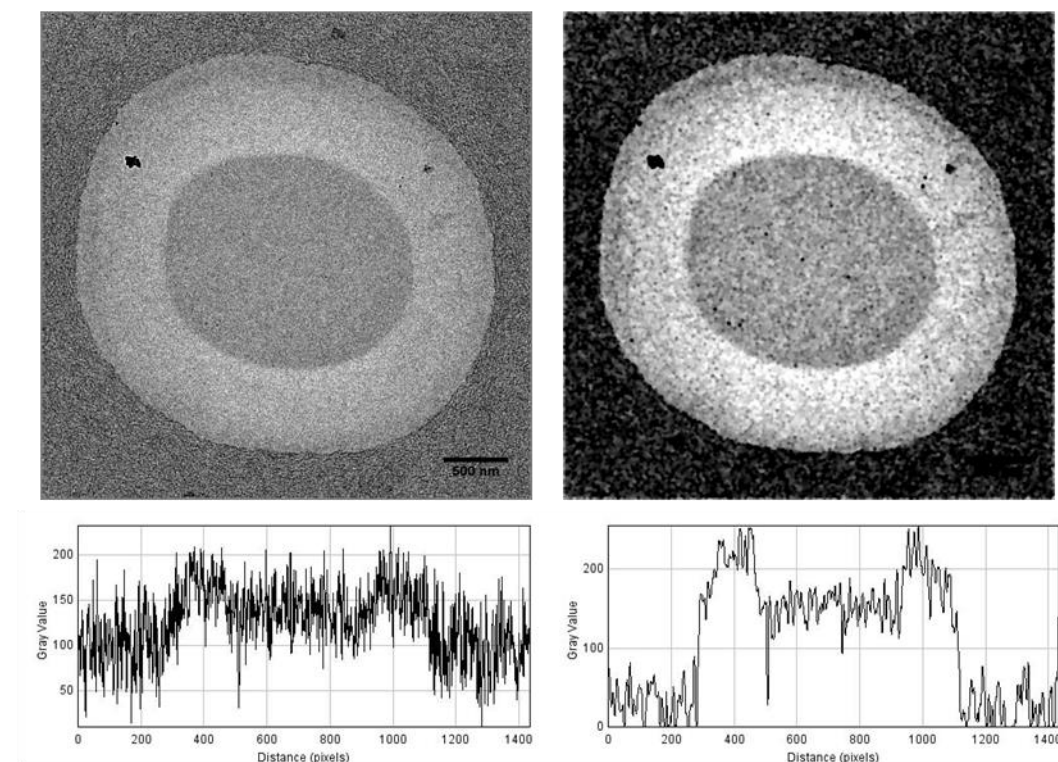


Figure 6-13 For the cross-sectional profiles an enhanced contrast was needed to evaluate the images with a standardized protocol using ImageJ<sup>94</sup>. Protocol: Filter Minimum (2 pixels + adjust B&C); enhance contrast 0.35 + adjust B&C; Filter Maximum (2 pixels + adjust B&C); enhance contrast 0.35 + adjust B&C, repeat this procedure and plot a profile from the lower left to upper right

corner. Thus, we were able to identify the PVA/EPON interface at  $\pm 50\%$  change of the gray scale value.

#### 6.6.4 Mathematical procedure of random slicing correction

True thickness  $H$  of the capsule wall is given by the difference of the true outer  $R$  and inner radius  $r$  at the equatorial plane (see Figure 6-14). All measured sizes are indicated by an index  $i$  and are affected by the position, where the capsule is sectioned for TEM. For random slicing, the both radii are underestimated ( $\langle R_i \rangle \leq R, \langle r_i \rangle \leq r$ ) and the wall thickness is overestimated ( $\langle H_i \rangle = \langle R_i - r_i \rangle \geq H$ ). In the following, radii are always considered as pairs ( $N_{R_i} = N_{r_i}$ ), since these values are correlated. The angle of the outer radius  $\Phi$  is limited between  $[-\Phi_{\text{limit}}, +\Phi_{\text{limit}}]$  with  $\Phi_{\text{limit}} = \sin^{-1}((R - H)/R) = \pi/2 - \sin^{-1}(-H/R)$ , where the angle of the inner radius  $\phi$  is not limited ( $[-\pi/2, +\pi/2]$ ).

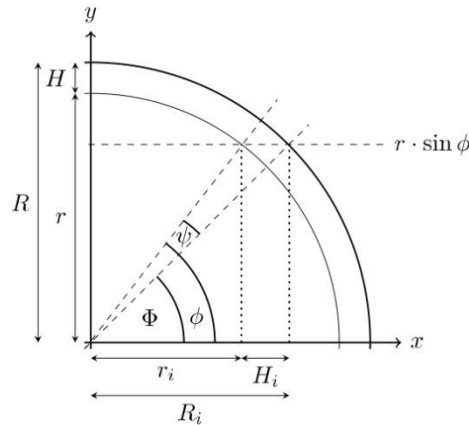


Figure 6-14: Definition of geometry of a sphere of uniform thickness used in the mathematical analysis that corrects for random slicing along the  $y$ -axis during TEM sample preparation.<sup>2</sup>

The assumption is that if we have good statistical data, we can apply a mathematical correction introduced by Smith *et al.* to calculate the true values.<sup>95</sup> This approach is based on a geometrical function  $H(R_i, H_i, \Phi)$  and  $\psi = \phi - \Phi$ .

$$H = \left( \frac{R_i}{\cos(\Phi)} \right) - \sqrt{H_i^2 - \left( \frac{R_i}{\cos(\Phi)} \right)^2 + 2R_i \left( \frac{R_i - H_i \cos^2(\Phi)}{\cos^2(\Phi)} \right)}$$

(5)

The mean corrected thickness  $\langle H \rangle$  is then given by a triple integral:

$$\langle H \rangle = \int_{-\Phi \text{ limit}}^{+\Phi \text{ limit}} \int_{H_{i,\min}}^{H_{i,\max}} \int_{R_{i,\min}}^{R_{i,\max}} H(R_i, H_i, \Phi) f_R(R_i) f_H(H_i) f_\Phi(\Phi) dR_i dH_i d\Phi \quad (6)$$

The functions  $f_R$ ,  $f_H$ , and  $f_\Phi$  are the normalized probability density functions of  $R_i$ ,  $H_i$ , and  $\Phi$ , respectively. If  $f_R$  and  $f_H$  (obtained from the statistics of the image analysis data) are normally distributed then they can be described by Gaussian distributions (mean and standard deviation).

Smith *et al.* assumed that if there is an equal probability of slicing at any angle  $\Phi$  then  $f_{\Phi, \text{Smith}}(\Phi) = 1/\pi$ .<sup>95</sup> Mercade-Prieto et al. reported that this assumption is incorrect since this would mean, that there is an equal probability to cut from  $0^\circ$  to  $45^\circ$  and from  $45^\circ$  to  $90^\circ$ .<sup>96</sup> They suggested that the distance from the equator ( $r \sin(\phi)$  or  $R \sin(\Phi)$ ) should be the parameter of equal probability. Therefore we introduced a new probability density function  $f_{\Phi, \text{new}} = 0.5 \cos(\Phi)$ . Table 6-5 compares the old and new function  $f_\Phi$ .

Table 6-5 Comparison of the angular probability density function and integrations for different angular ranges

Angular range	-90° to 90°	0° to 45°	45° to 90°
Integration	$\int_{-\pi/2}^{+\pi/2} f_\Phi d\Phi$	$\int_0^{+\pi/4} f_\Phi d\Phi$	$\int_{+\pi/4}^{+\pi/2} f_\Phi d\Phi$
$f_{\Phi, \text{Smith}}(\Phi) = 1/\pi$	1	0.25	0.25
$f_{\Phi, \text{new}} = 0.5 \cos(\Phi)$	1	0.35	0.15

The corrected inner radius  $r$  is given by:

$$\langle r_i \rangle = \int_\phi \int_r r_i f_r(r) f_\phi(\phi) dr d\phi \quad (7)$$

The measured radius  $r_i$  can be substituted by  $r \cos(\phi)$ . If  $r$  and  $\phi$  are independent, the integrals can be separated. Using  $f_\phi$  and integrating over  $\phi$  and  $r$  yields the correction factor of the inner radius.

$$\langle r_i \rangle = \int_{-\frac{\pi}{2}}^{+\frac{\pi}{2}} \cos(\phi) f_\phi(\phi) d\phi \int_0^r r f_r(r) dr \quad (8)$$

$$\langle r_i \rangle = \frac{\pi}{4} \langle r \rangle \quad (9)$$

The mean corrected outer radius  $\langle R \rangle$  can be calculated from the following equation:

$$\langle R \rangle = \frac{4}{\pi} (\langle R_i \rangle - \langle H_i \rangle) + \langle H \rangle \quad (10)$$

Since solid disks (slicing inside of the capsule wall) were excluded from the statistical analysis, the integration of  $\Phi$  is limited. This limit is given by

$$\Phi_{\text{limit}} = \sin^{-1} \left( \frac{\langle R \rangle - \langle H \rangle}{\langle R \rangle} \right) \quad (11)$$

Solution procedure: 2

Determine mean and standard deviation for  $R_i$  and  $H_i$  from the TEM data. Only include data pairs of  $R_i$  and  $r_i$ . Exclude solid discs.

Guess  $\Phi_{\text{limit}}$ .

Solve for  $\langle H \rangle$  by integration within  $\pm 4$  standard deviation of  $R_i$  and  $H_i$ .

Solve for  $\langle R \rangle$ .

Check whether  $\Phi_{\text{limit}}(\langle R \rangle, \langle H \rangle)$  is satisfied. If not, repeat from step 3-5 using new  $\Phi_{\text{limit}}$ .

### 6.6.5 Acoustic Modeling

As Table 6-4 indicates, the concentration is less important for plain MBs and MBs-phys than for MBs-chem. MBs-chem appear to be more sensitive to the variation of the concentration. Even though the static terms of both viscoelastic moduli,  $G_{\text{eq}}$  and  $\mu_0$ , seems to be consistent among all concentration values the dynamic terms,  $G_1$  and  $\mu_1$ , are different. For instance, at low concentration  $\mu_1$  is approaching zero, while at high concentration  $G_1$  can be neglected. The possible explanation of this phenomenon might be found in the experimental set-up itself. In particular, for assessment of the attenuation coefficient the ultrasound probe at a central frequency of 10 MHz was employed. The frequency of the probe matches the resonance frequency of the MBs-chem. As a result, maximum radial expansion of the bubble occurs; scattering intensity of the wave is increased by several folds compare to the one predicted by Rayleigh scattering model<sup>97</sup> at high concentration (typically above  $10^6$  MB/mL) multiple scattering and reradiation of the waves might occur in the suspension<sup>98</sup>. In

addition, it was reported by de Jong *et al.*,<sup>99</sup> that MBs driven within 10% of their resonance frequency generate strong nonlinear harmonic response. Keeping in mind that linearized theoretical model accounts only for small oscillations around equilibrium, and consider only fundamental response, the frequency dependent or dynamic terms probably are not correctly assessed, while frequency independent or static terms are still possible to recover. This is in line with the fact that de Jong and Hoff<sup>100</sup> manage to predict sharp resonance peak for thin shelled Albunex<sup>®</sup> or Sonazoid<sup>®</sup> bubble using frequency independent shear modulus  $G$ , and viscosity  $\mu_0$  at about 2 and 4 MHz respectively. Worth to be noted is that plain MBs and MBs-phys oscillate far from their resonance and modified theoretical model manages to predict the attenuation profile with one set of coefficients for all concentrations. Worth noting that dynamic storage and loss modulus are characteristics of the shell material itself, but not the suspension of the MBs in general. As a result dynamic viscoelastic moduli should be independent on the microbubble concentration if multiple reradiation of energy, multiple scattering, interaction between the MBs and resonance are disregarded.

## References

1. Lindner, J. R., *Nat. Rev. Drug Discov.* **2004**, 3, (6), 527-532.
2. Massoud, T. F.; Gambhir, S. S., *Genes Dev.* **2003**, 17, (5), 545-580.
3. Weissleder, R., *Science* **2006**, 312, (5777), 1168-1171.
4. Pysz, M. A.; Gambhir, S. S.; Willmann, J. K., *Clin. Radiol.* **2010**, 65, (7), 500-516.
5. Cherry, S. R., *Semin. Nucl. Med.* **2009**, 39, (5), 348-353.
6. Judenhofer, M. S.; Wehrl, H. F.; Newport, D. F.; Catana, C.; Siegel, S. B.; Becker, M.; Thielscher, A.; Kneilling, M.; Lichy, M. P.; Eichner, M.; Klingel, K.; Reischl, G.; Widmaier, S.; Rocken, M.; Nutt, R. E.; Machulla, H.-J.; Uludag, K.; Cherry, S. R.; Claussen, C. D.; Pichler, B. J., *Nat Med* **2008**, 14, (4), 459-465.
7. Beyer, T.; Townsend, D. W.; Brun, T.; Kinahan, P. E.; Charron, M.; Roddy, R.; Jerin, J.; Young, J.; Byars, L.; Nutt, R., *J Nucl Med* **2000**, 41, (8), 1369-1379.
8. Hricak, H.; Choi, B. I.; Scott, A. M.; Sugimura, K.; Muellner, A.; von Schulthess, G. K.; Reiser, M. F.; Graham, M. M.; Dunnick, N. R.; Larson, S. M., *Radiology* **2010**, 257, (2), 498-506.
9. Cuocolo, A.; Breatnach, É., *European Journal of Nuclear Medicine and Molecular Imaging* **2009**, 37, (1), 163-167.
10. Louie, A. Y., *Chem. Rev.* **2009**, 110, (5), 3146-3195.
11. Curiel, L.; Chopra, R.; Hynynne, K., *IEEE Trans. Med. Imaging* **2007**, 26, (12), 1740-1746.
12. Feinberg, D. A.; Giese, D.; Bongers, D. A.; Ramanna, S.; Zaitsev, M.; Markl, M.; Gunther, M., *Magn. Reson. Med.* **2010**, 63, (2), 290-296.
13. Chandrana, C.; Bevan, P.; Hudson, J.; Pang, I.; Burns, P.; Plewes, D.; Chopra, R., *Phys Med Biol* **2011**, 56, (3), 861-877.
14. Mehrabian, H.; Chandrana, C.; Pang, I.; Chopra, R.; Martel, A. L., *Eur. Radiol.* **2012**, 22, (8), 1735-1747.
15. Claudon, M.; Cosgrove, D.; Albrecht, T.; Bolondi, L.; Bosio, M.; Calliada, F.; Correas, J. M.; Darge, K.; Dietrich, C.; D'Onofrio, M.; Evans, D. H.; Filice, C.; Greiner, L.; Jager, K.; de Jong, N.; Leen, E.; Lencioni, R.; Lindsell, D.; Martegani, A.; Meairs, S.; Nolsoe, C.; Piscaglia, F.; Ricci, P.; Seidel, G.; Skjoldbye, B.; Solbiati, L.; Thorelius, L.; Tranquart, F.; Weskott, H. P.; Whittingham, T., *Ultraschall Med* **2008**, 29, (1), 28-44.
16. Piscaglia, F.; Nolsoe, C.; Dietrich, C. F.; Cosgrove, D. O.; Gilja, O. H.; Nielsen, M. B.; Albrecht, T.; Barozzi, L.; Bertolotto, M.; Catalano, O.; Claudon, M.; Clevert, D. A.; Correas, J. M.; D'Onofrio, M.; Drudi, F. M.; Eyding, J.; Giovannini, M.; Hocke, M.; Ignee, A.; Jung, E. M.; Klauser, A. S.; Lassau, N.; Leen, E.; Mathis, G.; Saftoiu, A.; Seidel, G.; Sidhu, P. S.; ter Haar, G.; Timmerman, D.; Weskott, H. P., *Ultraschall Med* **2012**, 33, (1), 33-59.
17. Cosgrove, D.; Harvey, C., *Med Biol Eng Comput* **2009**, 47, (8), 813-826.
18. Kim, J.; Piao, Y.; Hyeon, T., *Chem. Soc. Rev.* **2009**, 38, (2), 372-390.
19. Bonnemain, B., *J Drug Target* **1998**, 6, (3), 167-174.
20. Wang, Y.-X.; Hussain, S.; Krestin, G., *Eur. Radiol.* **2001**, 11, (11), 2319-2331.
21. Malvindi, M. A.; Greco, A.; Conversano, F.; Figuerola, A.; Corti, M.; Bonora, M.; Lascialfari, A.; Doumari, H. A.; Moscardini, M.; Cingolani, R.; Gigli, G.; Casciaro,

- S.; Pellegrino, T.; Ragusa, A., *Advanced Functional Materials* **2011**, 21, (13), 2548-2555.
22. Liu, Z.; Lammers, T.; Ehling, J.; Fokong, S.; Bornemann, J.; Kiessling, F.; Gatzjens, J., *Biomaterials* **2011**, 32, (26), 6155-6163.
  23. Brismar, T. B.; Grishenkov, D.; Gustafsson, B.; Harmark, J.; Barrefelt, A.; Kothapalli, S. V. V. N.; Margheritelli, S.; Oddo, L.; Caidahl, K.; Hebert, H.; Paradossi, G., *Biomacromolecules* **2012**, 13, (5), 1390-9.
  24. Chow, A. M.; Chan, K. W. Y.; Cheung, J. S.; Wu, E. X., *Magn. Reson. Med.* **2010**, 63, (1), 224-229.
  25. Lu, R.; Xu, B.; Tao, K.; Dou, H. J.; Qiu, Y. Y.; Sun, K.; Zhang, Y. Q.; Wu, L. P.; Sun, K., *Colloid Polym Sci* **2012**, 290, (1), 63-71.
  26. Yang, F.; Li, Y. X.; Chen, Z. P.; Zhang, Y.; Wu, J. R.; Gu, N., *Biomaterials* **2009**, 30, (23-24), 3882-3890.
  27. Schutt, E. G.; Klein, D. H.; Mattrey, R. M.; Riess, J. G., *Angewandte Chemie-International Edition* **2003**, 42, (28), 3218-3235.
  28. de Jong, N.; Bouakaz, A.; Frinking, P., *Echocardiography-J. Cardiovasc. Ultrasound Allied Tech.* **2002**, 19, (3), 229-240.
  29. Qiao, R. R.; Yang, C. H.; Gao, M. Y., *J. Mater. Chem.* **2009**, 19, (35), 6274-6293.
  30. Baluk, P.; Hirata, A.; Thurston, G.; Fujiwara, T.; Neal, C. R.; Michel, C. C.; McDonald, D. M., *Am J Physiol* **1997**, 272, (1 Pt 1), 155-170.
  31. Reddy, S. T.; van der Vlies, A. J.; Simeoni, E.; Angeli, V.; Randolph, G. J.; O'Neil, C. P.; Lee, L. K.; Swartz, M. A.; Hubbell, J. A., *Nat Biotech* **2007**, 25, (10), 1159-1164.
  32. Zolnik, B. S.; González-Fernández, Á.; Sadrieh, N.; Dobrovolskaia, M. A., *Endocrinology* **2010**, 151, (2), 458-465.
  33. Desai, M. P.; Labhasetwar, V.; Amidon, G. L.; Levy, R. J., *Pharm. Res.* **1996**, 13, (12), 1838-1845.
  34. Lathia, J. D.; Leodore, L.; Wheatley, M. A., *Ultrasonics* **2004**, 42, (1-9), 763-8.
  35. Stride, E.; Edirisinghe, M., *Soft Matter* **2008**, 4, (12), 2350-2359.
  36. Ferrara, K.; Pollard, R.; Borden, M., *Annu. Rev. Biomed. Eng.* **2007**, 9, 415-447.
  37. Feinstein, S.; Coll, B.; Staub, D.; Adam, D.; Schinkel, A.; ten Cate, F.; Thomenius, K., *Journal of Nuclear Cardiology* **2010**, 17, (1), 106-115.
  38. Cai, X. W.; Yang, F.; Gu, N., *Theranostics* **2012**, 2, (1), 103-112.
  39. Park, J. I.; Jagadeesan, D.; Williams, R.; Oakden, W.; Chung, S.; Stanisiz, G. J.; Kumacheva, E., *Acs Nano* **2010**, 4, (11), 6579-6586.
  40. Postema, M.; Schmitz, G., *Ultrason. Sonochem.* **2007**, 14, (4), 438-444.
  41. Cavalieri, F.; El Hamassi, A.; Chiessi, E.; Paradossi, G., *Langmuir* **2005**, 21, (19), 8758-8764.
  42. Paradossi, G.; Cavalieri, F. PCT/EP2007/006886, 7 Feb, **2008**.
  43. Paradossi, G.; Tortora, M. PCT/IB2009/005215, 15 Oct, **2009**.
  44. Cavalieri, F.; El Hamassi, A.; Chiessi, E.; Paradossi, G.; Villa, R.; Zaffaroni, N., *Biomacromolecules* **2006**, 7, (2), 604-611.

45. Grishenkov, D.; Kari, L.; Brodin, L.-A.; Brismar, T. B.; Paradossi, G., *Ultrasonics* **2010**, 51, (1), 40-48.
46. Grishenkov, D.; Pecorari, C.; Brismar, T. B.; Paradossi, G., *Ultrasound Med Biol* **2009**, 35, (7), 1127-1138.
47. Grishenkov, D.; Pecorari, C.; Brismar, T. B.; Paradossi, G., *Ultrasound Med Biol* **2009**, 35, (7), 1139-1147.
48. Pecorari, C.; Grishenkov, D., *J Acoust Soc Am* **2007**, 122, (4), 2425-2430.
49. G. Paradossi; P. Pellegritti; Trucco, A., *Ultrasound contrast agents - Targeting and processing methods for theranostics*. Springer: **2010**.
50. Cerroni, B.; Chiessi, E.; Margheritelli, S.; Oddo, L.; Paradossi, G., *Biomacromolecules* **2011**, 12, (3), 593-601.
51. Dähne, L.; Egri, G. 10 2011 000 264.2-43, 11. January, **2011**.
52. Glynos, E.; Koutsos, V.; McDicken, W. N.; Moran, C. M.; Pye, S. D.; Ross, J. A.; Sboros, V., *Langmuir* **2009**, 25, (13), 7514-7522.
53. Glynos, E.; Sboros, V.; Koutsos, V., *Mater. Sci. Eng., B* **2009**, 165, (3), 231-234.
54. Sboros, V.; Glynos, E.; Pye, S. D.; Moran, C. M.; Butler, M.; Ross, J.; Short, R.; McDicken, W. N.; Koutsos, V., *Ultrasound Med Biol* **2006**, 32, (4), 579-585.
55. Sboros, V.; Glynos, E.; Pye, S. D.; Moran, C. M.; Butler, M.; Ross, J. A.; McDicken, W. N.; Koutsos, V., *Ultrasonics* **2007**, 46, (4), 349-354.
56. Buchner Santos, E.; Morris, J. K.; Glynos, E.; Sboros, V.; Koutsos, V., *Langmuir* **2012**, 28, (13), 5753-5760.
57. Grant, C. A.; McKendry, J. E.; Evans, S. D., *Soft Matter* **2012**, 8, (5), 1321-1326.
58. McKendry, J. E.; Grant, C. A.; Johnson, B. R. G.; Coletta, P. L.; Evans, J. A.; Evans, S. D., *Bubble Science, Engineering & Technology* **2010**, 2, (2), 48-54.
59. Church, C. C., *J Acoust Soc Am* **1995**, 97, (3), 1510-1521.
60. Hoff, L.; Sontum, P. C.; Hovem, J. M., *J Acoust Soc Am* **2000**, 107, (4), 2272-2280.
61. Schneider, C. A.; Rasband, W. S.; Eliceiri, K. W., *Nat Meth* **2012**, 9, (7), 671-675.
62. Hutter, J. L.; Bechhoefer, J., *Rev. Sci. Instrum.* **1993**, 64, (7), 1868-1873.
63. Ducker, W. A.; Senden, T. J.; Pashley, R. M., *Nature* **1991**, 353, (6341), 239-241.
64. Fernandes, P. A. L.; Tzvetkov, G.; Fink, R. H.; Paradossi, G.; Fery, A., *Langmuir* **2008**, 24, (23), 13677-13682.
65. Graf-Zeiler, B.; Fink, R. H.; Tzvetkov, G., *ChemPhysChem* **2011**, 12, (18), 3503-3509.
66. Tzvetkov, G.; Fernandes, P.; Wenzel, S.; Fery, A.; Paradossi, G.; Fink, R. H., *Phys Chem Chem Phys* **2009**, 11, (7), 1098-1104.
67. Tzvetkov, G.; Graf, B.; Fernandes, P.; Fery, A.; Cavalieri, F.; Paradossi, G.; Fink, R. H., *Soft Matter* **2008**, 4, (3), 510-514.
68. Tzvetkov, G.; Paradossi, G.; Tortora, M.; Fernandes, P.; Fery, A.; Graf-Zeiler, B.; Fink, R. H., *Mat Sci Eng C-Mater* **2010**, 30, (3), 412-416.
69. Cavalieri, F.; Finelli, I.; Tortora, M.; Mozetic, P.; Chiessi, E.; Polizio, F.; Brismar, T. B.; Paradossi, G., *Chemistry of Materials* **2008**, 20, (10), 3254-3258.
70. Smith, A. E.; Zhang, Z.; Thomas, C. R., *Chemical Engineering Science* **2000**, 55, (11), 2031-2041.

71. Dubreuil, F.; Elsner, N.; Fery, A., *Eur. Phys. J. E* **2003**, 12, (2), 215-221.
72. Fery, A.; Dubreuil, F.; Mohwald, H., *New J Phys* **2004**, 6, 13.
73. Pretzl, M.; Neubauer, M.; Tekaat, M.; Kunert, C.; Kuttner, C.; Leon, G.; Berthier, D.; Erni, P.; Ouali, L.; Fery, A., *ACS Appl. Mater. Interfaces* **2012**, 4, (6), 2940-2948.
74. Elsner, N.; Dubreuil, F.; Weinkamer, R.; Fischer, F. D.; Wasicek, F.; Fery, A., *Prog Coll Polym Sci* **2006**, 132, 117-132.
75. Fery, A.; Weinkamer, R., *Polymer* **2007**, 48, 7221-7235.
76. Reissner, E., *Journal of Mathematics and Physics* **1946**, 25, (2), 80-85.
77. Reissner, E., *Journal of Mathematics and Physics* **1946**, 25, (4), 279-300.
78. Bedard, M. F.; Munoz-Javier, A.; Mueller, R.; del Pino, P.; Fery, A.; Parak, W. J.; Skirtach, A. G.; Sukhorukov, G. B., *Soft Matter* **2009**, 5, (1), 148-155.
79. Dubreuil, F.; Shchukin, D. G.; Sukhorukov, G. B.; Fery, A., *Macromol. Rapid Commun.* **2004**, 25, (11), 1078-1081.
80. Krumova, M.; López, D.; Benavente, R.; Mijangos, C.; Pereña, J. M., *Polymer* **2000**, 41, (26), 9265-9272.
81. Hassan, C. M.; Peppas, N. A., *Macromolecules* **2000**, 33, (7), 2472-2479.
82. Morancho, J. M.; Salla, J. M.; Cadenato, A.; Fernández-Francos, X.; Colomer, P.; Calventus, Y.; Ramis, X.; Ruíz, R., *Journal of Applied Polymer Science* **2012**, 124, (S1), E57-E65.
83. Chan, C.-M.; Wu, J.; Li, J.-X.; Cheung, Y.-K., *Polymer* **2002**, 43, (10), 2981-2992.
84. Xie, X.-L.; Liu, Q.-X.; Li, R. K.-Y.; Zhou, X.-P.; Zhang, Q.-X.; Yu, Z.-Z.; Mai, Y.-W., *Polymer* **2004**, 45, (19), 6665-6673.
85. Solomon, M. J.; Almusallam, A. S.; Seefeldt, K. F.; Somwangthanaroj, A.; Varadan, P., *Macromolecules* **2001**, 34, (6), 1864-1872.
86. Liu, H.; Brinson, L. C., *Compos. Sci. Technol.* **2008**, 68, (6), 1502-1512.
87. Liang, J.; Huang, Y.; Zhang, L.; Wang, Y.; Ma, Y.; Guo, T.; Chen, Y., *Adv. Funct. Mater.* **2009**, 19, (14), 2297-2302.
88. Peng, Z.; Kong, L. X.; Li, S. D., *Synthetic Metals* **2005**, 152, (1&2), 25-28.
89. Klibanov, A. L.; Rasche, P. T.; Hughes, M. S.; Wojdyla, J. K.; Galen, K. P.; Wible, J. H.; Brandenburger, G. H., *Invest. Radiol.* **2004**, 39, (3), 187-195.
90. Ferry, J. D., *Viscoelastic Properties of Polymers*. 3rd ed. ed.; Wiley: New York, **1980**.
91. Hoff, L., *Acoustic Characterization of Contrast Agents for Medical Ultrasound Imaging*. Kluwer Academic Publishers: **2002**.
92. Rayleigh, L., *Philosophical Magazine Series 6* **1917**, 34, (200), 94-98.
93. Plesset, M. S., *Journal of Applied Mechanics-Transactions of the Asme* **1949**, 16, (3), 277-282.
94. Schneider, C. A.; Rasband, W. S.; Eliceiri, K. W., *Nat Meth* **9**, (7), 671-675.
95. Smith, A. E.; Zhang, Z.; Thomas, C. R., *Chem. Eng. Sci.* **2000**, 55, (11), 2031-2041.
96. Mercade-Prieto, R.; Nguyen, B.; Allen, R.; York, D.; Preece, J. A.; Goodwin, T. E.; Zhang, Z. B., *Chemical Engineering Science* **2011**, 66, (10), 2042-2049.

97. de Jong, N.; Ten Cate, F. J.; Lancée, C. T.; Roelandt, J. R. T. C.; Bom, N., *Ultrasonics* **1991**, 29, (4), 324-330.
98. Stride, E.; Saffari, N., *IEEE Trans. Ultrason. Ferroelectr. Freq. Control* **2005**, 52, (12), 2332-2345.
99. de Jong, N.; Cornet, R.; Lancée, C. T., *Ultrasonics* **1994**, 32, (6), 447-453.
100. de Jong, N.; Hoff, L.; Skotland, T.; Bom, N., *Ultrasonics* **1992**, 30, (2), 95-103.



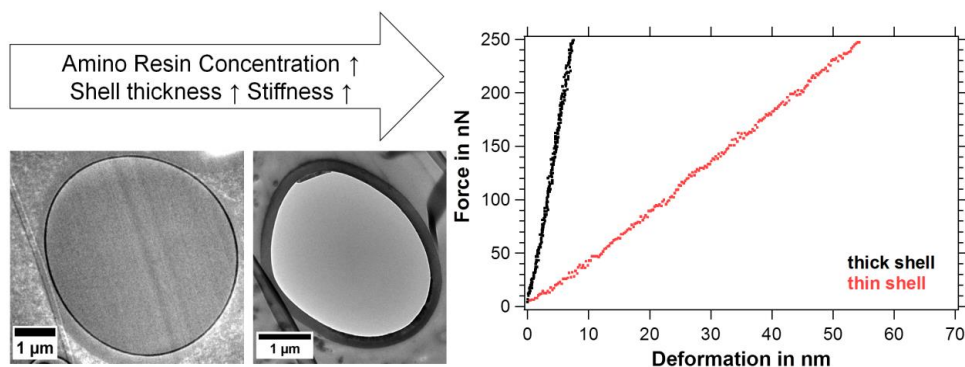
## 7. Formation and Mechanical Characterization of Aminoplast Core/Shell Microcapsules

Melanie Pretzl<sup>1</sup>, Martin Neubauer<sup>1</sup>, Melanie Tekaat<sup>1</sup>, Carmen Kunert<sup>1</sup>, Christian Kuttner<sup>1</sup>, Géraldine Leon<sup>2</sup>, Damien Berthier<sup>2</sup>, Philipp Erni<sup>2</sup>, Lahoussine Ouali<sup>2</sup>,  
Andreas Fery<sup>1\*</sup>

1) Department of Physical Chemistry II, University of Bayreuth, Universitätsstraße 30, D-95447 Bayreuth, Germany

2) Firmenich SA, Cooperate R&D Division, P.O. Box 239, CH-1211 Geneva 8, Switzerland

Published in: ACS Applied Materials & Interfaces **2012**, 4(6), 2940-2948



## **Abstract**

This work aims at establishing a link between process conditions and resulting micromechanical properties for aminoplast core/shell microcapsules. The investigated capsules were produced by the in situ polymerization of melamine formaldehyde resins, which represents a widely used and industrially relevant approach in the field of microencapsulation. Within our study, we present a quantitative morphological analysis of the capsules' size and shell thickness. The diameter of the investigated capsules ranged from 10 to 50  $\mu\text{m}$  and the shell thickness was found in a range between 50 and 200 nm. As key parameter for the control of the shell thickness, we identified the amount of amino resin per total surface area of the dispersed phase. Mechanical properties were investigated using small deformations on the order of the shell thickness by atomic force microscopy with a colloidal probe setup. The obtained capsule stiffness increased with an increasing shell thickness from 2 to 30 N/m and thus showed the same trend on the process parameters as the shell thickness. A simple analytical model was adopted to explain the relation between capsules' geometry and mechanics and to estimate the elastic modulus of the shell about 1.7 GPa. Thus, this work provides strategies for a rational design of microcapsule mechanics.

## 7.1 Introduction

Microcapsules are of broad interest not only in fundamental science<sup>1,2</sup>, but as well in a wide range of applications. Whenever the functionality of an active substance needs to be protected and/or a controlled release is demanded, microencapsulation is a frequently used solution.<sup>3-10</sup> Industrial relevant wall materials are amino resins, like melamine formaldehyde (MF), because this class of resins is produced from cheap raw materials, widely applicable, and economical to use.<sup>10</sup> In particular, aminoplast core/shell microcapsules are suitable for the encapsulation of pressure sensitive recording materials<sup>10</sup>, perfume fragrances<sup>11, 12</sup>, phase change materials<sup>13, 14</sup>, self healing composites<sup>15, 16</sup>, agrochemicals<sup>17</sup> or analytes in biosensors<sup>18</sup>. All these applications require a particular mechanical stability, compliance, release, shelf life, and adhesion of the microcapsules.<sup>19, 20</sup> Therefore, a rational process design of microcapsules is desired to individually tailor their mechanical properties<sup>21</sup>. In order to establish correlations between process parameters and the resulting capsule mechanics, methods are favored that allow an investigation of microcapsule mechanics on the single-particle level.<sup>20</sup>

So far, reported mechanical characterizations on aminoplast microcapsules were focused on compression experiments with the single capsule compression apparatus described by Keller and Sottos<sup>22</sup> and the micromanipulation technique described by Zhang and co-workers<sup>23</sup>. With both setups, individual microcapsules were deformed in the range of micrometers under applied force loads of millinewtons. Thus, the authors were able to access a deformation regime where rupture forces and the failure of microcapsules can be successfully determined.<sup>24-28</sup> To understand how our approach differs from the ones used in previous studies, the definition of the terms *small deformation* and *large deformation* is crucial. In general, the mechanical response of a material can be elastic or plastic. In brief, an elastic response is characterized by a full recovery of the material's original shape while a plastic response is accompanied by a permanent change of the material's shape (e.g. buckling or capsule failure). In material sciences, small deformations are often referred to compression tests carried out in the elastic regime. We would like to stress that for our approach the critical parameter used for the definition of small and large deformations is the microcapsule's shell thickness and not the yield point, which describes the transition between the elastic and plastic regime. Hence, small

deformations are understood in this publication as compressions below or on the order of the shell thickness and large deformations as compressions larger than the shell thickness. There is one pioneering paper by Mercadé-Prieto<sup>29</sup> where finite element modeling has been used to estimate the wall thickness to radius ratio and the elastic modulus of individual capsules from compression experiments in the elastic regime. We appreciate the approach of the authors because it offers the possibility to estimate the critical mechanical parameters for individual capsules. However, also for this publication the included experimental data concentrates on fractional deformations between small deformations on the order of the shell thickness and very high deformations.<sup>29</sup>

In contrast to previous studies, our interest is concentrated on the mechanical response of capsules in the small deformation regime, which refers to a compression of the capsule on the order of the shell thickness. This regime has not yet been explored for aminoplast microcapsules, which is unfortunate, because it offers the possibility to link the capsules' mechanical response to its geometric design. For polyelectrolyte multilayer capsules it has been shown<sup>30</sup> that this regime is also relevant for adhesion properties. Atomic force microscopy (AFM) is an ideal tool to carry out deformations of capsules on the order of the shell thickness, because it offers a displacement resolution of nanometers and a force resolution of piconewtons. The compression apparatuses used in previous studies show with a resolution of a few hundred nanonewtons a sufficient resolution to investigate the elastic response of many capsule systems. Indeed the limiting factor for small deformation experiments is also often not the force resolution but the resolution of the induced deformation.

Several strategies exist for the synthesis of aminoplast core/shell microcapsules<sup>10, 31</sup>, but the most applied and industrially relevant is the in situ polymerization<sup>32, 33</sup>, which sometimes is also referred to as phase separation method<sup>12</sup>. In this emulsion-templated process, the hydrophobic core material is dispersed in form of small oil droplets in the aqueous continuous phase, where the MF prepolymer is dissolved. The polycondensation of the prepolymers starts under acidic conditions and elevated temperatures. Formed oligomers are deposited at the oil/water interface, where they polymerize to a three-dimensional shell around the oil droplet<sup>13, 34</sup>. To control capsule mechanics process parameters are interesting that affect size, shell thickness and the elastic modulus of the wall material. Typically, a polydispersity in size is

observed for capsules manufactured with the in situ polymerization. These size distributions are determined by the produced emulsion droplets, which serve as soft templates for the buildup of the shell. Key parameters for the adjustment of the emulsion droplet size are the interfacial tension between core and continuous phase and the energy dissipation of the stirrer<sup>13, 27</sup>. In general, the in situ polymerization yields aminoplast microcapsules between 5 and 50 micrometers<sup>32</sup>, where smaller capsules show narrower size distributions than larger capsules<sup>35</sup>. The shell thickness is expected to be between 30 and 300 nanometers<sup>32</sup> and can be adjusted by the ratio of melamine to formaldehyde<sup>12</sup>, the reaction time<sup>24</sup>, pH<sup>34</sup>, and the core to shell mass ratio per created surface area of the emulsion droplets<sup>13</sup>. The elastic modulus of the shell depends on the used wall material<sup>36</sup> and can be changed through chemical modifications and/or the cross linking density.

In this paper, we investigate aminoplast core/shell microcapsules and strategies to rationally design their mechanical properties. The motivation to focus on aminoplast core/shell microcapsules is based on their regular application in different industrial fields<sup>5, 11</sup>. Challenging for the presented work was the polydispersity of the studied capsules that is very well reflecting the actual industrial situation for amino resin microcapsules produced by an emulsion-templated in situ polymerization. Structure property relations are often not efficiently resolved by standard methods employed during industrial quality assurance. Therefore, the characterization on the single particle level is crucial for such size-dispersed systems. For this reason, we have chosen methods that are able to resolve and quantify the geometry and mechanics of single microcapsules. In particular, we used transmission electron microscopy (TEM) to determine the shell thickness from ultrathin sections of epon-embedded microcapsules. With AFM and a colloidal probe setup we studied the mechanical response of single capsules in the small deformation regime, which refers to a capsule compressions on the order of the shell thickness. Subsequently, we correlated the obtained shell thickness with the process parameters and then via a simple analytical model with the resulting capsule mechanics. The full correlation between process parameters and resulting mechanical properties suggests strategies to rationally tailor microcapsules produced by an industrial relevant process.

## 7.2 Experimental

**Materials.** The key ingredients for the microcapsules synthesis are the melamine-formaldehyde resin (Urecoll SMV, BASF); a colloidal stabilizer (Poly(acrylamide 20%, acrylic acid 80%) sodium salt, Sigma Aldrich); a formaldehyde scavenger (ethylene urea, Fluka); acetic acid and sodium hydroxide for pH adjustments. The core liquid is a mixture of a 5-‘model’ fragrance compound, as described previously<sup>5</sup>: hexyl salicylate 20% w/w, (+-)-methyl 2,2-dimethyl-6-methylene-1-cyclohexanecarboxylate 20% w/w (Romascone), 3-(4-tert-butylphenyl)-2-methylpropanal 20% w/w (Lilial), cis/trans-4-tert-butyl-1-cyclohexyl acetate 20% w/w (Vertenex) and (+-)-2-tert-butyl-1-cyclohexyl acetate 20% w/w (Verdox). As dispersant we used demineralized water.

**Synthesis of microcapsules.** Standard core/shell capsules were synthesized according to protocols described previously.<sup>12, 32, 33</sup> The specified amounts of the resin, colloidal stabilizer, and water were introduced into a 250 ml reactor at room temperature (pH = 7.50). The reaction mixture was sheared at 800 rpm with an anchor stirrer. A resin to oil mass ratio of 0.149 g/g was chosen for the standard core/shell capsules. Then acetic acid (0.78 g) was added for the adjustment of the pH (pH = 5.14). The perfume oil (95.00 g) containing Rhodamine (0.1% w/w, Fluka) was added, and the reaction mixture was warmed up to 40°C and stirred for 1 hour. Afterwards the reaction mixture was stirred at 55°C for 3 hours. Finally, ethylene urea (50% in water w/w, 16.00 g) was added, and the reaction mixture was stirred at 60°C for 1 hour. Then, the mixture was cooled down to room temperature (pH = 5.65) and neutralized with NaOH (30% in water w/w, 0.92 g) to give a final pH of 6.57 in the aqueous dispersion.

**Morphological Characterization.** Size distributions were determined with a Flow Particle Image Analyzer FPIA (Sysmex FPIA-300, Malvern Instruments). Zeta potential measurements (Zetasizer, Malvern) of the diluted capsule slurries yielded negative values, which typically range from -30 to -50 mV (see Table 7-1). With TEM (Zeiss CEM 902) thin sections of about 50 nm to 60 nm, produced by an ultracut microtome (Leica EM UC7), were imaged at 80 eV. The shell thickness was obtained from TEM images by extracting cross-sectional gray value profiles that were analyzed with ImageJ software. The start/end of the shell was determined at 50%

decrease/increase of the gray value intensity. TEM samples were prepared by mixing the capsule solution in a 1:1 ratio with 2% aqueous solution of agar (Agar Noble, Difco). After curing, the flexible gel was cut with a scalpel into small cubes. Next, the agar-embedded capsules were solidified by one hour incubation with a 2% glutaraldehyde solution (Serva Electrophoresis GmbH) in phosphate buffer (0.05 M Phosphate Buffer, pH 7.4 Merck). Afterwards three washing steps with phosphate buffer (0.05 M, pH 7.4, Merck) were used to remove the excess of glutaraldehyde. Then the samples were dehydrated in ethanol-water mixtures with increasing ethanol content (30% / 50% / 70% / 95%) and three times to pure ethanol (VWR International). The dehydration exposure time was 15 minutes for each step. Then the dried samples were mixed with Epon 812 (Serva Electrophoresis GmbH): Epon 812/ethanol mixture (1:1) for 12 hours, followed by an Epon 812/ethanol mixture (3:1) for 3-4 hours and finished with three immersion steps (3-4 hours) in 100% Epon 812.

**Mechanical Characterization.** Force spectroscopy experiments were performed in aqueous environment with a commercial AFM setup: Nanowizard (JPK Instruments, Germany) combined with an inverted optical microscope Axiovert 200 (Zeiss, Germany). The optical microscope was used to determine the size of the microcapsule before the deformation experiment and to align the cantilever probe with the center of the immobilized microcapsule. During the capsules' compression we used the microinterferometry<sup>37</sup> mode of the microscope to follow in situ the change of the apparent contact area between microcapsule and substrate. Only elastic and uniform capsule deformations were used for evaluation. The deformations were performed using the colloidal probe technique<sup>38,39</sup>, in which silica particles (diameter 30-40  $\mu\text{m}$ ; Polysciences Inc., USA) were attached to tipless silicon cantilevers (ACT-TL,  $k_c = 25\text{-}75\text{ N/m}$ ,  $f_c = 200\text{-}400\text{ kHz}$ , AppNano). The colloids were attached using a micromanipulator (MP-285; Sutter Instruments) and two-component epoxy glue (UHU Plus Endfest 300, UHU GmbH & Co. KG, Germany). After attachment, the colloidal probe cantilevers were cleaned by exposure to atmospheric plasma (5 min, high intensity, Plasma Technology). Spring constants of the cantilevers were determined with the thermal noise method<sup>40, 41</sup>, which is implemented in the commercial JPK software. Only cantilevers were used that were in accordance with the frequency and spring constant range reported by the manufacturer. The

experiments in aqueous solution were carried out in liquid cells, made of a plastic ring (diameter 24 mm, height 5 mm) and a cover slip (diameter 24 mm, thickness 0.13-0.16 mm, Menzel). The liquid cells were cleaned with an isopropanol/ethanol/water mixture (1:1:1) and through exposure to an atmospheric plasma (5 min, high intensity, Plasma Technology). To keep the negatively charged microcapsules immobilized in the liquid cell we used branched polyethyleneimine (PEI,  $M_w$  25.000 g/mol, 1g/L aqueous solution, Sigma Aldrich) as surface coating. To obtain individual and separated microcapsules for force spectroscopy experiments and to remove non-immobilized capsules the sample was washed several times with purified water (Millipore Advantage) in the liquid cell. Reference curves on hard substrates were obtained before and after each capsule deformation to ensure a constant optical lever sensitivity, which is necessary for reliable and comparable force deformation curves<sup>42</sup>.

## 7.3 Result and Discussion

### 7.3.1 Morphology of Aminoplast Core/Shell Microcapsules.

As mentioned in the introduction the size, shell thickness and the used wall material are important parameters for the mechanics of microcapsules. A possible parameter to adjust the shell thickness of aminoplast microcapsules is the resin concentration<sup>13</sup>. For the microcapsules production the fragrance oil is dispersed by emulsification in the continuous aqueous phase. The melamine formaldehyde prepolymer, which is dissolved in the continuous phase, will start to form oligomers under acidic conditions and elevated temperatures. These oligomers then deposit at the oil/water interface of the emulsified droplets and form under further condensation an impermeable shell around the fragrant oil. The typical amount of melamine formaldehyde resin<sup>11</sup> used for this encapsulation is here referred to as 100% or standard amount. The resin amount was decreased from 100% to 75% to 50% and 25% to obtain microcapsules with thinner shells. All other process parameters were kept constant.

The dispersity in size of the studied microcapsules is typical for an emulsion droplet based in situ polymerization. Microcapsules with smaller average diameters show a narrower size distribution than capsules with larger average diameters<sup>43, 44</sup>. Figure 7-1 presents the optical micrographs and size distributions of the produced capsules with a corresponding average diameter  $d$  for each sample size distribution summarized in Table 7-1. The size distributions of two additional samples produced from 100% and 50% amount of amino resin are indicated in the Table 7-1, but not shown in Figure 7-1. In particular, we observed for the produced capsules a mean diameter  $d_{\text{mean}}$  of about 30 micrometers. Samples that significantly deviated from this mean diameter were microcapsules produced from 75% and 25% amino resin with an average diameter of 18  $\mu\text{m}$  and 43  $\mu\text{m}$  respectively. Such variations in size as well as the dispersity of the microcapsules are well known and reflect the actual situation for their industrial production, which already has been reported previously.<sup>13, 44</sup> The success and/or failure of the encapsulation process are clearly indicated in the optical micrographs in Figure 7-1.

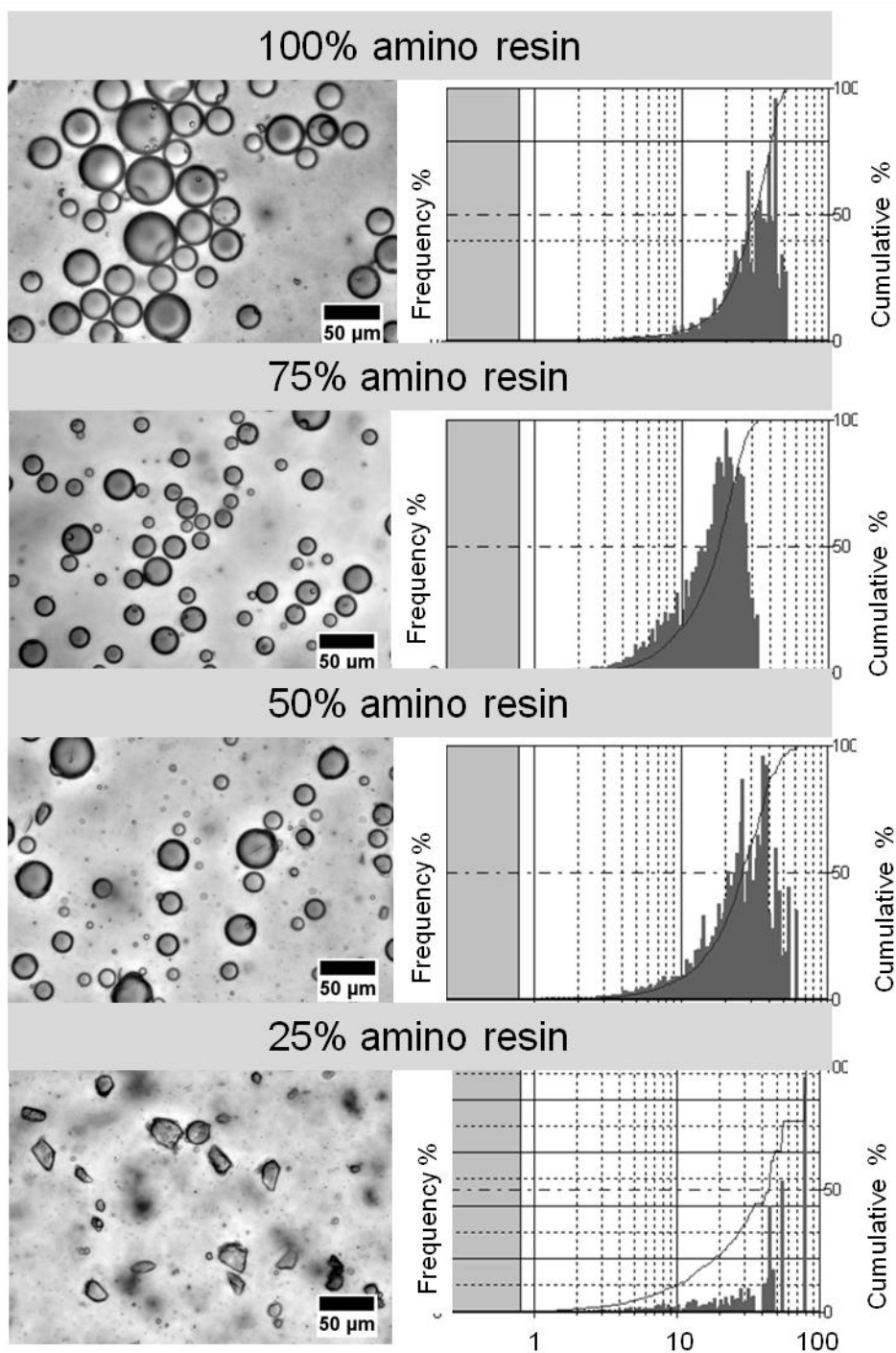


Figure 7-1: Optical micrographs and size distributions of the produced aminoplast core/shell microcapsules. For a 25% level of amino resin, the encapsulation process failed and microcapsules with a deformed capsule shape were produced that were not able to form a stable shell around the dispersed oil droplets.

Spherical-shaped capsules with an amino resin level of 100%, 75% and 50% indicate a successful encapsulation of the oil phase. The shape of the microcapsules produced from a 25% level of amino resin was in contrast to the other batches strongly

deformed as illustrated by the optical micrographs in Figure 7-1. Here the encapsulation process was not successful, and the formed shell was not stable enough to encapsulate the oil phase.

To access the shell thickness of the microcapsules we used ultrathin sections of epon-embedded microcapsules, which we analyzed with TEM. In Figure 7-2 examples of such sections are shown for capsules produced from different amount of amino resin. For all investigated samples, we observed a smooth shell with uniform density and rather uniform thickness. For microcapsules produced from 25% amino resin we were not able to obtain any ultrathin sections of the embedded capsules. The measured shell thickness of one section is denoted  $h_i$  and refers to an average of six analyzed cross-sections, which were extracted from one TEM image. With this method, we were able to determine the shell thickness  $h_i$  with an accuracy of 12%. For each microcapsule batch, we used  $n$  number of sections to quantify the shell thickness indicated in the histograms displayed in Figure 7-2. All samples showed a normal distribution of  $h_i$  and allowed us to determine a mean measured shell thickness  $h_i$  from the maximum of the gauss fit.

In general, we observed a decrease of the mean measured shell thickness  $h_i$  from 285 nm to 103 nm when we reduced the amount of amino resin from 100% to 50%. The observed mean shell thickness can be found in Table 7-1. In Figure 7-2, we grouped our results according to the employed amount of amino resin and the average capsule diameter. The size distribution of the produced capsules is as important as the resin concentration for the final shell thickness of the capsules. If the volume of the dispersed phase and the resin concentration were constant, thinner shells would be expected for batches with smaller capsules compared to those with larger capsules.<sup>13</sup> The change in thickness is caused by the change in the total surface area of the dispersed phase available during the polymerization reaction, which will be larger for smaller emulsion droplets than for larger droplets. We observed this trend as well for the two samples produced from 100% amino resin, where the mean shell thickness was reduced from 285 nm to 215 nm, when the average diameter of the capsules decreased from 34  $\mu\text{m}$  to 31  $\mu\text{m}$ , as indicated in Figure 7-2. For both samples the average diameter was reproduced, as for capsules made of 50% amino resin and average diameter of 28  $\mu\text{m}$ , no significant difference in the shell thickness was

observed. Therefore, we combined  $h_i$  values of both samples in one diagram, shown in Figure 7-2.

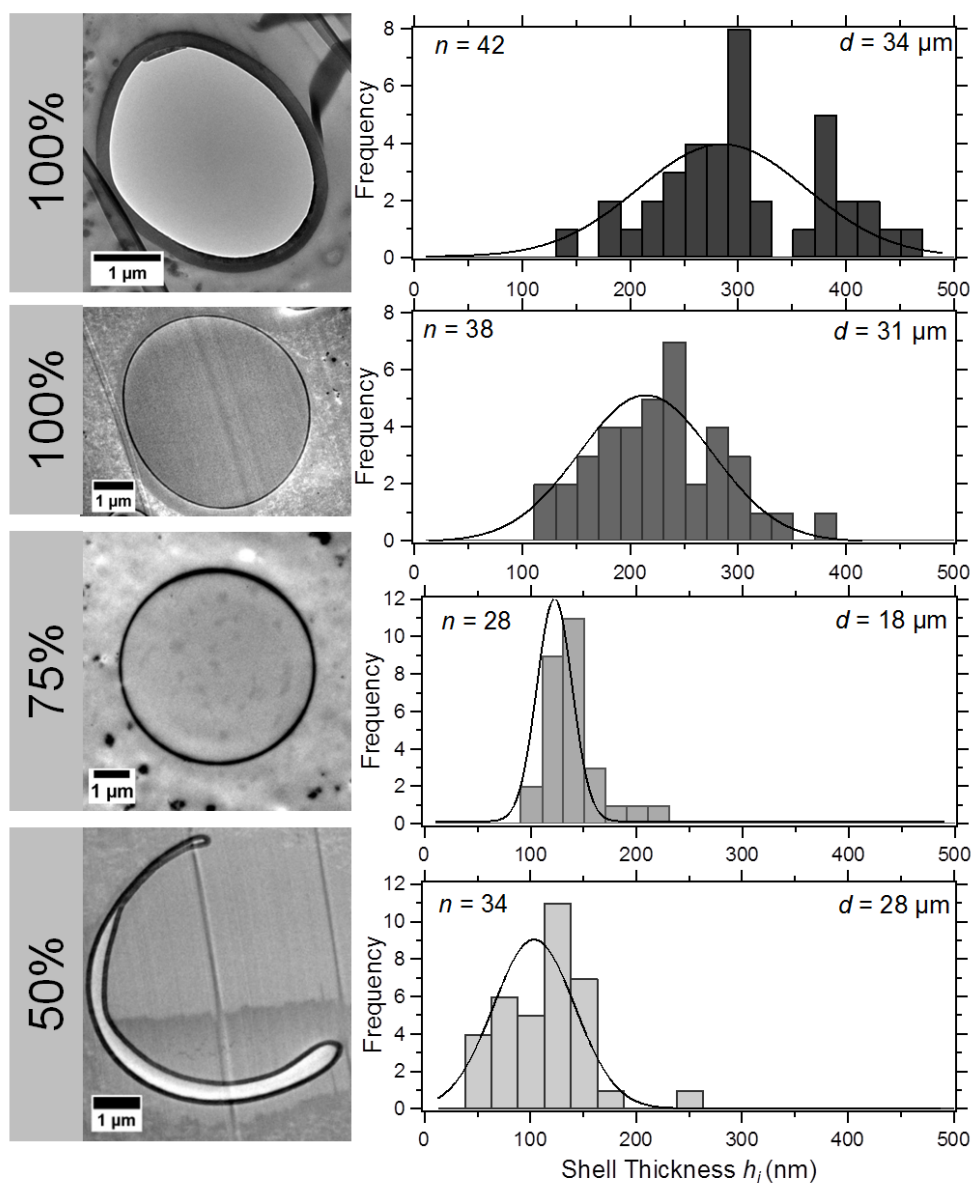


Figure 7-2: TEM images of embedded microcapsules sectioned with an ultra microtome and the quantified distribution of the measured shell thickness. The number of analyzed sections  $n$  is indicated along with the used amount of resin in percentage and the average diameter  $d$ .

When spherical particles are sectioned at random distance from the center, the measured diameter  $r_i$  will be smaller than the true diameter  $r$  and the measured thickness  $h_i$  will be larger than the true thickness  $h$ . On average, we obtained a standard deviation of the mean measured shell thickness of about 26%. This deviation is higher than the accuracy of the method of 12% and reflects the uncertainty of the

random sectioning process. Smith and co-workers<sup>45</sup> introduced a correction factor accounting for the thickness artifacts produced by the random slicing process. The shell thickness  $h$  can be described as a function of the slicing angle, the measured radius, and the measured shell thickness. With an estimated limit for the slicing angle about  $80^\circ$ , we determined the correction factor  $f$  to be about 0.62. The obtained correction factor for each batch and the corresponding corrected shell thickness  $h$  can be found in Table 7-1.

Table 7-1: Microcapsules prepared with different amounts of resin and the obtained results from the morphological and mechanical characterization: average diameter  $d$ , zeta potential  $\zeta$ , measured shell thickness  $h_i$ , correction factor  $f$ , corrected shell thickness  $h$  and capsule stiffness  $F/D$ :

Amino resin (%)	Perfume (%)	$d$ ( $\mu\text{m}$ )	$\zeta$ (mV)	$h_i$ (nm)*	$f$	$h$ (nm)	$F/D$ (N/m)
100	43.5	34	-48	285 ± 71	0.64	182	29 ± 11
100	45.3	31	-50	214 ± 61	0.57	122	19 ± 7
75	43.5	18	-48	122 ± 16	0.63	77	5.2 ± 2.0
50	44.8	28	-46	103 ± 38	0.63	65	1.7 ± 3
50	46.4	28	-56	103 ± 38	0.63	65	1.7 ± 3
25	47.9	43	-28	-	-	-	-

\* The standard deviation  $\sigma$  of the thickness distribution refers to the fit coefficient width  $w$  by the following relation  $\sigma = w/(2^{1/2})$ .

To estimate the available mean total surface area we used for calculation a mean diameter of 30  $\mu\text{m}$ , mean mass of 95 g and a density of 0.96 g/mL for the used

fragrance composition. For a constant volume of the dispersed phase, the total surface area of the emulsion droplets will decrease with increasing particle radius. In equation 1, the change of the total surface area  $A_{\text{total}}$  of microcapsules is shown when their radius is changed from  $r_1$  to  $r_2$ . The index 1 refers to capsules characterized by the radius  $r_1$  and index 2 to the capsule characterized by the radius  $r_2$ .  $A_{\text{total}}$  of the dispersed phase can be described by the surface area  $A_1$  of the individual oil droplets multiplied by the number  $n$  of droplets. The number  $n$  of particles is obtained by the volume of the dispersed phase  $V$  divided by the volume of the dispersed particles  $V_1$ . With regard to the application the volume of the dispersed phase  $V$  can be easily controlled at the start of the synthesis and the mean radius of micrometer-sized capsules that is determined by the emulsion droplet size can be assessed by standard techniques for quality assurance. As equation 1 shows, the ratio of the total surface area for microcapsules with different diameters is the same like the ratio between the two capsule radii when the volume of the dispersed phase is constant:

$$A_{1,\text{total}}/A_{2,\text{total}} = (n_1A_1/n_2A_2) = (V/V_1)A_1/(V/V_2)A_2 = r_2/r_1 \quad (1)$$

with  $V_1 = V_2 = V$ ;  $V_i = 4/3\pi r_i^3$ ; and  $A_i = 4\pi r_i^2$  it follows for  $A_i/V_i = (4\pi r_i^2)/(4/3\pi r_i^3) = 3/r_i$

For the production of the studied capsules, the volume of the dispersed phase was constant for the different amounts of amino resin. For microcapsules that showed a deviation from the expected mean radius of 30  $\mu\text{m}$  the average total surface area could be corrected by the ratio of the capsule radii, where  $r_1$  refers to the expected mean capsule radius and  $r_2$  to the radius of the actual produced microcapsules. Figure 7-3 describes the shell thickness as a function of the amount of amino resin per total surface area. Both results of the measured and the corrected shell thickness are displayed. As trend, we can observe an increase of the shell thickness with an increase of the MF amount per total surface area, which was already reported for MF microcapsules by Sgraia *et al*<sup>13</sup>. In view of the complex nature of the manufacturing process inherent to the application-oriented study and the characterization method, the observed error margins are to be expected. We are confident that our analysis of a relatively large number of sections and the performed correction of the random sectioning process takes these variations into account. The morphological characterization and the correlation to simple and accessible process parameters

showed that it is possible to adjust and predict the thickness for the investigated process. Both analysis and correlation provide strategies to realize an adjustment of the shell thickness for microcapsules produced by in situ polymerization.

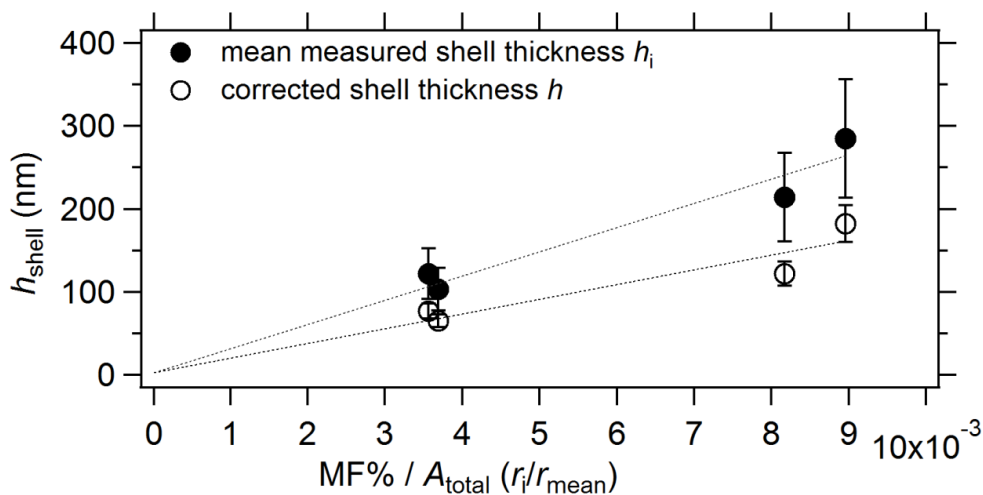


Figure 7-3: Shell thickness is a function of the ratio of resin amount (MF%) per total surface area of the dispersed phase. The lines were added as a guide to the eye.

### 7.3.2 Mechanical Properties.

The mechanical response of immobilized microcapsules was studied by force-deformation experiments with atomic force microscopy (AFM). We used cantilevers modified with a colloidal probe to ensure an axisymmetric and uniform compression of the microcapsules. An AFM mounted on an optical microscope ensures optical control over the alignment of probe and sample. Immobilized capsules were recognized by the presence of an apparent contact area, which was observed with the microscope in microinterferometry mode<sup>37</sup>. In Figure 7-4 the typical change of the apparent contact area for an elastic response of the microcapsule is shown. The time in seconds displayed on the  $x$ -axis corresponds to the length of the video that can be found in the Supporting Information. The apparent contact area refers to the dark spot in the middle of the interference pattern, shown in the insets in Figure 7-4. During the first five seconds there is no compression of the capsule and the contact area shows the immobilized capsule in uncompressed state. After five seconds the cantilever reaches the capsule and the contact area linearly increases with further compression until the maximum deformation is reached. The cantilever retraction ends the deformation cycle and indicates the same curve progression as for the

compression. The apparent contact area returns to its initial state before it is deformed again. The constant and periodic change of the apparent contact area during the presented three consecutive load-unload cycles clearly indicates a uniform and elastic compression of the capsule and the recovery of its original contact area and shape.

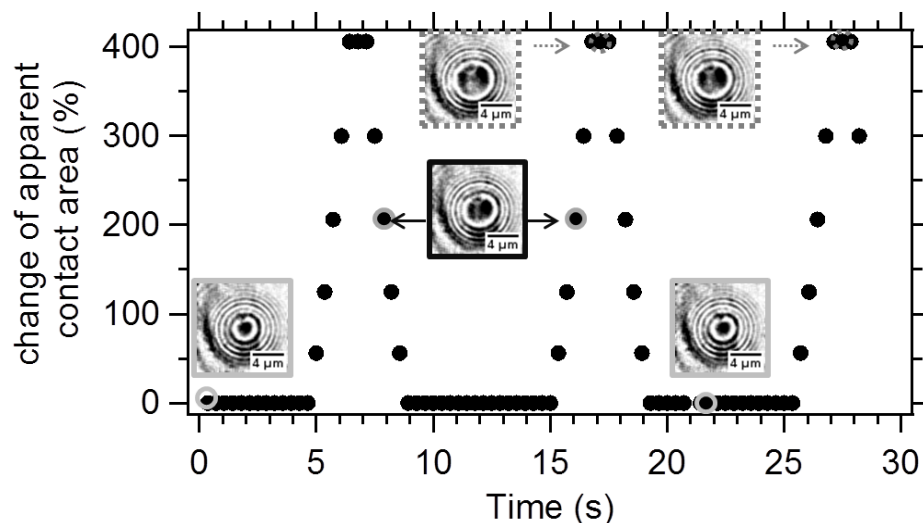


Figure 7-4: Uniform and elastic deformation of a microcapsule observed with an optical microscope using microinterferometry (corresponds to the video in the Supporting Information file). The investigated capsule with a diameter of  $30\ \mu\text{m}$  was deformed by  $870\ \text{nm}$ , corresponding to a relative deformation of  $2.91\%$ .

To assess the mechanical properties of the microcapsule shell we performed all deformation experiments in the small deformation regime. For our approach as already highlighted in the introduction, the critical parameter to distinguish between small and large deformations is the shell thickness. In Figure 7-5 (A) the deformation process of a thick-shelled and a thin-shelled microcapsule is illustrated. As expected for capsules with comparable size, the thin-shelled capsule deforms stronger than the thick-shelled capsule under the same force load. In this example, the thick-shelled capsules synthesized from the standard amount of amino resin show a mean shell thickness about  $185\ \text{nm}$ . The thin-shelled microcapsules were produced from MF 50% and refer to a thin shell with about  $65\ \text{nm}$ . The capsule with the thick shell deforms less than  $10\ \text{nm}$  while the capsule with a thin shell deforms by  $50\ \text{nm}$ . In both cases, we observe a linear increase of the deformation with increasing load force, which represents a typical scaling behavior for a capsule deformation in the small deformation regime<sup>46</sup>.

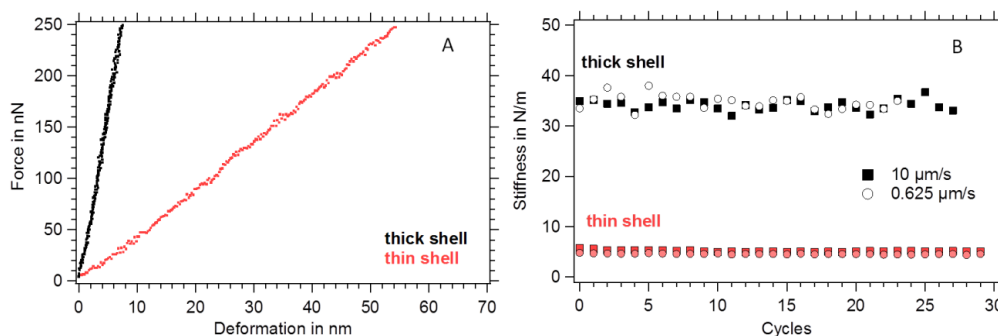


Figure 7-5 (A) Compression of capsules under the same force will yield larger deformations for thin-shelled capsules compared with thick-shelled capsules. (B) Microcapsules compression is elastic and the stiffness is constant over thirty load–unload cycles.

The slope of the force-deformation curves reflects the compression of the capsule under the applied force load, referred to as the capsule's stiffness in units of N/m. In Figure 7-5 (B), thirty repeated force deformation cycles of the thin- and thick-shelled capsules are shown. The observed stiffness values are constant for both capsules throughout the repeated compression, illustrating that no altering of the capsules' stiffness is obtained through consecutive deformation. We also investigated the influence of fast and slow deformation rate on the microcapsules' stiffness. The used deformation rates of 10  $\mu\text{m/s}$  and 0.625  $\mu\text{m/s}$  did not significantly affect the mechanical response of thick-shelled microcapsules. For thin-shelled capsules, we observed an increase of the stiffness about 12% for fast deformation rates.

To quantify the stiffness of the capsules produced from different amount of amino resin, we measured a representative number  $n$  of aminoplast microcapsules with a slow deformation rate of 0.5  $\mu\text{m/s}$ . In Figure 7-6, the distributions of the measured stiffness values present a decrease of the mean stiffness from about 30 N/m to 2 N/m for a change of the shells thickness from 285 nm to 103 nm respectively. The capsules' stiffness strongly depends on the capsules' diameter. Hence, smaller microcapsules will be stiffer than larger capsules, if they were produced from the same batch and have the same shell thickness. For example, standard core/shell microcapsules with a mean shell thickness of 214 nm showed an increase in the capsule stiffness from 14 N/m to 35 N/m when the diameter of the capsule was decreased from 30  $\mu\text{m}$  to 14  $\mu\text{m}$ . Therefore, the width of the stiffness histograms is also reflecting the size distribution of the capsules within one batch. The mean

stiffness value determined from the histogram for each capsule batch can be found in Table 7-1.

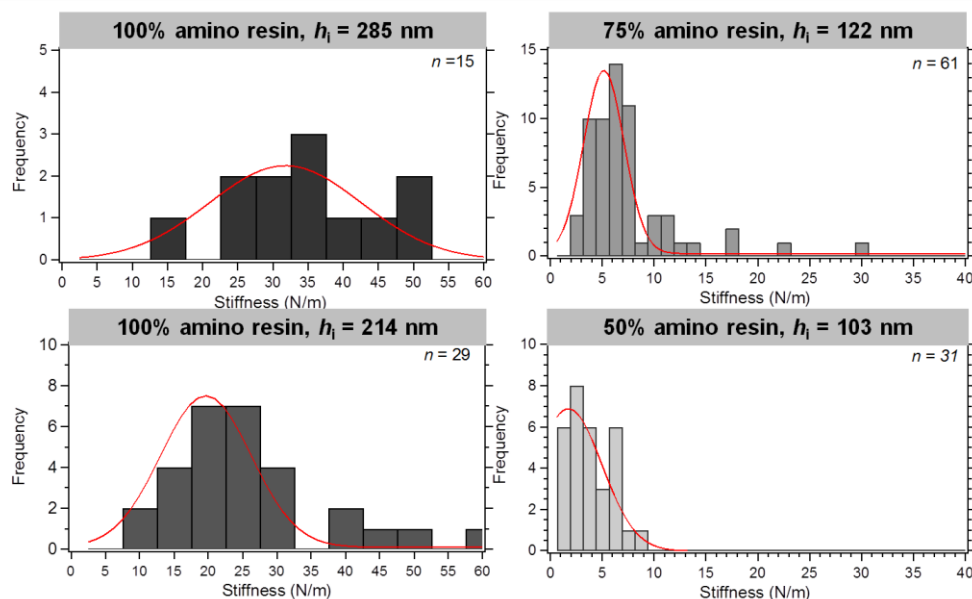


Figure 7-6: Capsules become softer with thinner shells, shown by the decrease of the mean stiffness for capsules with reduced shell thickness.

In Figure 7-7 all results obtained from the morphological and mechanical characterization of the aminoplast capsules are displayed in relation to the used process parameters. Both shell thickness and capsule stiffness increase with the amount of amino resin per total surface area. It already has been shown<sup>30</sup> that properties determined in the small deformation regime play an important role for macroscopic properties such as the capsule's adhesion. In the case of melamine-formaldehyde-shelled microcapsules, with a uniform, closed, and rather strong shell, it would be interesting to link the results gained from the small deformation regime with the already well investigated rupture force of aminoplast microcapsules<sup>22, 23</sup>.

Zhang and co-workers<sup>23, 29</sup> showed that the deformation at burst is one of the key parameters for the rupture of aminoplast microcapsules. As discussed before the deformation behavior of microcapsules is strongly linked to the thickness of their shell, as shown in Figure 7-5 (A), where thin-shelled capsules deform much more under an applied load than thick-shelled capsules. Microcapsules burst when a critical compression is reached, which was for melamine formaldehyde capsules reported by Zhang about 68% relative deformation at burst. The force loads needed for a burst

will be reached for smaller force loads in the case of thin-shelled capsules compared with thick-shelled capsules. Therefore, the observed correlations present a potential strategy to be further linked with the reported macroscopic rupture forces. Such a relation would be beneficial for the tailoring of aminoplast microcapsule mechanics used in various applications with very different requirements.

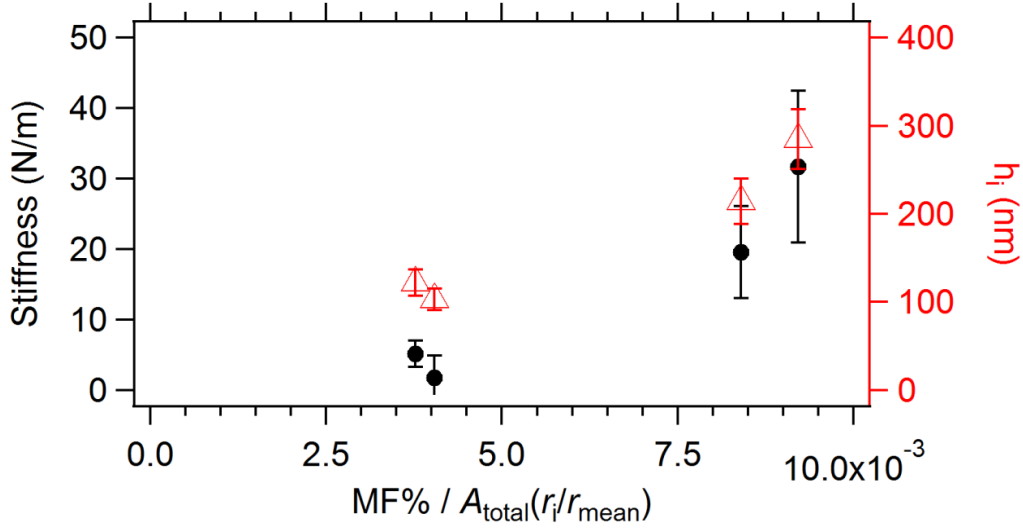


Figure 7-7: Summary of the morphological and mechanical characterization

The tendency observed in Figure 7-7 can be further analyzed to understand how the shell thickness influences the microcapsule mechanics. The mechanical response obtained from the small deformation regime can be used to understand structure property relations, because the mechanical response can be linked to the capsule's geometry and the shell's material properties.<sup>20</sup> According to Reissner the measured stiffness  $F/D$  is a function of the capsules geometric parameters, radius  $R$  and the shell thickness  $h$  and the properties of the shell material, elastic modulus  $E$  and Poisson ratio  $\nu$ :

$$FD^{-1} = (h_{\text{shell}}^2 R^{-1})(E(3(1-\nu^2)/4)^{-1/2}) \quad (2)$$

As described in a previous study<sup>46</sup> the regime valid for Reissner's prediction<sup>47, 48</sup> of a linear scaling behavior of the applied force  $F$  with the resulting deformation  $D$  can be easily estimated based on the shell thickness  $h$  and the radius  $r$  of the capsule:

$$\varepsilon_{\text{crossover}} \approx (h/(4\pi r))^{1/2} \quad (3)$$

A critical relative deformation  $\varepsilon$  is obtained that refers to the crossover of the linear deformation regime with the deformation caused by volume forces, which scales proportional to  $D^3$ . Thus, the morphological characterization can be used to estimate the deformation regime where Reissner's prediction is valid.

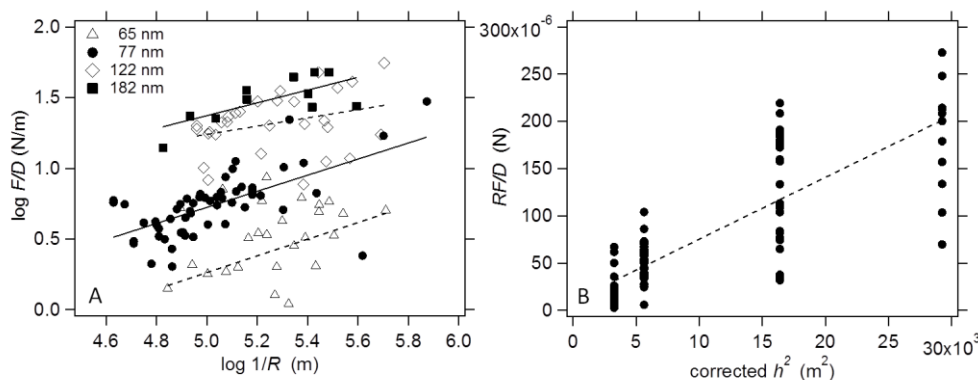


Figure 7-8 (A) Stiffness displayed in relation to the reciprocal radius clearly indicates an increase in the stiffness for capsules with thicker shell and comparable radius. (B) Linear relationship displayed in this graph can be correlated to the material constants of the shell material and an elastic modulus of 1.7 GPa can be estimated.

In Figure 7-8 (A) the measured stiffness is displayed in relation to the capsule radius. All samples show an increase in the stiffness with decreasing capsule diameter, which is in accordance with Reissner's model. The linear relation is then described by the proportionality factor, which is the square of the shell thickness and the material constants  $E$  and  $\nu$ . The stiffness of microcapsules with comparable diameters increases with increasing shell thickness as Figure 7-8 (A) clearly indicates. The stiffness normalized by the size plotted versus the shell thickness shows a linear relation that can be used to estimate Young's modulus of the microcapsules' shell Figure 7-8 (B).<sup>41, 49</sup> The Poisson ratio  $\nu$  is expected to be between 0.33 for a solid-like material and 0.5 for rubber-like materials. Equation 2 describes the impact of Poisson's ratio on the resulting elastic modulus. In order to make the impact of  $\nu$  transparent, we calculated the elastic modulus for both extremes. From Figure 7-8 (B) we are able to estimate the elastic modulus of the shell material of about 1.7 GPa for a Poisson ratio of 0.5, which is in good agreement with the elastic modulus reported recently by Mercadé-Prieto *et al.*<sup>29</sup>, and for a Poisson ratio 0.33 of about 2.2 GPa. However, as Figure 7-8 displays a certain spread of the individual data remains even after the normalization of the data by size and shell thickness. One reason for

this spread can be due to differences in the shell density caused by kinetic differences during the shell formation. Salaun and co-workers<sup>50</sup> showed that different surface morphologies of the capsules shell are dependent on the formation of the melamine formaldehyde precondensate. They concluded that a rather rapid shell formation will yield higher oligomers or even small melamine formaldehyde particles in the continuous phase, which will be deposited at the oil/water interface<sup>32, 50</sup>. The melamine to formaldehyde ratio, pH and temperature were identified as important parameters to affect the kinetics of the precondensate formation. Based on the formed oligomers, which represent the building blocks of the shell, a rougher or smoother capsule shell is obtained<sup>12</sup>. From this perspective and based on the results of our mechanical characterization we think that the size of the formed oligomers and their assembly to a shell is an important aspect for shell mechanics that would be of interest for further studies.

#### **7.4 Conclusion**

In conclusion, we showed how mechanical properties of aminoplast microcapsules correlate with process parameters for an industrially relevant microencapsulation process, the in situ polymerization of amino resins. With the help of a thorough morphological analysis we were able to determine the microcapsule's geometric parameters, radius and shell thickness. The mechanical response of the microcapsules was investigated in form of small deformations on the order of the shell thickness, using an AFM and the colloidal probe technique. Both results, from geometrical and micromechanical characterization, were explained in the framework of a simple analytical model for microcapsule deformation, the Reissner shell theory. Based on the results, we identified the ratio of amino resin to total emulsion surface area as key parameter for controlling the microcapsules geometry and mechanical properties. Thus, a rational design of mechanical properties of aminoplast microcapsules is in reach.

## References

1. Sukhorukov, G.; Fery, A.; Möhwald, H., *Progress in Polymer Science* **2005**, 30, (8-9), 885-897.
2. Becker, A. L.; Johnston, A. P. R.; Caruso, F., *Small* **2010**, 6, (17), 1836-1852.
3. Nelson, G., *Int. J. Pharm.* **2002**, 242, (1-2), 55-62.
4. Madene, A.; Jacquot, M.; Scher, J.; Desobry, S., *Int. J. of Food Sci. Technol.* **2006**, 41, (1), 1-21.
5. Jacquemond, M.; Jeckelmann, N.; Ouali, L.; Haefliger, O. P., *J. Appl. Polym. Sci.* **2009**, 114, (5), 3074-3080.
6. Rokka, S.; Rantamaki, P., *Eur. Food Res. Technol.* **2010**, 231, (1), 1-12.
7. Sanchez, L.; Lacasa, E.; Carmona, M.; Rodriguez, J. F.; Sanchez, P., *Ind. Eng. Chem. Res.* **2008**, 47, (23), 9783-9790.
8. Mauldin, T. C.; Kessler, M. R., *Int. Mat. Rev.* **2010**, 55, (6), 317-346.
9. Quellet, C.; Schudel, M.; Ringgenberg, R., Flavors & Fragrance Delivery Systems. In *Chimia*, 2001; 55, 421-428.
10. Dietrich, K.; Herma, H.; Nastke, R.; Bonatz, E.; Teige, W., *Acta Polym.* **1989**, 40, (4), 243-251.
11. Haefliger, O. P.; Jeckelmann, N.; Ouali, L.; Leòn, G., *Anal. Chem.* **2010**, 82, (2), 729-737.
12. Lee, H. Y.; Lee, S. J.; Cheong, I. W.; Kim, J. H., *Journal of Microencapsulation* **2002**, 19, (5), 559-569.
13. Sgraja, M.; Blömer, J.; Bertling, J.; Jansens, P. J., *J. Appl. Polym. Sci.* **2008**, 110, (4), 2366-2373.
14. Su, J.-F.; Wang, L.-X.; Ren, L.; Huang, Z., *J. Appl. Polym. Sci.* **2007**, 103, (2), 1295-1302.
15. Yuan, Y. C.; Rong, M. Z.; Zhang, M. Q., *Polymer* **2008**, 49, (10), 2531-2541.
16. Balazs, A. C., *Mater. Today* **2007**, 10, (9), 18-23.
17. Sliwka, W., *Angew. Chem., Int. Ed.* **1975**, 14, (8), 539-550.
18. Roitman, D. B. US 07312040, Dec 26 **2007**.
19. Esser-Kahn, A. P.; Odom, S. A.; Sottos, N. R.; White, S. R.; Moore, J. S., *Macromolecules* **2011**, 44, (14), 5539-5553.
20. Fery, A.; Weinkamer, R., *Polymer* **2007**, 48, 7221-7235.
21. Chen, P. W.; Erb, R. M.; Studart, A. R., *Langmuir* **2011**, 28, (1), 144-152.
22. Keller, M. W.; Sottos, N. R., *Exp. Mech.* **2006**, 46, (6), 725-733.
23. Zhang, Z.; Saunders, R.; Thomas, C. R., *Journal of Microencapsulation* **1999**, 16, (1), 117-124.
24. Hu, J. F.; Chen, H. Q.; Zhang, Z. B., *Mater. Chem. Phys.* **2009**, 118, (1), 63-70.
25. Long, Y.; York, D.; Zhang, Z. B.; Preece, J. A., *J. Mater. Chem.* **2009**, 19, (37), 6882-6887.
26. Sun, G.; Zhang, Z., *Journal of Microencapsulation* **2001**, 18, (5), 593-602.

27. Yang, J.; Keller, M. W.; Moore, J. S.; White, S. R.; Sottos, N. R., *Macromolecules* **2008**, 41, (24), 9650-9655.
28. Caruso, M. M.; Blaiszik, B. J.; Jin, H. H.; Schelkopf, S. R.; Stradley, D. S.; Sottos, N. R.; White, S. R.; Moore, J. S., *ACS Appl. Mater. Interfaces* **2010**, 2, (4), 1195-1199.
29. Mercade-Prieto, R.; Nguyen, B.; Allen, R.; York, D.; Preece, J. A.; Goodwin, T. E.; Zhang, Z. B., *Chemical Engineering Science* **2011**, 66, (10), 2042-2049.
30. Elsner, N.; Dubreuil, F.; Fery, A., *Phys Rev E* **2004**, 69, (3), 6.
31. Arshady, R.; George, M. H., *Polym. Eng. Sci.* **1993**, 33, (14), 865-876.
32. Dietrich, K.; Bonatz, E.; Geistlinger, H.; Herma, H.; Nastke, R.; Purz, H. J.; Schlawne, M.; Teige, W., *Acta Polym.* **1989**, 40, (5), 325-331.
33. Hong, K.; Park, S., *Mater. Chem. Phys.* **1999**, 58, (2), 128-131.
34. Alic, B.; Sebenik, U.; Krajnc, M., *J. Appl. Polym. Sci.* **2010**, 119, (6), 3687-3695.
35. Yuan, L.; Liang, G. Z.; Xie, J. Q.; Li, L.; Guo, J., *Polymer* **2006**, 47, (15), 5338-5349.
36. Sun, G.; Zhang, Z., *Int. J. Pharm.* **2002**, 242, (1-2), 307-311.
37. Dubreuil, F.; Elsner, N.; Fery, A., *Eur. Phys. J. E* **2003**, 12, (2), 215-221.
38. Butt, H. J., *Biophys. J.* **1991**, 60, (6), 1438-1444.
39. Ducker, W. A.; Senden, T. J.; Pashley, R. M., *Nature* **1991**, 353, (6341), 239-241.
40. Hutter, J. L.; Bechhoefer, J., *Rev. Sci. Instrum.* **1993**, 64, (7), 1868-1873.
41. Elsner, N.; Dubreuil, F.; Weinkamer, R.; Fischer, F. D.; Wasicek, F.; Fery, A., *Prog. Coll. Polym. Sci.* **2006**, 132, 117-132.
42. Butt, H. J.; Cappella, B.; Kappl, M., *Surf. Sci. Rep.* **2005**, 59, (1-6), 1-152.
43. Yuan, L.; Gu, A.; Liang, G., *Mater. Chem. Phys.* **2008**, 110, (2-3), 417-425.
44. Wang, H.; Yuan, Y.; Rong, M.; Zhang, M., *Colloid Polym. Sci.* **2009**, 287, (9), 1089-1097.
45. Smith, A. E.; Zhang, Z.; Thomas, C. R., *Chemical Engineering Science* **2000**, 55, (11), 2031-2041.
46. Fery, A.; Dubreuil, F.; Mohwald, H., *New J Phys* **2004**, 6, 18.
47. Reissner, E., *Journal of Mathematics and Physics* **1946**, 25, (4), 279-300.
48. Reissner, E., *Journal of Mathematics and Physics* **1946**, 25, (2), 80-85.
49. Zoldesi, C. I.; Ivanovska, I. L.; Quilliet, C.; Wuite, G. J. L.; Imhof, A., *Phys. Rev. E* **2008**, 78, (5), 8.
50. Salaun, F.; Vroman, I., *Eur. Polym. J.* **2008**, 44, (3), 849-860.



## List of Abbreviations and Symbols

$E_c$	2 dimensional elastic modulus// cortical tension
$E_s$	2-dimensional elastic modulus
$A$	Area
$K_A$	Area Elastic Modulus
AFM	Atomic Force Microscopy
$\epsilon_n$	Axial Strain
$E_{\text{bend}}$	Bending Energy
$k_{\text{bend.}}$	Bending Rigidity
$\kappa$	Bending Stiffness
$k_B$	Boltzmann Constant
$K$	Bulk Modulus
$\epsilon_b$	Bulk Strain
$\sigma_b$	Bulk Stress
$R_c$	Capsule Radius
$f$	Correction Factor
$\pi_c$	Critical Osmotic Pressure
$Z_c$	Deflection
$\delta$	Deformation
$\rho_f$	Density of Fluid
DSC	Differential Scanning Calorimetry
$K_s$	Dilation Modulus
$E$	Elastic Modulus, Young's Modulus
$\mu$	Elasticity Modulus
$\Delta L$	Elongation
$l_{1,2}$	Extension Ratios
$\chi$	Extensional Stiffness
FEM	Finite Element Modeling
$\gamma$	Föppl-von Kármán Number
$F$	Force
$H$	Height
$Z_p$	Height Position of the Piezo
$\Gamma$	Hydrodynamic Function
InvOLS	Inverted Optical Lever Sensitivity

## List of Abbreviations and Symbols

---

K	Compression Modulus
$\epsilon_n^l$	Lateral Strain
LbL	Layer - by - Layer
L	Length
MRI	Magnetic Resonance Imaging
I	Major Axis
MBs-chem	MBs with SPIONs chemically attached
MBs-phys	MBs with SPIONs physically embedded
$d_{\text{mean}}$	Mean Diameter
$h_i$	Measured Shell Thickness
MF	Melamine Formaldehyde
MB	Microbubble
b	Minor Axis
N	Newton
$F_n$	Normal Force
$\epsilon_n$	Normal Strain
$\sigma_n$	Normal Stress
n	Number
Pa	Pascal
v	Poisson Ratio
PVA	Poly(vinyl alcohol)
PAH	Polyallylaminhydrochlorid
PDADMAC	Polydiallyldimethylammoniumchlorid
PEM	Polyelectrolyt Multilayer
PEMC	Polyelectrolyt Multilayer Capsules
PSS	Polystyrenesulfonate
PSD	Position Sensitive Detector
$\Delta P$	Pressure
$T_{1,2}$	Principle Tension
Q	Quality Factor
R	Radius
R	Radius of Curvature
$R_p$	Radius of Pipette
RICM	Reflection Interference Contrast Microscopy
$\Delta$	Relative Deformation
$\omega_0$	Resonance Frequency
Re	Reynold's Number
SNOM	Scanning Near Field Optical Microscopy

SPM	Scanning Probe Microscopes
STXM	Scanning Transmission X-ray Microscopy
STM	Scanning Tunneling Microscopy
$\Delta x$	Separation Distance
$G$	Shear Modulus
$\gamma$	Shear Rate
$\epsilon_t$	Shear Strain
$\sigma$	Shear Stress
$\sigma_t$	Shear Stress
$h$	Shell Thickness
$k_c$	Spring Constant
$k_{shell}$	Spring Constant of the Shell
$m^2$	Square Meters
$\sigma$	Standard Deviation
$F/D$	Stiffness
$\sigma$	Stress
$E_{stretch}$	Stretching Energy
SPIONs	Super-Paramagnetic Nanoparticles
$A_{surface}$	Surface Area
$\nu_s$	Surface Poisson Ratio
$F_t$	Tangential Force
$T$	Temperature
$\rho$	Density
$t_c$	Thickness of Cantilever
$U$	Total Deformation Energy
TEM	Transmission Electron Microscopy
US	Ultrasound
$\Delta v$	Velocity
$\eta$	Viscosity
$V$	Volume
$w$	Width
$\xi$	Zeta-Potential



---

## List of Publications

1. **A Lithography-Free Pathway for Chemical Microstructuring of Macromolecules from Aqueous Solution Based on Wrinkling.** M. Pretzl, A. Schweikart, C. Hanske, A. Chiche, U. Zettl, A. Horn, A. Boker, A. Fery; *Langmuir*, **2008**, 24, (22), 12748-12753.
2. **Novel Characterization Techniques of Microballoons.** P. Fernandes, M. Pretzl, A. Fery, G. Tzvetkov, R. Fink; In *Ultrasound Contrast Agents*, Editors: G. Paradossi, P. Pellegritti, A. Trucco, Springer Milan **2010**, 109-127.
3. **Systematic Modification of the Rheological Properties of Colloidal Suspensions with Polyelectrolyte Multilayers.** A. Hess, M. Pretzl, L. Heymann, A. Fery, N. Aksel; *Physical Review E*, **2011**, 84, (3), 031407.
4. **Evolution and Control of Complex Curved Form in Simple Inorganic Precipitation Systems.** M. Kellermeier, J. Eiblmeier, E. Melero-Garcia, M. Pretzl, A. Fery, W. Kunz; *Crystal Growth & Design*, **2012**, 12, (7), 3647-3655.
5. **Formation and Mechanical Characterization of Aminoplast Core/Shell Microcapsules.** M. Pretzl, M. Neubauer, M. Tekaat, C. Kunert, C. Kuttner, G. Leon, D. Berthier, P. Erni, L. Ouali, A. Fery, *ACS Applied Materials & Interfaces*, **2012**, 4(6), 2940-2948.
6. **On the Interplay of Shell Structure with Low and High-Frequency Mechanics of Multifunctional Magnetic Microbubbles.** M. Poehlmann, D. Grishenkov, S. V.V.N. Kothapalli, J. Harmark, H. Hebert, A. Philipp, R. Hoeller, M. Seuss, C. Kuttner, S. Margheritelli, G. Paradossi, Andreas Fery; *Soft Matter*, **2014**, 10 (1), 214 - 226.
7. **Microcapsule Mechanics: From Stability to Function.** M. Neubauer, M. Poehlmann, A. Fery; *Advances in Colloid and Interface Science*, **2014**, 207, 65-80.

## List of Conference Contributions

### Oral Presentations:

1. **Micromechanics and Adhesion Properties of Smart Polymeric Microballoons studied by Colloidal Probe AFM and Microinterferometry**, M. Poehlmann, P. Fernandes, A. Fery, *12<sup>th</sup> European Student Conference (ESC)*, **2009**, Almeria, Spain.
2. **Micromechanics, Adhesion and Shell Properties of PVA MBs**.  
M. Pretzl, A. Fery, *Spring Meeting of Cost D43: Colloid and Interface Chemistry for Nanotechnology*, **2011**, Madrid, Spain.
3. **Magnetic microbubbles for multimodality imaging: The importance of the shell structure for low and high frequency mechanics**  
M. Poehlmann, S.V.V.N Kothapalli, D. Grishenkov, J. Haermark, H. Hebert, A. Philipp, R. Hoeller, M. Seuss, S. Magerithelli, G. Paradossi, A. Fery, *Proceeding of European Symposium on Biomaterials and Related Areas*, **2013**, Weimar, Germany.

### Poster Presentations:

1. **Microstructured surfaces for templating colloidal particle assembly**,  
*DPG Frühjahrstagung*, **2008**, Berlin, Germany.
2. **Microballoon arrays on patterned substrates**, *107. Bunsen Tagung*,  
**2008**, Saarbrücken, Germany.
3. **AFM Imaging and Force Spectroscopy Combined with Optical Technique**, *22. Conference of the European Colloid and Interface Society*,  
**2008**, Kraków, Poland.
4. **Adhesion of microbubbles studied by AFM and RICM**, *7. SPM Science Symposium*, Berlin, **2008**, Berlin, Germany.
5. **Adhesion of microbubbles studied by AFM and RICM**, *5. Zigmondy Kolloquium*, **2009**, Bayreuth, Germany.
6. **Adhesion Properties of Polymer MBs studied with AFM and RICM**,  
*DPG Frühjahrstagung*, **2009**, Dresden, Germany.

7. **Adhesion Properties of Polymer MBs studied with AFM and RICM**, *Frontiers in Polymer Science*, **2009**, Mainz, Germany.
8. **Micromechanics and Adhesion Properties of Smart Polymeric Microballoons**, *12<sup>th</sup> European Student Conference (ESC)*, **2009**, Almeria, Spain.
9. **Micromechanics and Adhesion Properties of Smart Polymeric Microballoons**, *23. Conference of the European Colloid and Interface Society*, **2009**, Antalya, Turkey.
10. **Smart Polymeric Gas-filled PVA Microballoons – Shell Properties, Micromechanics and Adhesion**, *3<sup>rd</sup> European Chemistry Congress EuCheMS*, **2010**, Nurnberg, Germany.
11. **Microballoons: Gas-tight Particles with a Soft Polyvinyl alcohol Shell**, *24. Conference of the European Colloid and Interface Society (ECIS)*, **2010**, Prague, Czech Republic.
12. **Multimodality Contrast Agents: Micromechanics, Adhesion and Shell Properties**, *Particles 2011 – Stimuli-Responsive Particles and Particle Assemblies*, **2011**, Berlin, Germany.



## Danksagung

Am Ende ist eine Doktorarbeit nicht nur ein gebundenes Buch sondern eine besondere Erfahrung im Leben, die einen verändert hat. Zu den schönsten Veränderungen zählen die Menschen, die man während dieser Zeit kennenlernen durfte. Einige davon haben sich zu unverzichtbaren Mentoren, wunderbaren Freunden und wichtigen Diskussionspartnern entwickelt. Deswegen möchte ich mich am Ende dieser Arbeit bei all jenen bedanken, die zum Gelingen dieser Doktorarbeit beigetragen haben.

Zuallererst möchte ich mich bei meinem Doktorvater Prof. Dr. Andreas Fery bedanken. Die Aufnahme an der Universität Bayreuth, in der Physikalischen Chemie II, war der Start dieser spannenden Phase. Es hat mir sehr viel Freude bereitet auf diesem anwendungsrelevantem Thema zu arbeiten. Die Erfahrung meine Forschungsergebnisse in einer interdisziplinären Gruppe europäischer Wissenschaftler aus Hochschulen und Unternehmen zu diskutieren, und dies auch noch oft an sehr schönen Orten in Europa wie zum Beispiel Genf, Stockholm, Dublin, oder Rom, war großartig und wird mir sicherlich lange in positiver Erinnerung bleiben. Mein besonderer Dank gilt v.a. den wissenschaftlichen, philosophischen und strategischen Diskussionen, die mich motiviert und weitergebracht haben. Herzlichen Dank dafür Andreas!

Eine Doktorarbeit ist ohne finanzielle Unterstützung nicht möglich. Hier gilt mein Dank zum einem der Europäischen Kommission. Ohne sie hätte dieser interdisziplinäre, internationale und wissenschaftliche Austausch nicht stattgefunden. Aus diesem Grund sind hier das FP6-IST-033700 Projekt SIGHT *Systems for in-situ theranostics using micro-particles triggered by ultrasound* und das FP7-NMP-2009-LARGE-245572 Projekt 3MiCRON *Three modality contrast imaging using multifunctionalized microballoons* zu nennen. Für die offene und herzliche Atmosphäre in unserem EU-Konsortium möchte ich mich bei allen Kooperationspartnern bedanken. Mein besonderer Dank gilt Dr. habil. Lars Dähne von der Surflay Nanotec GmbH und Prof. Dr. Gaio Paradossi von der Universität Tor Vergata. Für weitere finanzielle Unterstützung möchte ich mich bei Firmenich SA bedanken, sowie für das spannende gemeinsame Projekt. Dr. Ouali Lahoussine, Dr. Damien Berthier, Géraldine Leon

und Dr. Phillip Erni möchte ich für die offene und unkomplizierte Zusammenarbeit danken. Dr. Phillip Erni möchte ich danken für die hilfreichen Anregungen und die konstruktive Kritik während des Schreibens des gemeinsamen Manuskripts.

Wer die Doktorarbeit gelesen hat, hat sicherlich bemerkt, dass Einzel-Partikel-Experimente sehr zeitaufwendig sind und man für eine signifikante Statistik eine Menge Messungen braucht. Ganz herzlich möchte ich mich deswegen an dieser Stelle bei Nicolas Helfricht, Melanie Tekaas, Alexandra Philipp, Roland Höller und Maximilian Seuss bedanken, die Ihre Bachelorarbeit engagiert und interessiert auf meinem Doktorarbeitsthema absolviert haben. Martin Neubauer, der das Kapselthema fortführt und Christian Kuttner, der es immer wieder punktuell begleitet hat möchte ich ebenfalls ganz herzlich danken für zahlreiche Diskussionen zum Thema Mikromechanik sowie dem Korrekturlesen von Forschungsberichten, Publikationen und der Doktorarbeit.

Meine Doktorarbeit an der PCII wurde außerdem durch eine familiäre Atmosphäre, passende jahreszeitliche Dekoration, Dienstagsjogging, Lehrstuhlkochkurse tägliche Gummibärchenversorgung, Lehrstuhl-Frühstück bzw. Grillabend und einen perfekten Durchblick bei allen administrativen Abläufen unterstützt. Ganz herzlichen Dank dafür liebe Sybille Zimmermann! Herzlichen Dank auch an Sybille, Petra, Carmen und Undine für die immer wieder schönen Außenseminare.

Arbeitskollegen, die zu wunderbaren Freunden geworden sind, haben die Zeit an der Universität Bayreuth zusätzlich bereichert. Vielen Dank an dieser Stelle an Dr. Öznur Kaftan, Dr. Eva Max, Dr. Daniel Kluge, Benedikt Neugirg, Dr. Johann Erath, Dr. Nathalie Mougin, Dr. Maria Sanchez Luz, Dr. Martin Neubauer, Dr. Christian Kutter, Bernhard Glatz, Dr. Heiko Schoberth, Moritz Tebbe, Christoph Hanske, Dr. Munish Chanana, Dr. Kerstin Schindler, Nicole Popp, und vielen mehr...

Zuletzt möchte ich mich bei meiner Familie bedanken, die mir das Beginnen, Durchführen und auch das Beenden dieser Arbeit ermöglicht hat. Neben meinen Eltern und meinen beiden Schwestern, möchte ich auch meinen Großeltern Erika, Siegfried, Anneliese und Franz, und der Familie meines Patenkindes Magdalena, Christine, Norbert, Elisa und Benjamin dafür danken, dass mich diese große wundervolle Familie schon ein Leben lang in allen Lebenssituationen unterstützt hat und es mir dadurch ermöglicht hat meine Wünsche zu verwirklichen. Vielen lieben

Dank Euch Allen! Meinen Schwiegereltern Arno und Theresa möchte ich ebenfalls herzlich danken, dass sie mich beim Beenden und Durchhalten dieser Arbeit unterstützt haben. Mein größter Dank gilt meinem geliebten Mann, Tobi, der immer für mich da war, mich stets motiviert hat und mir unvergessliche Erinnerungen beschert hat – wie z.B. Hochzeit, Afrika-Safari und Angelschein.

Vielen Dank!

## **Eidesstaatliche Versicherungen und Erklärungen**

(§ 5 Nr. 4 PromO)

Hiermit erkläre ich, dass keine Tatsachen vorliegen, die mich nach der gesetzlichen Bestimmung über die Führung akademischer Grade zur Führung des Doktorgrades unwürdig erscheinen lassen.

(§8 S. 2 Nr. 5 PromO)

Hiermit erkläre ich mich damit einverstanden, dass die elektronische Fassung meiner Dissertation unter Wahrung meiner Urheberrechte und des Datenschutzes einer gesonderten Überprüfung hinsichtlich der eigenständigen Anfertigung der Dissertation unterzogen werden kann.

(§8 S. 2 Nr. 7 PromO)

Hiermit erkläre ich eidesstattlich, dass ich die Dissertation selbstständig verfasst und keine anderen als die von mir angegebenen Quellen und Hilfsmittel benutzt habe. Ich habe die Dissertation nicht bereits zur Erlangung eines akademischen Grades anderweitig eingereicht und habe auch nicht bereits diese oder eine gleichartige Doktorprüfung endgültig nicht bestanden.

(§8 S.2 Nr. 9 PromO)

Hiermit erkläre ich, dass keine Hilfe von gewerblichen Promotionsberatern bzw. -vermittlern in Anspruch genommen habe und auch künftig nicht nehmen werde.

.....

Ort, Datum, Unterschrift